

RICE UNIVERSITY

**Engineering the Structural Properties of Self-assembled
Polymer/Nanoparticle Capsules**

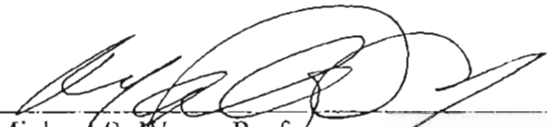
by

Shyam Benegal (Benny) Kadali


A THESIS SUBMITTED
IN PARTIAL FULFILLMENT OF THE
REQUIREMENTS FOR THE DEGREE

Doctor of Philosophy

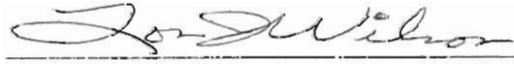
APPROVED, THESIS COMMITTEE:



Michael S. Wong, Professor
Chemical and Biomolecular Engineering, Chemistry



Sibani Lisa Biswal, Assistant Professor
Chemical and Biomolecular Engineering



Lon J. Wilson, Professor
Chemistry

HOUSTON, TEXAS

MAY 2011

ABSTRACT

Engineering the Structural Properties of Self-assembled Polymer/Nanoparticle Capsules

by

Shyam Benegal (Benny) Kadali

A materials synthesis technique was recently developed to generate polymer/nanoparticles composite microcapsules in which synthetic polyamines such as polyallylamine and/or polylysine were crosslinked with multivalent anions to form polymer-salt aggregates, that then served as templates for deposition of nanoparticles (NPs) of various compositions to form micron-sized hollow spheres or "nanoparticle-assembled capsules" (NACs). This electrostatically-driven "polymer-salt aggregate" or "PSA" assembly route is attractive for encapsulation and scale-up because encapsulation and materials formation occur in water, at mild pH values, and at room temperature. NACs can potentially find wide-ranging applications in pharmaceutical, food, and consumer products.

It is of crucial importance to address the physical property aspects of NACs in view of their use and applicability. While most applications may require that NACs not disassemble or deform under shear stress, some may require triggered release under specific conditions to release the encapsulated material (e.g., enzymes or drugs). Comparatively, little has been done to assess the physical properties of NACs. The behavior of NACs under varying pH and ionic strength conditions were determined. The capsules were found to be structural intact in the pH range of 4-9 at an ionic strength of 10 mM. The pH range in which they were intact narrowed with increasing ionic strength;

the capsules fragmented into smaller pieces at 500 mM. The NACs could be made stable at ionic strengths as high as 1M by the addition of multivalent anions to the suspending fluid. The structurally intact NACs were found to vary in compressive strength from 1 atm to $> \sim 25$ atm, via osmotic pressure studies.

The benign assembly conditions of NACs allowed for encapsulation studies of various molecules such as fluorescein, $\text{Gd}[\text{DOTP}]^{5-}$ (MRI contrast agent), doxorubicin (an anticancer drug), and uracil (pharmaceutical drug with anticancer properties). X-ray irradiation was studied as a potential external trigger for cargo release. A thorough experimental analysis on diffusive release of a dye molecule (fluorescein) from NACs was carried out.

Manipulation of the PSA assembly process was carried out in several studies to explore the generality of the synthesis method. Positively-charged aluminosilicate NPs were studied in place of negatively-charged silica NPs. Surprisingly, these led to solid microspheres instead of hollow microspheres. Following the diffusion-deposition model for microsphere formation, it seems that the NPs, with positively charged alumina patches on top of a negatively charged silica surface, can fully penetrate into the polymer-salt aggregate to form the solid microspheres.

The viscoelastic nature of polymer-salt aggregates was exploited to produce non-sphere-shaped NACs through the use of a high-shear flow instrument (Reynolds number of $\sim 21,000$). A mathematical model was developed to understand the formation of elongated NACs, which indicated the shear and elongational stresses within the boundary layer zones along the flow channel walls were responsible for the observed formation of rod-like microparticles.

ACKNOWLEDGMENTS

I would like to thank many people who had an impact on my dissertation, research and on me personally. I wish to express my deep gratitude to Prof. Michael S. Wong, for being an excellent mentor, and advisor. I am very thankful for his encouragement, support, and flexibility. I appreciate the multiple opportunities he gave me to work on during my stay at Rice. In addition to the scientific training and motivation, his pragmatic solutions and understanding towards other life aspects had a remarkable influence on my entire research career. I could not have accomplished my work without his dedication

I appreciate members of my thesis committee, Prof. Biswal and Prof. .Wilson for technical discussions, suggestions, and constant academic support throughout my graduate studies. I would like to express my warm and sincere gratitude to my collaborators Dr. McGary (Baylor), Enrique Munoz, Dr. Sherry (UT-Dallas), Prof. Woods (Portland State University), Jamison, Dr. Matthews, and Dr. Colvin.

I specially thank Prof. Biswal, Prof. Li for granting me access to their labs to use their instruments. I thank Prof. Tomson and Prof. Pasquali for technical discussions. I am very grateful to Prof. Hirasaki, Prof. Miller, and Prof. Nagrath for fruitful discussions all sorts of interesting topics both technical and not technical, for their advices. I would like to thank my undergraduate student Amy Liu. She has worked incredibly hard on various projects with me. Special thanks to Vinit Murthy, for his guidance and mentoring me during my first year. I would like to acknowledge Paco for his support, encouragement, willingness to help me with thermodynamics.

I would like to thank the current and former staff of the Chemical and Biomolecular Engineering department at Rice. I am deeply grateful to Dr. Adria Baker, from the OISS.

My appreciation goes to my colleagues and excellent friends Sushant, Khapli, Vivek, Sandeep, Jose, Ruiqiang, Jie, Arjun, Arshad, Jay, Bishnu, Jeyram, Pramit, Andreas, Goutham, Murali, Abhishek Shetty, Argod, Tilok, Priyank–Vandana, Hemanth, Niranjana, Phani (Bussu), for technical and non-technical assistance, constant feedback, interesting chats and unconditional friendship. I thank Hitesh for his suggestions and guidance how to manage and handle things, always being open for discussions on any issue. Special thanks to Gautam Kini, Nurgul for their support especially during my PhD proposal. I thank all of my current and past lab members for their support. I enjoyed discussions and humor of Nikos, Yu-lun, Quang, Sukit, and Juan. I would like to thank Lori for always being ready to correct my drafts and helping me to improve my resume/curriculum vitae. Thanks to all my NITK students at Rice for their support.

I would like to convey my special thanks to my uncle Mediseti Tirumala Kumar (income tax commissioner, Bangalore) for inspiring me right from my childhood and standing as a role model. I am very thankful to M.V.S. Brahmaji sir (Narayana Educational Institutions' IIT academic in-charge, Vijayawada) for always encouraging me to aim high and supporting me during my intermediate days. I am always indebted especially to Prof. Srinikethan (NITK) for encouraging me to pursue my doctorate in chemical engineering. Thanks to Dr. Sitaraman (Scientist, DRDO, India) and Dr. Kitko (P&G) for motivation and encouragement. Thanks to Prof. Pushpavanam (IIT-Madras) for his support and guidance during my grad school applications. I thank all my current and former members of our research group.

I am deeply thankful to my parents Satyanarayana, Rama Tulasi, and my in-laws Venkata Rao, and Vijaya Bharathi for their love, constant support and encouragement:

My brothers, Dr. Prasad and Ravi Sastry, for being supportive and a good example of hard-work and sincerity. My sister-in-law, Alekhya for always being proud of my achievements and would always be ready to do whatever I ask her. Their endless love, listening, understanding, intelligence, and great sense of humor, has helped me to get through the difficult times and provided me with further motivation to complete this work. I would like to thank the Babuji anna and the Mashetty anna families for their support and encouragement. Thanks to Rice University badminton club members for lot of fun during our badminton sessions. And last but most importantly, I heartily express my endless gratitude to my wife Babita, for her source of unconditional love, constant support, motivation and encouragement. Without these many friends, co-workers, and family friend, I would not have gone this far.

This thesis is dedicated to my mom & dad and all the members of my KADALI family.

TABLE OF CONTENTS

Abstract	ii
Acknowledgements	iv
Table of Contents	vii
List of Tables	xi
List of Figures	xii
Chapter 1. Introduction	1
1.1. Background and research motivation	1
1.2. Synthesis approaches to hollow spheres	2
1.2.1. Sacrificial core method or layer-by-layer (LbL) assembly technique	2
1.3. Responsive LbL capsules	5
1.3.1. pH responsive capsules	5
1.3.2. Salt responsive capsules	6
1.3.3. Light-responsive capsules	7
1.3.4. Magnetic field responsive capsules	8
1.3.5. Osmotic pressure responsive capsules	10
1.4. Research motivation and thesis layout	11
1.4.1. Current challenges in PSA assembly	15
1.4.1. Thesis layout	16
1.4.2. Other works	19
1.5. References	22
Chapter 2. Assembling colloidal particles into porous hollow and solid microspheres	35
2.1. Introduction	35
2.2. Experimental Methods	38
2.2.1. Materials	38
2.2.2. Synthesis	39
2.2.3. Characterization	41
2.3. Results and Discussion	44

2.3.1. Effect of dilution of colloidal SiO ₂ precursor.....	44
2.3.1. Effect of surface charge of polymer-salt aggregates	46
2.3.2. Calcined NACs	48
2.3.3. Synthesis of aluminosilicate spheres	53
2.3.4. Effect of surface charge of polymer-salt aggregates	54
2.3.5. Effect of first aging time or floc aging time	58
2.3.6. TGA and effect of calcination on aluminosilicate spheres.....	59
2.3.7. Nitrogen adsorption studies	61
2.4. Conclusions	62
2.5. References	64

Chapter 3. Ionic strength and pH effects on nanoparticle-polyamine microcapsules	68
3.1. Introduction.....	68
3.2. Experimental Methods	71
3.2.1. Materials	71
3.2.2. PAH volumetric titrations	73
3.2.3. Synthesis of NACs.....	73
3.2.4. pH and Ionic strength stability studies.....	73
3.2.5. Osmotic pressure studies.....	74
3.2.6. Ionic strength study using multivalent anions.....	74
3.2.7. Characterization	75
3.3. Results and discussions.....	76
3.3.1. pH effect.....	76
3.3.2. Ionic strength effect	81
3.3.3. pH and ionic strength effects on mechanical strength	83
3.3.4. Effect of multivalent anions.....	87
3.3.5. Rescue of NACs by addition of multivalent anions.....	88
3.3.6. NACs stability in PBS and in sea water (Gulf of Mexico, Galveston, TX, USA).....	89
3.4. Conclusions.....	90
3.5. References.....	92

Chapter 4. Encapsulation and responsive studies of capsules	99
4.1. Introduction	99
4.2. Experimental Methods	100
4.2.1. Materials	100
4.2.2. Synthesis of NACs	101
4.2.3. Synthesis of dye-encapsulated NACs.....	101
4.2.4. Dye release study.....	102
4.2.5. Gd- NAC Synthesis	102
4.2.6. Encapsulation of Uracil	103
4.2.7. Encapsulation of Doxorubicin.....	104
4.2.8. Synthesis of Fe ₃ O ₄ NPs	104
4.2.9. Synthesis of Fe ₃ O ₄ – NACs.....	105
4.2.10. Encapsulation of indocyanine green (ICG) in Fe ₃ O ₄ -NACs	105
4.2.11. Characterization.....	106
4.3. Results and discussions	107
4.3.1. Experimental analysis of dye-containing capsule structure	107
4.3.2. Experimental dye release data	113
4.3.3. Synthesis of gadolinium encapsulated nanoparticle assembled capsules.....	116
(Gd-NACs)	116
4.3.4. Encapsulation of Uracil and Doxorubicin	121
4.3.5. Concept of X-ray-sensitive capsules	123
4.3.6. Polyamine - Iron oxide composite microcapsules and responsive studies....	126
4.3.7. Responsive to pH and salt	133
4.3.8. Responsive to physical pressure and temperature	134
4.4. Conclusions	135
4.5. References	137
Chapter 5. Formation of elongated nanoparticle/polyamine-assembled microcapsules using microfluidizer	143
5.1. Introduction.....	143

5.2. Experimental methods	146
5.2.1. Materials	146
5.2.2. Synthesis of elongated NACs	146
5.2.3. Characterization	147
5.3. Results and discussions.....	148
5.3.1. Formation of polymer-composite elongated structures	148
5.3.2. Effect of pressure.....	149
5.3.3. Mathematical model.....	151
5.3.4. Impact of high shear zone on polymer-salt aggregates elongation.....	159
5.3.5. Effect of polymer-salt aggregate size.....	161
5.3.5. Formation of polymer composite micro-wires.....	164
5.4. Conclusions.....	165
5.5. References.....	168
Chapter 6. Summary and recommendations for future work	174
6.1. Recommendations.....	175
6.1.1. Mechanical properties of single NAC using molecular force probe technique	175
6.1.2. Concept of reverse charge assembly	178
6.1.3. Thermo-sensitive NACs.....	180
6.1.4. NACs to encapsulate MRI contrast agents	181
Appendix A. Ionic strength and pH effects on nanoparticles-polyamine microcapsules	182
Appendix B. Quartz crystal microbalance-(QCM-D) for determining diffusion coefficient of various molecules in polymer-salt film systems	187
Appendix C. Mathematical modeling for understanding the formation of elongated NACs	203

LIST OF TABLES

Table 2. 1. Summary of nitrogen physisorption calculations.....	52
Table 2. 2. Summary of nitrogen physisorption calculations.....	62
Table 4. 1. Amount of Na-Flu released from 1.5 ml of NACs solution. The reported values are within an error of $\pm 6\%$	114
Table 4. 2. Percentage encapsulation of Na-Flu in NACs. Various initial amounts of Na-Flu were added in synthesis of dye-encapsulated NACs. The reported values are within an error of $\pm 6\%$	114
Table 4. 3. Percentage encapsulation of uracil in NACs. Various initial amounts of uracil were added in synthesis of encapsulated NACs.	121
Table 4. 4. Percentage encapsulation of doxorubicin in NACs. Various initial amounts of doxorubicin were added in synthesis of encapsulated NACs.	122
Table B.1. Summary of QCM-D Results.....	196

LIST OF FIGURES

- Figure 1.1. Sacrificial core templating method to prepare hollow spheres.¹¹ 4
- Figure 1.2. Open (a, c) at pH 3.5 and closed (b, d) at pH 10 states of polyelectrolyte shells prepared on melamine formaldehyde (MF) particles (a, b) and CdCO₃ crystals (c, d).⁹³ .. 6
- Figure 1.3. Scheme of encapsulation and release of macromolecules through the switching of the permeability by means of the salt concentration. The black and dark gray lines represent the polyelectrolytes of the capsule wall and the bright gray lines are the probe polymers.⁹⁴ 7
- Figure 1.4. E_{FRET} in dependence of the salt concentration for capsules containing PAH-fluo in the 10th layer and PAH-rho in the 12th layer. The dashed line represents a sigmoidal fit of the experimental results. The inset shows the fluorescence spectrum of these capsules in pure water. The excitation wavelength was set at 495 nm.⁹⁴ 7
- Figure 1.5. Confocal microscope images demonstrating remote release of encapsulated rhodamine-labeled PSS polymers from a polyelectrolyte multilayer capsule containing gold sulfide core/gold shell nanoparticles in its walls. Fluorescence intensity profiles along the line through the capsule show that it is filled with fluorescent polymers before (a) and empty after (b) laser illumination. After the release of encapsulated polymers, the leftover fluorescent intensity is observed only in the walls of the capsule, (b). Insets show black and white transmission microscope images of the same capsule. Incident intensity of laser diode operating at 830 nm was set at 50 mW.⁹⁶ 8
- Figure 1.6. (a, b) Fluorescence microscope images of hybrid capsules formed with polyelectrolytes, Fe₃O₄ nanoparticles and a dioctadecyldimethylammonium chloride (DDAC) bilayer membrane loaded with calcein (a) before and (b) after alternating magnetic field irradiation at 360 kHz and 234 Oe for 30 min. Temperature profile (c) of the aqueous dispersion of Fe₃O₄/polyelectrolytes hollow capsules as a function of irradiation time of alternating magnetic field at 360 kHz and 234 Oe. A 5 mL capsular dispersion with a concentration of 5.5 × 10⁸ capsules/mL was used for the measurement.⁹⁷ 9
- Figure 1.7. Confocal images of polyelectrolyte capsules consisting of 10 layers of PSS/PDADMAC as a function of the PSS (Mw 70000) bulk concentration. The PSS concentrations represented as wt % are indicated in the insets. A higher magnification of the corresponding image in (c) is shown in the inset.¹⁰³ 10
- Figure 1.8. Hypothetical schematic diagram depicting the hierarchical self-assembly of gold and silica NPs into hollow spheres with a two-layer shell structure. The addition of gold NPs (gold) to the disulfide cross-linked block copolyptide produced globules of

gold particles. The introduction of silica NPs (gray) then drove the formation of hollow micron-sized spheres whose walls were composed of a distinct inner layer of gold NPs followed by an outer layer of silica NPs.¹¹¹ 12

Figure 1.9. Proposed flocculation-based-assembly of organic-inorganic hollow spheres from PLL, Au NPs, and SiO₂ NPs.¹⁰⁹ 13

Figure 1.10. Schematic of formation of SnO₂ microcapsules (“NACs”) from SnO₂ NPs, PAH, and phosphate anions.¹¹² 14

Figure 2. 1. Schematic of two-step NP assembly of silica/polymer microcapsules. 36

Figure 2.2. Silica/polymer microcapsules prepared with SiO₂ NP precursor concentrations of (a,d) 20.3 wt%, (b,e) 0.12 wt%, and (c,f) 0.02 wt%, imaged through (a-c) optical DIC microscopy and (d-f) SEM images. Scale bar: 5 μm. 44

Figure 2.3. Silica/polymer microcapsules prepared at (a-c) $R = 1.5$ and (d-f) $R = 10$, imaged through (a,d) optical brightfield microscopy and (b,e) SEM. (c,f) SEM images of microtomed microcapsules. Scale bar for SEM images: 2 μm. 47

Figure 2.4. Histograms of NACs prepared with $R = 10$ and polymer-salt aggregate aging time of (a) 30 min and (b) 10 sec. 48

Figure 2.5. TGA weight-loss and weight-loss-rate profiles of NACs ($R = 10$ and aggregate aging time of 30 min). 49

Figure 2.6. (a) SEM image and (b) EDX spectrum of NACs ($R = 10$ and aggregate aging time of 30 min) calcined at 600 °C. Scale bar: 5 μm. 50

Figure 2.7. (a) Nitrogen adsorption isotherms for uncalcined NACs, calcined NACs, and calcined SiO₂ NPs. Inset: re-scaled isotherm for uncalcined NACs. (b) Pore size distributions calculated for calcined NACs and calcined SiO₂ NPs. 51

Figure 2. 8. Electrophoretic mobility of polymer-salt aggregates as a function of R for $[PAH] = 1.0$ mg/ml. 53

Figure 2.9. Optical image a) Fluorescence image b) Bright field of NACs synthesized by PAH, citrate and Ludox-CL NPs, $R = 10$, 30 min aging of PAH-Cit, scale bar 5 micron. 54

Figure 2. 10. (a) Optical bright field image b) SEM image, and c) SEM image of microtomed aluminosilicate spheres made at $R = 10$; (d) Optical bright field image e) SEM image, and f) SEM image of microtomed aluminosilicate spheres made at $R = 1.5$ Zeta potential on the aggregates for R ratios of 1.5 and 10 are + 7 mV and - 8 mV

respectively, both at near neutral pH, scale bar 2micron.	55
Figure 2. 11. Number of sites on Ludox-CL NP and Zeta potential as a function of pH.	56
Figure 2.12. Number of sites on silica NP (Snowtex-O) and Zeta potential as a function of pH.....	57
Figure 2.13. a) Optical bright field image b) SEM image of aluminosilicate spheres made at R = 10 and 10 sec aging time. c) Optical bright field image d) SEM image of aluminosilicate spheres made at R = 10 and 30 min aging time, scale bar 5 μ m.	59
Figure 2.14. (a)TGA weight-loss and weight-loss-rate profiles of aluminosilicate spheres ($R = 10$ and aggregate aging time of 30 min), (b) calcined aluminosilicate spheres ($R = 10$ and aggregate aging time of 30 min), scale bar 2 μ m.....	60
Figure 2.15. (a) Nitrogen adsorption isotherms for uncalcined aluminosilicate spheres, calcined aluminosilicate spheres, and calcined aluminosilicate NPs. Inset: re-scaled isotherm for uncalcined aluminosilicate spheres. (b) Pore size distributions calculated for calcined aluminosilicate spheres and calcined aluminosilicate NPs.....	61
Figure 3.1. Confocal microscopy and bright field images of NACs as made (mother liquor), in DI- water, suspended in various final pH conditions from (L to R, pH range of 2-12) and various ionic strength solutions, 10 mM NaCl, 150 mM NaCl, 0.5 M NaCl, 1.0 M NaCl .Left half image is confocal image and the other half is the bright field image of the same spot.....	78
Figure 3.2. (a) Total number of positive charges per PAH chain vs. pH, (b) Total number of negative charges per silica NP vs. pH, (c) Average charge per citrate anion vs.pH.	79
Figure 3.3. Confocal microscopy images of NACs subjected to various osmotic pressure levels with PSS-Na, in NACs initially suspended in DIW (a-e), (f-j) NACs initial condition, pH 6.0 in 10 mM NaCl, and (k-o) and NACs initial conditions, pH 6.0 in 150 mM NaCl.	85
Figure 3.4. Percentage of deformed capsules as a function of the PSS wt %concentration, (b) Correlation between capsule diameter and shell thickness based on intensity line profiles of NACs.....	86
Figure 3.5. Confocal microscopy images of NACs suspended in 1M ionic strength solution in (a) NaCl, (b) Phos,(c) Sulf, (d) Cit, and e) indicates the graph of % of unbroken NACs vs ionic strength of various multivalent anions. Scale bar is 5 micron.	88
Figure 3.6. Confocal microscopy images of NACs suspended in (a) as made -mother	

liquor, (b) 1.0 M NaCl + 0 mM Cit, (c) 1.0 M NaCl + 10 mM Cit, (d) 1.0 M NaCl + 25 mM Cit. Scale bar is 5 micron. 89

Figure 3.7. Confocal microscopy images of NACs suspended in (a) PBS, (b) Sea water-Gulf of Mexico (Galveston, Texas, USA). Scale bar is 5 micron. 90

Figure 4.1. Schematic showing the synthesis of fluorescein-encapsulated NACs, with the shell made of NPs and polymer. 108

Figure 4.2. (a) Differential interference contrast optical image and (b) corresponding fluorescence image of Na-Flu encapsulated NACs. (c) Confocal microscopy image showing the three regions in Na-Flu encapsulated NACs. Scale bars: 10 μ m. 109

Figure 4.3. Fluorescence images of NACs dispersed in PBS and in glycine buffers of pH 9, 9.6 and 10.3, for shell thickness estimation purposes. Scale bars: 10 μ m. 110

Figure 4.4. (a) Schematic of shell thickness analysis. (b) Correlation between particle size and shell thickness based on intensity line profiles of NACs at pH 9.6 (shown in Fig. 4). 111

Figure 4.5. (a) Scanning electron microscope (SEM) image of NACs and (b) Capsule diameter distribution data from SEM images and Coulter counter measurements fitted to log-normal distribution. 112

Figure 4.6. UV- visible absorbance profiles of Na-Flu in the supernatant. 113

Figure 4.7. Experimental release profile, obtained as an average from three independent release studies, displayed with error bars. 115

Figure 4.8. Schematic of nanoparticle assembly using Gd (III) salts. 117

Figure 4.9. a) Optical bright field image b) SEM image Gd-NACs. Scale bar is 500 nm. 118

Figure 4.10. Temperature-dependent relaxivity of Na₅[GdDOTP] (■), polymer-Gd salts aggregate (○) and Gd-NACs (●), data collected by Dr. Zhou. 120

Figure 4.11. a) SEM images of irradiated NACs with various dosages (shown in inset) 124

Figure 4.12. a) SEM images of irradiated Albumin NACs with various dosages (shown in inset) Scale bar 2 μ m. 125

Figure 4.13. (a) Fe ₃ O ₄ -NACs in DI-water and (b) shows the Fe ₃ O ₄ -NACs in suspension and its sensitivity towards a magnet. Scale bar is 10 μm	127
Figure 4.14. TGA weight-loss and weight-loss-rate profiles of Fe ₃ O ₄ -NACs	128
Figure 4.15. (a) Fe ₃ O ₄ -NACs in Brownian motion no magnetic field applied,(b) applied magnetic field in X direction (c). in Y direction, and (d) after removing magnetic field. Magnetic field strength of 0.01 T is applied. Scale bar is 10 μm.	129
Figure 4.16. (a) Nova Star 2 kW RF Power Supply, Ameritherm, b) Fe ₃ O ₄ – NACs in 1.5 ml centrifuge vial placed at the centre of the coil, c) temperature detector. Magnetic heating experiments were carried at current: 208.3 A, frequency: 267 kHz, Magnetic field strength - H = 20 KA/m, Magnetic flux density - B = 0.025 T.	130
Figure 4.17. Temperature vs time of Fe ₃ O ₄ – NACs in suspension at various concentrations of Fe ₃ O ₄ , magnetic field applied for 20 mins.	131
Figure 4.18. (a) SEM image of Fe ₃ O ₄ -NACs in DI-water, (b) SEM image Fe ₃ O ₄ -NACs after subjecting to magnetic field for 20 mins. Scale bar is 2 μm	132
Figure 4.19. Bright field images and confocal images of a) ICG-Fe ₃ O ₄ NACs in DI- water, no magnetic field was applied b) ICG-Fe ₃ O ₄ NACs, after magnetic field applied for 2 mins. Right half image is confocal image and the other half is the bright field image of the same spot.	133
Figure 4.20. Confocal microscopy images of NACs suspended in various final pH conditions (a) pH =2.0, b) pH = 6.0, c) pH = 12.0, and various ionic strength solutions, d) DI-water, e) 150 mM NaCl, and f) 0.5 M NaCl. Scale bar is 5 μm.	134
Figure 4.21. Confocal microscopy images of NACs (a) after applying physical pressure=2.0, b) pH = 6.0, c) subjecting to a temperature of 80 °C. Scale bar is 10 μm.	135
Figure 5.1. (a) Schematic of the microfluidizer chamber (redrawn from microfluidicscorp.com), (b) schematic showing the formation of elongated polymer-salt aggregates in Y –junction. and (c) high shear zone	149
Figure 5.2. SEM images of elongated NACs formed by subjecting polymer-salt aggregates to various to (a) 0K, (b) 5K, (c) 10K, (d) 20K PSI pressure. Approximately 300 particles were counted on the SEM images using ImagePro software to determine the particle size of spherical NACs shown in (a) (mean particle size is 1.5 micron with a relative standard deviation of 28 %) Initial particle size of polymer- salt aggregate is 1.5 micron. Scale micron. Scale bar is 5 micron	150

Figure 5.3. (a) Relative distribution plots for length (a) and width (b) for 5K, 10K, 20K PSI pressure along with log-normal fits respectively.	151
Figure 5.4. Variables used in the transformation technique. The analysis of the boundary layer and the flow is done in section shown as a red dashed line rectangle.	152
Figure 5.5. Dimensionless velocity profiles, this section corresponds to the zone of dashed red line box in the Fig. 5.4 near point $S_{(0,0)}$. If $y/\delta = 1.0$ indicates the end region of boundary layer. $(x/\delta, y/\delta) = (0,0)$ corresponds to $S_{(0,0)}$	155
Figure 5.6. The extensional strain in the zone of the dashed red rectangle in Fig. 5.4. Plot indicates the zone for higher deformation of particles is the point where the fluid stream splits in the corner ($S_{(0,0)}$) having the highest value of extensional strain. The calculations are done for 5K PSI and a duct of 300 micron region is considered.	156
Figure 5.7. Schematic showing the deformation of polymer-salt aggregates at position $(x/\delta, y/\delta)$ with respect to various pressures. Position $(x/\delta, y/\delta)$ are related to A, B and C as shown in Fig. 5.4.	158
Figure 5.8. Schematic showing the deformation of polymer-salt aggregates at position $(x/\delta, y/\delta)$ keeping x/δ at 0.5.	159
Figure 5.9. Schematic showing the deformation of polymer-salt aggregates at various positions $(x/\delta, y/\delta)$ in high shear-zone.	161
Figure 5.10. SEM images of elongated NACs formed by subjecting polymer-salt aggregates to various to (a) 0K, (b) 5K, (c) 10K, (d) 20K PSI pressure. Approximately 300 particles were counted on the SEM images using ImagePro software to determine the particle size of spherical NACs shown in (a) (mean particle size is 1.0 micron with a relative standard deviation of 33) Initial particle size of polymer-salt aggregate is 1.0 micron. Scale bar is 5 micron	162
Figure 5.11. (a) Relative distribution plots for length (a) and width (b) for 5K, 10K, 20K PSI pressure along with log-normal fits respectively.	163
Figure 5.12. Selectivity vs. Pressure for 5K, 10K, 20K PSI pressure along for initial polymer-salt aggregate size of 1.5 and 1 microns.	164
Figure 5.13. (a) SEM images of NACs formed by PSS as shell material, (b) Micro-wires formed by subjecting polymer-salt aggregates to elongation/shear and followed by addition of PSS and subjecting to elongation/shear.	165
Figure 6. 1. Schematic showing the proposed experiment using Asylum MFP-3D atomic	

force microscopy.....	177
Figure 6. 2. Optical DIC image of PAA-EDA-Silica capsules.....	180
Figure A.1. Bright field microscopy images of NACs as made (mother liquor), in DI-water, suspended in various pH conditions from (L to R, pH range of 2-12) and various ionic strength solutions, 10 mM NaCl, 150 mM NaCl, 0.5 M NaCl , 1.0 M NaCl	182
Figure A.2. Osmotic pressure calibration curve.....	183
Figure A.3. Confocal microscopy images of NACs suspended in various ionic strength solutions (a-c) NaCl, (d-f) Phos,(g-i) Sulf , (j-l) Cit.	183
Figure A.4. Capsule diameter distributions of NACs obtained from Coulter counter measurements and the solid lines indicate distribution fit to lognormal distributions. Table1: indicates the mean diameter and standard deviation for NACs suspended in DIW, 10 mM, 150 mM, 500 mM, 1000 mM ionic strength solutions using cit and pH maintained at 8.0.....	184
Figure A.5. Total # of NACs count NACs obtained from Coulter counter measurements. NACs suspended in DIW, 10 mM, 150 mM, 500 mM, 1000 mM ionic strength solutions using cit and pH maintained at 8.0.....	184
Figure A.6. Confocal microscopy images of NACs suspended in phos (ionic strength 1.5M, molar concentration of phos is 0.5M) and cit (ionic strength 6M, molar concentration of cit is 1M) for 1 day and 4 weeks, pH maintained at 8.0, and in sea water (Gulf of Mexico, Galveston, Tx, USA) for 1 day and 1 week.....	185
Figure A.7. Percentage protonation of amine group vs pH of PAH solution. $pH = pK_a$ when % protonation is 50.	186
Figure B.1. Schematic of QCM-D experimental set up, PTFE (Poly(tetrafluoroethylene)).	189
Figure B.2. Schematic of Na- Fluorescein diffusing in PAH-Cit film.....	190
Figure B.3. Experimental data obtained from QCM-D. Frequency and Energy dissipation vs Time are plotted.....	192
Figure B.4. Thickness vs. time of PAH/cit film on gold-coated sensor. Thickness of the film was estimated using both the models.....	193
Figure B.5. Adsorbed mass of Na-Flu on PAH/cit film vs. time	194

Figure B.6. Mass of fluorescein adsorbed on PAH/cit film vs. time. Eq(7) and experimental data are plotted vs time.	196
Figure C. 1. Magnitude of the stream function for a flow past a wedge (135°). Position (x,y) are shown in Fig. 5.4.	207
Figure C. 2. Boundary layer assuming average velocity of 9.72 m/s. See appendix notes for justification of the use of this velocity as a reference. Position (x,y) are shown in Fig. 5.4.....	207
Figure C.3. Particle tracking of PS aggregate. Position (x,y) are shown in figure 5.4. Tau presents the dimensionless time scale. The transformation from spherical (blue circle) to elongated circle (green) could clearly be observed. Particle tracking code is given at the end appendix.	208
Figure C.4. TEM image of elongated NACs. Elongated NACs made at 20K PSI, initial particle size of polymer- salt aggregate is 1.5 micron.	208

Chapter 1. Introduction

1.1. Background and research motivation

Recently, the investigation, manufacturing, and application of colloidal particles have increased rapidly. The International Union of Pure and Applied Chemistry (IUPAC) defines colloidal particles as having diameters in the 1-1000 nm range. As a sub-category, particles with diameters in the 1-100 nm range are called nanoparticles (NPs). Those with diameters in the 100 to 1000 nm range are called submicron particles. The advanced technology in nanoparticles requires scientists to study colloidal science from many angles such as the investigation of chemical and physical properties of nanoparticles. NPs offer a wide spectrum of chemical, mechanical, and optical properties. As a specific example SiO₂ NPs, is used in applications as diverse as papermaking, investment casting, coatings, chemical-mechanical planarization, and photography, and as additives for cements and waxes^{1, 2}. In heterogeneous catalysis, it finds great use as a binder for catalyst particles as it provides attrition resistance to, and disperses the particles within, the formed catalyst pellet. There has been a tremendous interest in recent years to generate new materials using colloidal particles, particularly for particles in the size range of 1 to 1000 nm. The general approach involves the careful manipulation of interparticle and surface interactions to yield NP-based assemblies with well-controlled structure and morphology. Such NP assembly techniques may be quite applicable for increasing the usefulness of colloidal particles.

In the midst of the many ordered structures formed via NPs, there has been a plethora of interest in the synthesis of a class of materials called hollow spheres or capsules in the micron, sub-micron, and nanometer size ranges. A capsule is basically a container which

is hollow in nature and comprise of shell wall as outer material. This shell wall helps in protecting the active ingredient or cargo molecule. Capsules find extensive applications in pharmaceutical, food, chemicals, and consumer industry by serving as tiny containers to store, deliver, and/or release substances³⁻¹⁰. The shell can be designed in such a way that the cargo can be released at desired time intervals, by triggering the capsules by varying either one or more of the following parameters such as pH, ionic strength, external pressure, and interaction with near infrared (IR) laser light. It is of interest to make hollow structured material using nanoparticles (NPs), since NPs show different mechanical, chemical and optical properties from that of bulk material. Various single compositional NPs, multi compositional NPs or functionalized NPs can be used in the synthesis of new nanomaterial for particular applications. In this chapter, an overview of capsules or hollow spheres, various approaches to make hollow spheres, and responsive studies of layer-by-layer capsules are depicted.

1.2. Synthesis approaches to hollow spheres

The fabrication of hollow spheres to make organic and inorganic hollow spheres can be classified into four categories such as sacrificial core or template-directed method, emulsion-phase separation technique, nozzle generator technique, and vesicles - liposomes. Each technique has its own advantages and disadvantages.

1.2.1. Sacrificial core method or layer-by-layer (LbL) assembly technique

Sacrificial core method is an approach to prepare capsules through charge interactions. Polyelectrolyte capsules or LbL capsules were first introduced in by Caruso *et al.*¹¹, and it is most widely reported as LbL assembly technique. These LbL capsules

are synthesized by the step-wise adsorption of polyelectrolytes onto charged colloidal templates, followed by decomposition of the templates (solid or liquid core) as shown in Fig. 1.1. The shell is formed by depositing oppositely charged polymers/and or NPs. Although the removal of a colloidal core is easier, the fast dissolution of colloidal core (such as polystyrene) in organic solvents creates an osmotic pressure which may weaken the polyelectrolyte shell¹². To avoid destroying the shell, inorganic templates, such as calcium carbonate or manganese carbonate have recently been introduced as a template for the fabrication of hollow polyelectrolyte capsules^{4, 11, 13-24} like polystyrene (PS) or cross-linked melamine formaldehyde. Polyelectrolyte shells are known to be permeable to molecules with a molecular weight below 5 kDa and they don't suffer an osmotic stress during the dissolution of the inorganic templates²⁵. The shell of LbL capsules can consist either only polyelectrolytes or inorganic (nanoparticles) –organic(polyelectrolytes) composite material as shown by Caruso *et al*¹⁶. Polyelectrolyte capsules may find applications in varied fields. Many researchers have shown that these capsules could potentially be used as microreactors for the synthesis, separation of materials, as sensors, and drug delivery vehicles²⁶⁻³¹. The sacrificial core templating method is a promising technique to yield stable monodispersed hollow spheres. Though sacrificial core method approach is very flexible, it requires lot of processing routes than the self-assembly routes. The biggest disadvantage of this method is that the encapsulation of sensitive compounds is very complex and utmost care should be taken so as to not damage the encapsulated material during the encapsulation^{13, 14, 25, 32-74}.

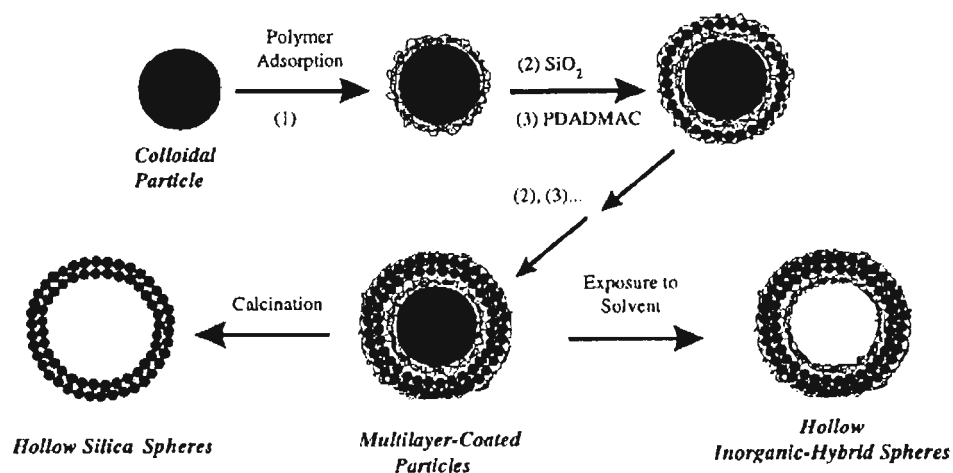


Figure 1.1. Sacrificial core templating method to prepare hollow spheres.¹¹

Other techniques such as emulsion-phase separation technique, nozzle generator technique, and vesicles -liposomes have their own advantages and disadvantages. One of the advantages of emulsion-phase separation or emulsification method is that a large variety of hydrophobic substances can be encapsulated in the core. However, the encapsulation of water-soluble compounds is difficult *via* this technique⁷⁵⁻⁷⁹. In the case of nozzle generator technique, the excellent feature of this technique in general is that the capsule size can be varied continuously over a wide range from hundreds of microns to tens of nanometer. However, attaining encapsulation in well-defined size range, controlled thickness of the shell, and production of monodisperse spheres, all at the same time, is a challenge⁸⁰⁻⁸². In the case of vesicles –liposomes, although self-assembly of amphiphilic molecules are a safe and facile technique to form hollow spheres, there are some major disadvantages. Vesicles are may not stable at high temperatures and extreme pH's; are not resist to strong mechanical force. Block copolymer is not easily synthesized; the morphology of block copolymer hollow spheres is sensitive to molecular structure, solubility, and temperature⁸³⁻⁹³. A related approach to preparing capsules through charge

interactions is the LbL assembly. Its responsive studies are explained in detail in further sections.

1.3. Responsive LbL capsules

A related approach to preparing capsules through charge interactions is the LbL assembly. Its responsive studies are explained in detail in further sections.

1.3.1. pH responsive capsules

LbL capsules have been shown to have interesting behavior in response to different pH and ionic strength values. LbL capsules made of PSS/PAH started to swell when the pH was above 11 and disassembled when the pH was above 12. The capsules are permeable in the acidic region whereas they are impermeable in the alkaline region. Schuler *et al.*, has demonstrated the polyelectrolyte capsules decomposable by suspending the capsules in higher ionic strength solutions⁸⁸. Also, polyelectrolyte capsule collapse or deflate once they are dried. Antipov *et al.*, has reported that depending on the pH, the permeability of these capsules could be changed⁷². Fig. 1.2 shows the results of the permeability studies of hollow capsules templated on melamine formaldehyde MF and CdCO₃ cores and consisting of 4 PSS-PAH bilayers⁷³. FITC-labeled dextrans (75 kDa and 2000 kDa) have been used as probe molecules to study their permeability as a function of pH. The capsule interior remains dark while the bulk is fluorescent (Fig. 1.2 (b, d)). However, at pH 3.5 the capsule interior becomes fluorescent within few seconds after FITC-dextran is added as observed in Fig. 1.2 (a, c). All capsules remained open at pH values up to 6 and 90% of the capsules were closed at pH values of 8 and above. Weakening of the connectivity of the polyelectrolytes, could be responsible for the

enhanced permeability.

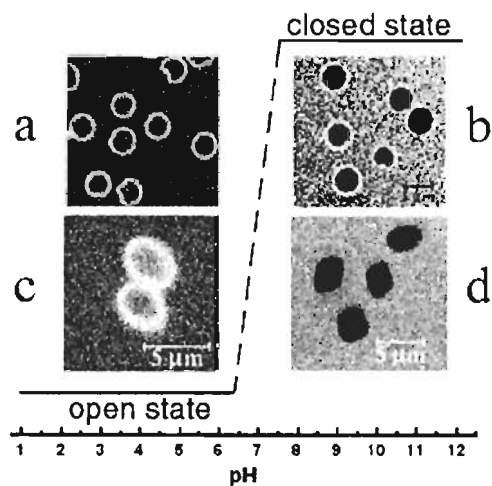


Figure 1.2. Open (a, c) at pH 3.5 and closed (b, d) at pH 10 states of polyelectrolyte shells prepared on melamine formaldehyde (MF) particles (a, b) and CdCO_3 crystals (c, d).⁹⁴

1.3.2. Salt responsive capsules

Caruso *et al.*, reported that polyelectrolyte capsules made of DNA/spermidine decomposed by suspending them in high ionic strength⁸⁸. Fig. 1.3 shows the schematic of the effect of salt on polyelectrolyte capsules. Ibarz *et al.*, reported the structural changes within the multilayer of the polyelectrolyte capsules made of PSS/PAH via Förster resonance energy transfer (FRET) studies⁹⁵. A quick decrease in FRET indicates the longer distance between the polyelectrolyte layers as shown in Fig. 1.4. At 0.01 M salt concentration this effect was observed. The presence of high amount salt screens the charges on the polyelectrolytes and lowers the interaction between the oppositely charged polyelectrolytes.

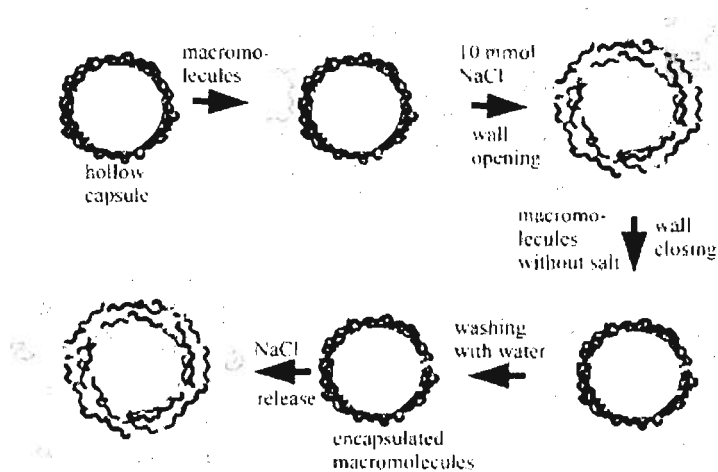


Figure 1.3. Scheme of encapsulation and release of macromolecules through the switching of the permeability by means of the salt concentration. The black and dark gray lines represent the polyelectrolytes of the capsule wall and the bright gray lines are the probe polymers.⁹⁵

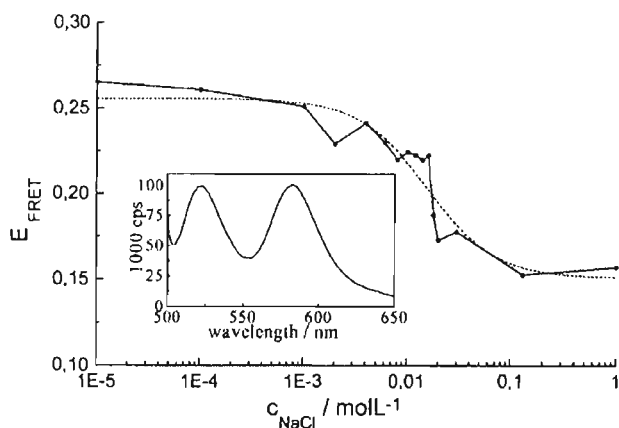


Figure 1.4. E_{FRET} in dependence of the salt concentration for capsules containing PAH-fluo in the 10th layer and PAH-rho in the 12th layer. The dashed line represents a sigmoidal fit of the experimental results. The inset shows the fluorescence spectrum of these capsules in pure water. The excitation wavelength was set at 495 nm.⁹⁵

1.3.3. Light-responsive capsules

Tao *et al.* were the first one to report optically sensitive polyelectrolyte capsules⁹⁶. The Caruso group was the first to demonstrate the release of encapsulated

biomacromolecules upon NIR (near-infrared) irradiation of polyelectrolyte capsules. Skirtach *et al.* in 2005 reported near IR sensitive polyelectrolyte capsules⁹⁷. Fig. 1.5a shows confocal and transmission images of a PSS/PAH capsule, with gold nanoparticles, filled with rhodamine-labelled PSS⁹⁷. When NIR-laser light was impinged, (Fig. 1.5b) the capsule breaks open, observed from the strongly deformed structure, leading to the release of the encapsulated material. They clearly exhibited the strong impact of IR-light on the morphology of the capsules.

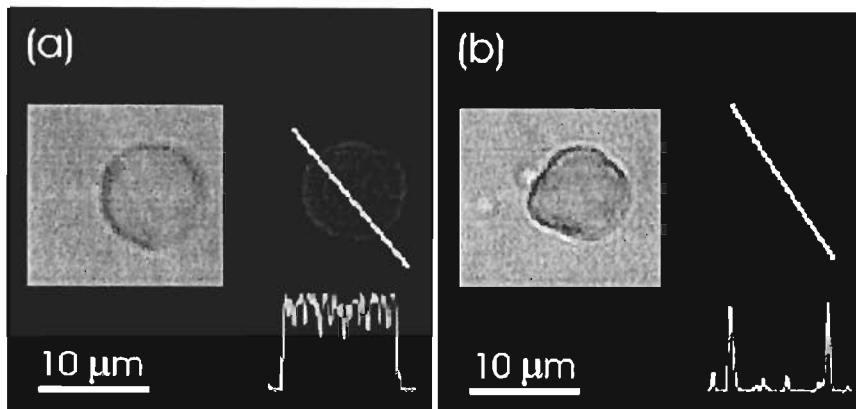


Figure 1. 5. Confocal microscope images demonstrating remote release of encapsulated rhodamine-labeled PSS polymers from a polyelectrolyte multilayer capsule containing gold sulfide core/gold shell nanoparticles in its walls. Fluorescence intensity profiles along the line through the capsule show that it is filled with fluorescent polymers before (a) and empty after (b) laser illumination. After the release of encapsulated polymers, the leftover fluorescent intensity is observed only in the walls of the capsule, (b). Insets show black and white transmission microscope images of the same capsule. Incident intensity of laser diode operating at 830 nm was set at 50 mW.⁹⁷

1.3.4. Magnetic field responsive capsules

Effect of magnetic field on the hybrid capsules formed with Fe_3O_4 nanoparticles and the lipid bilayer was investigated by Katagiri *et al* in 2010. Polyelectrolyte capsules were made of PAH/PSS/dioctadecyldimethylammonium chloride (DDAC) bilayer and calcein was used as a probe molecule⁹⁸. Fig. 1.6 shows the fluorescence microscope images of

the hybrid capsules loaded with calcein. From Fig. 1.6a it is clearly observed that green fluorescence was observed only on the inner side of capsules. After applying alternating magnetic field at 360 kHz and 234 Oe (Oersted (Oe) is the unit of magnetizing field) for 30 min, it can be seen from Fig. 1.6b that fluorescence was observed both inside and outside of the capsules. Chen *et al.* also showed release behavior of capsules under applied magnetic field⁹⁹. Also, from Fig. 1.6c the temperature of the capsules suspension reached ~ 60 °C in 30 minutes. The alternating magnetic field irradiation was carried out at 360 kHz and 234 Oe.

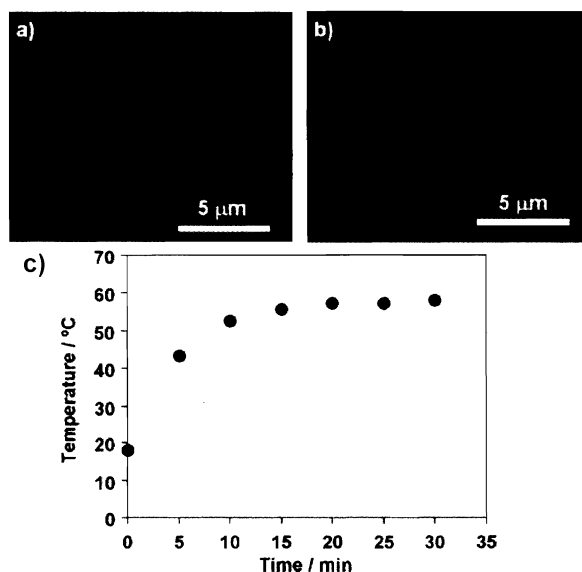


Figure 1.6. (a, b) Fluorescence microscope images of hybrid capsules formed with polyelectrolytes, Fe₃O₄ nanoparticles and a dioctadecyldimethylammonium chloride (DDAC) bilayer membrane loaded with calcein (a) before and (b) after alternating magnetic field irradiation at 360 kHz and 234 Oe for 30 min. Temperature profile (c) of the aqueous dispersion of Fe₃O₄/polyelectrolytes hollow capsules as a function of irradiation time of alternating magnetic field at 360 kHz and 234 Oe. A 5 mL capsular dispersion with a concentration of 5.5×10^8 capsules/mL was used for the measurement.⁹⁸

1.3.5. Osmotic pressure responsive capsules

Gao *et al.* studied the effect of osmotic pressure on polyelectrolyte capsules as shown in Fig. 1.7. The stability of capsules was tested by inducing osmotic pressure through PSS-Na¹⁰⁰⁻¹⁰⁶. The critical PSS concentration was defined as the concentration necessary to induce the deformation of 50% of the intact capsules. It can be seen from the figure that unbroken capsules undergo a shape conversion from spherical into a cup shape at a certain critical PSS concentration¹⁰⁴ (Fig. 1.7b).

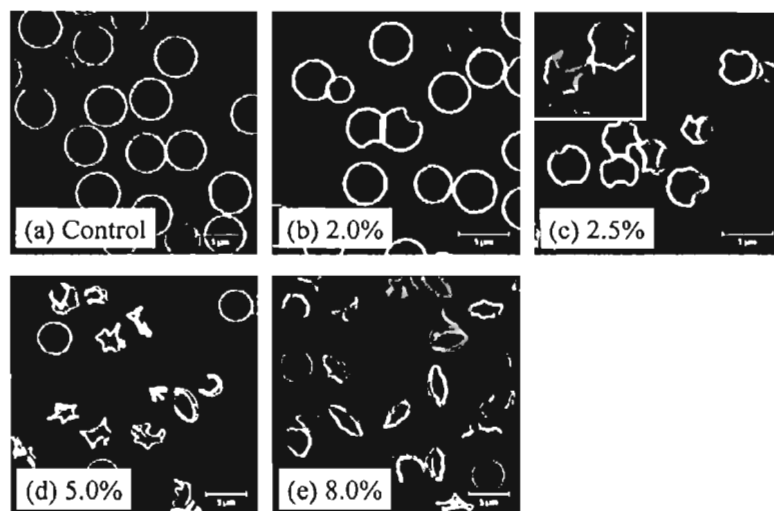


Figure 1.7. Confocal images of polyelectrolyte capsules consisting of 10 layers of PSS/PDADMAC as a function of the PSS (Mw 70000) bulk concentration. The PSS concentrations represented as wt % are indicated in the insets. A higher magnification of the corresponding image in (c) is shown in the inset.¹⁰⁴

The critical PSS concentration was defined as the concentration necessary to induce the deformation of 50% of the intact capsules. At a higher PSS concentration, the capsules contract further as shown in Fig. 1.7 (c,d). A model has been developed to correlate mechanical strength of the capsules (elasticity modulus) with applied osmotic pressure. For a capsule radius of 2.2 μm, and the capsule wall thickness of 40 nm, they can withstand an osmotic pressure of 140 MPa.

1.4. Research motivation and thesis layout

A materials synthesis technique was recently developed to generate polyamine/silica composite microcapsules in which synthetic polyamines such as polyallylamine and/or polylysine were crosslinked with multivalent anions like citrate to form polymer-salt aggregates, that then served as templates for deposition of nanoparticles to form micron-sized hollow spheres or "nanoparticle-assembled capsules" (NACs)¹⁰⁷⁻¹¹¹. As a general synthesis methodology, this electrostatically-driven "polymer-salt aggregate" or "PSA" assembly route is attractive for encapsulation and scale-up because encapsulation and materials formation occur in water, at mild pH values, and at room temperature.

In 2002, Wong and coworkers reported a new and facile method to make hollow spheres. Instead of using pure inorganic or organic template, copolyptide -poly (L-lysine_x-b-L-cysteine_y) and citrate-tagged Au NPs (or CdSe quantum dot) are mixed firstly and templates are formed rapidly due to the association of -SH groups (from polymer) and -COOH groups (from citrate)¹¹². Silica NPs are added into the polymer/Au aggregates suspension and hollow structure are generated immediately¹¹² as shown in the Fig. 1.8.

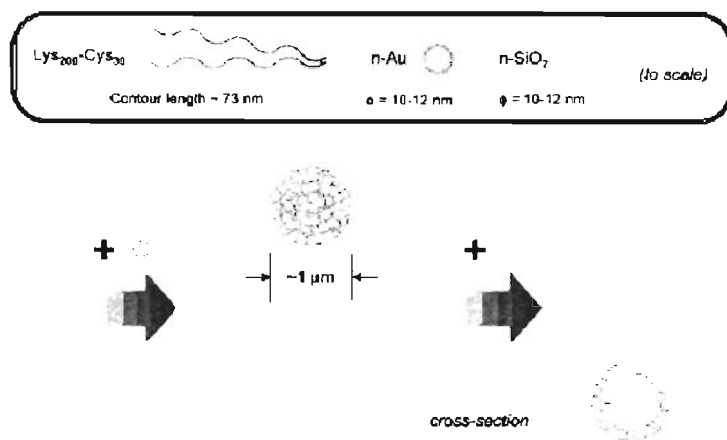


Figure 1.8. Hypothetical schematic diagram depicting the hierarchical self-assembly of gold and silica NPs into hollow spheres with a two-layer shell structure. The addition of gold NPs (gold) to the disulfide cross-linked block copolypeptide produced globules of gold particles. The introduction of silica NPs (gray) then drove the formation of hollow micron-sized spheres whose walls were composed of a distinct inner layer of gold NPs followed by an outer layer of silica NPs.¹¹²

Murthy and coworkers replaced copolypeptide with homopolymer-p (L-lysine), and generated templates with Au NPs to and generated similar hollow spheres are formed by adding silica NPs as shown in Fig. 1.9¹¹⁰.

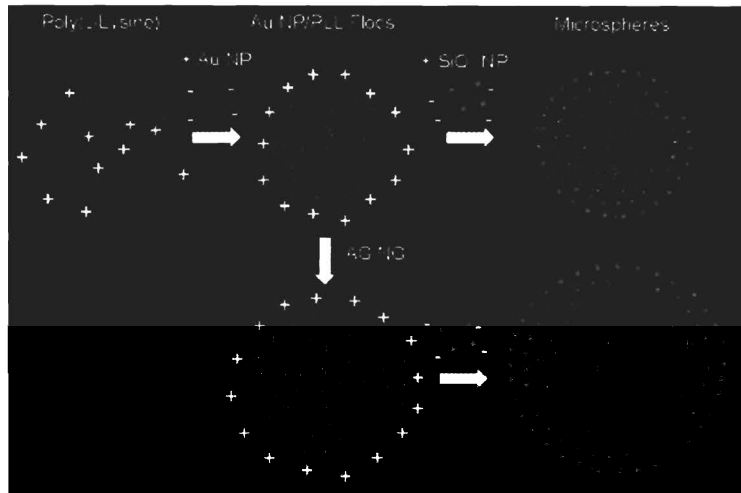


Figure 1.9. Proposed flocculation-based-assembly of organic-inorganic hollow spheres from PLL, Au NPs, and SiO₂ NPs.¹¹⁰

The NPs self-assembly technique is extremely facile and fast to produce hollow spheres with multicomponents. These hollow spheres have size range between 1-10 μm . Because of silica shell, they are thermal stable, robust and resistant to normal external force, such as shearing, sonication and heating. The-art technique provides great future for hollow spheres preparation, encapsulation and controlled release.

It is clear that nanoparticle self-assembly around nanoparticle-polymer aggregates is an extremely simple method to make hollow spheres, in our lab; an easier and straightforward method is developed recently. It is found that nanoparticle self-assembly can be made around polymer/phosphate, polymer/citrate aggregates resulting in NACs¹¹³ as shown in Fig. 1.10. This new synthesis decreases the cost of hollow spheres quite a lot.

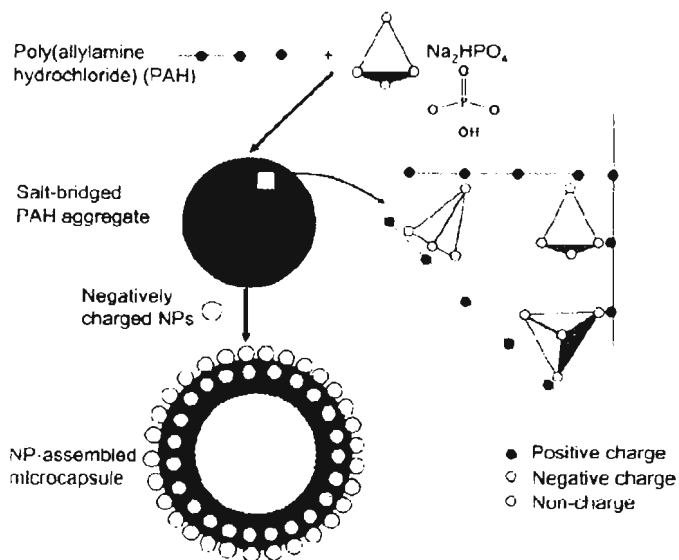


Figure 1.10. Schematic of formation of SnO_2 microcapsules (“NACs”) from SnO_2 NPs, PAH, and phosphate anions.¹¹³

A diffusion deposition model had been hypothesized to explain the mechanism of microcapsules formation. The model basically explains that the NPs penetrate the surface exterior of the polymer aggregate and that the penetration depth determines the shell thickness, with the implication that smaller particles diffuse deeper into the polymer aggregate than larger particles.

Various type of NACs¹¹³⁻¹²⁰ have been synthesized using polymers such as polyallylamine, polylysine, and polyethylene amine and using multivalent anions such as phosphate, citrate, EDTA, indocyanine green (ICG), and macromolecule chelate – $\text{Gd}[\text{DOTP}]^{5-}$.^{107-111, 113-115, 121, 122} Shell material of NACs could be comprised of NPs such as silica, tin oxide, titania, zinc oxide, iron oxide, and CdSe quantum dots or proteins such as human serum albumin, and bovine serum albumin or polymers such as poly acrylic acid, and polystyrene sulfonate. NACs showed potential applications in using them as MRI contrast agents - showing larger gains in relaxivity, phototherapy, protease

imaging, and siRNA therapy¹²³.

1.4.1. Current challenges in PSA assembly

Various type of NACs have been synthesized using polymers such as polyallylamine, polylysine, and polyethylene amine and using multivalent anions such as phosphate, citrate, and EDTA. Shell material of NACs could be comprised of nanoparticles such as silica, tin oxide, titania, zinc oxide, iron oxide, and CdSe quantum dots or proteins such as human serum albumin, and bovine serum albumin or polymers such as polyacrylic acid, and polystyrene sulfonate.

NACs can potentially find wide-ranging applications in pharmaceutical, food, and consumer. It is of crucial importance to address the physical property aspects of NACs in view of their use and applicability. While most applications may require that NACs not disassemble or deform under shear stress, some may require triggered release under specific conditions to release the encapsulated material (e.g., enzymes or drugs). Comparatively, little has been done to assess the physical properties of NACs. The behavior of NACs under varying pH and ionic strength conditions are lacking. The mechanical stability of NACs is not explored. Based on the applications, conditions, NACs needs to be engineered to meet the requirements. The scalability of charge-driven PSA assembly and the renewed potential of colloidal silica as a precursor to porous catalyst supports are so far not explored. Structural properties of NACs by using multicompositional NPs such as aluminosilicate NPs are done previously.

Most of the NACs prepared earlier are spherical in shape. Spherical particles are the most helpful carriers for drug delivery, researchers are finding that rod-shaped carriers may give a benefit of having longer circulation time in the blood stream (eg: longer

circulation times are needed for phototherapy). Researchers have shown that non-spherical particle suspensions influence the rheology behaviour. It will be valuable, at the same time challenging, to synthesize various shapes of NACs. In order to perform this, the visco-elastic nature of polymer-salt aggregates needs to be investigated thoroughly. Also, in the field of drug delivery, there is a vital need for time and space controlled drug delivery systems. Therefore, a PSA assembly technique needs to be applied to prepare stimuli responsive capsules for controlled drug delivery. Various responsive studies such as magnetic, radiation (X-rays), physical pressure, and temperature are yet to be explored. The formation of PSA assembly was limited to few salts such as EDTA, citrate, and phosphate. Other multi-valency salts such as Gd[DOTP]⁵⁻, were not explored.

It was previously shown that NACs can encapsulate hydrophilic and negative charged molecules. However, there is little information on encapsulation properties of cargo molecules that are hydrophobic or positively charged. Studies on transport and structural properties of NACs have been lacking so far. By addressing the above issues, NACs can be rationally engineered to meet the specific requirement for the applications in encapsulation and controlled delivery of drugs, and other compounds. My thesis works involves in addressing the above issues.

1.4.1. Thesis layout

My initial work was on developing a new procedure to make 100-mg amounts of silica/polymer microcapsules, improving on the materials yield by over two orders of magnitude while retaining the processing advantages of the original two-step NP assembly method. In Chapter 2, experimental results are discussed to explain the

mechanism of the PAH-cit aggregate surface charge dependence on microcapsule synthesis. These inorganic/organic hybrid composite capsules can be thermally treated to eliminate completely the organic fraction of the material without morphological damage. The polymer, which holds the nanoparticles together in the shell, leads to pores after its removal. This work demonstrates the scalability of charge-driven nanoparticle assembly chemistry, its general applicability to colloidal ceramics, and the renewed potential of colloidal silica as a precursor to porous catalyst supports. This work was published in *Topics in Catalysis* in 2008. The formation of porous aluminosilicate microspheres via nanoparticle assembly will be discussed in this chapter. Somewhat surprisingly; we were able to generate aluminosilicate/polymer solid spheres when aluminosilicate NPs were used as shell material. I will discuss the formation mechanism of these spheres.

Comparatively, little has been done to assess the physical properties of NACs under varying pH and ionic strength conditions. In Chapter 3, Ionic strength and pH effects on nanoparticle/polyamine microcapsules experimental work will be discussed in detail. Through this study, we studied the effects of pH (in the range of 2 to 12), ionic strength (from 10 mM to 1 M), and nature of the multivalent anions or salt such as (phosphate, citrate, seawater). Detailed studies to explain the behavior of microcapsules under various conditions are elucidated. In the aqueous phase range where the capsules were intact, we studied their mechanical strength through osmotic pressure testing. This work is being prepared for submission to *Journal of Materials Chemistry*.

It has been shown earlier that NACs allows a simple way of encapsulating water soluble compounds such as drugs, dyes and biomolecules (Murthy, PhD thesis 2006). In Chapter 4, encapsulation properties of capsules and responsive studies will be discussed.

Encapsulation studies of various molecules such as Gd[DOTP]⁵⁻, doxorubicin, and uracil are reported. A thorough experimental analysis on diffusive release of a dye molecule (fluorescein) from NACs was carried out. Our experimental results helped in validating the analytical model developed by Tavera *et al.* To provide experimental validation of the diffusion coefficient of the NAC-core, we studied the diffusion of fluorescein through polymer-salt matrix films through the quartz crystal microbalance-with dissipation monitoring (QCM-D) technique. Studies such as x-ray-sensitive NACs, effect of magnetic field on magnetic NACs, effect of applying physical pressure on NACs will be discussed in this chapter.

Our hollow spheres synthesis is facile and flexible. In this work, we reveal an interesting phenomenon of polymer-salt aggregates. On subjecting the polymer-salt aggregates to shear and elongation flow and elongate them and generate elongated NACs. With these hybrid structures taking on the shape of the polyamine-salt aggregate precursors, shape anisotropy was induced through manipulation of fluid flow in a "microfluidizer." Our results show that elongated NACs of various lengths (1 μm to 8 μm) can be generated by varying the process parameters such as velocity of fluid flow (250 m/s to 500 m/s). Selectivity of elongated vs spherical can be reached as high as 90%. A fluid mechanics model has been developed to quantify the extensional and shear rates at various locations in the microfluidizer (Y – junction & impact zone). This manuscript is being prepared for submission to *Industrial & Engineering Chemistry*. Chapter 6 is about Summary and recommendations for future work.

1.4.2. Other works

I successfully finished six collaborations that resulted in the following publications.

Experimental and modeling analysis of diffusive release from single-shell microcapsules (Collaboration with Tavera *et.al.*, Rice University)

I was involved in performing the experimental work for this project. Encapsulation of Na-Flu (model molecule) was performed to understand the encapsulation properties of NACs. The presented experiment-modeling approach allows optical microscopy images and release measurements to be readily analyzed for estimating diffusion coefficients in capsule core and shell walls. Based on the analytical model, I estimated diffusion coefficients in the capsule shell and core using QCM-D, which is comparable to experimental values for the similar systems reported in the literature. Published in *AIChE Journal*, 2009, 55, 11, 2950-2965.

Polyamine-guided synthesis of anisotropic, multicompartement microparticles (Collaboration with Dr. Murthy from CETL, The Procter and Gamble Company)

The concept of synthesizing anisotropic, multicompartement particles via NACs methodology was developed by Murthy *et al.* I was involved in controlled experiments to probe the mechanism of anisotropic particles formation. I used characterization techniques such as confocal microscopy, SEM, and microtoming to characterize some of the samples. Published in *Applied Materials and Interfaces*, 2009, 1, 590-596.

Nanoassembled capsules as delivery vehicles for large payloads of high relaxivity Gd³⁺ agents (Collaborated with researchers from the Advanced Imaging Research Center at the University of Texas Southwestern Dallas, Department of Chemistry at the University of Texas at Dallas, and Portland State University)

I successfully encapsulated a MRI contrast agent (GdDOTP⁵⁻) in NACs. The

formation of NACs using GdDOTP⁵⁻ as salt is not trivial. I developed a novel method of making NACs using co-solvent technique. It involves using PAH, GdDOTP⁵⁻ in ethanol, and silica NPs. Plush *et al.*, extended the concept of GdDOTP⁵⁻ encapsulation in NACs to other cationic polymers such as poly-L-lysine, poly-L-arginine. Additionally they also explored using solvents such as acetonitrile. Encapsulated GdDOTP⁵⁻ in NACs showed a five fold increase in the relaxivity signal compared to non-encapsulated GdDOTP⁵⁻. This has implications for the field of targeted MR imaging. Published in *JACS*, 2009, 131, 15918-15923.

Altering protein surface charge with chemical modification modulates protein–gold nanoparticle aggregation (Collaborated with researchers from the Department of Chemistry, and Bio-engineering at Rice University)

In this work, I used dynamic light scattering (DLS) as a tool to study the interactions between citrate-stabilized AuNPs and proteins such as lysozyme, α -lactalbumin, and myoglobin that have different surface charges. The DLS hydrodynamic diameters were in agreement with TEM diameters of the nanoparticles-protein aggregates and helped in to demonstrate that protein modification provides a dominant tool for modulating whether nanoparticle–protein interactions result in material aggregation. Published in *J. Nanopart. Res.*, (online) DOI: 10.1007/s11051-010-0057-5.

Nanoparticle Assembled Capsules for Target Drug Delivery, Controlled Release and Hyperthermia (Collaborated with Dr. McGary from Baylor College of Medicine)

The objective was to develop a combined drug release and hyperthermia delivery system for simultaneous multitreatment using radiation therapy. Magnetic iron oxide nanoparticles (Fe₃O₄) of ~ 20 nm were synthesized. Capsules loaded with iron oxide

magnetic nanoparticles were synthesized and their responsiveness to magnetic field was studied. The heating rates of Fe₃O₄ – NACs under an applied magnetic field were studied through an induction coil. Fe₃O₄ – NACs with a Fe₃O₄ concentration of 2.5 mg/mL heats up the suspension to a temperature of 60 °C in 20 min. Indocyanine green (ICG) was successfully encapsulated in magnetic capsules and was controllably released in the presence of a magnetic field. My studies indicate that NACs could be potentially used to encapsulate cargo molecules and controllably release them when a magnetic field is applied. This manuscript is in preparation.

Shell thickness control of nanoparticle/polymer assembled microcapsules

(Collaboration with Dr. Bagaria, Department of Chemical & Biomolecular Engineering, Rice University)

Through these studies we found that the shell wall of NACs can be thickened by contacting the as-synthesized capsules with silicic acid. I optimized and scaled up our established NACs synthesis to make ~ 100-mg amounts of silica/polymer microcapsules while improving on the materials yield by over two orders of magnitude by retaining the processing advantages of the original two-step NP assembly method. I was involved in characterizing the samples using techniques such as confocal microscopy, SEM, and microtoming. Additionally I assisted in the design of experiments, and interpretation of results. Adjustable shell wall thicknesses in hybrid microcapsules provide enhanced capability for chemical encapsulation, storage, and release applications. Published in *Chemistry of Materials*, 2010, 23 (2), pp. 301-308.

1.5. References

1. Iler, R. K., The Chemistry of Silica: Solubility, Polymerization, Colloid and Surface properties, and Biochemistry. *John Wiley and Sons, New York* **1979**.
2. Bergna, H. E.; Roberts, W. O., Colloidal Silica: Fundamentals and Applications. *CRC Press, Boca Raton* **2006**.
3. Barenholz, Y., Liposome application: problems and prospects. *Current Opinion in Colloid & Interface Science* **2001**, 6, (1), 66-77.
4. Caruso, F., Nanoengineering of particle surfaces. *Advanced Materials* **2001**, 13, (1), 11-+.
5. Chah, S.; Fendler, J. H.; Yi, J., Nanostructured gold hollow microspheres prepared on dissolvable ceramic hollow sphere templates. *Journal of Colloid and Interface Science* **2002**, 250, (1), 142-148.
6. Gibbs, B. F.; Kermasha, S.; Alli, I.; Mulligan, C. N., Encapsulation in the food industry: a review. *International Journal of Food Sciences and Nutrition* **1999**, 50, (3), 213-224.
7. Philippot, J. R.; Schuber, F., Liposomes as Tools in Basic Research and Industry. *CRC Press: Boca Raton* **1995**.
8. Uludag, H.; De Vos, P.; Tresco, P. A., Technology of mammalian cell encapsulation. *Advanced Drug Delivery Reviews* **2000**, 42, (1-2), 29-64.
9. Wilcox, D. L., Sr.; Berg, M.; Bernat, T.; Kellerman, D.; Cochran, J. K., Jr. , Hollow and Solid Spheres and Microspheres: Science and Technology Associated with Their Fabrication and Application. *Materials Research Society: Pittsburgh* **1995**.
10. Yang, M.; Ma, J.; Zhang, C. L.; Yang, Z. Z.; Lu, Y. F., General synthetic route toward functional hollow spheres with double-shelled structures. *Angewandte Chemie-International Edition* **2005**, 44, (41), 6727-6730.

11. Caruso, F.; Caruso, R. A.; Mohwald, H., Nanoengineering of inorganic and hybrid hollow spheres by colloidal templating. *Science* **1998**, 282, (5391), 1111-1114.
12. Dejugnat, C.; Sukhorukov, G. B., pH-Responsive Properties of Hollow Polyelectrolyte Microcapsules Templated on Various Cores. *Langmuir* **2004**, 20, (17), 7265-7269.
13. Volodkin, D. V.; Larionova, N. I.; Sukhorukov, G. B., Protein Encapsulation via Porous CaCO₃ Microparticles Templating. *Biomacromolecules* **2004**, 5, (5), 1962-1972.
14. Sukhorukov, G. B.; Volodkin, D. V.; Gunther, A. M.; Petrov, A. I.; Shenoy, D. B.; Mohwald, H., Porous calcium carbonate microparticles as templates for encapsulation of bioactive compounds. *Journal of Materials Chemistry* **2004**, 14, (14), 2073-2081.
15. Petrov, A. I.; Volodkin, D. V.; Sukhorukov, G. B., Protein—Calcium Carbonate Coprecipitation: A Tool for Protein Encapsulation. *Biotechnology Progress* **2005**, 21, (3), 918-925.
16. Caruso, F.; Caruso, R. A.; Mohwald, H., Production of Hollow Microspheres from Nanostructured Composite Particles. *Chemistry of Materials* **1999**, 11, (11), 3309-3314.
17. Caruso, F.; Donath, E.; Mohwald, H., Influence of polyelectrolyte multilayer coatings on Forster resonance energy transfer between 6-carboxyfluorescein and rhodamine B-labeled particles in aqueous solution. *Journal of Physical Chemistry B* **1998**, 102, (11), 2011-2016.
18. Caruso, F.; Donath, E.; Mohwald, H.; Georgieva, R., Fluorescence studies of the binding of anionic derivatives of pyrene and fluorescein to cationic polyelectrolytes in aqueous solution. *Macromolecules* **1998**, 31, (21), 7365-7377.
19. Caruso, F.; Lichtenfeld, H.; Donath, E.; Mohwald, H., Investigation of electrostatic interactions in polyelectrolyte multilayer films: Binding of anionic fluorescent probes to layers assembled onto colloids. *Macromolecules* **1999**, 32, (7), 2317-2328.
20. Caruso, F.; Lichtenfeld, H.; Giersig, M.; Mohwald, H., Electrostatic self-assembly of silica nanoparticle - Polyelectrolyte multilayers on polystyrene latex particles. *Journal of the American Chemical Society* **1998**, 120, (33), 8523-8524.

21. Caruso, F.; Mohwald, H., Protein multilayer formation on colloids through a stepwise self-assembly technique. *Journal of the American Chemical Society* **1999**, 121, (25), 6039-6046.
22. Caruso, F.; Mohwald, H., Preparation and characterization of ordered nanoparticle and polymer composite multilayers on colloids. *Langmuir* **1999**, 15, (23), 8276-8281.
23. Caruso, F.; Susha, A. S.; Giersig, M.; Mohwald, H., Magnetic core-shell particles: Preparation of magnetite multilayers on polymer latex microspheres. *Advanced Materials* **1999**, 11, (11), 950-+.
24. Caruso, F.; Trau, D.; Mohwald, H.; Renneberg, R., Enzyme encapsulation in layer-by-layer engineered polymer multilayer capsules. *Langmuir* **2000**, 16, (4), 1485-1488.
25. Sukhorukov, G. B.; Brumen, M.; Donath, E.; Mohwald, H., Hollow Polyelectrolyte Shells: Exclusion of Polymers and Donnan Equilibrium. *The Journal of Physical Chemistry B* **1999**, 103, (31), 6434-6440.
26. Zhu, H.; McShane, M. J., Loading of Hydrophobic Materials into Polymer Particles: Implications for Fluorescent Nanosensors and Drug Delivery. *Journal of the American Chemical Society* **2005**, 127, (39), 13448-13449.
27. Shchukin, D. G.; Sukhorukov, G. B., Nanoparticle Synthesis in Engineered Organic Nanoscale Reactors. *Advanced Materials* **2004**, 16, (8), 671-682.
28. Shchukin, D. G.; Sukhorukov, G. B., Selective YF3 Nanoparticle Formation in Polyelectrolyte Capsules as Microcontainers for Yttrium Recovery from Aqueous Solutions. *Langmuir* **2003**, 19, (10), 4427-4431.
29. Chinnayelka, S.; McShane, M. J., Microcapsule Biosensors Using Competitive Binding Resonance Energy Transfer Assays Based on Apoenzymes. *Analytical Chemistry* **2005**, 77, (17), 5501-5511.
30. Brown, J. Q.; Srivastava, R.; McShane, M. J., Encapsulation of glucose oxidase and an oxygen-quenched fluorophore in polyelectrolyte-coated calcium alginate microspheres as optical glucose sensor systems. *Biosensors and Bioelectronics* **2005**, 21, (1), 212-216.

31. Ai, H.; Jones, S. A.; de Villiers, M. M.; Lvov, Y. M., Nano-encapsulation of furosemide microcrystals for controlled drug release. *Journal of Controlled Release* **2003**, 86, (1), 59-68.
32. Volodkin, D. V.; Petrov, A. I.; Prevot, M.; Sukhorukov, G. B., Matrix Polyelectrolyte Microcapsules: A New System for Macromolecule Encapsulation. *Langmuir* **2004**, 20, (8), 3398-3406.
33. Voigt, A.; Lichtenfeld, H.; Sukhorukov, G. B.; Zastrow, H.; Donath, E.; Baumler, H.; Mohwald, H., Membrane filtration for microencapsulation and microcapsules fabrication by layer-by-layer polyelectrolyte adsorption. *Industrial & Engineering Chemistry Research* **1999**, 38, (10), 4037-4043.
34. Voigt, A.; Buske, N.; Sukhorukov, G. B.; Antipov, A. A.; Leporatti, S.; Lichtenfeld, H.; Baumler, H.; Donath, E.; Mohwald, H., Novel polyelectrolyte multilayer micro- and nanocapsules as magnetic carriers. *Journal of Magnetism and Magnetic Materials* **2001**, 225, (1-2), 59-66.
35. Vinogradova, O. I.; Lebedeva, O. V.; Vasilev, K.; Gong, H. F.; Garcia-Turiel, J.; Kim, B. S., Multilayer DNA/poly(allylamine hydrochloride) microcapsules: Assembly and mechanical properties. *Biomacromolecules* **2005**, 6, (3), 1495-1502.
36. Vinogradova, O. I.; Lebedeva, O. V.; Kim, B. S., Mechanical behavior and characterization of microcapsules. *Annual Review of Materials Research* **2006**, 36, 143-178.
37. Vinogradova, O. I.; Andrienko, D.; Lulevich, V. V.; Nordschild, S.; Sukhorukov, G. B., Young's modulus of polyelectrolyte multilayers from microcapsule swelling. *Macromolecules* **2004**, 37, (3), 1113-1117.
38. Vinogradova, O. I., Mechanical properties of polyelectrolyte multilayer microcapsules. *Journal of Physics-Condensed Matter* **2004**, 16, (32), R1105-R1134.
39. Sukhorukov, G. B.; Shchukin, D. G.; Dong, W. F.; Mohwald, H.; Lulevich, V. V.; Vinogradova, O. I., Comparative analysis of hollow and filled polyelectrolyte microcapsules templated on melamine formaldehyde and carbonate cores. *Macromolecular Chemistry and Physics* **2004**, 205, (4), 530-535.

40. Sukhorukov, G. B.; Mohwald, H.; Decher, G.; Lvov, Y. M., Assembly of polyelectrolyte multilayer films by consecutively alternating adsorption of polynucleotides and polycations. *Thin Solid Films* **1996**, 284, 220-223.
41. Sukhorukov, G. B.; Mohwald, H., Multifunctional cargo systems for biotechnology. *Trends in Biotechnology* **2007**, 25, (3), 93-98.
42. Sukhorukov, G. B.; Fery, A.; Brumen, M.; Mohwald, H., Physical chemistry of encapsulation and release. *Physical Chemistry Chemical Physics* **2004**, 6, (16), 4078-4089.
43. Sukhorukov, G. B.; Donath, E.; Moya, S.; Susha, A. S.; Voigt, A.; Hartmann, J.; Mohwald, H., Microencapsulation by means of step-wise adsorption of polyelectrolytes. *Journal of Microencapsulation* **2000**, 17, (2), 177-185.
44. Sukhorukov, G. B.; Donath, E.; Lichtenfeld, H.; Knippel, E.; Knippel, M.; Budde, A.; Mohwald, H., Layer-by-layer self assembly of polyelectrolytes on colloidal particles. *Colloids and Surfaces a-Physicochemical and Engineering Aspects* **1998**, 137, (1-3), 253-266.
45. Sukhorukov, G. B.; Donath, E.; Davis, S.; Lichtenfeld, H.; Caruso, F.; Popov, V. I.; Mohwald, H., Stepwise polyelectrolyte assembly on particle surfaces: a novel approach to colloid design. *Polymers for Advanced Technologies* **1998**, 9, (10-11), 759-767.
46. Sukhorukov, G. B.; Antipov, A. A.; Voigt, A.; Donath, E.; Mohwald, H., pH-controlled macromolecule encapsulation in and release from polyelectrolyte multilayer nanocapsules. *Macromolecular Rapid Communications* **2001**, 22, (1), 44-46.
47. Sukhorukov, G.; Fery, A.; Mohwald, H., Intelligent micro- and nanocapsules. *Progress in Polymer Science* **2005**, 30, (8-9), 885-897.
48. Sukhorukov, G.; Dahne, L.; Hartmann, J.; Donath, E.; Mohwald, H., Controlled precipitation of dyes into hollow polyelectrolyte capsules based on colloids and biocolloids. *Advanced Materials* **2000**, 12, (2), 112-115.
49. Lulevich, V. V.; Vinogradova, O. I., Effect of pH and salt on the stiffness of polyelectrolyte multilayer microcapsules. *Langmuir* **2004**, 20, (7), 2874-2878.

50. Lulevich, V. V.; Nordschild, S.; Vinogradova, O. I., Investigation of molecular weight and aging effects on the stiffness of polyelectrolyte multilayer microcapsules. *Macromolecules* **2004**, *37*, (20), 7736-7741.
51. Lulevich, V. V.; Andrienko, D.; Vinogradova, O. I., Elasticity of polyelectrolyte multilayer microcapsules. *Journal of Chemical Physics* **2004**, *120*, (8), 3822-3826.
52. Leporatti, S.; Voigt, A.; Mitlohner, R.; Sukhorukov, G.; Donath, E.; Mohwald, H., Scanning force microscopy investigation of polyelectrolyte nano- and microcapsule wall texture. *Langmuir* **2000**, *16*, (9), 4059-4063.
53. Leporatti, S.; Gao, C.; Voigt, A.; Donath, E.; Mohwald, H., Shrinking of ultrathin polyelectrolyte multilayer capsules upon annealing: A confocal laser scanning microscopy and scanning force microscopy study. *European Physical Journal E* **2001**, *5*, (1), 13-20.
54. Lebedeva, O. V.; Kim, B. S.; Vinogradova, O. I., Mechanical properties of polyelectrolyte-filled multilayer microcapsules studied by atomic force and confocal microscopy. *Langmuir* **2004**, *20*, (24), 10685-10690.
55. Lebedeva, O. V.; Kim, B. S.; Vasilev, K.; Vinogradova, O. I., Salt softening of polyelectrolyte multilayer microcapsules. *Journal of Colloid and Interface Science* **2005**, *284*, (2), 455-462.
56. Lebedeva, O. V.; Kim, B. S.; Grohn, F.; Vinogradova, O. I., Dendrimer-encapsulated gold nanoparticles as building blocks for multilayer microshells. *Polymer* **2007**, *48*, (17), 5024-5029.
57. Kreft, O.; Skirtach, A. G.; Sukhorukov, G. B.; Mohwald, H., Remote control of bioreactions in multicompartament capsules. *Advanced Materials* **2007**, *19*, (20), 3142-+.
58. Kreft, O.; Prevot, M.; Mohwald, H.; Sukhorukov, G. B., Shell-in-shell microcapsules: A novel tool for integrated, spatially confined enzymatic reactions. *Angewandte Chemie-International Edition* **2007**, *46*, (29), 5605-5608.
59. Kreft, O.; Georgieva, R.; Baumler, H.; Steup, M.; Muller-Rober, B.; Sukhorukov, G. B.; Mohwald, H., Red blood cell templated polyelectrolyte capsules: A novel vehicle for the stable encapsulation of DNA and proteins. *Macromolecular Rapid Communications* **2006**, *27*, (6), 435-440.

60. Kim, B. S.; Vinogradova, O. I., pH-Controlled swelling of polyelectrolyte multilayer microcapsules. *Journal of Physical Chemistry B* **2004**, 108, (24), 8161-8165.
61. Kim, B. S.; Lobaskin, V.; Tsekov, R.; Vinogradova, O. I., Dynamics and stability of dispersions of polyelectrolyte-filled multilayer microcapsules. *Journal of Chemical Physics* **2007**, 126, (24).
62. Kim, B. S.; Lebedeva, O. V.; Koynov, K.; Gong, H. F.; Glasser, G.; Lieberwith, I.; Vinogradova, O. I., Effect of organic solvent on the permeability and stiffness of polyelectrolyte multilayer microcapsules. *Macromolecules* **2005**, 38, (12), 5214-5222.
63. Kim, B. S.; Lebedeva, O. V.; Koynov, K.; Gong, H. F.; Caminade, A. M.; Majoral, J. P.; Vinogradova, O. I., Effect of dendrimer generation on the assembly and mechanical properties of DNA/phosphorus dendrimer multilayer microcapsules. *Macromolecules* **2006**, 39, (16), 5479-5483.
64. Kim, B. S.; Lebedeva, O. V.; Kim, D. H.; Caminade, A. M.; Majoral, J. P.; Knoll, W.; Vinogradova, O. I., Assembly and mechanical properties of phosphorus dendrimer/polyelectrolyte multilayer microcapsules. *Langmuir* **2005**, 21, (16), 7200-7206.
65. Kim, B. S.; Fan, T. H.; Lebedeva, O. V.; Vinogradova, O. I., Superswollen ultrasoft polyelectrolyte microcapsules. *Macromolecules* **2005**, 38, (19), 8066-8070.
66. Kim, B. S.; Choi, J. W., Polyelectrolyte multilayer microcapsules: Self-assembly and toward biomedical applications. *Biotechnology and Bioprocess Engineering* **2007**, 12, (4), 323-332.
67. De Geest, B. G.; Van Camp, W.; Du Prez, F. E.; De Smedt, S. C.; Demeester, J.; Hennink, W. E., Degradable multilayer films and hollow capsules via a 'Click' strategy. *Macromolecular Rapid Communications* **2008**, 29, (12-13), 1111-1118.
68. De Geest, B. G.; Sukhorukov, G. B.; Mohwald, H., The pros and cons of polyelectrolyte capsules in drug delivery. *Expert Opinion on Drug Delivery* **2009**, 6, (6), 613-624.
69. De Geest, B. G.; Skirtach, A. G.; De Beer, T. R. M.; Sukhorukov, G. B.; Bracke, L.; Baeyens, W. R. G.; Demeester, J.; De Smedt, S. C., Stimuli-responsive multilayered hybrid nanoparticle/polyelectrolyte capsules. *Macromolecular Rapid Communications* **2007**, 28, (1), 88-95.

70. De Geest, B. G.; Dejugnat, C.; Verhoeven, E.; Sukhorukov, G. B.; Jonas, A. M.; Plain, J.; Demeester, J.; De Smedt, S. C., Layer-by-layer coating of degradable microgels for pulsed drug delivery. *Journal of Controlled Release* **2006**, 116, (2), 159-169.
71. De Geest, B. G.; De Koker, S.; Sukhorukov, G. B.; Kreft, O.; Parak, W. J.; Skirtach, A. G.; Demeester, J.; De Smedt, S. C.; Hennink, W. E., Polyelectrolyte microcapsules for biomedical applications. *Soft Matter* **2009**, 5, (2), 282-291.
72. Antipov, A. A.; Sukhorukov, G. B.; Mohwald, H., Influence of the ionic strength on the polyelectrolyte multilayers' permeability. *Langmuir* **2003**, 19, (6), 2444-2448.
73. Antipov, A. A.; Sukhorukov, G. B.; Leporatti, S.; Radtchenko, I. L.; Donath, E.; Mohwald, H., Polyelectrolyte multilayer capsule permeability control. *Colloids and Surfaces a-Physicochemical and Engineering Aspects* **2002**, 198, 535-541.
74. Antipov, A. A.; Sukhorukov, G. B.; Fedutik, Y. A.; Hartmann, J.; Giersig, M.; Mohwald, H., Fabrication of a novel type of metallized colloids and hollow capsules. *Langmuir* **2002**, 18, (17), 6687-6693.
75. Arshady, R., Preparation of biodegradable microspheres and microcapsules: 2. Polyactides and related polyesters. *Journal of Controlled Release* **1991**, 17, (1), 1-21.
76. Dowding, P. J.; Atkin, R.; Vincent, B.; Bouillot, P., Oil Core/Polymer Shell Microcapsules Prepared by Internal Phase Separation from Emulsion Droplets. I. Characterization and Release Rates for Microcapsules with Polystyrene Shells. *Langmuir* **2004**, 20, (26), 11374-11379.
77. Dowding, P. J.; Atkin, R.; Vincent, B.; Bouillot, P., Oil Core/Polymer Shell Microcapsules by Internal Phase Separation from Emulsion Droplets. II: Controlling the Release Profile of Active Molecules. *Langmuir* **2005**, 21, (12), 5278-5284.
78. Jain, R. A., The manufacturing techniques of various drug loaded biodegradable poly(lactide-co-glycolide) (PLGA) devices. *Biomaterials* **2000**, 21, (23), 2475-2490.
79. Loxley, A.; Vincent, B., Preparation of Poly(methylmethacrylate) Microcapsules with Liquid Cores. *Journal of Colloid and Interface Science* **1998**, 208, (1), 49-62.

80. Burnham, A. K.; Grens, J. Z.; Lilley, E. M., Fabrication of polyvinyl alcohol coated polystyrene shells. *Journal of Vacuum Science & Technology A: Vacuum, Surfaces, and Films* **1987**, 5, (6), 3417-3421.
81. Gañán-Calvo, A. M.; Dávila, J.; Barrero, A., Current and droplet size in the electro spraying of liquids. Scaling laws. *Journal of Aerosol Science* **1997**, 28, (2), 249-275.
82. Loscertales, I. G.; Barrero, A.; Guerrero, I.; Cortijo, R.; Marquez, M.; Gañán-Calvo, A. M., Micro/Nano Encapsulation via Electrified Coaxial Liquid Jets. *Science* **2002**, 295, (5560), 1695-1698.
83. Antonietti, M.; Förster, S., Vesicles and Liposomes: A Self-Assembly Principle Beyond Lipids. *Advanced Materials* **2003**, 15, (16), 1323-1333.
84. Discher, B. M.; Won, Y.-Y.; Ege, D. S.; Lee, J. C. M.; Bates, F. S.; Discher, D. E.; Hammer, D. A., Polymersomes: Tough Vesicles Made from Diblock Copolymers. *Science* **1999**, 284, (5417), 1143-1146.
85. Jenekhe, S. A.; Chen, X. L., Self-Assembly of Ordered Microporous Materials from Rod-Coil Block Copolymers. *Science* **1999**, 283, (5400), 372-375.
86. Kaler, E. W.; Murthy, A. K.; Rodriguez, B. E.; Zasadzinski, J. A., Spontaneous vesicle formation in aqueous mixtures of single-tailed surfactants. *Science* **1989**, 245, (4924), 1371-1374.
87. Nardin, C.; Hirt, T.; Leukel, J. r.; Meier, W., Polymerized ABA Triblock Copolymer Vesicles. *Langmuir* **1999**, 16, (3), 1035-1041.
88. Schuler, C.; Caruso, F., Decomposable Hollow Biopolymer-Based Capsules. *Biomacromolecules* **2001**, 2, (3), 921-926.
89. Stoenescu, R.; Meier, W., Vesicles with asymmetric membranes from amphiphilic ABC triblock copolymers. *Chemical Communications* **2002**, (24), 3016-3017.
90. Zhang, L.; Eisenberg, A., Multiple Morphologies of "Crew-Cut" Aggregates of Polystyrene-b-poly(acrylic acid) Block Copolymers. *Science* **1995**, 268, (5218), 1728-1731.

91. Zhang, L.; Yu, K.; Eisenberg, A., Ion-Induced Morphological Changes in "Crew-Cut" Aggregates of Amphiphilic Block Copolymers. *Science* **1996**, *272*, (5269), 1777-1779.
92. Zhou, S.; Burger, C.; Chu, B.; Sawamura, M.; Nagahama, N.; Toganoh, M.; Hackler, U. E.; Isobe, H.; Nakamura, E., Spherical Bilayer Vesicles of Fullerene-Based Surfactants in Water: A Laser Light Scattering Study. *Science* **2001**, *291*, (5510), 1944-1947.
93. Zu Putlitz, B.; Landfester, K.; Forster, S.; Antonietti, M., Vesicle-Forming Single-Tail Hydrocarbon Surfactants with Sulfonium Headgroup. *Langmuir* **2000**, *16*, (7), 3003-3005.
94. Peppas, N. A., Is there a future in glucose-sensitive, responsive insulin delivery systems? *Journal of Drug Delivery Science and Technology* **2004**, *14*, (4), 247-256.
95. Ibarz, G.; Dähne, L.; Donath, E.; Möhwald, H., Smart Micro- and Nanocontainers for Storage, Transport, and Release. *Advanced Materials* **2001**, *13*, (17), 1324-1327.
96. Tao, X.; Li, J.; Möhwald, H., Self-Assembly, Optical Behavior, and Permeability of a Novel Capsule Based on an Azo Dye and Polyelectrolytes. *Chemistry – A European Journal* **2004**, *10*, (14), 3397-3403.
97. Skirtach, A. G.; Dejughnat, C.; Braun, D.; Susha, A. S.; Rogach, A. L.; Parak, W. J.; Mohwald, H.; Sukhorukov, G. B., The role of metal nanoparticles in remote release of encapsulated materials. *Nano Letters* **2005**, *5*, (7), 1371-1377.
98. Katagiri, K.; Nakamura, M.; Koumoto, K., Magneto-responsive Smart Capsules Formed with Polyelectrolytes, Lipid Bilayers and Magnetic Nanoparticles. *ACS Applied Materials & Interfaces* **2**, (3), 768-773.
99. Hu, S.-H.; Tsai, C.-H.; Liao, C.-F.; Liu, D.-M.; Chen, S.-Y., Controlled Rupture of Magnetic Polyelectrolyte Microcapsules for Drug Delivery. *Langmuir* **2008**, *24*, (20), 11811-11818.
100. Donath, E.; Moya, S.; Neu, B.; Sukhorukov, G. B.; Georgieva, R.; Voigt, A.; Baumler, H.; Kiesewetter, H.; Mohwald, H., Hollow polymer shells from biological templates: Fabrication and potential applications. *Chemistry-a European Journal* **2002**, *8*, (23), 5481-5485.

101. Gao, C.; Donath, E.; Moya, S.; Dudnik, V.; Mohwald, H., Elasticity of hollow polyelectrolyte capsules prepared by the layer-by-layer technique. *European Physical Journal E* **2001**, 5, (1), 21-27.
102. Gao, C. Y.; Donath, E.; Mohwald, H.; Shen, J. C., Spontaneous deposition of water-soluble substances into microcapsules: Phenomenon, mechanism, and application. *Angewandte Chemie-International Edition* **2002**, 41, (20), 3789-3793.
103. Gao, C. Y.; Leporatti, S.; Donath, E.; Mohwald, H., Surface texture of poly(styrenesulfonate sodium salt) and poly(diallyldimethylammonium chloride) micron-sized multilayer capsules: A scanning force and confocal microscopy study. *Journal of Physical Chemistry B* **2000**, 104, (30), 7144-7149.
104. Gao, C. Y.; Leporatti, S.; Moya, S.; Donath, E.; Mohwald, H., Stability and mechanical properties of polyelectrolyte capsules obtained by stepwise assembly of poly(styrenesulfonate sodium salt) and poly(diallyldimethyl ammonium) chloride onto melamine resin particles. *Langmuir* **2001**, 17, (11), 3491-3495.
105. Gao, C. Y.; Leporatti, S.; Moya, S.; Donath, E.; Mohwald, H., Swelling and shrinking of polyelectrolyte microcapsules in response to changes in temperature and ionic strength. *Chemistry-a European Journal* **2003**, 9, (4), 915-920.
106. Khapli, S.; Kim, J. R.; Montclare, J. K.; Levicky, R.; Porfiri, M.; Sofou, S., Frozen Cyclohexane-in-Water Emulsion as a Sacrificial Template for the Synthesis of Multilayered Polyelectrolyte Microcapsules. *Langmuir* **2009**, 25, (17), 9728-9733.
107. Rana, R. K.; Murthy, V. S.; Yu, J.; Wong, M. S., Nanoparticle self-assembly of hierarchically ordered microcapsule structures. *Advanced Materials* **2005**, 17, (9), 1145-+.
108. Rana, R. K.; Murthy, V.; Wong, M. S. In *Charge-driven assembly of silica nanoparticles and salt-bridged polyamine-aggregates forming microshells*, 2004; 2004; pp 268-COLL.
109. Murthy, V. S.; Rana, R. K.; Wong, M. S., Nanoparticle-assembled capsule synthesis: Formation of colloidal polyamine-salt intermediates. *Journal of Physical Chemistry B* **2006**, 110, (51), 25619-25627.

110. Murthy, V. S.; Cha, J. N.; Stucky, G. D.; Wong, M. S., Charge-driven flocculation of poly(L-lysine)-gold nanoparticle assemblies leading to hollow microspheres. *Journal of the American Chemical Society* **2004**, 126, (16), 5292-5299.
111. Kadali, S. B.; Soultanidis, N.; Wong, M. S., Assembling Colloidal Silica into Porous Hollow Microspheres. *Topics in Catalysis* **2008**, 49, (3-4), 251-258.
112. Wong, M. S.; Cha, J. N.; Choi, K.-S.; Deming, T. J.; Stucky, G. D., Assembly of Nanoparticles into Hollow Spheres Using Block Copolypeptides. *Nano Letters* **2002**, 2, (6), 583-587.
113. Yu, J.; Murthy, V. S.; Rana, R. K.; Wong, M. S., Synthesis of nanoparticle-assembled tin oxide/polymer microcapsules. *Chemical Communications* **2006**, (10), 1097-1099.
114. Plush, S. E.; Woods, M.; Zhou, Y. F.; Kadali, S. B.; Wong, M. S.; Sherry, A. D., Nanoassembled Capsules as Delivery Vehicles for Large Payloads of High Relaxivity Gd³⁺ Agents. *Journal of the American Chemical Society* **2009**, 131, (43), 15918-15923.
115. Yu, J.; Yaseen, M. A.; Anvari, B.; Wong, M. S., Synthesis of near-infrared-absorbing nanoparticle-assembled capsules. *Chemistry of Materials* **2007**, 19, (6), 1277-1284.
116. Yu, J.; Javier, D.; Yaseen, M. A.; Nitin, N.; Richards-Kortum, R.; Anvari, B.; Wong, M. S., Self-Assembly Synthesis, Tumor Cell Targeting, and Photothermal Capabilities of Antibody-Coated Indocyanine Green Nanocapsules. *Journal of the American Chemical Society* 132, (6), 1929-1938.
117. Yaseen, M. A.; Yu, J.; Jung, B. S.; Wong, M. S.; Anvari, B., Biodistribution of Encapsulated Indocyanine Green in Healthy Mice. *Molecular Pharmaceutics* **2009**, 6, (5), 1321-1332.
118. Yaseen, M. A.; Yu, J.; Wong, M. S.; Anvari, B., In-vivo fluorescence imaging of mammalian organs using charge-assembled mesocapsule constructs containing indocyanine green. *Optics Express* **2008**, 16, (25), 20577-20587.
119. Yaseen, M. A.; Yu, J.; Wong, M. S.; Anvari, B., Laser-induced heating of dextran-coated mesocapsules containing indocyanine green. *Biotechnology Progress* **2007**, 23, (6), 1431-1440.

120. Yaseen, M. A.; Yu, J.; Wong, M. S.; Anvari, B., Stability assessment of indocyanine green within dextran-coated mesocapsules by absorbance spectroscopy. *Journal of Biomedical Optics* **2007**, 12, (6).
121. Tavera, E. M.; Kadali, S. B.; Bagaria, H. G.; Liu, A. W.; Wong, M. S., Experimental and Modeling Analysis of Diffusive Release from Single-Shell Microcapsules. *Aiche Journal* **2009**, 55, (11), 2950-2965.
122. Bagaria, H. G.; Kadali, S. B.; Wong, M. S., Shell Thickness Control of Nanoparticle/Polymer Assembled Microcapsules. *Chemistry of Materials* 23, (2), 301-308.
123. Zhao, N.; Bagaria, H.; Wong, M.; Zu, Y., A nanocomplex that is both tumor cell-selective and cancer gene-specific for anaplastic large cell lymphoma. *Journal of Nanobiotechnology* 9, (1), 2.

Chapter 2. Assembling colloidal particles into porous hollow and solid microspheres

2.1. Introduction

A non-surfactant-based synthesis approach to mesoporous hollow spheres through the use of colloidal silica is presented. Based on nanoparticle assembly chemistry developed previously for silica/polymer hybrid microcapsules, the room-temperature preparation follows a two-step sequence: 1) the electrostatic reaction of cationic polymer with an anionic salt solution, resulting in a suspension of salt-bridged polymer aggregates; and 2) the electrostatic reaction between this suspension and an aqueous suspension of nanoparticles (NPs).

Colloidal silica is a suspension of SiO_2 particles with diameters in the 1 to 1000 nm range. Commercially available since the 1930's, this material is used in applications as diverse as papermaking, investment casting, coatings, chemical-mechanical planarization, and photography, and as additives for cements and waxes^{1,2}. In heterogeneous catalysis, it finds great use as a binder for catalyst particles as it provides attrition resistance to, and disperses the particles within, the formed catalyst pellet. On the other hand, the colloidal form of silica is not used as commonly as a catalyst support. The difficulties lie in handling the oxide as a suspension, depositing the active phase on the particle surface, and recovering the solid as a porous solid. Sol-gel processing methods have been studied previously to address some of these issues^{3,4}.

There has been a tremendous interest in recent years to generate new materials using colloidal particles, particularly for particles in the size range of 1 to 100 nm

* Part of the work in this chapter got published as Kadali et al., Assembling Colloidal Silica into Porous Hollow Microspheres. Topics in Catalysis 2008, 49, (3-4), 251-258.

(nanoparticles, or NPs)⁵⁻⁸. The general approach involves the careful manipulation of interparticle and surface interactions to yield NP-based assemblies with well-controlled structure and morphology. Such NP assembly techniques may be quite applicable for increasing the usefulness of colloidal SiO₂ as a catalyst support material.

We recently developed a NP assembly method in which negatively charged NPs, cationic polymers, and multivalent anions are combined in such a way to generate silica/polymer microcapsule structures⁹⁻¹⁶. The synthesis is a two-step mixing process, in which a polymer solution and a salt solution are combined, followed by the addition of an aqueous suspension of SiO₂ NPs (Fig. 2.1). The salt acts to crosslink the polymer chains

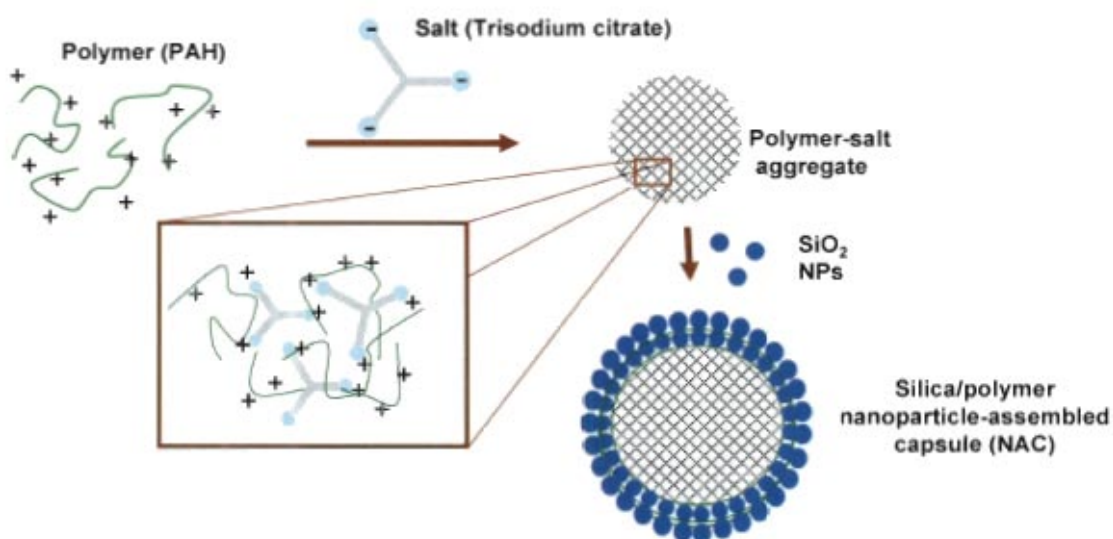


Figure 2. 1. Schematic of two-step NP assembly of silica/polymer microcapsules.

ionically to form metastable polymer-salt aggregates onto which the NPs deposit to form a thick shell. Taking only minutes to prepare, the resulting material (NP-assembled capsules, or "NACs") already has a capsular structure, in which the shell contains the NPs and polymer. The core can contain polymer/salt aggregate (polymer-filled capsules) or water (water-filled capsules), depending on initial synthesis conditions¹³. NAC synthesis

can be readily modified to encapsulate enzyme molecules, in which the immobilized enzymes interact with reactant molecules that diffuse through the semipermeable shell wall¹³. Such NACs would function as batch-type microreactors in water. Hollow sphere catalysts have a weight-effectiveness advantage over solid sphere catalysts for certain catalytic processes. For reactions in which the catalytic reaction rate is significantly faster than the rate of reactant diffusion (*i.e.*, large Thiele modulus) such that reactions would not occur in the catalyst interior, hollow spheres are more desirable. Hollow silica particles were recently reported as supports for polymerization catalysis, for example¹⁷.

As a specific example, 13-nm silica particles, combined with polyallylamine and sodium citrate, gave silica/polymer hollow spheres with a mean diameter of 2.1 μm and a BET surface area of 4 m^2/g . After calcination at 600 $^\circ\text{C}$, the resulting silica-only microcapsules had a BET surface area of 259 m^2/g , a modal pore size of 4.0 nm, and a pore volume of 0.38 cc/g , values that exceeded those of calcined silica NPs. This colloidal silica-based material is an example of the simultaneous control of pore size (at the nanometer scale) and particle morphology (at the micrometer scale) that is possible through charge-driven NP assembly. In our studies so far, the typical synthesis batch sizes have been kept small, on the order of ~ 0.5 mg of solids/batch as yield¹⁸. The preparation of NACs should be quite scalable, since the assembly process occurs rapidly; the synthesis conditions are room temperature and atmospheric pressure; water is the only solvent used; and the materials are not subjected to high temperatures or to any organic solvents. These are features that layer-by-layer assembly and other hollow sphere techniques do not necessarily have¹⁹⁻²¹. Scalability becomes an important issue if NP assembly is to be a useful method for preparing well-structured catalyst supports out of

colloidal SiO₂. In this work, we present a synthesis method that improves the yield to 100-mg amounts of material. We find that the polymer can be removed from the silica/polymer hollow spheres through calcination without disrupting the particle morphology, leading to porous SiO₂ hollow spheres. Also, we have tested NP assembly chemistry to make by replacing negatively-charged silica NPs with positively-charged NPs (Ludox brand, alumina-doped silica NPs). Surprisingly, we were able to generate aluminosilicate/polymer solid spheres. We studied the effect of synthesis parameters like NP concentration, final solution pH, and polymer-salt aggregate aging time. We will discuss the formation mechanism of these spheres and their resultant mesoporous properties after calcination at 600 °C. These results indicate that the polymer-aggregate templating mechanism underlying NP assembly chemistry can be modified to yield mesoporous aluminosilicates of controlled porosity and particle size. Scale-up methods to produce hundreds of milligrams of aluminosilicate spheres was investigated.

2.2. Experimental Methods

2.2.1. Materials

Poly(allylamine hydrochloride) (“PAH,” 70,000 g/mol, ~750 allylamine units per molecule, chloride counterion, Sigma-Aldrich), trisodium citrate (“cit”, Fisher Scientific), and colloidal SiO₂ (Snowtex-O type, 20.3 wt% SiO₂, pH 3.4, ionic strength I = 16.9 mM, Nissan Chemicals) were the precursors used. The SiO₂ NP diameter was measured to be 13±3 nm by dynamic light scattering. The NPs had a zeta potential of -16 mV, calculated from electrophoretic mobility measurements using Henry’s equation. Aluminosilicate NPs (Ludox-CL) was obtained from Grace-Davison and was available as aqueous

colloidal suspension (30 wt. %, pH 3.5). The NPs measured 20 ± 3 nm by dynamic light scattering. Zeta potential of Ludox-CL NPs in the original sol condition was calculated from its electrophoretic mobility (1.8 ($\mu\text{m}/\text{sec})/\text{V}/\text{cm}$) to be 30 mV in the Henry's limit. Deionized water (18.2 M Ω , Barnstead Nanopure Diamond System) was used for the PAH and cit stock solutions, and a HCl solution (1 N, Fisher Science) was diluted with deionized water to a pH value of 3.5. The SiO₂ NP suspension was diluted with this HCl solution to three different concentrations of 20.3 wt%, 0.12 wt%, and 0.024 wt%. The Ludox-CL NP suspension was diluted with HCl (pH = 3.5) solution to obtain a concentration of 0.12 wt%.

2.2.2. Synthesis

An aqueous PAH solution (35 ml, 1 mg/ml) was mixed with an aqueous cit solution (87.5 ml) in a 250 ml beaker and stirred with a magnetic stirrer for 10 seconds at low speed ('5' speed on a 1-10 scale). For the two R charge ratios of 1.5 and 10 studied in this work, the cit concentrations were 2.12 mM and 14.2 mM, respectively. R is defined as the ratio of total number of negative charges from the salt to the total number of positive charges from the polyamine. A turbid mixture immediately resulted, indicating the formation of polymer-salt aggregates. This suspension was aged for 10 sec or 30 min, before a diluted aqueous SiO₂ NP suspension (87.5 ml; concentration of 20.3 wt%, 0.12 wt%, or 0.024 wt%) was added. The final SiO₂ concentration was 8.45 wt%, 0.05 wt%, and 0.01 wt%, respectively. The resultant mixture was stirred vigorously (at '7' speed) for 10 min and aged for 2 hrs. The precipitate was recovered through centrifugation (Beckman-Coulter Allegra X-22 centrifuge at 6000 rpm for 7 min). Most of the supernatant (2/3 volume) was removed and replaced with the same volume of deionized

water, and the mixture was re-agitated and re-centrifuged. This cleaning procedure was repeated twice to remove any unreacted precursors. The washed material is the silica/polymer microcapsules or NACs. The recovered material was then calcined at 600 °C for 6 hrs at a ramp rate of 2.6 °C/min and with an air flow rate of 100 cm³/min. For the preparation of the calcined SiO₂ NP comparison sample, colloidal SiO₂ was dried in a heated oven at 70 °C overnight, and the residue was calcined in the manner described above. For capsule size distribution analysis, approximately 800 particles were measured using ImageJ software. The above procedure was repeated for the Ludox-CL NPs. The Ludox-CL NPs are diluted to 0.12 wt % by diluting the NPs suspension with pH = 3.5 HCl solution to maintain the same pH as the initial pH of the NP suspension. The final Ludox-CL NPs concentration was 0.05 wt%. This new recipe is optimized for higher materials yield using efficient use of NPs when compared to the recipe by Rana et al. (2005).

Dye conjugation of PAH was performed in the following manner: 4 mg of FITC was dissolved in 500 µl of dimethylsulfoxide (DMSO, 99.8+%, EM Science). 500 mg of PAH was dissolved in 6 ml deionized water, with the solution pH adjusted to 8.4 using NaOH. The two solutions were combined and stirred for two days at room temperature in the dark. The resulting solution was dialyzed against deionized water for 48 hr (molecular cut-off of 2000 Da, POR® 7 dialysis membrane, Spectrum Laboratories). PAH-FITC (10 mg/mL) stock solutions were prepared in water and refrigerated. The concentration of PAH-FITC stock solution was characterized by total organic carbon analysis (TOC). A calibration curve is initially obtained for various PAH concentrations correlating to its total organic carbon content. The concentration of unknown PAH-FITC stock solution is

determined by running the TOC analysis and the concentration is obtained from the calibration. It is assumed that FITC interference is very minimal in PAH-FITC stock solution calculations, since the molar concentration of FITC added for PAH conjugation is $\sim 0.07\%$ of the PAH monomer molar concentration. From the molar extinction coefficient of FITC ($\epsilon_0 = 70,000 \text{ M}^{-1} \text{ cm}^{-1}$), the mean molar ratio of labeled monomers of PAH was estimated. The average number of dye molecules for 3 PAH chains is 1 dye molecules per PAH polymer chain of ~ 600 amine groups.

2.2.3. Characterization

Dynamic Light Scattering (DLS): Hydrodynamic diameter and zeta potential analysis was carried out with a Brookhaven ZetaPALS dynamic light scattering instrument²² with a BI-9000AT digital autocorrelator at a laser wavelength of 656 nm. All studies were carried out at a 90° scattering angle, and all samples were temperature controlled at 25°C during analysis.

Zeta Potential Analysis: Zeta potentials were calculated from electrophoretic mobility measurements through phase analysis light scattering (PALS) using the DLS instrument and a dip-in electrode. Henry's equation relates the zeta potential (ζ) of the SiO_2 NPs to their electrophoretic mobility (μ_E , units of (microns/s)/(V/m)): $\mu_E = (\zeta\epsilon/\eta)f(\kappa a)$, where ϵ is the dielectric constant of water (78.9), η is viscosity of water (0.89 cP), and $f(\kappa a)$ is a function of κa ²³. This ζ - μ_E relation is valid in the Henry's limit (when $0.1 \leq \kappa a \leq 100$), where κ is proportional to ionic strength I ²⁴ and a is the particle radius. The ζ -potential of SiO_2 NPs was measured from a sample of Snowtex-O (50 μl) diluted with HCl solution (1.5 ml, pH = 3.5). The κa of this suspension was ~ 0.4 . The ζ -potential of Ludox-CL NPs was measured from a sample of Ludox-CL (50 μl) diluted with HCl

solution (1.5 ml, pH = 3.5). The κa of this suspension was ~ 0.6 . For the polymer-salt aggregate mixtures, $\kappa a = 400$ and 1100 for R ratios of 1.5 and 10, respectively. In this case ($\kappa a > 100$), the appropriate ζ - μ_E relation is Smoluchowski's equation, $\mu_E = \zeta\varepsilon/\eta$.

Scanning Electron Microscopy (SEM): SEM was carried out using a FEI Quanta 400 field emission scanning electron microscope, equipped with secondary electron, backscatter, and energy dispersive X-ray (EDX) detectors. Secondary electron images were taken at 15 kV with a working distance of 10 mm. A droplet of NACs suspension was placed on the aluminum stub and dried in air; the sample was then sputter-coated with gold for 1 min. For microtomed samples, the NACs were dried for 12 hr at room temperature and suspended in a fluid resin medium (Pelco Eponate 12TM Kit with BDMA, Ted Pella, Inc.) and heated at 65 °C for 16 hr. The hardened resin block was then cut into 700-nm thick wafers (about 0.5×0.5 mm² in size) using a glass knife on a Leica Ultracut microtome. The wafers were placed on the aluminum stub and dried in air; the sample was then sputter-coated with gold for 1 min. For EDX analysis, the accelerating voltage was set to 15 kV and GENESIS microanalysis version 4.61 software was used.

Optical Microscopy: Optical microscopy was performed on a Leica DM2500 upright microscope equipped with 100 \times oil immersion objective (numerical aperture = 1.4). Bright field and differential interference contrast (DIC) images were taken at 100 \times magnification.

Thermogravimetric Analysis (TGA): The weight loss-temperature profile for NACs was collected on a TA Instruments (SDT 2960 Simultaneous DSC-TGA) thermogravimetric analyzer. The temperature ramp rate was 5 °C/min and the air flow

rate was 100 cm³/min. The NACs (~100 mg) were dried under vacuum at 80 °C overnight prior to analysis.

Nitrogen Physisorption Porosimetry: Specific surface area, pore size distribution, and pore volume measurements were performed using a Micromeritics ASAP 2010 gas adsorption analyzer. Samples (uncalcined NACs, calcined NACs, and calcined SiO₂ NPs) were vacuum dried overnight at 250 °C until the vacuum pressure did not increase at a rate of 3×10⁻³ mmHg/min or higher. Nitrogen adsorption/desorption isotherms were obtained by a 91-point analysis in the relative pressure (P/P₀) range of 0.01 and 0.99. The pore size distribution was calculated using the BJH (Barrett-Joyner-Halenda) method²⁵; the adsorption branch of the isotherm was used instead of the desorption branch, as the former provided more realistic results²⁶. Micropore analysis was performed by examining the t-plots of the isotherms, in which volume of N₂ adsorbed is plotted against thickness of the adsorbed N₂ layer. The adsorbed layer thickness *t* was calculated using the Halsey

equation $(t = 3.54 \left[\frac{-5.00}{\ln\left(\frac{P}{P_0}\right)} \right]^{1/3})$ ²⁷. The specific surface area was calculated using the

BET (Brunauer-Emmett-Teller) equation²⁸ in the P/P₀ range of 0.06 to 0.20, and the pore volume (PV) was determined at P/P₀ = 0.99. Porosity, defined as the particle's void volume divided by its total volume, is calculated from PV/(PV+1/ρ), where ρ is the density of the solid fraction of the particle. The instrumentation accuracy was calibrated using a SiO₂ reference standard and its surface area accuracy is approximately ±1.3%.

2.3. Results and Discussion

The larger-scale synthesis route provided typical yields in the range of 100-110 mg, which was a >100-fold increase over the ~0.5-mg batch sizes from the original synthesis method¹³. Several interesting aspects of the NP assembly chemistry were uncovered during the optimization of the synthesis.

2.3.1. Effect of dilution of colloidal SiO₂ precursor

In the original synthesis method, only 1% of the SiO₂ NPs added was incorporated into the microcapsules¹³. To reduce the excess amount of NPs in the larger-scale synthesis method, we studied SiO₂ NP suspensions with different weight concentrations as precursors. The 20.3 wt% suspension led to typical-looking microcapsules (Fig. 2.2a). However, under dried condition, significant agglomeration and structural collapse of the capsules were observed (Fig. 2.2d).

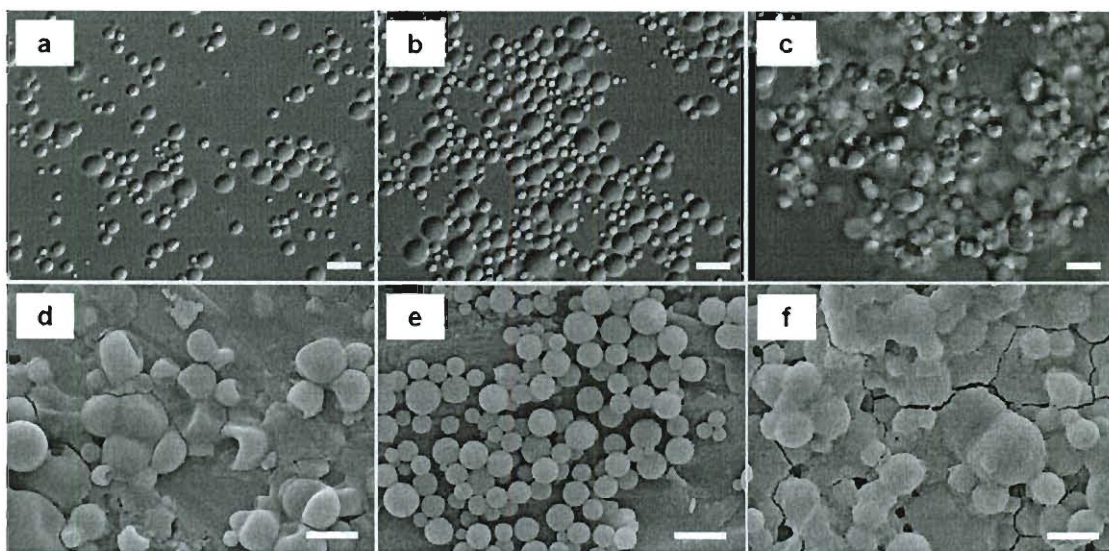


Figure 2.2. Silica/polymer microcapsules prepared with SiO₂ NP precursor concentrations of (a,d) 20.3 wt%, (b,e) 0.12 wt%, and (c,f) 0.02 wt%, imaged through (a-c) optical DIC microscopy and (d-f) SEM images. Scale bar: 5 μm.

There seemed to be additional disordered material between the capsules, likely coming from excess SiO₂ NPs that could not be removed completely during the centrifugation/washing steps. The 0.12 wt% suspension was found to have the optimum concentration, leading to unaggregated and structurally robust NACs (Fig. 2.2b,e); this precursor concentration was used for all subsequent NAC preparations. On the other hand, the 0.02 wt% suspension led to highly agglomerated NACs under both wet and dry conditions (Fig. 2.2c,f).

How do these observations reconcile with our two-step NP assembly mechanism (Fig. 2.1)? It is known that the polymer-salt aggregates grow as a function of time as soon as they nucleate after the polymer and salt solutions are combined, and that they grow through a coalescence process like that for emulsion droplets¹¹. Adding SiO₂ NPs can be thought as interrupting and arresting aggregate coalescence. To explain why the formed shells were not a single monolayer of NPs, we had hypothesized a diffusion-deposition process, in which SiO₂ NPs diffused through the outer part (the corona) of the polymer-salt aggregate and then deposited. The penetration depth determined the shell thickness as additional NPs deposited within the corona. The SiO₂ NPs were negatively charged at the synthesis pH, and therefore able to bind to the cationic PAH chains electrostatically.

The proper amount of SiO₂ NPs allowed the shell to form and thicken at a rate much higher than the rate of aggregate coalescence (Fig. 2.2b,e). Then, a low NP concentration (5× less) led to a low shell thickening rate, such that the polymer-salt aggregates (with the incompletely formed shell) were able to continue interacting and coalescing (Fig. 2.2c,f). A very high NP concentration (169× more) quenched coalescence to yield unaggregated capsules (Fig. 2.2a). The unreacted NPs could not be removed completely from the

supernatant. As the NAC droplet on the SEM stub began to dry, the NP concentration (and therefore osmotic pressure) increased. It is known that the capsule shell wall behaves as a semipermeable membrane, allowing water and small dye molecules to travel across the shell but not larger macromolecules like enzymes^{13, 29}. It is conceivable that the shell wall buckled once a critical osmotic pressure was reached during the drying step, resulting to the observed partially collapsed morphology (Fig. 2.2d).

2.3.1. Effect of surface charge of polymer-salt aggregates

The implicit assumption in the shell formation step is that the polymer-salt aggregates need to be positively charged for the negatively charged SiO₂ NPs to interact electrostatically. To probe this assumption, we prepared PAH-cit aggregate suspensions at two different *R* values, such that the surface charge (as characterized by the zeta potential) was either positively or negatively charged. We aged the suspensions for 30 min before combining with dilute colloidal SiO₂ (0.12 wt%).

At *R* = 1.5, the PAH-cit aggregates were positively charged with a ζ -potential of +7 mV. The resulting material had morphological features similar to NACs synthesized previously (Fig. 2.3a-b). From our earlier work, confocal microscopy analysis of fluorescently labeled NACs showed that the shells were composed of both NPs and polymer chains^{11, 13}. The shell wall thickness (hundreds of nm's) and hollow sphere structure of the material could clearly be seen after microtoming (Fig. 2.3c). NACs prepared with PAH chains are generally polymer-filled^{11, 15, 16}. When dried, it is thought that the polymer-salt aggregate (in the core) dehydrates and the dried residue deposits on the inner shell wall.

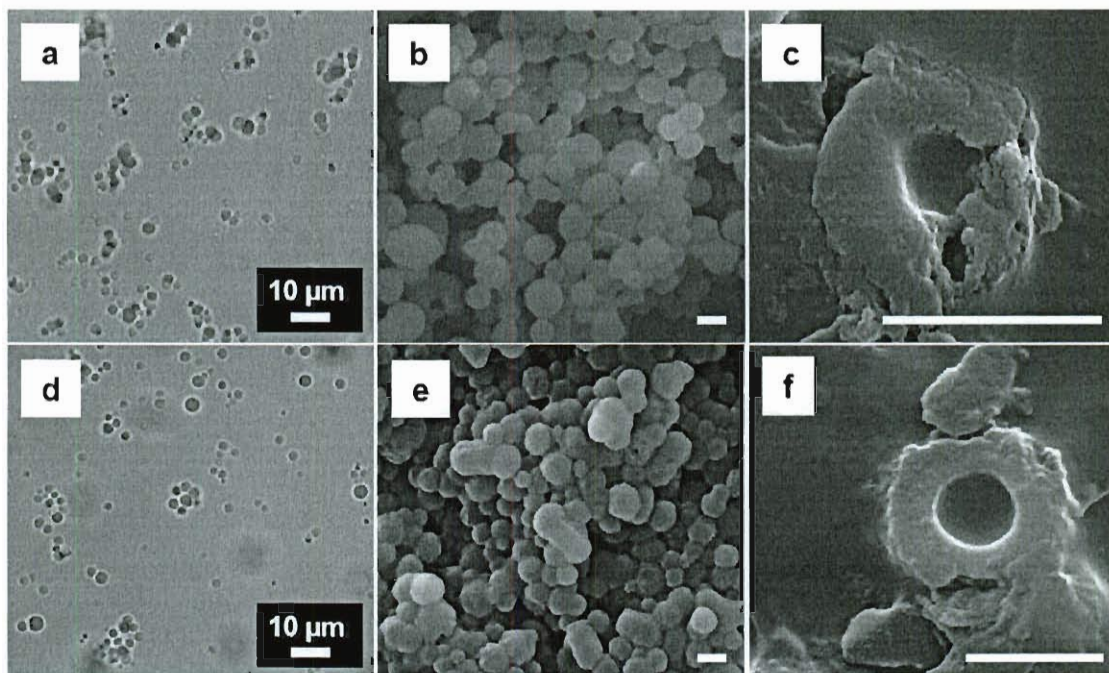


Figure 2.3. Silica/polymer microcapsules prepared at (a-c) $R = 1.5$ and (d-f) $R = 10$, imaged through (a,d) optical brightfield microscopy and (b,e) SEM. (c,f) SEM images of microtomed microcapsules. Scale bar for SEM images: $2 \mu\text{m}$.

Surprisingly, negatively charged aggregates also led to NACs (Fig. 2.3d-f). At $R = 10$, the PAH-cit aggregates had a ζ -potential of -8 mV , due to increased cit binding on the aggregate surface. The ζ -potential measurements represent the net surface charge but not the more realistic scenario of non-uniform surface distribution of charge, for which the diffusion-deposition model for shell formation does not currently account. These results suggest that the polymer-salt aggregate zeta potential is less important than the intrinsic positive charge of the polymer. Careful analysis of NACs prepared at $R = 10$ had a mean particle size distribution of $2.1 \mu\text{m}$ with a relative standard deviation of 28% (Fig. 2.4a). To demonstrate microcapsule size control, we synthesized materials in which the PAH-cit aggregate suspension was aged for 10 sec instead of 30 min. Since the aggregates are known to grow with time, the NACs were indeed smaller at short aging times. The mean

particle size was $0.8 \mu\text{m}$ and the relative standard deviation was 33%, spanning the mesoparticle/microparticle size range (Fig. 2.4b). The capsule size distribution improved with aggregate aging time.

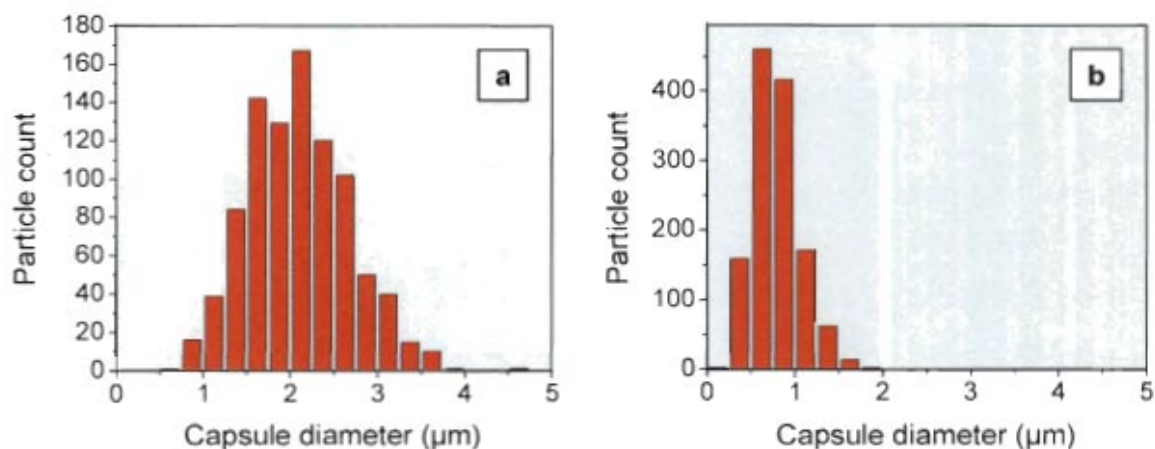


Figure 2.4. Histograms of NACs prepared with $R = 10$ and polymer-salt aggregate aging time of (a) 30 min and (b) 10 sec.

2.3.2. Calcined NACs

A TGA study of as-synthesized NACs indicated that 55% of the material was non-volatile (*i.e.*, composed of SiO_2), and the balance was the PAH and cit compounds (Fig. 2.5). Mass balance calculations indicated that $\sim 55\%$ of the SiO_2 NP precursor was incorporated into the microcapsules. The loss of volatiles occurred in three stages: $<100^\circ\text{C}$, $185\text{-}265^\circ\text{C}$, and $265\text{-}600^\circ\text{C}$. The first stage was likely due to the loss of water. The second and third stages could be due to the decomposition of cit anions and PAH chains, respectively.

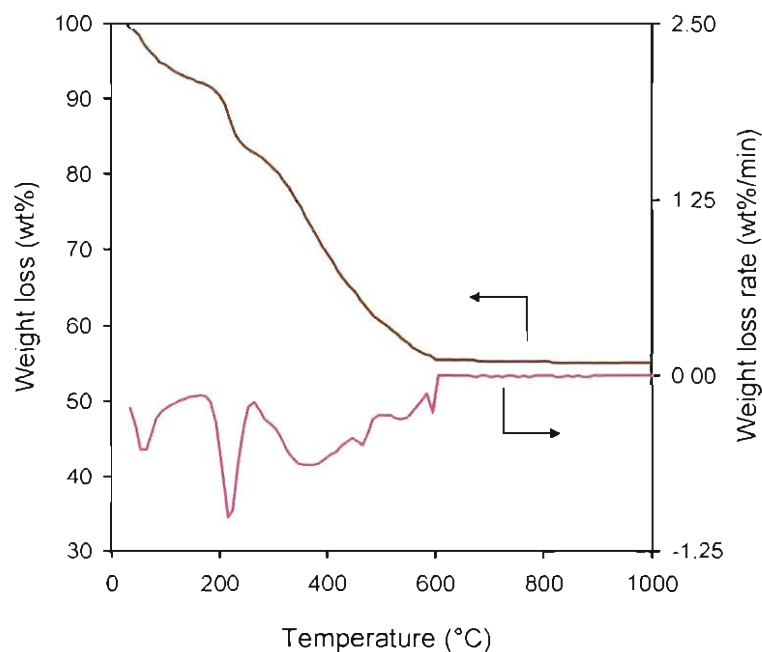


Figure 2.5. TGA weight-loss and weight-loss-rate profiles of NACs (R = 10 and aggregate aging time of 30 min).

Since all the organics were volatilized from the NACs by 600 °C, we used a calcination temperature of 600 °C. The resultant SiO₂-only capsules retained the spherical morphology; their hollowness could be observed in the partially open microcapsule (Fig. 2.6a). Qualitative compositional analysis via EDX on calcined NACs indicated the elements of C, O, Mg, Al, Si, and Au were present (Fig. 2.6b). Al and Mg came from the SEM stub, and the Au came from the sputter coating of the sample prior to SEM imaging. Carbon was detected in the calcined NACs, indicating incomplete volatilization of the organic content.

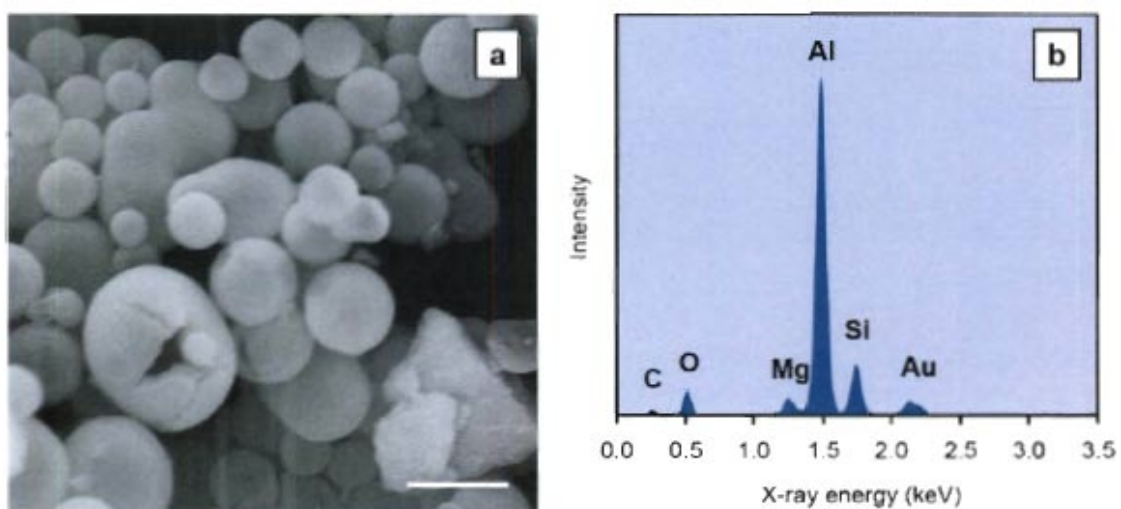


Figure 2.6. (a) SEM image and (b) EDX spectrum of NACs ($R = 10$ and aggregate aging time of 30 min) calcined at 600 °C. Scale bar: 5 μm .

Nitrogen adsorption isotherms for uncalcined NACs, calcined NACs, and calcined SiO_2 NPs were collected (Fig. 2.7a). All the isotherms had a Type 4 shape, indicating that the materials were mesoporous, *i.e.*, the pores were in the 2-50 nm diameter range³⁰. Both calcined materials clearly had a significantly higher N_2 adsorption capacity than the uncalcined NACs.

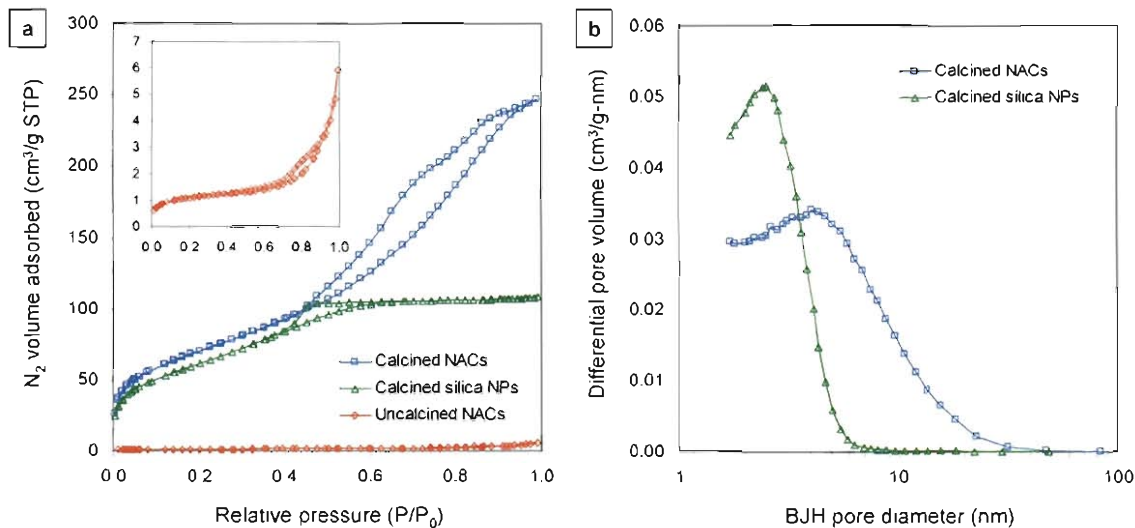


Figure 2.7. (a) Nitrogen adsorption isotherms for uncalcined NACs, calcined NACs, and calcined SiO_2 NPs. Inset: re-scaled isotherm for uncalcined NACs. (b) Pore size distributions calculated for calcined NACs and calcined SiO_2 NPs.

As mentioned above, the uncalcined NACs have a permeable shell wall, which allows water in the core (Fig. 2.3c,f) to be removed without breaking the capsule structure (Fig. 2.3b,e). Yet, the measured surface area was low and the pore size could not be determined (Table 2.1). These observations are seemingly incompatible, but it is recalled that nitrogen adsorption measurements were carried out on samples vacuum-dried at 250 °C. At this temperature, the uncalcined NACs were dehydrated, the cit anions were possibly decomposed, and the PAH chains remained in the shell (lodged between the SiO_2 NPs).

After calcination, the microcapsules significantly increased in surface area (by $>60\times$) and pore volume (by $>35\times$), with a mesopore size distribution that centered at 4.0 nm (Fig. 2.7b). For comparison, calcined colloidal SiO_2 had a $\sim 12\%$ lower surface area and a $\sim 55\%$ lower pore volume. It had a smaller pore size of 2.5 nm and a narrower pore size distribution. It seems that the SiO_2 NPs and PAH chains were arranged within the shell

wall in such a way that allowed for a more porous, higher surface-area material after high-temperature removal of the organics. The SiO₂ microcapsules had a higher porosity (46%) than calcined SiO₂ NPs (27%), which in turn had a much higher porosity than uncalcined SiO₂/polymer microcapsules (2%). We speculate that the polymer chains (which “glue” the NPs together into a flexible and permeable shell composite) remain in the shell at a high enough calcination temperature to reduce sintering of the SiO₂ NPs. That the PAH helps to prop up the SiO₂ NPs as they condense into a continuous oxide framework is consistent with the NACs having larger mesopores compared to the denser, and less porous, calcined SiO₂ NPs. Both materials contained no micropores (diameter < 2 nm), according to t-plot analysis ³¹.

Table 2. 1. Summary of nitrogen physisorption calculations.

Sample	BET surface area (m ² /g)	Pore volume (cm ³ /g)	Porosity (%)	BJH pore diameter range (nm)
Uncalcined SiO ₂ /polymer NACs	4	0.01	2%	Not available
Calcined SiO ₂ NACs	259	0.38	46%	1.7 – 32.0
Calcined SiO ₂ NPs	227	0.17	27%	1.7 – 7.5

The theoretical surface area (SA_{theo}) of SiO₂ NPs can be calculated using the geometrically derived relation $SA_{theo} = 6000/(D\rho)$, where D is diameter (13 nm) and ρ is density (2.2 g/cm³ for amorphous SiO₂). SA_{theo} was 210 m²/g, which should represent the surface area upper limit. Interestingly, both calcined SiO₂ NACs and calcined SiO₂ NPs had higher measured surface areas.

2.3.3. Synthesis of aluminosilicate spheres

The formation mechanism is a two step technique as depicted above: In the first step the polymer and the salt are mixed and they result in formation of aggregates. In the second step when the positively charged aluminosilicate (Ludox-CL) NPs are added, they form solid aluminosilicate spheres or solid Ludox-CL-NACs. Zeta potential on the aggregates for R ratios of 1.5 and 10 are +7 mV and -8 mV respectively (Fig. 2.8), both at near neutral pH. The polymer-salt aggregates are aged for 30 minutes and positively charged (Ludox-CL) NPs (0.5 wt % in total solution) were added.

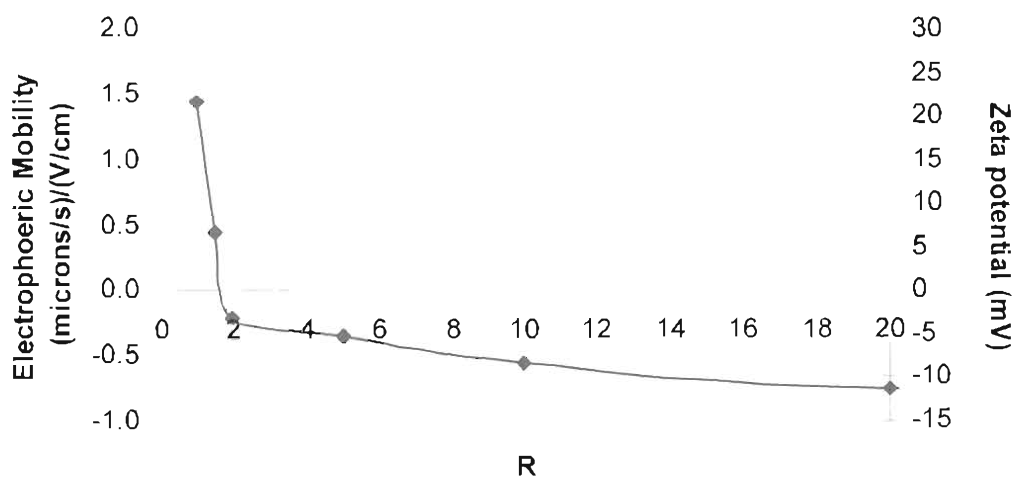


Figure 2. 8. Electrophoretic mobility of polymer-salt aggregates as a function of R for [PAH] = 1.0 mg/ml.

The structures thus formed are characterized using optical microscopy (Fig 2.9) The fluorescence images suggests that the polymer is present everywhere in the aluminosilicate spheres, scanning electron microscopy and ultramicrotome as shown in Fig 2.10.

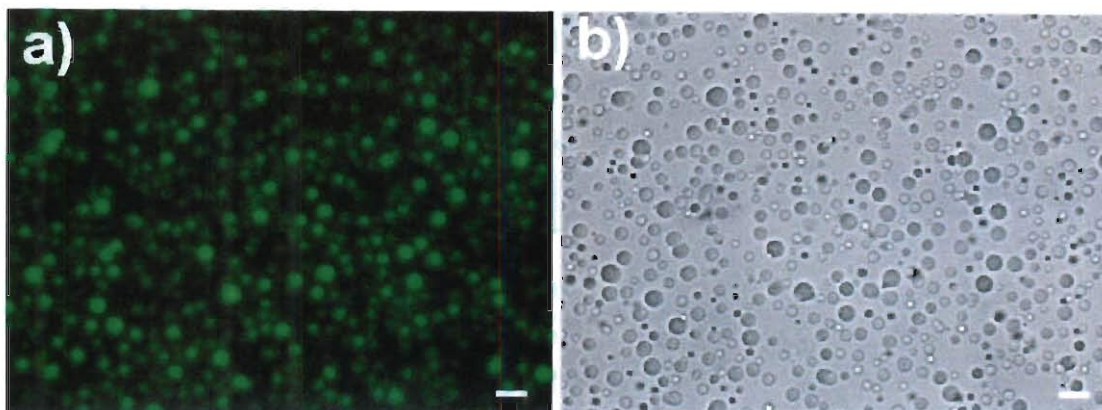


Figure 2.9. Optical image a) Fluorescence image b) Bright field of NACs synthesized by PAH, citrate and Ludox-CL NPs, $R = 10$, 30 min aging of PAH-Cit, scale bar 5 micron. PAH is conjugated with FITC as explained in methods.

2.3.4. Effect of surface charge of polymer-salt aggregates

We prepared PAH-cit aggregate suspensions at two different R values, such that the surface charge (as characterized by the zeta potential) was either positively or negatively charged (Fig 2.8). We aged the suspensions for 30 min before combining with dilute colloidal Ludox-CL (0.12 wt%). At $R = 1.5$, the PAH-cit aggregates were positively charged with a ζ -potential of +7 mV. The resulting material had morphological features similar to NACs synthesized previously (Fig. 2.10a-b). However, to probe the internal structure of the formed structures, ultramicrotome was performed. Surprisingly we observed that it formed solid aluminosilicate spheres. The solid structure of the material could clearly be seen after microtoming (Fig. 2.10c).

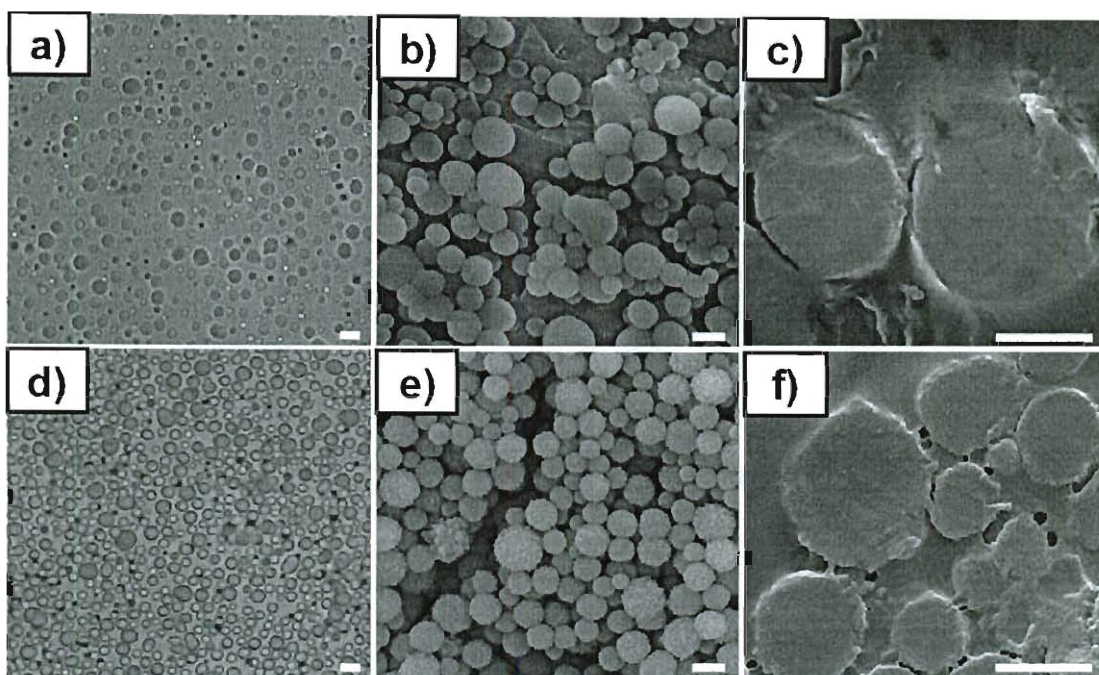


Figure 2. 10. (a) Optical bright field image b) SEM image, and c) SEM image of microtomed aluminosilicate spheres made at $R = 10$; (d) Optical bright field image e) SEM image, and f) SEM image of microtomed aluminosilicate spheres made at $R = 1.5$. Zeta potential on the aggregates for R ratios of 1.5 and 10 are $+7$ mV and -8 mV respectively, both at near neutral pH, scale bar 2micron.

Surprisingly, negatively charged aggregates also led to solid aluminosilicate spheres (Fig. 2.10d-f). At $R = 10$, the PAH-cit aggregates had a ζ -potential of -8 mV, due to increased cit binding on the aggregate surface. The ζ -potential measurements represent the net surface charge but not the more realistic scenario of non-uniform surface distribution of charge, for which the diffusion-deposition model for shell formation does not currently account. These results suggest that the polymer-salt aggregate zeta potential is less important than the intrinsic positive charge of the polymer. Ultramicrotome provides the evidence of the solid nature of the NACs. It is observed that irrespective of whether the polymer-salt aggregates are positively charged or negatively charged the final NACs formed are solid. We hypothesize that Ludox-CL NPs are able to penetrate

till the core of the polymer-salt aggregate. It has been reported by the Ludox-CL NPs supplier (Grace Davision) and by Meeren et al.³², that amount of alumina is 4 wt%. From our calculations using magic cluster model reported by Nutt et al.,³³ and also, Auffan et al.,³⁴ proposed a relation to quantify the percentage of atoms localized at the surface of a nanoparticle as a function of the nanoparticle diameter, it requires ~ 9 wt% to have monolayer coverage of alumina on 20 nm silica NP. It could be concluded that alumina has 45 % coverage over silica NP. Our calculation reveals that alumina is present like patches on silica NP. To understand the formation of solid aluminosilicate spheres, we have thoroughly investigated the nature of Ludox-CL NPs. Number of sites per Ludox-CL NP (Fig.2.11) is calculated as a function of pH. The calculations are performed based on method proposed by Behrens et al.³⁵. Isoelectric point (IEP) for Ludox-CL NPs is \sim pH = 8.1.

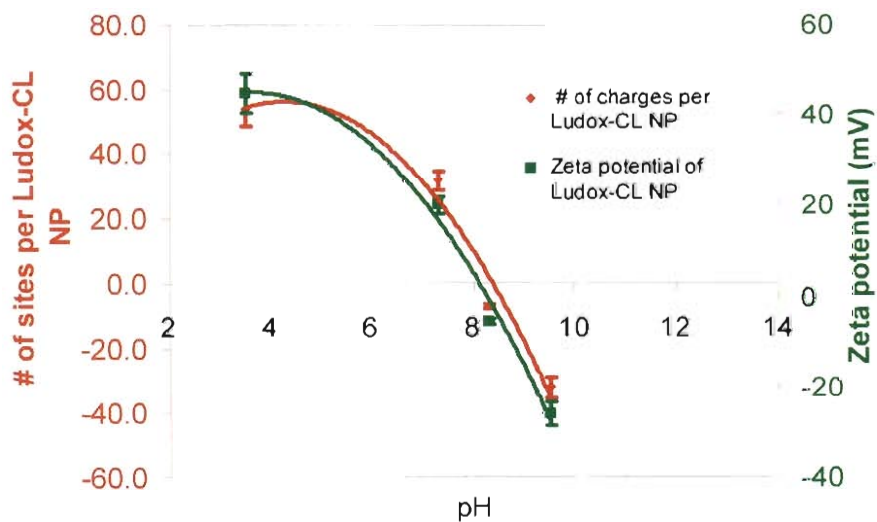


Figure 2. 11. Number of sites on Ludox-CL NP and Zeta potential as a function of pH.

For R=1.5 and 10, the pH of PAH +Cit suspension are 6.5 and 7.1 respectively. At these pH conditions, Ludox-CL NPs are positively charged and has ~ 30 positive sites

(Fig 2.11). After the addition of NPs, pH of the suspension for R= 1.5 and 10 conditions are 6.0 and 6.7 respectively. It should be noted that silica core of Ludox-CL NPs at pH 6.0 and 6.7 are negatively charged (Fig 2.12).

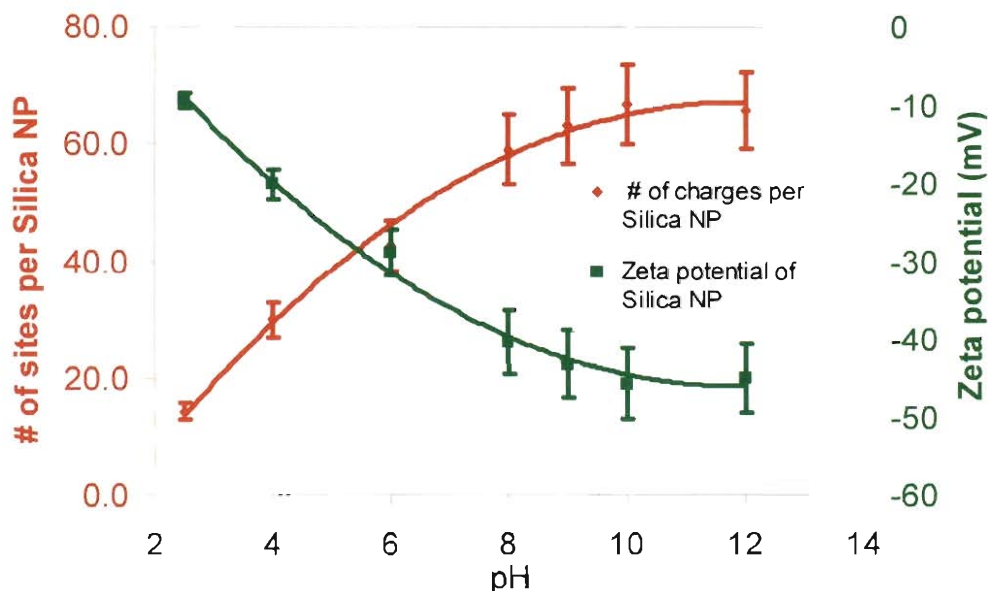


Figure 2.12. Number of sites on silica NP (Snowtex-O) and Zeta potential as a function of pH.

The ζ -potential measurements represent the net surface charge but not the more realistic scenario of non-uniform surface distribution of charge. Formation of aluminosilicate solid spheres follows earlier proposed diffusion deposition model¹³. Ludox-CL NPs deposit on PAH-Cit aggregates, and diffuse to form a thick shell. In this case, they are able to go all the way to the core of PAH-Cit, since the interactions between PAH-Cit and Ludox-CL are less compared to pure silica NP. Pure silica NP has completely negative sites and it starts binding to PAH and hinders the further penetration in the PAH-Cit matrix and results in the formation of thick shell as proposed in our earlier work. Hence, we hypothesize that for the case of R= 1.5 and 10, when Ludox-CL

NPs are added to PAH-Cit suspension they diffuse till the core. Positive sites on Ludox-CL NPs binds with Cit and negative sites bind to PAH resulting in the formation of solid structure. Ludox-CL

2.3.5. Effect of first aging time or floc aging time

To demonstrate microcapsule size control, we synthesized materials in which the PAH-cit aggregate suspension was aged for 10 sec instead of 30 min. Polymer-salt aggregates were found to grow in size as they are aged ¹¹, these aggregates grow maintaining their spherical shape. A longer aging time led to aggregates that were larger and shorter aging time leads to smaller aggregates. A theory has been established that PAH-cit aggregates grow by result of coalescence, in which the aggregates merge to form larger aggregates. The aluminosilicate spheres were indeed smaller at short aging times (10 sec) with a mean size 0.72 micron (Fig.2.13 a,b)and relative standard deviation of 26%. At 30 mins aging time of aggregates resulted in the formation of 2.01 micron (mean) size spheres (Fig.2.13 c,d) and relative standard deviation of 31%. The size distribution was done on the SEM images. Approximately 800 particles were calculated using the Image –Pro software.

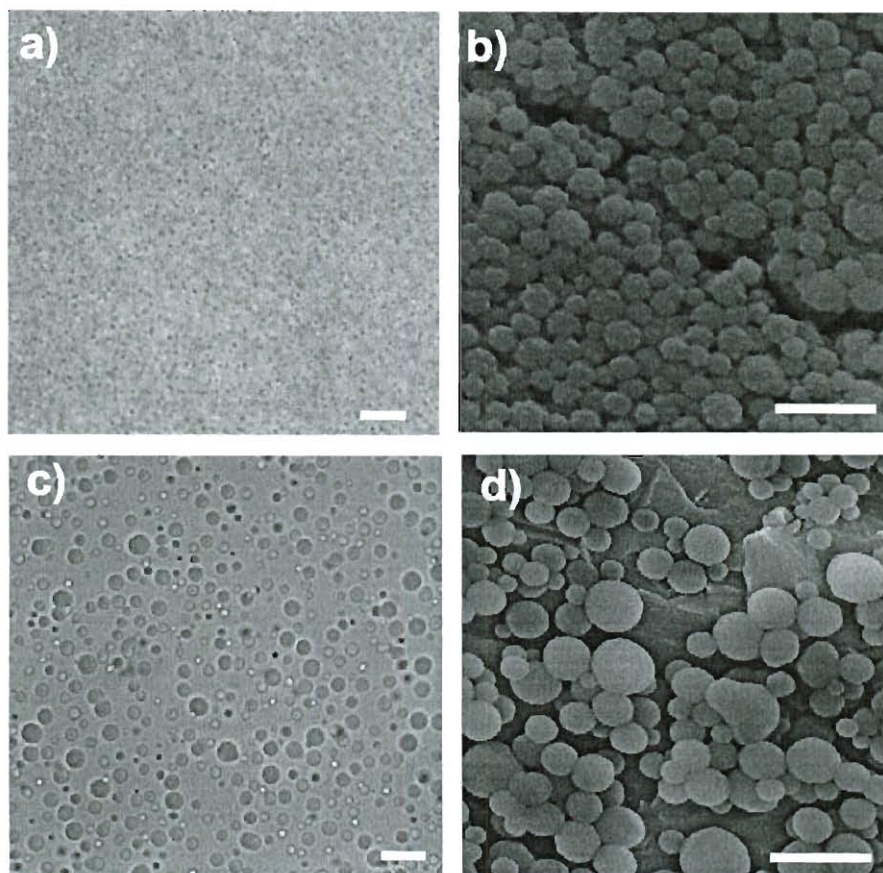


Figure 2.13. a) Optical bright field image b) SEM image of aluminosilicate spheres made at $R = 10$ and 10 sec aging time. c) Optical bright field image d) SEM image of aluminosilicate spheres made at $R = 10$ and 30 min aging time, scale bar 5 μm .

2.3.6. TGA and effect of calcination on aluminosilicate spheres

The aluminosilicate spheres and thus formed are subjected to thermo gravimetric analysis (TGA). The TGA analysis results reveal 52 % of volatile content (Fig. 2.14a) in aluminosilicate spheres, where as SiO_2 NACs TGA results show that 48 % of volatile content. The calcinations of the aluminosilicate spheres indicated little modification in the structure, thus indicating the robust structure of the spheres.

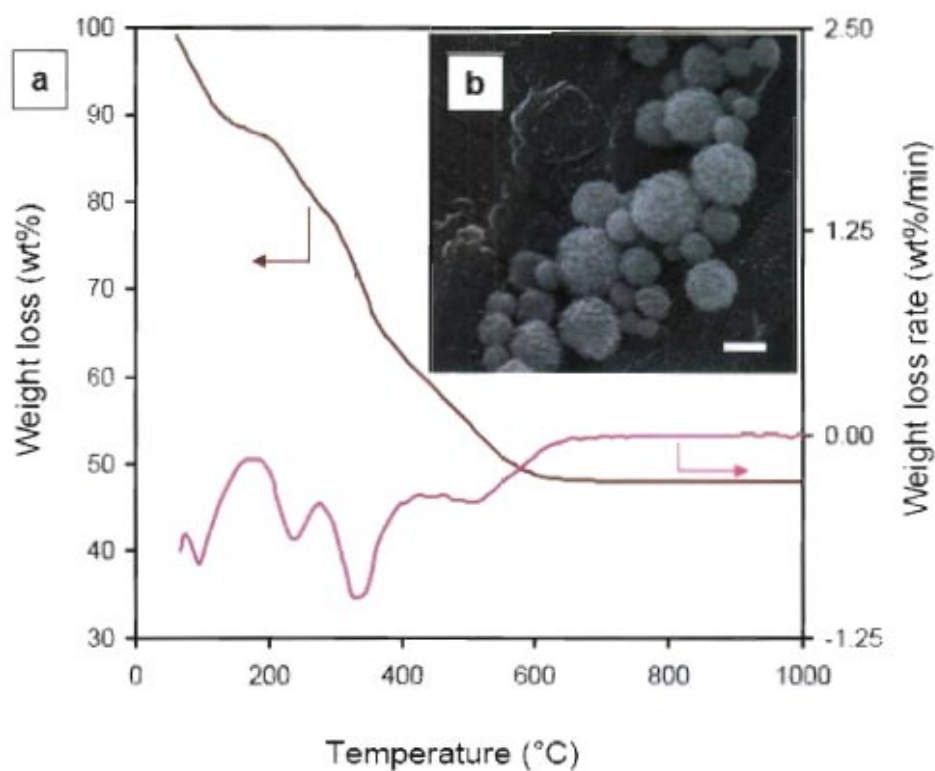


Figure 2.14. (a) TGA weight-loss and weight-loss-rate profiles of aluminosilicate spheres ($R = 10$ and aggregate aging time of 30 min), (b) calcined aluminosilicate spheres ($R = 10$ and aggregate aging time of 30 min), scale bar 2 μm .

The loss of volatiles occurred in three stages: <100 $^{\circ}\text{C}$, 185-265 $^{\circ}\text{C}$, and 265-600 $^{\circ}\text{C}$. The first stage was likely due to the loss of water. The second and third stages could be due to the decomposition of cit anions and PAH chains, respectively. Since all the organics were volatilized from the NACs by 600 $^{\circ}\text{C}$, we used a calcination temperature of 600 $^{\circ}\text{C}$. The resultant aluminosilicate-only spheres retained the spherical morphology; with some surface roughness (Fig 2.14b).

2.3.7. Nitrogen adsorption studies

Nitrogen adsorption isotherms for uncalcined aluminosilicate spheres, calcined aluminosilicate spheres, and calcined Ludox-CL NPs were collected (Fig. 2.15). All the isotherms had a Type 4 shape, indicating that the materials were mesoporous, *i.e.*, the pores were in the 2-50 nm diameter range³⁰. Table 2.2, summarizes the nitrogen physisorption calculations. Similar trends have been observed as seen in the case of silica-NACs.

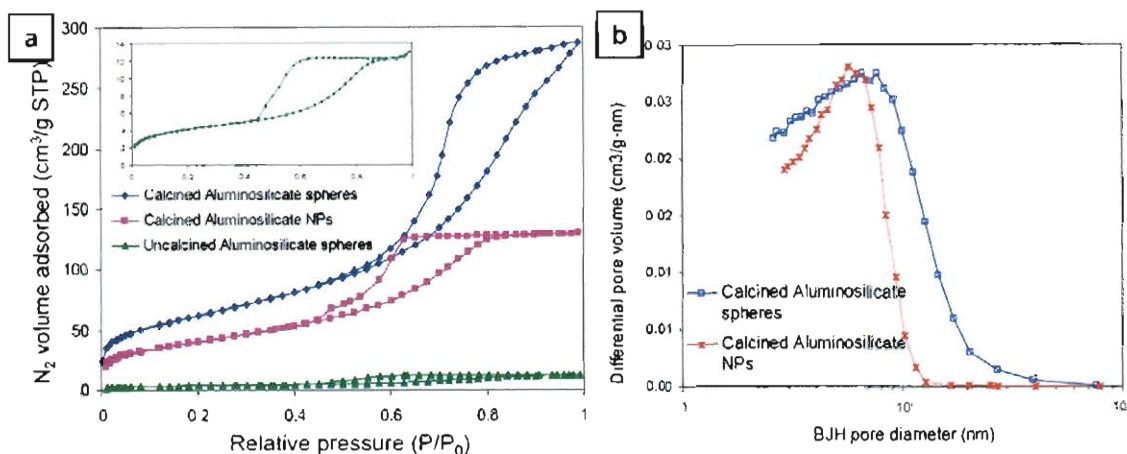


Figure 2.15. (a) Nitrogen adsorption isotherms for uncalcined aluminosilicate spheres, calcined aluminosilicate spheres, and calcined aluminosilicate NPs. Inset: re-scaled isotherm for uncalcined aluminosilicate spheres. (b) Pore size distributions calculated for calcined aluminosilicate spheres and calcined aluminosilicate NPs.

Uncalcined and calcined aluminosilicate spheres have the BET (Brunauer, Emmett, and Teller) surface areas of 15.0 and 226.3 m²/g (Fig. 2.15a). Both calcined materials clearly had a significantly higher N₂ adsorption capacity than the uncalcined aluminosilicate spheres. It is observed that the calcined material is more porous than the uncalcined material. Calcined aluminosilicate spheres shows significant increase in

surface area when compared with the uncalcined aluminosilicate spheres, thus suggesting potential applications in acid catalyst and can act as catalyst support material.

Table 2. 2. Summary of nitrogen physisorption calculations.

Sample	BET surface area (m ² /g)	Pore volume (cm ³ /g)	Porosity (%)	BJH pore diameter range (nm)
Uncalcined Aluminosilicate spheres	15	0.02	3%	Not available
Calcined Aluminosilicate spheres at 600 °C	226	0.45	47%	1.7 – 32.0
Calcined Aluminosilicate NPs at 600 °C	148	0.20	29%	1.7 – 7.5

2.4. Conclusions

A new procedure to 100-mg amounts of silica/polymer microcapsules was developed, improving on the materials yield by over two orders of magnitude while retaining the processing advantages of the original two-step NP assembly method. The PAH-cit aggregate surface charge was found to have little importance in microcapsule synthesis. The nanoparticle-assembled capsules were prepared with an average diameter of 2.1 μm, with the sizes readily adjustable by the polymer-salt aggregate aging time. These inorganic/organic hybrid composites can be thermally treated to eliminate completely the organic fraction of the material without morphological damage. The polymer, which holds the nanoparticles together in the shell, leads to pores after its removal. A temperature of 600 °C was sufficient to generate silica-only microcapsules. The material was mesoporous and had a higher porosity and pore volume than colloidal silica calcined

at 600 °C. The NP assembly chemistry can be extended to positively charged NPs such as aluminosilicate NPs. Solid microspheres are formed when Ludox-CL NPs were used in the assembly. This work demonstrates the scalability of charge-driven nanoparticle assembly chemistry, its general applicability to colloidal ceramics, and the renewed potential of colloidal silica as a precursor to porous catalyst supports.

2.5. References

1. Bergna, H. E.; Roberts, W. O., Colloidal Silica: Fundamentals and Applications. *CRC Press, Boca Raton* **2006**.
2. Iler, R. K., The Chemistry of Silica: Solubility, Polymerization, Colloid and Surface properties, and Biochemistry. *John Wiley and Sons, New York* **1979**.
3. Monaco, S. J.; Ko, E. I., Preparation of Silica and Alumina Single Oxides from Commercial Preformed Sols. *Chemistry of Materials* **1997**, 9, (11), 2404-2417.
4. Murrell, L. L., Sols and mixtures of sols as precursors of unique oxides. *Catalysis Today* **1997**, 35, (3), 225-245.
5. Davis, S. A.; Breulmann, M.; Rhodes, K. H.; Zhang, B.; Mann, S., Template-Directed Assembly Using Nanoparticle Building Blocks: A Nanotectonic Approach to Organized Materials. *Chemistry of Materials* **2001**, 13, (10), 3218-3226.
6. Rotello, V. M., Nanoparticles: Building Blocks for Nanotechnology. *Springer, New York* **2004**.
7. Shenhar, R.; Rotello, V. M., Nanoparticles: Scaffolds and Building Blocks. *Accounts of Chemical Research* **2003**, 36, (7), 549-561.
8. Shipway, A. N.; Katz, E.; Willner, I., Nanoparticle arrays on surfaces for electronic, optical, and sensor applications. *Chemphyschem* **2000**, 1, (1), 18-52.
9. Bagaria, H. G.; Kadali, S. B.; Wong, M. S., Shell Thickness Control of Nanoparticle/Polymer Assembled Microcapsules. *Chemistry of Materials* **2011**, 23, (2), 301-308.
10. Murthy, V. S.; Kadali, S. B.; Wong, M. S., Polyamine-Guided Synthesis of Anisotropic, Multicompartment Microparticles. *Acs Applied Materials & Interfaces* **2009**, 1, (3), 590-596.
11. Murthy, V. S.; Rana, R. K.; Wong, M. S., Nanoparticle-assembled capsule synthesis: Formation of colloidal polyamine-salt intermediates. *Journal of Physical Chemistry B* **2006**, 110, (51), 25619-25627.

12. Plush, S. E.; Woods, M.; Zhou, Y. F.; Kadali, S. B.; Wong, M. S.; Sherry, A. D., Nanoassembled Capsules as Delivery Vehicles for Large Payloads of High Relaxivity Gd³⁺ Agents. *Journal of the American Chemical Society* **2009**, 131, (43), 15918-15923.
13. Rana, R. K.; Murthy, V. S.; Yu, J.; Wong, M. S., Nanoparticle self-assembly of hierarchically ordered microcapsule structures. *Advanced Materials* **2005**, 17, (9), 1145-+.
14. Yaseen, M. A.; Yu, J.; Jung, B. S.; Wong, M. S.; Anvari, B., Biodistribution of Encapsulated Indocyanine Green in Healthy Mice. *Molecular Pharmaceutics* **2009**, 6, (5), 1321-1332.
15. Yu, J.; Murthy, V. S.; Rana, R. K.; Wong, M. S., Synthesis of nanoparticle-assembled tin oxide/polymer microcapsules. *Chemical Communications* **2006**, (10), 1097-1099.
16. Yu, J.; Yaseen, M. A.; Anvari, B.; Wong, M. S., Synthesis of near-infrared-absorbing nanoparticle-assembled capsules. *Chemistry of Materials* **2007**, 19, (6), 1277-1284.
17. Chen, J. F.; Song, J. R.; Wen, L. X.; Zou, H. K.; Shao, L., Preparation and characterization of agglomerated porous hollow silica supports for olefin polymerization catalyst. *Journal of Non-Crystalline Solids* **2007**, 353, (11-12), 1030-1036.
18. Wong, M. S., Unpublished results.
19. Caruso, F., Hollow Capsule Processing through Colloidal Templating and Self-Assembly. *Chemistry – A European Journal* **2000**, 6, (3), 413-419.
20. Dinsmore, A. D.; Hsu, M. F.; Nikolaides, M. G.; Marquez, M.; Bausch, A. R.; Weitz, D. A., Colloidosomes: Selectively Permeable Capsules Composed of Colloidal Particles. *Science* **2002**, 298, (5595), 1006-1009.
21. Wilcox, D. L.; Berg, M.; Bernat, T.; Kellerman, D.; Cochran, J. K.; Editors, Hollow and Solid Spheres and Microspheres Science and Technology Associated with their Fabrication and Application. *Materials Research Society Proceedings, Pittsburgh* **1995**, 372.
22. McNeil-Watson, F.; Tscharnuter, W.; Miller, J., A new instrument for the measurement of very small electrophoretic mobilities using phase analysis light scattering (PALS). *Colloids and Surfaces A: Physicochemical and Engineering Aspects* **1998**, 140, (1-3), 53-57.

23. Hiemenz, P.; Rajagopalan, R., *Principles of colloid and surface chemistry* **1997**, Marcel Dekker, Inc., New York
24. Hunter, R. J., *Foundations of Colloid Science. Oxford University Press, New York* **2001**.
25. Barrett, E. P.; Joyner, L. G.; Halenda, P. P., The Determination of Pore Volume and Area Distributions in Porous Substances. I. Computations from Nitrogen Isotherms. *Journal of the American Chemical Society* **1951**, 73, (1), 373-380.
26. Kruk, M.; Jaroniec, M.; Sakamoto, Y.; Terasaki, O.; Ryoo, R.; Ko, C. H., Determination of Pore Size and Pore Wall Structure of MCM-41 by Using Nitrogen Adsorption, Transmission Electron Microscopy, and X-ray Diffraction. *The Journal of Physical Chemistry B* **1999**, 104, (2), 292-301.
27. Halsey, G., Physical adsorption on non-uniform surfaces. *Journal of Chemical Physics* **1948**, 16, (10), 931-937.
28. Brunauer, S.; Emmett, P. H.; Teller, E., Adsorption of Gases in Multimolecular Layers. *Journal of the American Chemical Society* **1938**, 60, (2), 309-319.
29. Murthy, V. S.; Wong, M. S., Enzyme Encapsulation Using Nanoparticle-Assembled Capsules. In *Biomolecular Catalysis*, American Chemical Society: 2008; Vol. 986, pp 214-232.
30. Webb, P. A.; Orr, C., Analytical Methods in Fine Particle Technology. *Micromeritics Instrument Corp., Norcross* **1997**.
31. Gregg, S. J.; Sing, K. S. W., Adsorption, Surface Area, and Porosity. *Second Edition, Academic Press, London* **1982**.
32. Van der Meer, P.; Saveyn, H.; Bogale Kassa, S.; Doyen, W.; Leysen, R., Colloid-membrane interaction effects on flux decline during cross-flow ultrafiltration of colloidal silica on semi-ceramic membranes. *Physical Chemistry Chemical Physics* **2004**, 6, (7), 1408-1412.

33. Nutt, M. O.; Heck, K. N.; Alvarez, P.; Wong, M. S., Improved Pd-on-Au bimetallic nanoparticle catalysts for aqueous-phase trichloroethene hydrodechlorination. *Applied Catalysis B: Environmental* **2006**, 69, (1-2), 115-125.

34. Auffan, M.; Rose, J.; Bottero, J.-Y.; Lowry, G. V.; Jolivet, J.-P.; Wiesner, M. R., Towards a definition of inorganic nanoparticles from an environmental, health and safety perspective. *Nat Nano* **2009**, 4, (10), 634-641.

35. Behrens, S. H.; Grier, D. G., The charge of glass and silica surfaces. *Journal of Chemical Physics* **2001**, 115, (14), 6716-6721.

Chapter 3. Ionic strength and pH effects on nanoparticle-polyamine microcapsules

3.1. Introduction

A materials synthesis technique was recently developed to generate polyamine/silica composite microcapsules in which synthetic polyamines such as polyallylamine and/or polylysine were crosslinked with multivalent anions like citrate to form polymer-salt aggregates, that then served as templates for deposition of nanoparticles to form micron-sized hollow spheres or "nanoparticle-assembled capsules" (NACs)¹⁻⁴. As a general synthesis methodology, this electrostatically-driven "polymer-salt aggregate" or "PSA" assembly route is attractive for encapsulation and scale-up because encapsulation and materials formation occur in water, at mild pH values, and at room temperature.

Various type of NACs have been synthesized using polymers such as polyallylamine, polylysine, and polyethylene amine and using multivalent anions such as phosphate, citrate, EDTA, indocyanine green (ICG), and the macromolecule chelate Gd[DOTP]⁵⁻¹⁰. Usually NACs are spherical in shape, they could be either polymer-filled or water filled (hollow) based on the type of polymer, multivalent anions, and shell materials used. Most of the NACs have a thick shell wall and it could be controlled by size of the NPs added. indicate that the types of structures of "NACs. All have some sort of shell, but not all are strictly hollow. Shell material of NACs could be comprised of nanoparticles such as silica⁹, tin oxide¹, titania¹, zinc oxide¹, iron oxide¹¹, and CdSe quantum dots¹ or proteins such as human serum albumin¹², and bovine serum¹² albumin or polymers such as polyacrylic acid¹, and polystyrene sulfonate¹. Recently Zhao *et al.*, formed nanocomplexes of ~ 140 nm by adding siRNA and CD30 aptamer to the preformed

nanocore comprising of polyethyleneimine (PEI) and citrate¹³. NACs showed potential applications in using them as MRI contrast agents⁸ - showing larger gains in relaxivity, phototherapy^{11, 14}. Nanocomplexes for protease imaging, and siRNA therapy¹³. siRNA therapy¹³.

A related approach to preparing capsules through charge interactions is the layer-by-layer (LbL) assembly technique pioneered by Caruso and co-workers¹⁵⁻²². These LbL capsules are synthesized by the step-wise adsorption of polyelectrolytes onto charged colloidal templates, followed by decomposition of the templates. The core can be dissolved, for example, using organic solvents if the cores are polystyrene.²³ Inorganic particles, such as calcium carbonate or manganese carbonate, can be used as the sacrificial template for the fabrication of hollow organic capsules like polystyrene or cross-linked melamine formaldehyde.^{20, 24, 25} The inorganic templates are removed by exposing them to ethylenediaminetetraacetic acid (EDTA)²⁰. How are these templates removed? Polyelectrolyte shells are known to be permeable to molecules with a molecular weight below 5 kDa and they don't suffer an osmotic stress during the dissolution of the inorganic templates²⁶. The shell of LbL capsules can be incorporated with inorganic NPs.²⁷ LbL-assembled capsules have been shown to be promising as microreactors^{28, 29}, catalysis³⁰, separations^{31, 32}, separation of materials, sensors, and drug delivery materials.^{15, 28, 29, 33-35}

The driving force behind the LbL assembly at every step of the assembly is the electrostatic attraction between the charged surface and the incoming polyelectrolyte that is to be added to form a new layer. The properties and structure of LbL capsules are sensitive to a variety of physical and chemical conditions of the surrounding conditions²³.

^{36, 37}. Specifically, LbL capsules have been shown to have interesting behavior in response to different pH and ionic strength values^{23, 38-41}. LbL capsules made of PSS/PAH started to swell when the pH was above 11 and disassembled when the pH was above 12.²³ The capsules are permeable in the acidic region whereas they are impermeable in the alkaline region⁴². Schuler et al., has demonstrated the polyelectrolyte capsules decomposable by suspending the capsules in higher ionic strength solutions⁴². Polyelectrolyte capsule collapse or deflate once they are dried.^{22, 27, 43} Antipov *et al.*, has reported that depending on the pH, the permeability of these capsules could be changed.^{44, 45} This unique feature has helped in loading and releasing the cargo molecule from the capsules based on the operating pH conditions³⁷.

Comparatively, little has been done to assess the physical properties of NACs under varying pH and ionic strength conditions. To contribute to a better understanding of NACs, and use them for encapsulation and release applications, it is essential to study their physical properties. Here, we studied the effects of pH (in the range of 2 to 12), ionic strength (from 10 mM to 1 M), and nature of the salt (specifically phosphate, citrate, and seawater) of the suspending fluid. We analyzed the capsule size and shape through Coulter counter and laser confocal microscopy. In the aqueous phase range where the capsules were intact, we studied their mechanical strength through osmotic pressure testing.

3.2. Experimental Methods

3.2.1. Materials

Poly(allylamine hydrochloride) (“PAH,” 56,000 g/mol, ~600 allylamine units per molecule, chloride counterion, Sigma-Aldrich), Polystyrene sulfonate (“PSS” ~ 200,000 g/mol, sodium counterion, Sigma-Aldrich), trisodium citrate (“Cit”, Fisher Scientific), disodium phosphate (“Phos”, Fisher Scientific), disodium sulfate (“Sulf”, Fisher Scientific), sodium chloride (“NaCl”, Fisher Scientific), and a SiO₂ NP suspension (Snowtex-O type, 20.3 wt% SiO₂, pH 3.5, ionic strength I = 16.9 mM, Nissan Chemicals) were the precursors used. Premixed phosphate buffered saline (PBS) salt mixture was purchased from Sigma-Aldrich. Deionized water (18.2 MΩ, Barnstead Nanopure Diamond System) was used for the PAH and Cit stock solutions, and a HCl solution (1 N, Fisher Science) was diluted with deionized water to a pH value of 3.5. A NaOH solution (1 N, Fisher Science) was diluted with deionized water to various pH values accordingly. The SiO₂ NP suspension (NP diameter of 13±3 nm, according to dynamic light scattering; zeta potential of -16 mV, at pH 3.5 and I = 10 mM, calculated from electrophoretic mobility measurements using Henry’s equation) was diluted with HCl solution to 1.2 wt% (final pH = 3.5). Seawater was obtained from the Gulf of Mexico (Galveston, TX, USA).

Dye-conjugated PAH prepared in the following manner: 2 mg of RITC was dissolved in 500 µl of dimethylsulfoxide (DMSO, 99.8+%, EM Science). 500 mg of PAH was dissolved in 6 mL deionized water, with the solution pH adjusted to 9.5 using NaOH. The two solutions were combined and stirred for two days at room temperature in the dark. The resulting solution was dialyzed against deionized water for 48 hr (molecular cut-off

of 2000 Da, POR[®] 7 dialysis membrane, Spectrum Laboratories). PAH-RITC stock solutions (9.2 mg/mL) were prepared in water and refrigerated. The concentration of PAH-RITC stock solution was characterized by total organic carbon analysis (TOC). TOC is an indirect measure of organic molecules present in samples measured as carbon. The analyzer measures the CO₂ formed when organic carbon is oxidized. The sample is injected over a platinum catalyst at 680 °C. Any carbon present is converted to carbon dioxide, the CO₂ detector is a non-dispersive infrared detector (NDIR). A calibration plot was plotted between various PAH concentrations vs total organic carbon content. PAH-RITC carbon content was obtained by running the TOC analysis, and its concentration was extracted from the calibration curve. RITC interference is very minimal in PAH-RITC stock solution calculations. Molar concentration of RITC added for PAH conjugation was ~ 0.07% of the PAH monomer molar concentration.

A calibration curve is initially obtained for various PAH concentrations correlating to its total organic carbon content. The concentration of unknown PAH-RITC stock solution is determined by running the TOC analysis and the concentration is obtained from the calibration. It is assumed that RITC interference is very minimal in PAH-RITC stock solution calculations, since the molar concentration of RITC added for PAH conjugation is ~ 0.07% of the PAH monomer molar concentration. From the molar extinction coefficient of RITC ($\epsilon_0 = 10.7 \times 10^4 \text{ L mol}^{-1} \text{ cm}^{-1}$), the mean molar ratio of labeled monomers of PAH was estimated to be 1:3413. The average number of dye molecules for 5 PAH chains is 1 dye molecules per PAH polymer chain of ~ 600 amine groups.

3.2.2. PAH volumetric titrations

A volumetric titration has been performed to quantify the % degree of protonation of PAH at various pH levels. 100 ml of PAH (5 mg/mL or 53.2 mM monomer concentration) is titrated by adding 53.2 mM of NaOH, pH is noted after addition of NaOH to PAH solution. A plot is obtained between pH and amount of NaOH added. pKa of PAH was observed at a pH value of 8.5⁴⁶ obtained from the plot (Fig. A.7) . Our results matched exactly similar to the results obtained by Petrov et al⁴⁷.

3.2.3. Synthesis of NACs

An aqueous PAH solution with 5 % PAH-RITC doping (14 mL, 5 mg/mL) was mixed with an aqueous Cit solution (35 mL) in a 250 mL beaker and stirred with a magnetic stirrer for 10 seconds at low speed ('5' speed on a 1-10 scale). For the *R* charge ratio of 2 studied in this work, the Cit concentration was 14.2 mM, respectively. *R* is defined as the ratio of total number of negative charges from the salt to the total number of positive charges from the polyamine. A turbid mixture immediately resulted, indicating the formation of polymer-salt aggregates. This suspension was aged for 30 min, before a diluted aqueous SiO₂ NP suspension (35 mL; concentration of 1.2 wt %) was added. The resultant mixture was stirred vigorously (at '7' speed) for 10 min and aged for 2 hrs. The resulting material is the silica/polymer microcapsules or NACs.

3.2.4. pH and Ionic strength stability studies

The stability of NACs in solutions of pH 2 through 12 and ionic strengths of 10 mM to 1 M were tested. The solutions were prepared by a combination of NaCl, HCl and NaOH to achieve the desired pH and ionic strength. Several 2 mL NACs solution

aliquots were centrifuged, their supernatant removed and dispersed in 10 mL of the respective pH-ionic strength solution, such that the concentration of solids in water was approximately 7 mg/mL. The capsules were left overnight in the treated solutions before imaging them by confocal microscopy.

3.2.5. Osmotic pressure studies

The stability of NACs was tested by inducing osmotic pressure through PSS-Na. Several 2 mL NACs solution aliquots were centrifuged, their supernatant removed and dispersed in 10 mL of the respective concentrations of PSS-Na. The capsules were left overnight in the treated solutions before imaging them by confocal microscopy. Osmotic pressure studies were carried out on NACs suspended in DI-water, NACs previously subjected to pH 6.0 and ionic strength of 10 mM and 150 mM using NaCl. Statistical analysis was performed on confocal microscopy images taken to determine the number of deformed and undeformed capsules. The total number of capsules counted for each PSS concentration was at least 100. The deformation ratio was defined as the number of deformed capsules divided by the total number of capsules. The critical PSS concentration was defined as the concentration necessary to induce the deformation of 50% of the intact capsules⁴⁸.

3.2.6. Ionic strength study using multivalent anions

NACs stability in various multivalent anions such as sodium diphosphate, sodium disulfate, and trisodium citrate were tested. Ionic strengths of 10 mM to 1 M were prepared using above salts separately and NACs were tested by suspending in the corresponding ionic strength solutions for overnight. To test the effect of citrate anions on

NACs stability, a mixture of NaCl (1M) and trisodium citrate (10mM or 25mM) were prepared and NACs were suspended for overnight and tested. Rescue of NACs using trisodium citrate is carried out by preparing 10mM, 25mM trisodium citrate solution using 1M NaCl. NACs stability were studied in PBS and seawater.

3.2.7. Characterization

Confocal microscopy: Confocal images were captured with FluoView 1000 inverted microscope (IX81) equipped with a 100X Plan-Apochromat, (Numerical Aperture 1.4). The laser excitation wavelength of 543 nm was chosen for RITC ($\lambda_{ex} = 560$ nm, $\lambda_{em} = 580$ nm). Samples were mounted on conventional glass slides and sealed under a cover slip to prevent drying. All samples were prepared approximately 0.5 hr prior to imaging.

Osmometer: The osmotic pressure of the PSS solutions was measured by means of with a Vapor Pressure Osmometer, No. 5520, Wescor. PSS concentrations of 0, 2.0, 3.3, 6.6, 10, 20, and 30 wt% corresponded to osmotic pressure readings of 0, 2.3, 3.8, 7.5, 11.2, 23.7, and 39.8 bar.

Coulter counter measurements. Beckman Multisizer™ 3 Coulter counter having an orifice diameter of 100 μm was used to determine the NACs diameter and number count (total number of capsules). The lower limit for measuring sizes for this orifice was 2 μm . The instrument calibration was verified by measuring 3 μm standard latex beads. The diameter of capsules was measured by diluting ~100 μL of NACs in 20 mL of aqueous Isotone solution (composition: 7.93 g/L NaCl, 0.38 g/L Na_2EDTA , 0.40 g/L KCl, 0.19 g/L H_2NaPO_4 , 1.95 g/L HNa_2PO_4 , 0.30 g/L NaF; Beckman Coulter).

Dynamic Light Scattering (DLS): Hydrodynamic diameter and zeta potential analysis was carried out with a Brookhaven ZetaPALS dynamic light scattering

instrument⁴⁹ [Ref of Brookhaven] with a BI-9000AT digital autocorrelator at a laser wavelength of 656 nm. All studies were carried out at a 90° scattering angle, and all samples were temperature controlled at 25 °C during analysis.

Zeta Potential Analysis: Zeta potentials were calculated from electrophoretic mobility measurements through phase analysis light scattering (PALS) using the DLS instrument and a dip-in electrode. Zeta potential (ζ) of SiO₂ NPs was measured from a sample of Snowtex-O (50 μ L) diluted with HCl solution or NaOH (1.5 mL, appropriate pH and ionic strength).

3.3. Results and discussions

3.3.1. pH effect

The structure of NACs is held together by the electrostatic interactions of PAH, citrate and silica NPs. It can therefore be expected that the NACs structure will be sensitive to the solution pH. To test the pH sensitivity, silica NACs were dispersed in solutions of varying pH by keeping the ionic strength as constant. NACs in mother liquor are at pH 6.7 ($I \sim 17$ mM) and are mostly polymer filled with few regions of polymer-free cores. Suspended in DIW at pH 5.5 ($I \sim 0.02$ mM), the capsules had the same spherical shell structure and the same particle size distribution according to Coulter counter measurements, (Fig. 3.1). Most of the capsules were remained polymer-filled, i.e., the polymer resided throughout the interior.

At $I = 10$ mM, the capsules were stable in the pH range of 4-9, namely the capsules retained the same spherical structure but the core structures differed at different pH values. NACs in the mother liquor and in DIW were completely polymer-filled with few

regions of polymer-free cores^{7, 10}. At $I = 10$ mM, the NACs became mostly polymer-filled at pH 6 and 8. At pH 4 and 9, the core were polymer-filled with a "bubble" of water or regions of polymer-free cores. The percentage of polymer-filled capsules is 85 %, 98 %, 95 %, and 75 % corresponding to final pH suspension of 4, 6, 8, and 9 respectively. Capsules suspended at $\text{pH} > 9$ become weak and unstable as shown for $\text{pH} = 10$ case, capsules eventually disassemble at $\text{pH} = 12.0$. Likewise for capsules suspended in final $\text{pH} < 4.0$ capsules are disassembled. Also, it is observed that capsules are mostly polymer-filled in the pH range of 4-9.

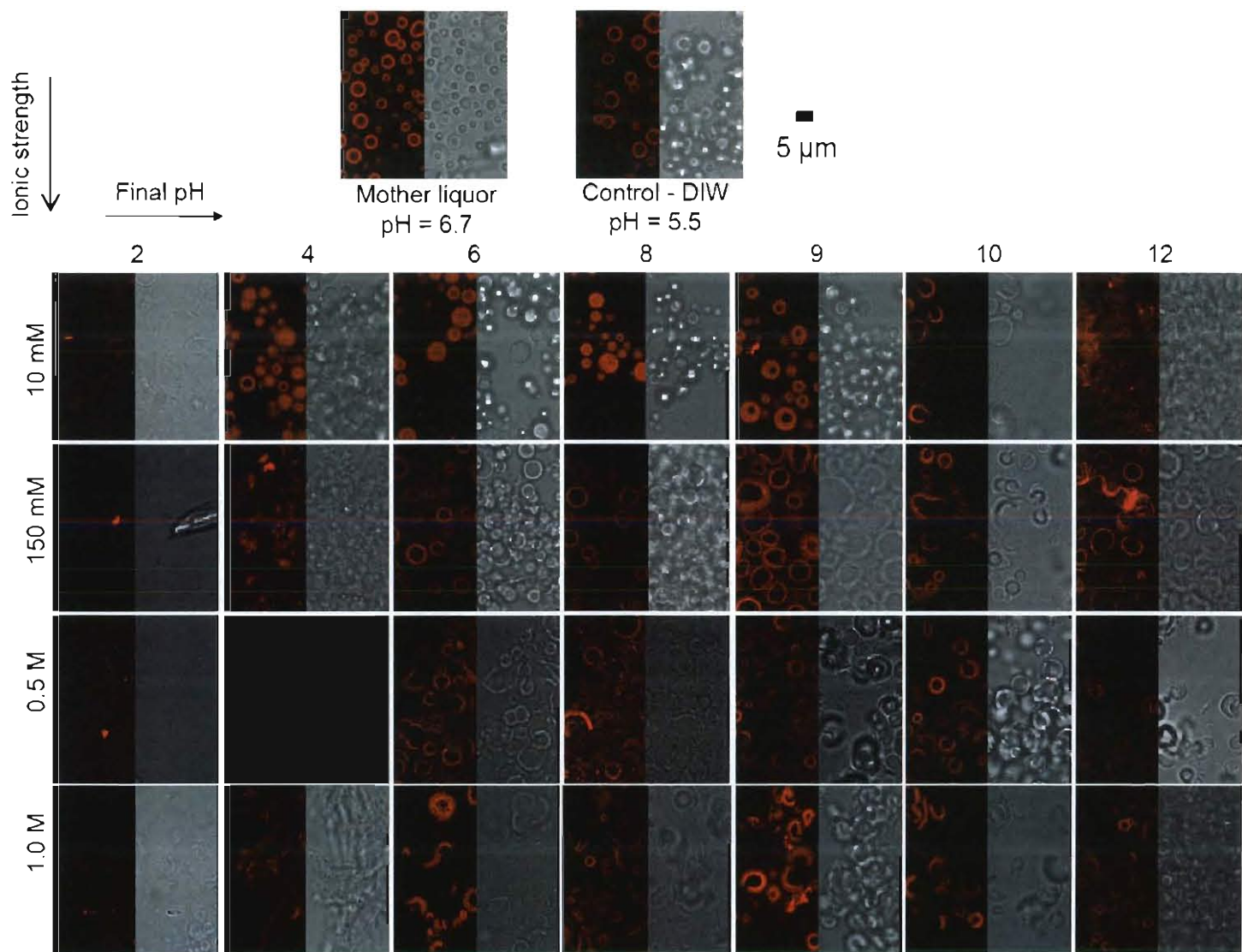


Figure 3.1. Confocal microscopy and bright field images of NACs as made (mother liquor), in DI- water, suspended in various final pH conditions from (L to R, pH range of 2-12) and various ionic strength solutions, 10 mM NaCl, 150 mM NaCl, 0.5 M NaCl, 1.0 M NaCl .Left half image is confocal image and the other half is the bright field image of the same spot.

To understand the shell stability of NACs in various pH conditions, it is of importance to look at the pKa values of PAH (pKa = 8.5) and isoelectric point (IEP) of silica⁵⁰ ~2.2. A volumetric titration has been performed to quantify the % extent of protonation of PAH at various pH levels. pKa of PAH was observed at a pH value of 8.5. The details are mentioned in the methods section. Trisodium citrate has three pKa values (pKa₁ = 3.13, pKa₂ = 4.76, and pKa₃ = 6.4).

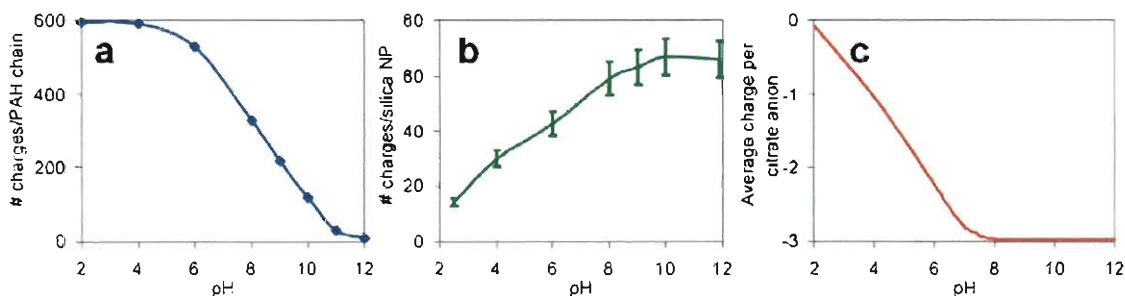


Figure 3.2. (a) Total number of positive charges per PAH chain vs. pH, (b) Total number of negative charges per silica NP vs. pH, (c) Average charge per citrate anion vs. pH.

As shown in Fig 3.2, the total number of charges of PAH, silica NP and average charge per citrate anion at various pH conditions are plotted. Citrate relative species distribution as a function of pH was performed by using acid-base equilibrium calculations. The citrate anions were mostly in the form of trivalent Cit³⁻ species (average charge per citrate anion is -3) when the pH > 8.0. The number of negative sites on a silica NP as function of pH are calculated from the surface charge density calculations which are in turn derived from zeta potential values⁵¹. Ionic strength was maintained at 10 mM using KCl. From Fig 3.2, it is observed that as pH goes from 2 to 12, the number of negative sites on silica NP increase upto a pH of 8.0 and then it reaches saturation. Considering at pH = 6.0, PAH is 88 % protonated (# of charges/PAH is 530) and citrate has the species distribution of approximately 27 % in the form of Cit³⁻, 65 % in the form

of HCit^{2-} , and 3 % in the form H_2Cit^- . At pH 6.0, silica NPs are negatively charged and a surface charge density⁵¹ of $-1.28 \mu\text{C}/\text{cm}^2$ or ~ 42 negative sites. Since our NACs are charge driven assembly, we believe that predominantly the electrostatic interactions among PAH and silica NPs holds the NACs structure as shown in Fig 3.1 ($I = 10 \text{ mM}$, $\text{pH} = 6$). The PAH and Cit interactions are responsible in determining whether the capsules are polymer filled or water filled. Thus most of the capsules are polymer filled at pH 6.0. As we look at capsules at pH 4.0, PAH is protonated by $\sim 99\%$ (# of charges/PAH is 590), citrate has the species distribution of approximately 12.5 % in the form of HCit^{2-} , and 75 % in the form H_2Cit^- and 12.5 % in the form H_3Cit . silica NPs are negatively charged and has a surface charge density of $-0.9 \mu\text{C}/\text{cm}^2$ or ~ 30 negative sites and thus by the electrostatic interactions of PAH, citrate and silica NPs capsules remained intact. At pH 2.0, PAH is completely protonated, citrate is in the form of H_3Cit , and silica NPs loses its charge, hence results in capsule disassembly.

At basic pH conditions, at pH 8.0, capsules remained intact and polymer filled since PAH is 55 % protonated (# of charges/PAH is 330) and citrate has the species distribution of approximately 98 % in the form of Cit^{3-} , and 2 % in the form of HCit^{2-} . At pH 8.0, silica NPs are negatively charged and has a surface charge density of $-1.78 \mu\text{C}/\text{cm}^2$ or ~ 60 negative sites. At pH 9.0, capsules remained intact and the core were polymer-filled with a "bubble" of water as shown in Fig 3.1. At pH 9.0, PAH is 36 % protonated (# of charges/PAH is 218) and citrate has the species distribution of approximately 100 % in the form of Cit^{3-} (average charge per citrate anion is -3) and silica NPs are negatively charged and has a surface charge density of $-1.9 \mu\text{C}/\text{cm}^2$ or ~ 63 negative sites.

3.3.2. Ionic strength effect

Salt concentration is an important physico-chemical parameter which will regulate the strength of electrostatics. The ionic cross-link density and conformations of PAH, Cit and NPs can be varied, therefore should effect the stability of NACs. As explained in previous section, a similar study was performed by varying the ionic strength from 10 mM to 1 M using NaCl. For I = 10 mM, the capsules stability was explained earlier. At I = 150 mM, the capsules were stable in the pH range of 6-8 and most of the capsules were water filled. The percentages of water-filled capsules are 97 %, and 91 %, corresponding to final pH suspension of 6, and 8 respectively. From the Fig. 3.1 we see that the stability spectrum narrows down in the pH range of 2-12 from a pH range of 4-9 for 10 mM case to a pH range of 6-8 for NACs suspended in 150 mM. NACs were completely disassembled for NACs suspended in a final pH < 6.0. At pH > 8.0, NACs were very fragile and start to buckle and most of the capsules are distorted. At pH > 9.0 most of the capsules are half broken.

To understand the shell stability of NACs in various ionic strength conditions, it is of importance to understand the strength of electrostatic interactions among PAH, Citrate and Silica NPs. Characteristic length or Debye length (κ^{-1}) describes the strength of electrostatic interactions. It is known that electric force falls exponentially with κ^{-1} . A solution with high ion concentrations has a high ionic strength and thus a short κ^{-1} . Conversely, a low ionic strength solution has a long κ^{-1} and the electric forces acts over longer distances. In our studies, 1:1 electrolyte NaCl is used to increase the ionic strength where $\kappa^{-1}(\text{nm}) = \frac{0.304}{\sqrt{I(\text{M})}}$)⁵². In our experiments for I of 10 mM, 150 mM, 500 mM and 1

M, κ^{-1} is 3.04 , 0.79, 0.43 and 0.304 nm respectively. The presence of more salt i.e, Na^+ , and Cl^- , could possibly bind to PAH, Cit, and silica and their respective charges are screened, which leads to a reduction in the number of ionic cross-links. The surface charge density on Silica NPs at pH 3.5 varied from $-0.75 \mu\text{C}/\text{cm}^2$ or ~ 24 negative sites to $-0.37 \mu\text{C}/\text{cm}^2$ or ~ 12 negative sites as I changes from 10 mM to 500 mM. As explained in earlier section that the structure of NACs is held together by the electrostatic interaction of PAH, Citrate and silica NPs. As the charge interaction decreases the capsule structure is weakly held by PAH, Citrate and Silica NPs.

At higher ionic strengths (I = 500 mM, and 1M) and at pH > 6.0, most of the capsules are half broken. At 1M, most of the NACs have broken (mostly into two halves). At pH < 6.0 NACs were completely disassembled. It was observed that NACs at high ionic strength becomes water filled. In specific, comparing NACs at pH 6.0 for 10 mM and 150 mM, % of polymer filled capsules goes down from 98 % to 3 %. It has been observed in our earlier work that at I = 10 mM NACs core comprises of polymer –citrate core, at I = 150 mM, the polymer-citrate core is disassembled. Since, the number of electrostatic interactions between PAH and silica NPs are much greater than the interactions between PAH and citrate. Suspending NACs at I of 150 mM (pH = 6) causes the dis-assembly of the PAH-citrate core and not cause the dis-assembly of the shell and retains the structure of NACs. The loss in fluorescence in the core region of NACs in 150 mM suspension indicated that NACs are water-filled capsules. This core can be broken by increasing ionic strength as discussed in our earlier work pH becomes a very good tool to enhance the loading of active ingredient in NACs by making them water or polymer filled.

3.3.3. pH and ionic strength effects on mechanical strength

The following section explores the osmotic pressure studies on NACs suspended in DI water, at pH 6.0 in 10 mM and 150 mM ionic strength cases. In this work we adopted the method followed by Khapli et al.,⁵³ that use osmotic pressure effects generated by using polyelectrolyte to exert forces on the microcapsules^{21, 38-40, 48, 54-79}. The occurrence of osmotic pressure arises from the affinity of a pure solvent to migrate through a semi-permeable membrane and into a solution containing a solute to which the membrane is impermeable. In case of polyelectrolytes such as PSS-Na, typically contains dissociable groups, to have the charge neutrality over distances of a screening length of usually <10 nm there is a counter-ion cloud creating an osmotic pressure (π), which depends on the degree of dissociation. NACs are suspended in various wt % of PSS-Na solution. PSS-Na is present outside the capsule and is higher in concentration than the NACs interior. NACs shell acts like a semi-permeable membrane, which is permeable to the smaller molecules (Na) but not to the larger molecules (PSS), and water can diffuse across the membrane. PSS could not permeate through the NACs shells, results in retaining an excess of Na⁺ counterions surrounding the microcapsules. In response, exchange of water, and Na across the polyelectrolyte shells occurred as a means to equalize the chemical potential of water and Na between NACs interior and the surroundings. This results in establishing Donnan equilibrium^{80, 81}. Thus, an excess of PSS outside the capsule creates an osmotic pressure. By observing the effect of osmotic pressure on intact NACs, we can elucidate the effect of pH and ionic strength on mechanical strength.

NACs are suspended in various wt % of PSS-Na solution, an unstable situation occurs since on one side (outside NACs) of the semi-permeable membrane contains a PSS⁻Na⁺

solution consisting of a permeable cation such as Na^+ with an impermeable anion (PSS^-), whereas the other side (NACs-core) doesn't contain PSS^- and Na^+ , To maintain electrical neutrality Na^+ moves from outside of NACs to NACs-core and in the due course of migration of Na^+ , PSS^- tries to migrate to the core but due the size constraint it cannot enter the core. This results in creating π environment from outside.

We studied NACs suspended in 3 different aqueous media: DI water, pH 6.0 in 10 mM NaCl, and pH 6.0 in 150 mM NaCl. NACs suspensions were prepared in PSS solutions ranging from 3.33 to 20 wt % over 12 hours (Fig. 3.3). It has been observed that there is no structural difference in terms of deformation or buckling of the capsule for NACs that were previously pre-suspended in DI water as shown in 3. 2(a-e) and pH 6.0 in 10 mM. Silica NACs are robust as shown in Fig. 3.2 (f-j), and stable to applied osmotic pressure of at least 25 atm. We hypothesize that the presence of the core/mesh interior and stable composite shell (polymer/silica) gives the stability to the capsule.

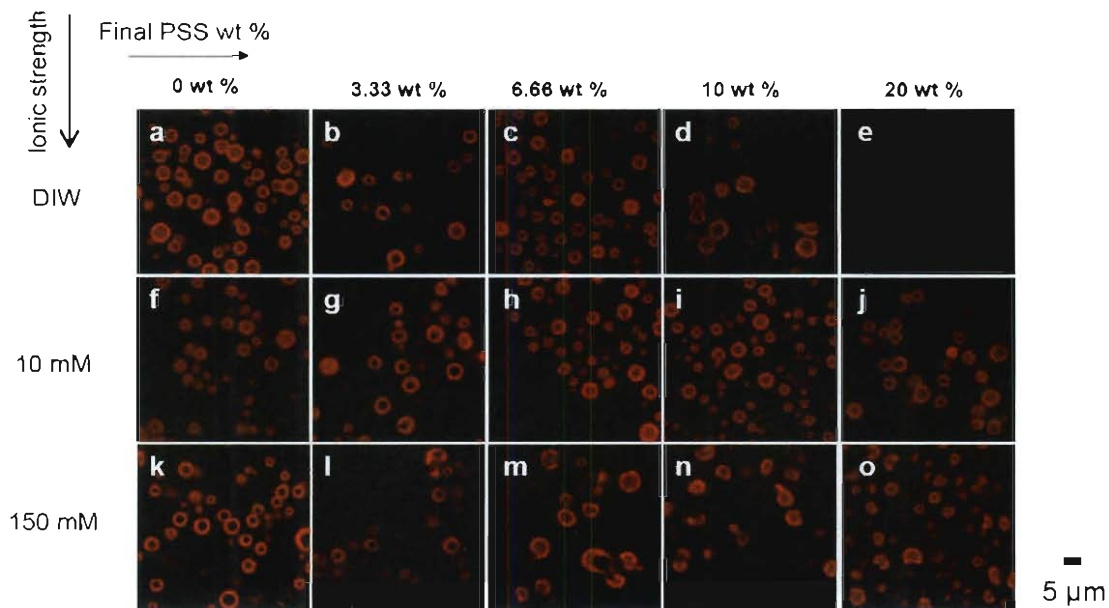


Figure 3.3. Confocal microscopy images of NACs subjected to various osmotic pressure levels with PSS-Na, in NACs initially suspended in DIW (a-e), (f-j) NACs initial condition, pH 6.0 in 10 mM NaCl, and (k-o) and NACs initial conditions, pH 6.0 in 150 mM NaCl.

It was observed that by treating the NACs with 150 mM NaCl breaks the polymer-citrate matrix core inside the capsules and changes the shell properties of NACs as shown in Fig. 3.3 (k). NACs treated with 150 mM NaCl are suspended in an increasing the outside polyelectrolyte (PSS) concentration. One realizes that at low PSS concentration (Fig. 3.3(l)) most of the capsules are nicely spherical; at 6.6 wt % (Fig. 3.3(m)) NACs begin to deform and this is more evident in 10 wt % sample (Fig. 3.3(n)). However, at high (20 wt % PSS, Fig. 3.3(o)) concentration they are all deformed.

By quantitatively measuring the fraction of deformed capsules as a function of PSS concentration a critical osmotic pressure π_c can be derived where most capsules are non-spherical as shown in Fig. 3.4 (π_c corresponds to PSS 9 wt %). Euler instability

Elasticity modulus or elasticity of capsule walls can be derived from $\mu = \frac{\pi_c}{4} \left(\frac{R}{h}\right)^2$ as given by Gao et al., where R is the capsule radius and h is the uniform shell thickness. By determining the modulus of elasticity, it provides the information about the capsules tendency to be deformed elastically.

The shell thickness was determined by collecting intensity line profiles across the confocal image of capsules dispersed in 150 mM NaCl and pH 6.0. The shell thickness was thus measured for 100 capsules of various sizes. Shell thickness is determined by drawing a correlation between shell thickness and capsule diameter from the confocal images as shown in Fig. 3.4b, the protocol has been described in our earlier work⁷. Hence, by knowing R and h, we can derive the elastic modulus μ from the data in Fig. 3.4a. In the specific case for an average diameter of ~ 5.2 micron, we obtain $\mu \sim 9$ atm. The shell wall is sufficiently homogeneous to enable application of this simple model.

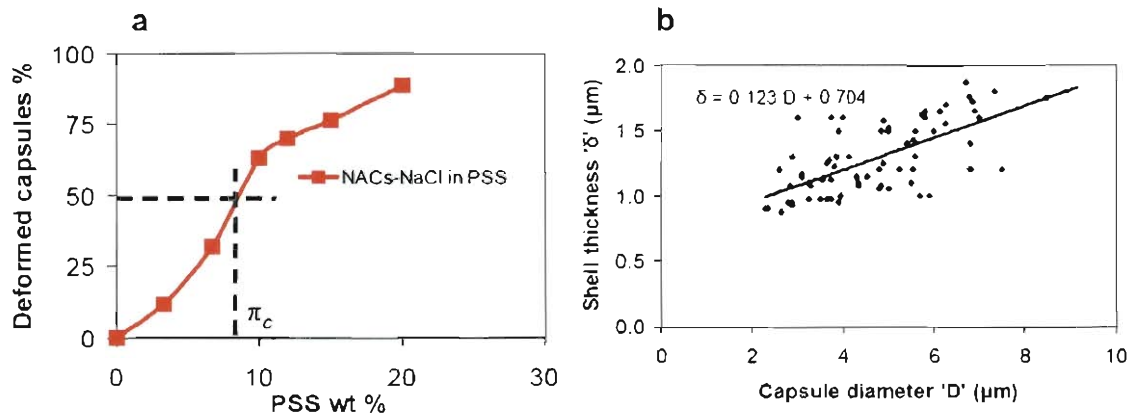


Figure 3.4. Percentage of deformed capsules as a function of the PSS wt % concentration, (b) Correlation between capsule diameter and shell thickness based on intensity line profiles of NACs

At a more fundamental level, this study helped us gain a better understanding between the electrostatic assembly of nanoparticle-assembled capsules. Mechanical stability of the capsules is absolutely important for a diversity of practical applications.

3.3.4. Effect of multivalent anions

Various multivalent anions such as Phos, Sulf, Cit are explored to determine the stability of NACs. It was found that NACs are surprisingly stable in multivalent anions at high ionic strengths. In Fig. 3.5a, we observe that almost ~ 98 % of NACs suspended in 1M of ionic strength made by monovalent NaCl are broken. However they remain intact and stable when suspended in ionic strength of 1M made of Phos, Sulf, and Cit separately. About ~ 95 % and 90 % of unbroken NACs are retained in Phos, Cit and Sulf respectively as shown in Fig. 3.5(b-e). A more detailed analysis is shown in appendix A (Fig. 3.A3). A thorough analysis was performed by coulter counter to determine the change in size NACs size and # count. Interestingly we have found that NACs remain intact and the size and NACs number count doesn't change (supporting information- Fig. A.4 and A.5). NACs were mostly polymer-filled with few regions of polymer-free core in presence of Phos or Sulf or Cit. We hypothesize that NACs disassemble in the case of monovalent NaCl because Na^+ screens the charges on silica NPs and Cl^- screens amine group of PAH there by the interactions are weakened between PAH/Cit/Silica NPs and finally loose its structure and eventually disassembles. Whereas in the case of multivalent ions such as Phos, Sulf, and Cit they screen the charge on silica NPs and PAH but they also have the tendency of forming bridges between amine groups of PAH and there by enhance the stability. To the best of our knowledge, this is the only charge-assembly based polymer microcapsule that is reported to be stable at such a high ionic strength.

This methodology could possibly be extended to capsules made by other polymer/nanoparticle composites.

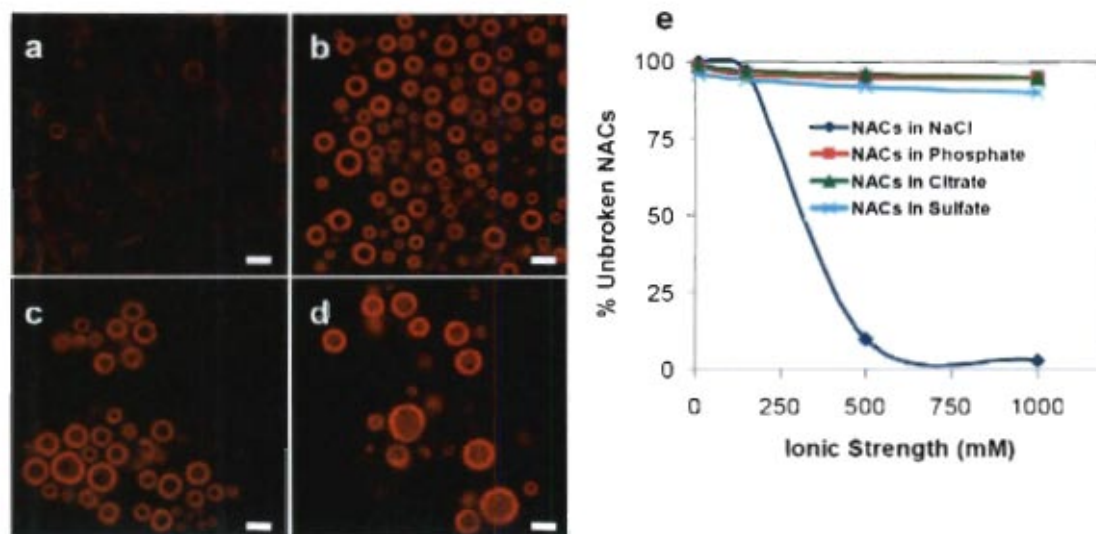


Figure 3.5. Confocal microscopy images of NACs suspended in 1M ionic strength solution in (a) NaCl, (b) Phos,(c) Sulf, (d) Cit, and e) indicates the graph of % of unbroken NACs vs ionic strength of various multivalent anions. Scale bar is 5 micron.

3.3.5. Rescue of NACs by addition of multivalent anions

It has been shown that multivalent anions enhance the stability of capsules. A controlled experiment has been carried out to determine the appropriate amount of Cit required in retaining the capsule structure. NACs were suspended in 1M NaCl in addition to various amounts of Cit. It was observed that at least 25 mM of Cit is required to retain the spherical structure of NACs as shown in Fig. 3.6. We have found an interesting feature of our NACs is that NACs can be rescued by adding multivalent anions to enhance the stability in high ionic strength.

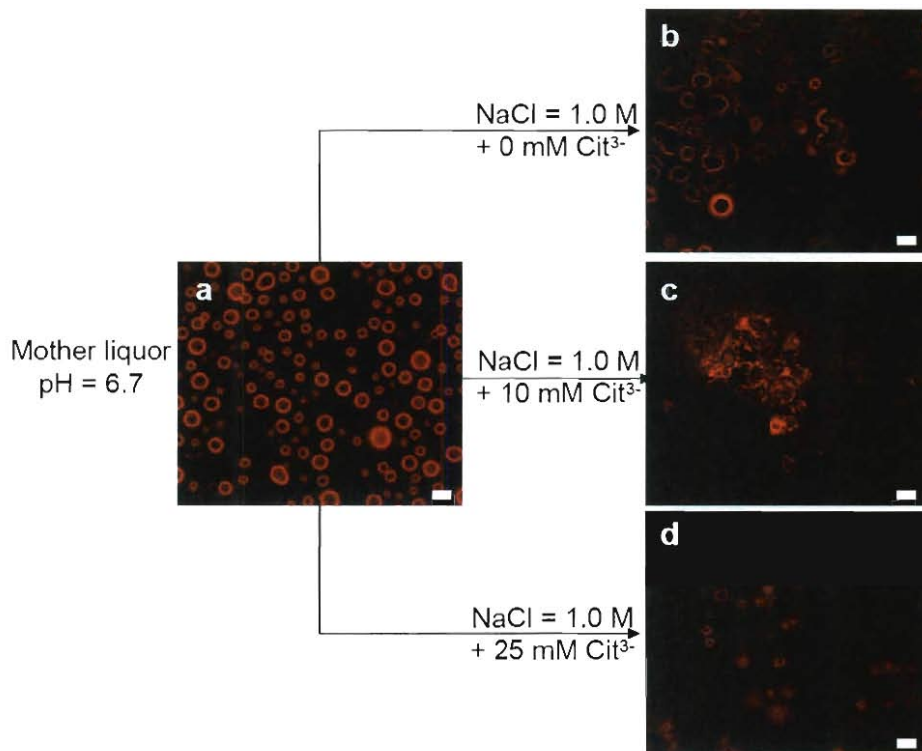


Figure 3.6. Confocal microscopy images of NACs suspended in (a) as made -mother liquor, (b) 1.0 M NaCl + 0 mM Cit, (c) 1.0 M NaCl + 10 mM Cit, (d) 1.0 M NaCl + 25 mM Cit. Scale bar is 5 micron.

3.3.6. NACs stability in PBS and in sea water (Gulf of Mexico, Gavleston, TX, USA)

NACs were suspended in PBS (ionic strength $\sim 0.15\text{M}$, pH 7.4) for overnight. Fig. 3.7a indicated that 95 % of the capsules are water filled and remained intact. It is known that sea water typically has a 3.5 wt% of total dissolved solids (give reference- marine biology book) and has an ionic strength $\sim 0.6\text{M}$. The presence of Sulf in sea water $\sim 26\text{ mM}$ ($\sim 7.5\text{ wt \%}$ of total solids) should be able to rescue NACs from breaking apart. Our results from confocal microscopy showed that 90 % of NACs (Fig. 3.7b) remain unbroken after they are left for overnight in sea water (collected from Gulf of Mexico,

Galveston, TX, USA, measured ionic strength $\sim 0.5\text{M}$). Most of the NACs were water filled (90%). To test NACs stability over a period of time, NACs in Galveston sea water were left for a week and the results indicate that they remain stable as shown in appendix A (Fig. 3.A6). NACs could potentially be used in applications where the operating condition demands high ionic strength (eg. sea water).

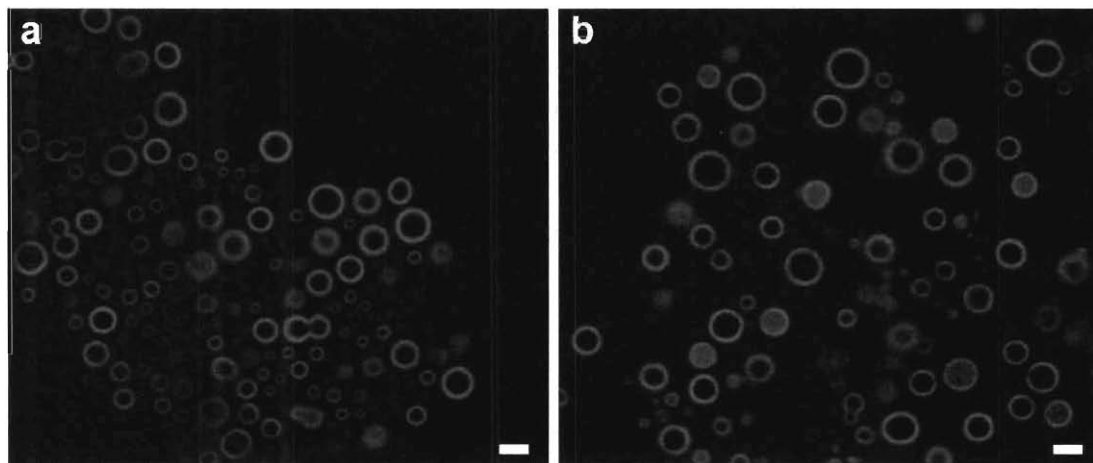


Figure 3.7. Confocal microscopy images of NACs suspended in (a) PBS, (b) Sea water-Gulf of Mexico (Galveston,Texas, USA). Scale bar is 5 micron.

3.4. Conclusions

In this work, stability conditions of nanoparticle-assembled microcapsules (NACs) were explored. At low ionic strength, the capsules were stable in the pH range of 4-9. As ionic strength increased, the pH range for stability narrowed. It was found that NACs get weakened at 0.15 M and at 0.5 M all the capsules were structurally unstable, fragmenting into smaller pieces. Mechanical strength of the capsules was carried out in suspension, using polystyrenesulfonate sodium salt to vary the applied osmotic pressure. The buckling of NACs can be understood as an osmotic pressure difference created between the bulk and the capsule interior. The spherical capsules were found to vary in

compressive strength ranging from 1 atm to at least ~25 atm. Interestingly, it was found that NACs could be made stable at ionic strengths as high as 1M by the addition of multivalent anions (like Citrate and Phosphate) at millimolar levels. NACs are stable in high ionic strength (I ~ 0.5 M) sea water (from Gulf of Mexico, Galveston, Texas, USA) due to naturally present sulfate anions. Understanding the sensitivity of NACs towards various conditions would help in better understanding and perhaps tailoring their properties for drug delivery and controlled release. Also, NACs could potentially be used in applications where the operating condition demands high ionic strength.

3.5. References

1. Rana, R. K.; Murthy, V. S.; Yu, J.; Wong, M. S., Nanoparticle self-assembly of hierarchically ordered microcapsule structures. *Advanced Materials* **2005**, 17, (9), 1145-+.
2. Rana, R. K.; Murthy, V.; Wong, M. S. In *Charge-driven assembly of silica nanoparticles and salt-bridged polyamine-aggregates forming microshells*, 2004; 2004; pp 268-COLL.
3. Murthy, V. S.; Rana, R. K.; Wong, M. S., Nanoparticle-assembled capsule synthesis: Formation of colloidal polyamine-salt intermediates. *Journal of Physical Chemistry B* **2006**, 110, (51), 25619-25627.
4. Murthy, V. S.; Cha, J. N.; Stucky, G. D.; Wong, M. S., Charge-driven flocculation of poly(L-lysine)-gold nanoparticle assemblies leading to hollow microspheres. *Journal of the American Chemical Society* **2004**, 126, (16), 5292-5299.
5. Yu, J.; Yaseen, M. A.; Anvari, B.; Wong, M. S., Synthesis of near-infrared-absorbing nanoparticle-assembled capsules. *Chemistry of Materials* **2007**, 19, (6), 1277-1284.
6. Yu, J.; Murthy, V. S.; Rana, R. K.; Wong, M. S., Synthesis of nanoparticle-assembled tin oxide/polymer microcapsules. *Chemical Communications* **2006**, (10), 1097-1099.
7. Tavera, E. M.; Kadali, S. B.; Bagaria, H. G.; Liu, A. W.; Wong, M. S., Experimental and Modeling Analysis of Diffusive Release from Single-Shell Microcapsules. *Aiche Journal* **2009**, 55, (11), 2950-2965.
8. Plush, S. E.; Woods, M.; Zhou, Y. F.; Kadali, S. B.; Wong, M. S.; Sherry, A. D., Nanoassembled Capsules as Delivery Vehicles for Large Payloads of High Relaxivity Gd³⁺ Agents. *Journal of the American Chemical Society* **2009**, 131, (43), 15918-15923.
9. Kadali, S. B.; Soultanidis, N.; Wong, M. S., Assembling Colloidal Silica into Porous Hollow Microspheres. *Topics in Catalysis* **2008**, 49, (3-4), 251-258.
10. Bagaria, H. G.; Kadali, S. B.; Wong, M. S., Shell Thickness Control of Nanoparticle/Polymer Assembled Microcapsules. *Chemistry of Materials* 23, (2), 301-308.
11. Yaseen, M. A.; Yu, J.; Jung, B.; Wong, M. S.; Anvari, B., Biodistribution of Encapsulated Indocyanine Green in Healthy Mice. *Molecular Pharmaceutics* **2009**, 6, (5), 1321-1332.
12. Wong, M. S., Unpublished results.
13. Zhao, N.; Bagaria, H.; Wong, M.; Zu, Y., A nanocomplex that is both tumor cell-selective and cancer gene-specific for anaplastic large cell lymphoma. *Journal of Nanobiotechnology* 9, (1), 2.

14. Yu, J.; Javier, D.; Yaseen, M. A.; Nitin, N.; Richards-Kortum, R.; Anvari, B.; Wong, M. S., Self-Assembly Synthesis, Tumor Cell Targeting, and Photothermal Capabilities of Antibody-Coated Indocyanine Green Nanocapsules. *Journal of the American Chemical Society* **2010**, 132, (6), 1929-1938.
15. Zhu, H.; McShane, M. J., Loading of Hydrophobic Materials into Polymer Particles: Implications for Fluorescent Nanosensors and Drug Delivery. *Journal of the American Chemical Society* **2005**, 127, (39), 13448-13449.
16. Zhu, G. D.; Alexeev, A.; Kumacheva, E.; Balazs, A. C., Modeling the interactions between compliant microcapsules and pillars in microchannels. *Journal of Chemical Physics* **2007**, 127, (3).
17. Zhu, G. D.; Alexeev, A.; Balazs, A. C., Designing constricted microchannels to selectively entrap soft particles. *Macromolecules* **2007**, 40, (14), 5176-5181.
18. Vinogradova, O. I.; Lebedeva, O. V.; Vasilev, K.; Gong, H. F.; Garcia-Turiel, J.; Kim, B. S., Multilayer DNA/poly(allylamine hydrochloride) microcapsules: Assembly and mechanical properties. *Biomacromolecules* **2005**, 6, (3), 1495-1502.
19. van Dongen, S. F. M.; de Hoog, H. P. M.; Peters, R.; Nallani, M.; Nolte, R. J. M.; van Hest, J. C. M., Biohybrid Polymer Capsules. *Chemical Reviews* **2009**, 109, (11), 6212-6274.
20. Sukhorukov, G. B.; Volodkin, D. V.; Gunther, A. M.; Petrov, A. I.; Shenoy, D. B.; Mohwald, H., Porous calcium carbonate microparticles as templates for encapsulation of bioactive compounds. *Journal of Materials Chemistry* **2004**, 14, (14), 2073-2081.
21. Sukhorukov, G. B.; Shchukin, D. G.; Dong, W. F.; Mohwald, H.; Lulevich, V. V.; Vinogradova, O. I., Comparative analysis of hollow and filled polyelectrolyte microcapsules templated on melamine formaldehyde and carbonate cores. *Macromolecular Chemistry and Physics* **2004**, 205, (4), 530-535.
22. Caruso, F.; Caruso, R. A.; Mohwald, H., Nanoengineering of inorganic and hybrid hollow spheres by colloidal templating. *Science* **1998**, 282, (5391), 1111-1114.
23. Dejugnat, C.; Sukhorukov, G. B., pH-Responsive Properties of Hollow Polyelectrolyte Microcapsules Templated on Various Cores. *Langmuir* **2004**, 20, (17), 7265-7269.
24. Volodkin, D. V.; Larionova, N. I.; Sukhorukov, G. B., Protein Encapsulation via Porous CaCO₃ Microparticles Templating. *Biomacromolecules* **2004**, 5, (5), 1962-1972.
25. Petrov, A. I.; Volodkin, D. V.; Sukhorukov, G. B., Protein—Calcium Carbonate Coprecipitation: A Tool for Protein Encapsulation. *Biotechnology Progress* **2005**, 21, (3), 918-925.

26. Sukhorukov, G. B.; Brumen, M.; Donath, E.; Mohwald, H., Hollow Polyelectrolyte Shells: Exclusion of Polymers and Donnan Equilibrium. *The Journal of Physical Chemistry B* **1999**, 103, (31), 6434-6440.
27. Caruso, F.; Caruso, R. A.; Mohwald, H., Production of Hollow Microspheres from Nanostructured Composite Particles. *Chemistry of Materials* **1999**, 11, (11), 3309-3314.
28. Shchukin, D. G.; Sukhorukov, G. B., Nanoparticle Synthesis in Engineered Organic Nanoscale Reactors. *Advanced Materials* **2004**, 16, (8), 671-682.
29. Ai, H.; Jones, S. A.; de Villiers, M. M.; Lvov, Y. M., Nano-encapsulation of furosemide microcrystals for controlled drug release. *Journal of Controlled Release* **2003**, 86, (1), 59-68.
30. Johnston, A. P. R.; Cortez, C.; Angelatos, A. S.; Caruso, F., Layer-by-layer engineered capsules and their applications. *Current Opinion in Colloid & Interface Science* **2006**, 11, (4), 203-209.
31. Kotov, N. A.; Magonov, S.; Tropsha, E., Layer-by-Layer Self-Assembly of Aluminosilicate-Polyelectrolyte Composites: Mechanism of Deposition, Crack Resistance, and Perspectives for Novel Membrane Materials. *Chemistry of Materials* **1998**, 10, (3), 886-895.
32. Caruso, F.; Mohwald, H., Protein Multilayer Formation on Colloids through a Stepwise Self-Assembly Technique. *Journal of the American Chemical Society* **1999**, 121, (25), 6039-6046.
33. Shchukin, D. G.; Sukhorukov, G. B., Selective YF₃ Nanoparticle Formation in Polyelectrolyte Capsules as Microcontainers for Yttrium Recovery from Aqueous Solutions. *Langmuir* **2003**, 19, (10), 4427-4431.
34. Chinnayelka, S.; McShane, M. J., Microcapsule Biosensors Using Competitive Binding Resonance Energy Transfer Assays Based on Apoenzymes. *Analytical Chemistry* **2005**, 77, (17), 5501-5511.
35. Brown, J. Q.; Srivastava, R.; McShane, M. J., Encapsulation of glucose oxidase and an oxygen-quenched fluorophore in polyelectrolyte-coated calcium alginate microspheres as optical glucose sensor systems. *Biosensors and Bioelectronics* **2005**, 21, (1), 212-216.
36. Ibarz, G.; Dähne, L.; Donath, E.; Möhwald, H., Resealing of Polyelectrolyte Capsules after Core Removal. *Macromolecular Rapid Communications* **2002**, 23, (8), 474-478.
37. Sukhorukov, G. B.; Antipov, A. A.; Voigt, A.; Donath, E.; Möhwald, H., pH-Controlled Macromolecule Encapsulation in and Release from Polyelectrolyte Multilayer Nanocapsules. *Macromolecular Rapid Communications* **2001**, 22, (1), 44-46.

38. Lebedeva, O. V.; Kim, B. S.; Vasilev, K.; Vinogradova, O. I., Salt softening of polyelectrolyte multilayer microcapsules. *Journal of Colloid and Interface Science* **2005**, 284, (2), 455-462.
39. Gao, C. Y.; Leporatti, S.; Moya, S.; Donath, E.; Mohwald, H., Swelling and shrinking of polyelectrolyte microcapsules in response to changes in temperature and ionic strength. *Chemistry-a European Journal* **2003**, 9, (4), 915-920.
40. Kim, B. S.; Vinogradova, O. I., pH-Controlled swelling of polyelectrolyte multilayer microcapsules. *Journal of Physical Chemistry B* **2004**, 108, (24), 8161-8165.
41. Ibarz, G.; Dähne, L.; Donath, E.; Möhwald, H., Smart Micro- and Nanocontainers for Storage, Transport, and Release. *Advanced Materials* **2001**, 13, (17), 1324-1327.
42. Schuler, C.; Caruso, F., Decomposable Hollow Biopolymer-Based Capsules. *Biomacromolecules* **2001**, 2, (3), 921-926.
43. De Geest, B. G.; Sanders, N. N.; Sukhorukov, G. B.; Demeester, J.; De Smedt, S. C., Release mechanisms for polyelectrolyte capsules. *Chemical Society Reviews* **2007**, 36, (4), 636-649.
44. Antipov, A. A.; Shchukin, D.; Fedutik, Y.; Petrov, A. I.; Sukhorukov, G. B.; Mohwald, H., Carbonate microparticles for hollow polyelectrolyte capsules fabrication. *Colloids and Surfaces a-Physicochemical and Engineering Aspects* **2003**, 224, (1-3), 175-183.
45. Antipov, A. A.; Sukhorukov, G. B.; Mohwald, H., Influence of the ionic strength on the polyelectrolyte multilayers' permeability. *Langmuir* **2003**, 19, (6), 2444-2448.
46. Bhatia, S. R.; Khattak, S. F.; Roberts, S. C., Polyelectrolytes for cell encapsulation. *Current Opinion in Colloid & Interface Science* **2005**, 10, (1-2), 45-51.
47. Petrov, A. I.; Antipov, A. A.; Sukhorukov, G. B., Base - Acid Equilibria in Polyelectrolyte Systems: From Weak Polyelectrolytes to Interpolyelectrolyte Complexes and Multilayered Polyelectrolyte Shells. *Macromolecules* **2003**, 36, (26), 10079-10086.
48. Gao, C.; Donath, E.; Moya, S.; Dudnik, V.; Mohwald, H., Elasticity of hollow polyelectrolyte capsules prepared by the layer-by-layer technique. *European Physical Journal E* **2001**, 5, (1), 21-27.
49. McNeil-Watson, F.; Tscharnuter, W.; Miller, J., A new instrument for the measurement of very small electrophoretic mobilities using phase analysis light scattering (PALS). *Colloids and Surfaces A: Physicochemical and Engineering Aspects* **1998**, 140, (1-3), 53-57.
50. Horacio, E. B.; William, O. R., *Colloidal Silica: Fundamentals and Applications* **2006**, 131 (Taylor & Francis Group, LLC).

51. Behrens, S. H.; Grier, D. G., The charge of glass and silica surfaces. *Journal of Chemical Physics* **2001**, 115, (14), 6716-6721.
52. Hiemenz, P.; Rajagopalan, R., *Principles of colloid and surface chemistry* **1997**, Marcel Dekker, Inc., New York
53. Khapli, S.; Kim, J. R.; Montclare, J. K.; Levicky, R.; Porfiri, M.; Sofou, S., Frozen Cyclohexane-in-Water Emulsion as a Sacrificial Template for the Synthesis of Multilayered Polyelectrolyte Microcapsules. *Langmuir* **2009**, 25, (17), 9728-9733.
54. Gao, C. Y.; Leporatti, S.; Moya, S.; Donath, E.; Mohwald, H., Stability and mechanical properties of polyelectrolyte capsules obtained by stepwise assembly of poly(styrenesulfonate sodium salt) and poly(diallyldimethyl ammonium) chloride onto melamine resin particles. *Langmuir* **2001**, 17, (11), 3491-3495.
55. Gao, C. Y.; Moya, S.; Lichtenfeld, H.; Casoli, A.; Fiedler, H.; Donath, E.; Mohwald, H., The decomposition process of melamine formaldehyde cores: The key step in the fabrication of ultrathin polyelectrolyte multilayer capsules. *Macromolecular Materials and Engineering* **2001**, 286, (6), 355-361.
56. Leporatti, S.; Gao, C.; Voigt, A.; Donath, E.; Mohwald, H., Shrinking of ultrathin polyelectrolyte multilayer capsules upon annealing: A confocal laser scanning microscopy and scanning force microscopy study. *European Physical Journal E* **2001**, 5, (1), 13-20.
57. Atkin, R.; Davies, P.; Hardy, J.; Vincent, B., Preparation of aqueous core/polymer shell microcapsules by internal phase separation. *Macromolecules* **2004**, 37, (21), 7979-7985.
58. Cordeiro, A. L.; Coelho, M.; Sukhorukov, G. B.; Dubreuil, F.; Mohwald, H., Effect of shear stress on adhering polyelectrolyte capsules. *Journal of Colloid and Interface Science* **2004**, 280, (1), 68-75.
59. Feng, J.; Wang, B.; Gao, C. Y.; Shen, J. C., Selective adsorption of microcapsules on patterned polyelectrolyte multilayers. *Advanced Materials* **2004**, 16, (21), 1940-+.
60. Fery, A.; Dubreuil, F.; Mohwald, H., Mechanics of artificial microcapsules. *New Journal of Physics* **2004**, 6.
61. Lebedeva, O. V.; Kim, B. S.; Vinogradova, O. I., Mechanical properties of polyelectrolyte-filled multilayer microcapsules studied by atomic force and confocal microscopy. *Langmuir* **2004**, 20, (24), 10685-10690.
62. Lulevich, V. V.; Andrienko, D.; Vinogradova, O. I., Elasticity of polyelectrolyte multilayer microcapsules. *Journal of Chemical Physics* **2004**, 120, (8), 3822-3826.

63. Lulevich, V. V.; Nordschild, S.; Vinogradova, O. I., Investigation of molecular weight and aging effects on the stiffness of polyelectrolyte multilayer microcapsules. *Macromolecules* **2004**, *37*, (20), 7736-7741.
64. Lulevich, V. V.; Vinogradova, O. I., Effect of pH and salt on the stiffness of polyelectrolyte multilayer microcapsules. *Langmuir* **2004**, *20*, (7), 2874-2878.
65. Pavor, P. V.; Bellare, A.; Strom, A.; Yang, D. H.; Cohen, R. E., Mechanical characterization of polyelectrolyte multilayers using quasi-static nanoindentation. *Macromolecules* **2004**, *37*, (13), 4865-4871.
66. Salomaki, M.; Laiho, T.; Kankare, J., Counteranion-controlled properties of polyelectrolyte multilayers. *Macromolecules* **2004**, *37*, (25), 9585-9590.
67. Sukhorukov, G. B.; Fery, A.; Brumen, M.; Mohwald, H., Physical chemistry of encapsulation and release. *Physical Chemistry Chemical Physics* **2004**, *6*, (16), 4078-4089.
68. Vinogradova, O. I., Mechanical properties of polyelectrolyte multilayer microcapsules. *Journal of Physics-Condensed Matter* **2004**, *16*, (32), R1105-R1134.
69. Vinogradova, O. I.; Andrienko, D.; Lulevich, V. V.; Nordschild, S.; Sukhorukov, G. B., Young's modulus of polyelectrolyte multilayers from microcapsule swelling. *Macromolecules* **2004**, *37*, (3), 1113-1117.
70. Yang, S. G.; Zhang, Y. J.; Yuan, G. C.; Zhang, X. L.; Xu, J. A., Porous and nonporous nanocapsules by H-bonding self-assembly. *Macromolecules* **2004**, *37*, (26), 10059-10062.
71. Yu, M.; Ivanisevic, A., Encapsulated cells: an atomic force microscopy study. *Biomaterials* **2004**, *25*, (17), 3655-3662.
72. Zhang, Y. J.; Guan, Y.; Yang, S. G.; Xu, J.; Miao, X. P.; Cao, W. X., Light-scattering study of polyelectrolyte hollow capsules. *Chinese Journal of Polymer Science* **2004**, *22*, (2), 111-115.
73. Alexeev, A.; Verberg, R.; Balazs, A. C., Modeling the motion of microcapsules on compliant polymeric surfaces. *Macromolecules* **2005**, *38*, (24), 10244-10260.
74. Butt, H. J.; Cappella, B.; Kappl, M., Force measurements with the atomic force microscope: Technique, interpretation and applications. *Surface Science Reports* **2005**, *59*, (1-6), 1-152.
75. Dejugnat, C.; Halozan, D.; Sukhorukov, G. B., Defined picogram dose inclusion and release of macromolecules using polyelectrolyte microcapsules. *Macromolecular Rapid Communications* **2005**, *26*, (12), 961-967.

76. Kim, B. S.; Fan, T. H.; Lebedeva, O. V.; Vinogradova, O. I., Superswollen ultrasoft polyelectrolyte microcapsules. *Macromolecules* **2005**, 38, (19), 8066-8070.
77. Kim, B. S.; Lebedeva, O. V.; Kim, D. H.; Caminade, A. M.; Majoral, J. P.; Knoll, W.; Vinogradova, O. I., Assembly and mechanical properties of phosphorus dendrimer/polyelectrolyte multilayer microcapsules. *Langmuir* **2005**, 21, (16), 7200-7206.
78. Kim, B. S.; Lebedeva, O. V.; Koynov, K.; Gong, H. F.; Glasser, G.; Lieberwith, I.; Vinogradova, O. I., Effect of organic solvent on the permeability and stiffness of polyelectrolyte multilayer microcapsules. *Macromolecules* **2005**, 38, (12), 5214-5222.
79. Nolte, A. J.; Rubner, M. F.; Cohen, R. E., Determining the young's modulus of polyelectrolyte multilayer films via stress-induced mechanical buckling instabilities. *Macromolecules* **2005**, 38, (13), 5367-5370.
80. Halozan, D.; Sukhorukov, G. B.; Brumen, M.; Donath, E.; Mohwald, H., Donnan equilibrium and osmotic pressure in hollow polyelectrolyte microcapsules. *Acta Chimica Slovenica* **2007**, 54, (3), 598-604.
81. Tsekov, R.; Vinogradova, O. I., Electro-osmotic equilibria for a semipermeable shell filled with a solution of polyions. *Journal of Chemical Physics* **2007**, 126, (9).

Chapter 4. Encapsulation and responsive studies of capsules

4.1. Introduction

In the midst of the many ordered structures formed via nanoparticles (NPs), there has been a plethora of interest in the synthesis of a class of materials called hollow spheres or capsules in the micron, sub-micron, and nanometer size ranges¹⁻¹¹. A capsule is basically a container which is hollow in nature and comprises of a shell wall as outer material. This shell wall helps in protecting the active ingredient or cargo molecule. Capsules find extensive applications in pharmaceutical, food, chemicals, and consumer industry by serving as tiny containers to store, deliver, and/or release substances¹²⁻²⁵. An encapsulation system containing components, such as enzymes, proteins, and detoxicants, was initially proposed by Chang as an “artificial cell”²⁶. The idea of the artificial cell has now been developed into varied biological encapsulated formulations, such as, microencapsulated invertase²⁷, glucose oxidase²⁸, cytochrome C²⁹, fungal proteases³⁰, asparaginase and catalase³¹. The overall benefit of encapsulating and releasing a cargo molecule from a capsule include shielding the sustained release of the encapsulated substances^{32, 33}. The use of capsules is very useful because of their small particle size, and large surface area. Capsules become very vital for therapeutics where they are administered to the body via injection or an oral route³⁴.

In our work, we studied the possible encapsulation of molecules such as fluorescein, Gd[DOTP]⁵⁻, anticancer drug - doxorubicin, uracil (used for drug delivery and as a pharmaceutical) in our NACs^{18-25, 35-38}. The result of our studies helps in better understanding about the encapsulation properties of NACs and its potential applications.

NACs responsive studies are explained in detail in further sections. The shell can be designed in such a way that the cargo can be released at desired time intervals, by triggering the capsules by varying either one or more of the following parameters such as pH, ionic strength, external pressure, and interaction with near infrared (IR) laser light. Our results indicate that NACs, have interesting behavior in response to various pH and ionic strength conditions. X-ray (via radiation therapy) sensitivity studies are carried out on NACs. Radiation therapy is based on high-energy photons, protons, and electrons; however, the majority of radiotherapy treatments are based on high-energy X-rays. Therefore, X-ray sensitivity is an important design parameter, either for release or protection. NACs could be engineered in such a way that becomes sensitive to X-rays with various levels of irradiation. Magnetic-NACs were synthesized and were tested for their sensitivity with the applied alternating magnetic field. Our results indicate that magnetic-NACs could heat up to ~ 60 °C in 20 mins.

4.2. Experimental Methods

4.2.1. Materials

Polyallylamine hydrochloride (PAH, 56,000 g/mol, ~ 600 allylamine units per molecule), fluorescein sodium salt, premixed phosphate buffered saline (PBS) salt mixture, human serum albumin (HSA), and glycine were purchased from Sigma-Aldrich. The premixed PBS salt was dissolved in deionized (DI) water to prepare the PBS buffer solution (pH=7.4, ionic strength $I = 165$ mM). Glycine and NaOH buffers were prepared for a wide range of pH values (8.5 through 10.3) by mixing 0.2 M glycine and 0.2 M NaOH solutions made with DI water. Trisodium citrate dihydrate salt (citrate), NaOH pellets and 1 N HCl solution were obtained from Fisher Scientific. An aqueous colloidal

suspension of silica NPs (Snowtex-O, 20.5 wt% silica, pH 3.5, ionic strength $I = 16.9$ mM)) was kindly provided by Nissan Chemicals. These NPs have a diameter of 13 ± 3 nm based on dynamic light scattering and a zeta potential value of -16 mV (Henry's equation) by electrophoretic measurements. Deionized water from a Barnstead Nanopure Diamond System (18.2 M Ω) was used to prepare all the solutions. Doxorubicin hydrochloride and Uracil were purchased from sigma-aldrich.

4.2.2. Synthesis of NACs

An aqueous PAH solution (14 ml, 5 mg/mL) was mixed with an aqueous Cit solution (35 ml) in a 250 ml beaker and stirred with a magnetic stirrer for 10 seconds at low speed ('5' speed on a 1-10 scale). For the R charge ratio of 2 studied in this work, the Cit concentration was 14.2 mM, respectively. R is defined as the ratio of total number of negative charges from the salt to the total number of positive charges from the polyamine. A turbid mixture immediately resulted, indicating the formation of polymer-salt aggregates. This suspension was aged for 30 min, before a diluted aqueous SiO₂ NP suspension (35 ml; concentration of 1.2 wt %) was added. The resultant mixture was stirred vigorously (at '7' speed) for 10 min and aged for 2 hrs. The resulting material is the silica/polymer microcapsules or NACs. The resulting NACs were aliquoted into 1.5 ml centrifuge vials.

4.2.3. Synthesis of dye-encapsulated NACs

NACs were synthesized by first mixing 14 ml of 5 mg/mL of PAH solution with 35 ml of 14.2 mM citrate solution in a 250 ml beaker under gentle magnetic stirring (speed '4' of 0 through 10) for 10 seconds. The resulting suspension turned turbid instantly

indicating the formation of polymer-salt aggregates. After aging these aggregates for 20 minutes, 35 ml of a 1 mg/mL fluorescein sodium salt (“Na-Flu”) dye solution was added under gentle magnetic stirring for 10 seconds. This mixture was aged for another 10 minutes and 35 ml of 1.2 wt% silica NP suspension (prepared by diluting with DI water and adjusting the pH to 3.5 with 1 N HCl solution) was added. The resulting mixture was stirred vigorously (speed ‘7’) for 10 min and aged for 2 hrs to form Na-Flu-encapsulated NACs. A schematic of this mixing synthesis process is shown in Fig. 4.1.

4.2.4. Dye release study

Prior to performing the dye release experiments, NACs were cleaned to remove the excess Na-Flu. The cleaning was performed by dispersing the NACs (by sonication for 30 secs. and stirring), and separating them by centrifugation (Beckman-Coulter Allegra X-22 centrifuge at 6000 rpm for 7 min). All the supernatant was carefully removed and capsules re-dispersed in 30 ml of PBS buffer solution. Another round of centrifugation was performed to ensure complete removal of any superficial Na-Flu. The supernatant was carefully decanted and NACs were re-dispersed in 30 ml of PBS to begin the dye release studies. The NACs solution was quickly pipetted into 1.5 ml aliquots and placed on a rocking platform to ensure that the capsules do not settle.

4.2.5. Gd- NAC Synthesis

Previous NACs have involved the addition of cationic polymer such as PAH and PLL and multivalent anions such as citrate, EDTA, and phosphate. Given the multi-valency of $\text{Gd}[\text{DOTP}]^{5-}$, we explored the possibility of using $\text{Gd}[\text{DOTP}]^{5-}$ as a multivalent anion in the aggregate formation. Aggregates were prepared by mixing a solution of $\text{Gd}[\text{DOTP}]^{5-}$

with a cationic polymer after which the solution became turbid. Initial attempts to form aggregates between Gd[DOTP]⁵⁻ and PAH or PLL in water were unsuccessful. However, it was found that by switching to mixed aqueous/organic solvent systems that aggregation could be achieved and stable NACs could be synthesized at room temperature. The following protocol is followed in the encapsulation of Gd[DOTP]⁵⁻. Generally, 20 µl of PAH water solution (5 mg/mL) was gently mixed with 240 µl of Gd[DOTP]⁵⁻-ethanol mixture is added (240 µl solution is prepared by mixing 120 µl Gd[DOTP]⁵⁻ (3 mM or 7 mM) and 120 µl of ethanol). The “R” ratio used in our studies were R = 4 and R= 10. After aging 20 min, the polymer-salt suspension was strongly mixed with 240 µl of 2 wt % silica NPs (ST-O) for 20 seconds and aged for 2 hours. The samples are centrifuged and washed twice with water prior to imaging. The samples are characterized by optical microscopy, SEM, DLS, and relaxometry studies were carried out by Dr. Sherry’s group in UT-Dallas using an inversion recovery pulse sequence on an Oxford MARAN Ultra resonance relaxometer operating at 23 MHz.

4.2.6. Encapsulation of Uracil

NACs were synthesized by first mixing 0.29 ml of 5 mg/mL of PAH solution with 0.735 ml of 14.2 mM citrate solution in a 2 ml centrifuge vials under gentle vortex mixing (speed ‘5’ of 0 through 10) for 10 seconds. The resulting suspension turned turbid instantly indicating the formation of polymer-salt aggregates. After aging these aggregates for 20 minutes, X ml (X= 0.025 to 0.735 ml) of a 0.735 mg/mL Uracil solution was added under vortex mixing (speed ‘5’ of 0 through 10) for 10 seconds. This mixture was aged for another 10 minutes and 0.735 ml of 1.2 wt% silica NP suspension (prepared by diluting with DI water and adjusting the pH to 3.5 with 1 N HCl solution)

was added. The resulting mixture was stirred vigorously (speed '7') for 10 sec and aged for 2 hrs to form Uracil-encapsulated NACs. A schematic of this mixing synthesis process is similar to the one shown for Na-Flu dye encapsulation.

4.2.7. Encapsulation of Doxorubicin

NACs were synthesized by first mixing 50 μL of 2 mg/mL of PAH solution with 300 μL of 0.01 M phosphate solution in a 2 ml centrifuge vials under gentle vortex mixing (speed '5' of 0 through 10) for 10 seconds. The resulting suspension turned turbid instantly indicating the formation of polymer-salt aggregates. After aging these aggregates for 10 minutes, X ml ($X = 10$ to 250 μL) of 2 mg/mL Doxorubicin (DOX) was added under vortex mixing (speed '5' of 0 through 10) for 10 seconds. This mixture was aged for another 20 minutes and 300 μL of bovine serum albumin of 1 mg/mL. The resulting mixture was stirred vigorously (speed '7') for 10 sec and aged for 2 hrs to form DOX-encapsulated NACs. A schematic of this mixing synthesis process is similar to the one shown for Na-Flu dye encapsulation.

4.2.8. Synthesis of Fe_3O_4 NPs

Magnetite particles were prepared by co-precipitation of Fe_3O_4 from a mixture of FeCl_2 and FeCl_3 (1:2 molar ratio) upon addition of NH_4OH as reported earlier by Sahoo et al³⁹. In a typical reaction, 0.86 g FeCl_2 and 2.35 g FeCl_3 were mixed in 40 ml water and heated to 80 $^\circ\text{C}$ under argon in a three-necked flask. While vigorously stirring the reaction mixture, 5 ml of NH_4OH was introduced by syringe, and the heating continued for 30 min. After that, 1 g of citric acid in 2 ml water was introduced, the temperature was increased to 95 $^\circ\text{C}$, and stirring continued for an additional 90 min. The formed NPs

were characterized by DLS and SEM, the mean particle size is ~ 20 nm. The concentration of Fe_3O_4 was measured by ICP-MS measurements (~ 5.6 mg/mL).

4.2.9. Synthesis of Fe_3O_4 – NACs

An aqueous PAH solution (1 ml, 2 mg/mL) was mixed with an aqueous phosphate solution (6 ml, 0.01M) in a 15 ml vial and stirred with a vortex mixing for 10 seconds at low speed ('5' speed on a 1-10 scale). A turbid mixture immediately resulted, indicating the formation of polymer-salt aggregates. This suspension was aged for 30 min, before a diluted aqueous Fe_3O_4 NP suspension (6 ml) was added. The resultant mixture was stirred vigorously (at '7' speed) for 20 sec and aged for 2 hrs. The resulting material is the Fe_3O_4 microcapsules or Fe_3O_4 -NACs. The resulting Fe_3O_4 -NACs were aliquoted into 1.5 ml centrifuge vials and washed 2 times with water before performing further analysis.

4.2.10. Encapsulation of indocyanine green (ICG) in Fe_3O_4 -NACs

An aqueous PAH solution (1 ml, 2 mg/mL) was mixed with an aqueous phosphate solution (6 ml, 0.01M) in a 50 ml vial and stirred with a vortex mixing for 10 seconds at low speed ('5' speed on a 1-10 scale). A turbid mixture immediately resulted, indicating the formation of polymer-salt aggregates. This suspension was aged for 30 min, before a diluted aqueous Fe_3O_4 NP suspension (6 ml) was added. The resultant mixture was stirred vigorously (at '7' speed) for 20 min and aged for 5 min. ICG (6 ml, 1mg/mL) was added to the suspension and aged for 2 hours. The resulting ICG- Fe_3O_4 -NACs were aliquoted into 1.5 ml centrifuge vials and washed 2 times with water before performing further analysis.

4.2.11. Characterization

Dynamic Light Scattering (DLS): Hydrodynamic diameter and zeta potential analysis was carried out with a Brookhaven ZetaPALS dynamic light scattering instrument with a BI-9000AT digital autocorrelator at a laser wavelength of 656 nm. All studies were carried out at a 90° scattering angle, and all samples were temperature controlled at 25 °C during analysis.

Zeta Potential Analysis: Zeta potentials were calculated from electrophoretic mobility measurements through phase analysis light scattering (PALS) using the DLS instrument and a dip-in electrode. Henry's equation relates the zeta potential (ζ) of the SiO₂ NPs to their electrophoretic mobility (μ_E , units of (microns/s)/(V/m)): $\mu_E = (\zeta\epsilon/\eta)f(\kappa a)$, where ϵ is the dielectric constant of water (78.9), η is viscosity of water (0.89 cP), and $f(\kappa a)$ is a function of κa ⁴⁰. This ζ - μ_E relation is valid in the Henry's limit (when $0.1 \leq \kappa a \leq 100$), where κ is proportional to ionic strength I ⁴¹ and a is the particle radius. The ζ -potential of SiO₂ NPs was measured from a sample of Snowtex-O (50 μ l) diluted with HCl solution (1.5 ml, pH = 3.5).

Scanning Electron Microscopy (SEM): SEM was carried out using a FEI Quanta 400 field emission scanning electron microscope, equipped with secondary electron, backscatter, and energy dispersive X-ray (EDX) detectors. Secondary electron images were taken at 15 kV with a working distance of 10 mm. A droplet of NACs suspension was placed on the aluminum stub and dried in air; the sample was then sputter-coated with gold for 1 min.

Optical Microscopy: Optical microscopy was performed on a Leica DM2500 upright microscope equipped with 100 \times oil immersion objective (numerical aperture = 1.4).

Bright field and differential interference contrast (DIC) images were taken at 100× magnification.

Thermogravimetric Analysis (TGA): The weight loss-temperature profile for NACs was collected on a TA Instruments (SDT 2960 Simultaneous DSC-TGA) thermogravimetric analyzer. The temperature ramp rate was 5 °C/min and the air flow

Siemens Primus linear accelerator: X-ray irradiation experiments were carried out on Siemens Primus linear accelerator (Siemens medical solutions USA, Inc, Malvern, PA). 1.5 ml centrifuge vials were placed in lucite cube with 25 holes – diameter of 1.5 cm and spacing of 2.5 cm. Vials were filled with NACs suspension to top. NACs suspensions were irradiated at various dose levels.

Magnetic heating: An alternating magnetic field (AMF) of 20 A/m at 267 kHz was used to study the effect of alternating magnetic field on NACs. Nova Star 2 kW RF Power Supply, Ameritherm, Inc, Scottsville, NY, USA), heating station (Induction Atmospheres).

4.3. Results and discussions

4.3.1. Experimental analysis of dye-containing capsule structure¹

Encapsulation of Na-Flu (model molecule) was performed to understand the encapsulation properties of NACs. A detailed experimental and modeling analysis was performed. The characterization of the release kinetics from delivery (in this case: capsules) structures is of primary importance for therapeutic applications, and

¹ Part of this work got published as: Tavera, E. M.; Kadali, S. B.; Bagaria, H. G.; Liu, A. W.; Wong, M. S., Experimental and Modeling Analysis of Diffusive Release from Single-Shell Microcapsules. Aiche Journal 2009, 55, (11), 2950-2965.

mathematical modeling provides insights into the transport properties of these spherical materials, as a necessary complement to the experimental data.

In this section, we present the experimental data to support the analytical solution developed by Tavera et al.,³³ the model that describes unsteady-state transport from multilayered spheres. Tavera et al., method is based on the finite Fourier-transform expansion of Eigen functions of self-adjoint, second-order Sturm-Liouville operators with discontinuous coefficients. This differs from other approaches based on Laplace transforms or semi-analytical methods. To validate Tavera et al's, analytical model with experimental dye-release results, NACs were used as a composite material comprised of a single layer (a polymer/nanoparticle shell with macroscopically uniform properties) surrounding a polymer/water interior. The presented experiment-modeling approach allows optical microscopy images and release measurements to be readily analyzed for estimating diffusion coefficients in capsule core and shell walls. Fig. 4.1 shows the schematic of Na-Flu encapsulation.

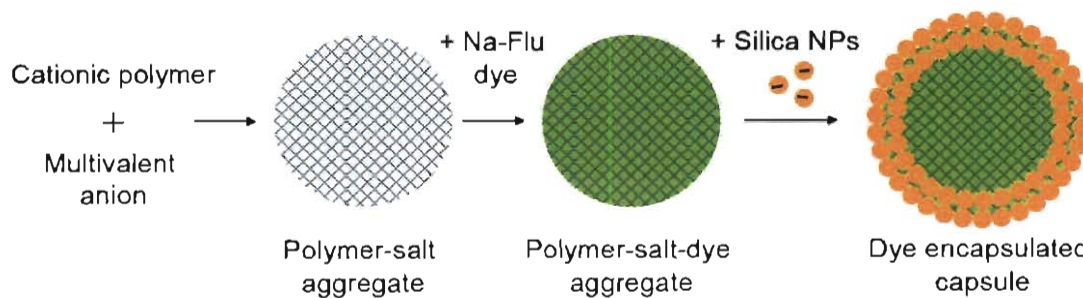


Figure 4.1. Schematic showing the synthesis of fluorescein-encapsulated NACs, with the shell made of NPs and polymer.

Optical DIC and fluorescence microscopy images of the Na-Flu encapsulated NACs were collected to know its structural properties (Fig. 4.2, 4.3 and 4.4). The brightfield

image in Fig. 4.2(a) shows that the capsules had a thick shell wall and, occasionally, an off-center core, and the fluorescence image in Fig. 4.2(b) suggests that the dye molecules were located throughout the capsule structure, with the negatively-charged dye associated with the positively-charged PAH polymer. With confocal microscopy providing cross-sectional imaging capability not available in fluorescence microscopy, the dye molecules were found located within the shell and polymer-salt regions of the capsules (“1” and “2,” respectively, in Fig. 4.2(c)) and not in these off-centered, polymer-free cores (“3”, Fig. 4.2(c)). We make the assumption that the non-dye-containing region does not affect the release of dye from the rest of the capsule.

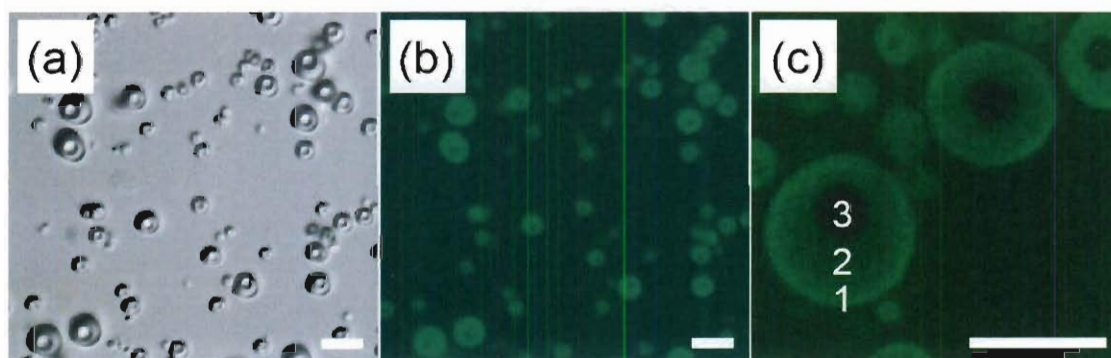


Figure 4.2. (a) Differential interference contrast optical image and (b) corresponding fluorescence image of Na-Flu encapsulated NACs. (c) Confocal microscopy image showing the three regions in Na-Flu encapsulated NACs. Scale bars: 10 μm .

Estimation of the shell thickness and the parameter ' x_1 ' can be performed using optical images of the capsules, but the fluorescence contrast between regions 1 and 2 is too slight to resolve (Fig. 4.2(b) and 4.2(c)). However, we addressed this problem by suspending the capsules in glycine-NaOH buffers of varying pH values and collecting their fluorescence images (Fig. 4.3). We anticipated that some higher pH value would

cause the polymer-salt aggregate inside the capsule (region 2) to dis-assemble completely (due to neutralization of the PAH), thereby revealing the location of the inner shell wall. We found a pH of ~ 9.6 to be most appropriate for dis-assembling region 2 and not region 1 (the shell).

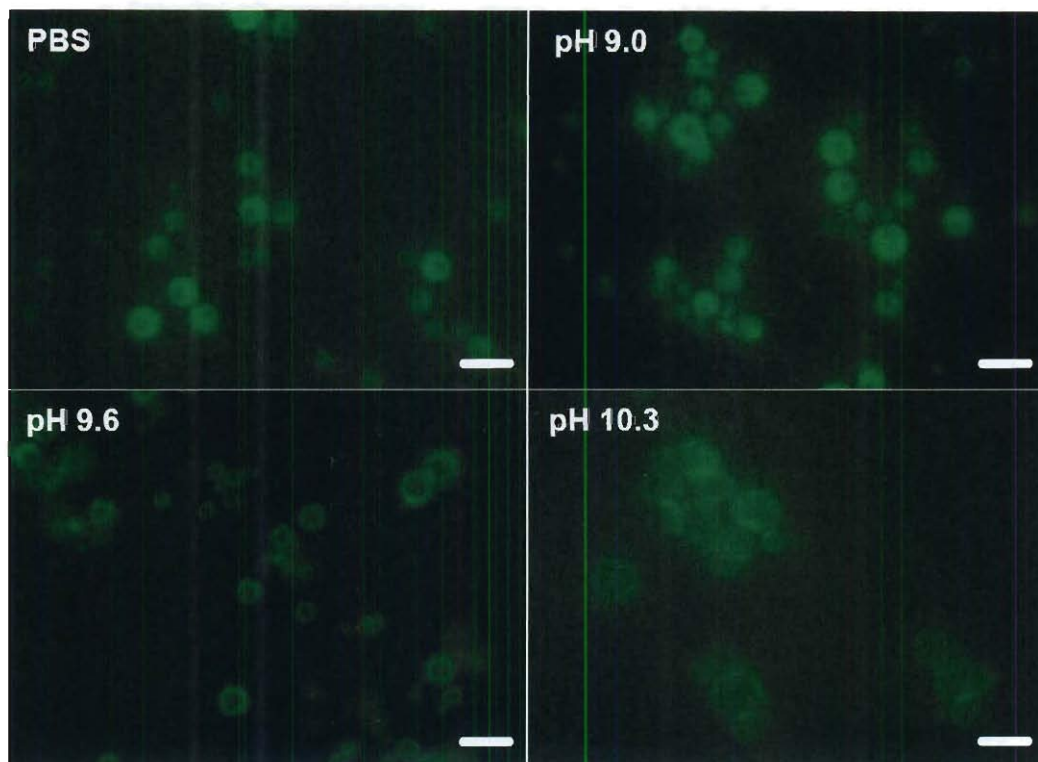


Figure 4.3. Fluorescence images of NACs dispersed in PBS and in glycine buffers of pH 9, 9.6 and 10.3, for shell thickness estimation purposes. Scale bars: 10 μm .

The shell thickness was determined by collecting intensity line profiles across the fluorescence image of capsules dispersed in pH 9.6 and measuring the average distance between the intensity midpoints on both sides of the left-hand and right-hand peaks (Fig. 4.4(a)). The shell thickness was thus measured for 75 capsules of various sizes, resulting in the interesting observation that larger NACs had thicker shells (Fig. 4.4(b)). The

thickness-capsule diameter correlation was a linear one, yielding a slope from which the value of x_1 was calculated.

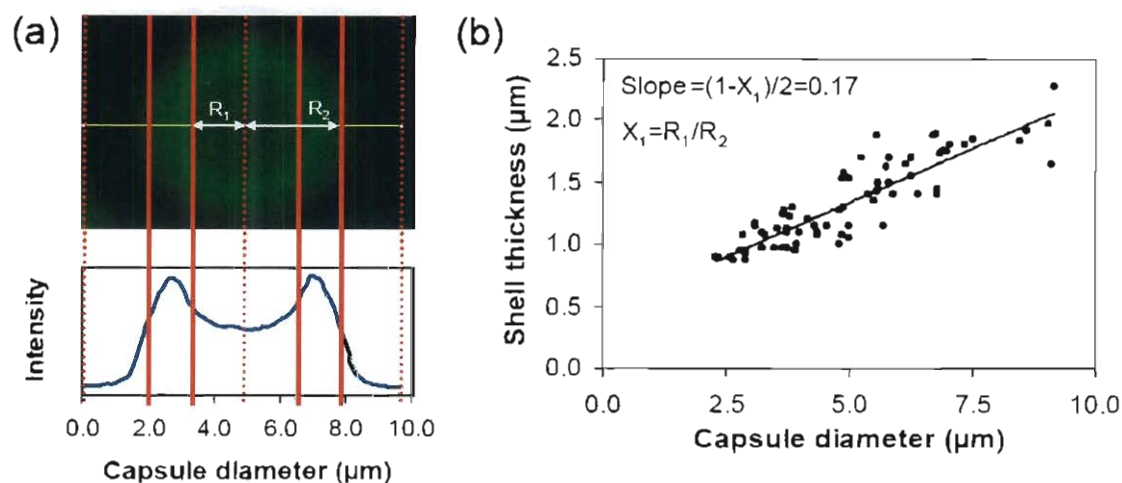


Figure 4.4. (a) Schematic of shell thickness analysis. (b) Correlation between particle size and shell thickness based on intensity line profiles of NACs at pH 9.6 (shown in Fig. 4).

Finally, the mean particle size and distribution of the capsules were estimated. Measuring the capsule size from optical images (Fig. 4.2) would yield incorrect, skewed values because capsules below $\sim 0.5 \mu\text{m}$ cannot be resolved with optical microscopy. On the other hand, SEM images (Fig. 4.5(a)) can clearly resolve capsules from 10's of nm to microns covering the entire range of capsule sizes. The mean capsule diameter and distribution was determined by Coulter counter that was supported with SEM images (Fig. 4.5). The capsule diameter distribution determined from SEM images gave a mean size of $3.12 \pm 0.42 \mu\text{m}$ (relative standard deviation, $\text{RSD} = 0.42/3.12 = 13.5\%$) based on a lognormal distribution fit of the data (Fig. 4.5(b)).

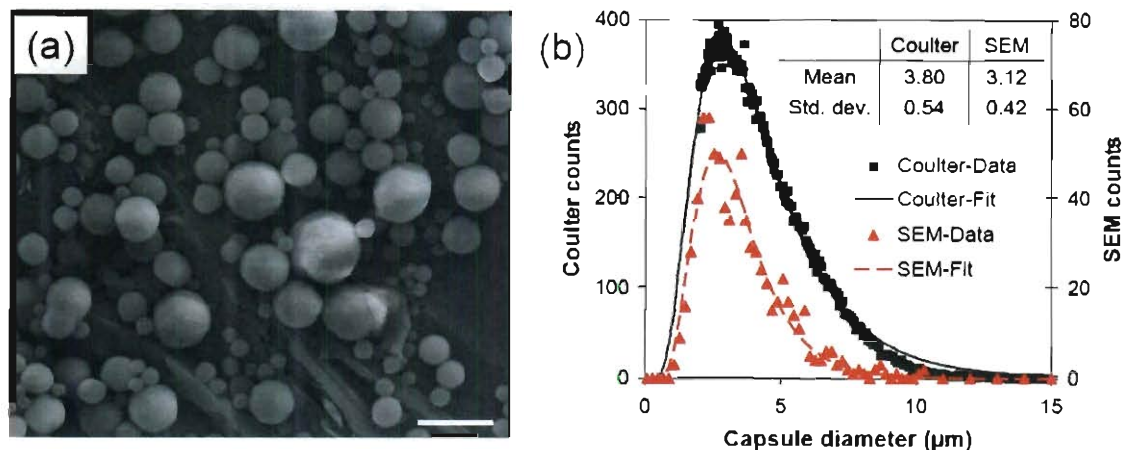


Figure 4.5. (a) Scanning electron microscope (SEM) image of NACs and (b) Capsule diameter distribution data from SEM images and Coulter counter measurements fitted to log-normal distribution.

There was, however, a concern about capsules contracting when dried for SEM imaging, as was observed for other NAC materials^{32, 35}. To address this issue, we measured the diameter distribution of “wet” capsules using a Coulter counter. The Coulter counter allows for size distribution measurements of capsules in their wet state and with high statistical count (~33,000 capsules). Although capsules below 2 μm could not be sized, a lognormal distribution reasonably fit the collected data (Fig. 4.5(b)). The mean size was $3.8 \pm 0.54 \mu\text{m}$ (RSD = 14.2%), suggesting that the capsule diameter shrunk by ~18% after drying. The similarity in size distribution shape and the closeness in relative standard deviations for the wet and dry capsules gave confidence that the mean capsule diameter of $3.8 \pm 0.54 \mu\text{m}$ accurately describes the size distribution of the dye-containing NACs.

4.3.2. Experimental dye release data

At various intervals the aliquots were centrifuged and UV-vis was performed on the supernatant to quantify the dye released. The amount of Na-Flu remaining in the capsules was also determined by breaking NACs with 1N NaOH solution and performing UV-vis for mass balance verification. The mass balance of dye was found to be within 93% for all samples. The total amount of dye (capsule and supernatant) was found to be 1.5 μg in each aliquot. It should be noted that we assume dye release does not stop during the centrifugation. Fig.4.6 clearly indicates that at increasing time intervals, absorbance of UV signal increase from 7.5 min to 185 min. Table 4.1 indicates the amount of Na-Flu released at various time intervals. The highest percentage of encapsulation was $\sim 0.3\%$, when 0.34 mg of Na-Flu was initial added in the synthesis of dye encapsulated NACs.

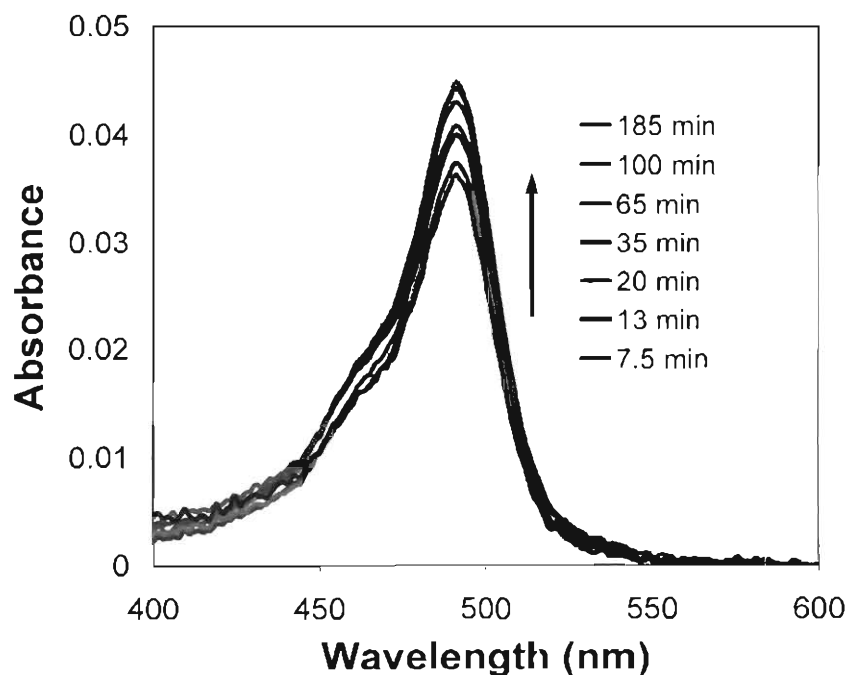


Figure 4.6. UV- visible absorbance profiles of Na-Flu in the supernatant.

Table 4. 1. Amount of Na-Flu released from 1.5 ml of NACs solution. The reported values are within an error of $\pm 6\%$.

Time (min)	Amount of Na-Flu released (μg)/ml
7.5	0.34
13	0.36
20	0.38
35	0.40
65	0.42
100	0.44
185	0.44

Table 4. 2. Percentage encapsulation of Na-Flu in NACs. Various initial amounts of Na-Flu were added in synthesis of dye-encapsulated NACs. The reported values are within an error of $\pm 6\%$.

Amount of Na-Flu (mg)	Amount encapsulated based on NACs (mg)	% encapsulation
34.93	0.026	0.07
3.34	0.0044	0.13
0.34	0.0013	0.31
0.17	0.0003	0.16

Our experimental release data was verified by analytic model equations developed for from single-shell nanoparticle/polymer capsules by Tavera et al (Eq. 21 and Eq 24)³³ as shown in Fig. 4.7. The analytical solution for dye release successfully captured the asymptotic plateau effect of diffusive release. The modeling approach presented here can be extended to multi-layered capsular materials and to chemical reaction-transport scenarios. Our studies helped in determining the new structural information about the nanoparticle-assembled capsules, such as the presence of a polymer-free region within the polymer/salt network in the capsule interior, and the linear dependence of shell

thickness on capsule diameter. Based on the analytical model, we estimated diffusion coefficients in the capsule shell and core, which is comparable to experimental values for the similar systems reported in the literature⁴².

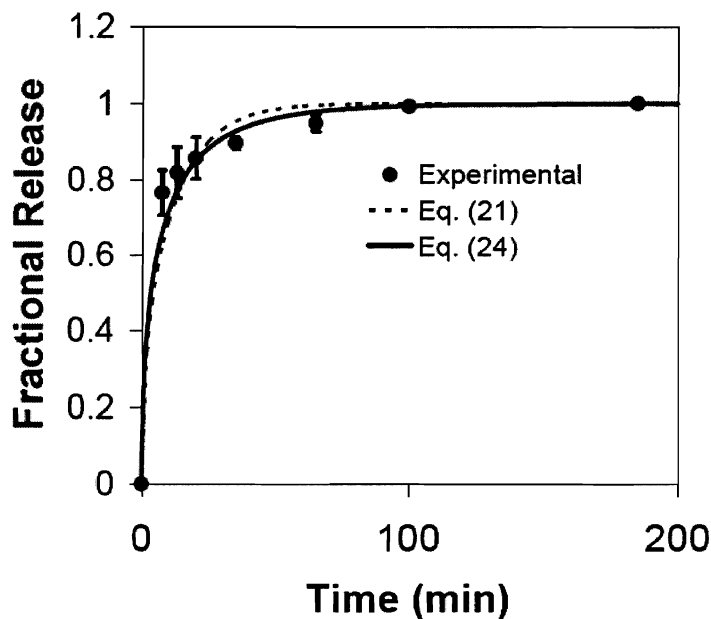


Figure 4.7. Experimental release profile, obtained as an average from three independent release studies, displayed with error bars.

We measured the diffusion coefficient of sodium fluorescein in the polymer-salt matrix alone, using QCM-D technique (detailed procedure is given in Appendix B). This involves a planar, rather than a spherical geometry. Polymer-salt films were developed for ~ 25 hours, prior to the flow of Na-Flu. Based on the dissipation values the film could be considered a rigid, non-viscoelastic film and the Sauerbrey model could be used for mass and thickness calculations⁴³. The calculated thickness of the deposited PAH/cit film was ~150 nm after 25 hours, as estimated by both the Sauerbrey model. To perform the quantitative analysis, a molecular transport in one dimension was assumed and using

Fick's second law, the mass diffused with respect to time was modeled. The diffusion coefficient was found to be $\sim 10^{-19}$ m²/sec. This is in good agreement with what has already been reported for diffusion of rhodamine in polyelectrolyte films⁴².

4.3.3. Synthesis of gadolinium encapsulated nanoparticle assembled capsules (Gd-NACs)²

Gadolinium, is a lanthanide element in the middle of the periodic table, it has procured a lot of significance in the last couple of years in medical diagnostics. As compared to platinum in cancer therapeutics and technetium in cardiac scanning, the distinct magnetic properties of the gadolinium (III) ion brought a drastic development in medicine in magnetic resonance imaging (MRI)⁴⁴⁻⁴⁸. Gd is an FDA approved contrast agent for MRI. It provides greater contrast between normal tissue and abnormal tissue in the body. Gadolinium looks clear like water and is non-radioactive. After it is injected into a vein, gadolinium accumulates in the abnormal tissue that may be affecting the body or head. Gadolinium causes these abnormal areas to become very bright (enhanced) on the MRI. This makes it very easy to see. Gadolinium is then rapidly cleared from the body by the kidneys. Gd³⁺ is paramagnetic and is unique for its high magnetic movement.

MRI is formerly referred to as magnetic resonance tomography (MRT) or in chemistry, nuclear magnetic resonance (NMR), is a non-invasive technique used to render images of the inside of an object. It is primarily used in medical imaging to demonstrate pathological like brain tumor from normal tissue or other physiological alterations of living tissues without harming the tissues. One advantage of an MRI scan is

² Part of this work got published as: Plush, S. E.; Woods, M.; Zhou, Y. F.; Kadali, S. B.; Wong, M. S.; Sherry, A. D., Nanoassembled Capsules as Delivery Vehicles for Large Payloads of High Relaxivity Gd³⁺ Agents. *Journal of the American Chemical Society* 2009, 131, (43), 15918-15923.

that it is harmless to the patient. It uses strong magnetic fields and non-ionizing radiation in the radio frequency ranges that are evaluated using computer technology to view three-dimensional images of the body. Various types of MRI contrast agents have been developed such as iron particle-based agent and manganese (II) chelate. But gadolinium (III) continues to be the potential starting material. The reasons for this include the direction of MRI development and the nature of Gd chelates. The challenge is to enhance relaxation enhancement for the Gd(III) ligands such as GdDOTP⁵⁻, GdDOTA⁴⁻. These salts are stable, highly negatively charged polyanions.

Our goal was to make Gd-NACs and enhance the relaxivity signal considerably. Formation of Gd- NACs through nanoparticle assembly is shown in schematic (Fig.4.8). The idea was to make use of these polyanions as salts and form aggregates with positively charged polymers such as PLL, PAH and finally make Gd-NACs with silica as shell material.

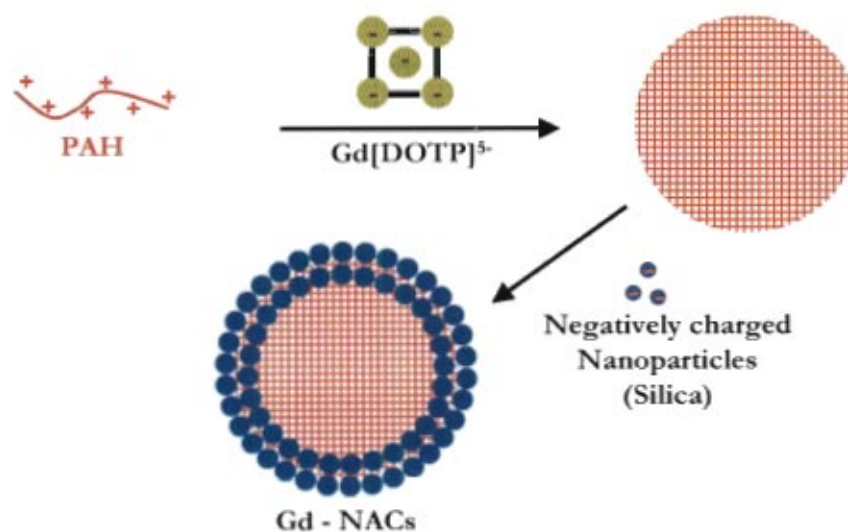


Figure 4.8. Schematic of nanoparticle assembly using Gd (III) salts.

The conformation of PAH ($pK_a \sim 8.5$) in aqueous solution depends on the degree of protonation of the amino group of the side chain. At neutral pH, the polymer would be in an extended, random coil conformation due to complete protonation. The addition of the negatively charged GdDOTP⁵⁻ - ethanol mixture to PAH clearly led to the formation of PAH-Gd flocs, characterized by DLS, the mean diameter shown is approximately 500 nm. SiO₂ NP addition to the PAH-Gd aged suspension resulted instantaneously in the formation of microcapsules called as Gd-NACs.

In solution Gd-NACs looks like as shown in Fig 4.9a in solution under optical bright field. Gd-NACs are not clearly visible since the particles are in sub-micron size and optical microscopy cannot resolve particles well in the submicron regime. When the spheres were dried and under SEM they look as shown in Fig 4.9b. The Gd-NACs hollow spheres are pressed on one side. The structure of a sphere being pressed on a side is attributed to the very thin shell wall and/or when the water that is present in the Gd-NACs dries collapses the structure on a side.

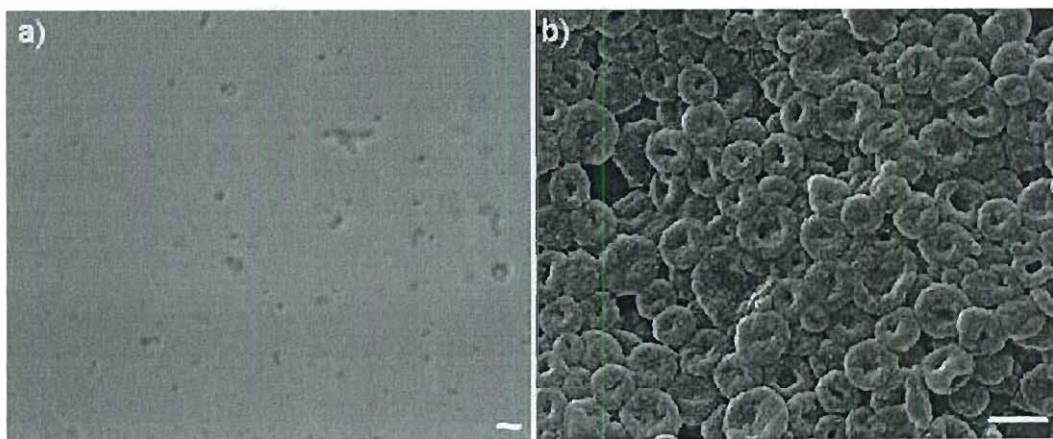


Figure 4.9. a) Optical bright field image b) SEM image Gd-NACs. Scale bar is 500 nm.

The interaction of GdDOTP^{5-} with a cationic polymer in the polymer-salt aggregate would be anticipated to limit the freedom of motion of the chelate so, providing that water molecules have continued access to the second-hydration sphere, the increased rigidity afforded by the aggregate should result in a longer relaxivities. In addition to controlling the rigidity of the system, and thus the motion of the contrast agent (CA) when designing NP systems for MRI one must ensure that water molecules associated with the CA (GdDOTP^{5-}) have access to bulk water as this is critical to the function of an MRI CA. Addition of SiO_2 - NPs are known to be permeable to small molecules such as water and ions, hence should allow access of water to an encapsulated MRI CA.

The water relaxation enhancement studies were carried out in Dr Sherry's research group in UT-Dallas. As a control, polymer-Gd salts aggregate, Gd-NACs samples were prepared. Water relaxation studies are carried on these samples. The results show that there is considerable (5 times more) increase in the relaxation time for the polymer-Gd salt aggregates and Gd-NACs as compared to bare GdDOTP^{5-} as shown in Fig. 4.10.

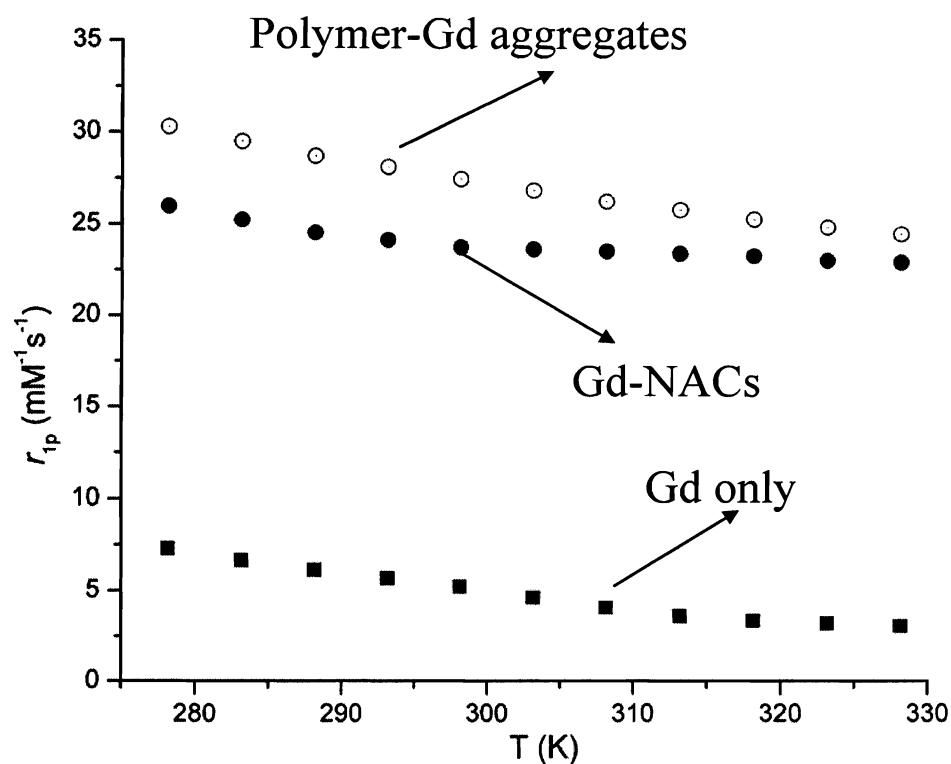


Figure 4.10. Temperature-dependent relaxivity of $\text{Na}_5[\text{GdDOTP}]$ (■), polymer-Gd salts aggregate (○) and Gd-NACs (●), data collected by Dr. Zhou.

The polymer-Gd salt aggregated particles with no SiO_2 coating (open circles) and the one with SiO_2 coating (solid circles) show an enhanced relaxivity compared to GdDOTP^{5-} alone. This could be due to interactions of GdDOTP^{5-} -water-polymer by catalytic exchange of adjacent protons on the amine. The shape of the temperature dependent data for the aggregate is similar to that of GdDOTP^{5-} - both are consistent with water and/or proton exchange. However the shape of the encapsulated system is a bit more flat. This indicates that water exchange is a bit slower with Gd-NACs system compared to polymer-Gd salt aggregates. Since the outer layers of SiO_2 nanoparticles would effect on interaction between the bound GdDOTP^{5-} inside the particles and the exterior water. These results indicate that the encapsulated Gd salt has higher relaxation

time and thus have potential applications in enhancing the image contrast during MRI. Plush et al., has extended the concept of GdDOTP⁵⁻ encapsulation in NACs to other cationic polymers such as poly-L-lysine, poly-L-arginine and also by using solvents such as acetonitrile. Plush et al., performed inductively coupled plasma mass spectrometry (ICP-MS) studies on Gd-NACs made in the similar fashion as explained in synthesis of Gd-NACs²⁵. The solutions of the NACs were filtered through 10kD MWCO membranes, and analysis of the filtrate for Gd³⁺ by ICP-MS showed that level of Gd³⁺ in the filtrate was below the detection limits of ICP, indicating that essentially all the GdDOTP⁵⁻ was trapped within the NAC core.

4.3.4. Encapsulation of Uracil and Doxorubicin

We have studied the encapsulation of uracil and doxorubicin in NACs. Uracil can be used for drug delivery and as a pharmaceutical. Doxorubicin is a drug used as cancer chemotherapy. Table 4.3 and 4.4 indicates % encapsulation of uracil and doxorubicin respectively with respect to various volumes of drug added in NACs synthesis. The highest percentage encapsulation for uracil was ~ 0.07 % and for doxorubicin it is ~ 0.06 %.

Table 4. 3. Percentage encapsulation of uracil in NACs. Various initial amounts of uracil were added in synthesis of encapsulated NACs.

Volume of Uracil added in - NACs synthesis (μ l)	% encapsulation
25	0.00
50	0.06
184	0.06
367.5	0.07
735	0.07

Table 4. 4. Percentage encapsulation of doxorubicin in NACs. Various initial amounts of doxorubicin were added in synthesis of encapsulated NACs.

Volume of DOX added in albumin – NACs synthesis (μ l)	% encapsulation
10	0.00
25	0.05
50	0.06
100	0.06
250	0.06

Uracil and doxorubicin have very less encapsulation in NACs since, uracil is hydrophobic and scarcely soluble in water, and has no negative sites to bind to polymer PAH. Doxorubicin is soluble in water, has hydrophobic groups but its positive charge results in repelling from PAH and hence results in low encapsulation. Na-Flu also has low encapsulation in NACs. Na-Flu is water soluble, hydrophilic and has negative sites. Since it is highly water soluble, the encapsulated Na-Flu leaks from NACs and finally results in low encapsulation. It was shown in our studies that NACs are able to encapsulate cargo molecules which are water soluble and have predominantly hydrophilic and hydrophobic groups. The extended of loading depends on the features of cargo molecules. Typically in our NACs synthesis, the cargo molecules is added to polymer-salt aggregates and aged for few minutes before adding the shell material. Yu et al., showed that NACs can encapsulate NIR dye ICG to as high as 26 % by weight. It is hypothesized that ICG has high loading in NACs since the hydrophobic part of ICG plays an important role in interacting with hydrophobic back bone polymer PAH. Also, the net negative charge of ICG interacts electrostatically with positive sites of PAH. Our studies showed that the ideal cargo molecule should be water soluble, have a net negative charge,

and hydrophobic backbone to have a high loading in NACs. Highly negatively charged molecules such as $\text{Gd}[\text{DOTP}]^{5-}$ could be used as multivalent anions to form aggregates with positively charged polymer, this results in high loading of the cargo molecules. Carotene molecules which have features similar to ICG and $\text{Gd}[\text{DOTP}]^{5-}$ might have high loading in NACs.

4.3.5. Concept of X-ray-sensitive capsules

Microcapsule delivery devices have the potential to treat cancer where the protected contents can be released at the tumor site. Designing a targeted release system for cancer treatment requires knowledge of the various treatment methods to ensure that the delivery and release system avoids unexpected damage. Since treatment methods include radiation therapy, chemotherapy, hyperthermia, ultrasound, and photodynamic therapy. Microcapsule delivery systems need to be protected from a wide variety of potentially damaging sources. In contrast, microcapsule delivery systems could be designed to interact with an external stimulus to release the protected contents. In this case, the design would be sensitive to one specific treatment but protected from others. Radiation therapy is widely used for cancer treatment. Typically, this is used as an independent method or combined with other treatment methods.

X-rays generate chemical species when irradiated with water, leading to e^- free radical, H^+ , H^\bullet radical, OH^\bullet radical, H_2 , H_2O_2 , and other species. It has been shown earlier that radicals can interact with groups such as amino, thiol and result in either cleaving them from its attached polymer chain. We tested the response of our NACs to the radicals generated by X-rays. The shell wall could be engineered in such a way that it can efficiently open upon contact with the X-ray generated radicals.

Demonstration of the surface deformation of Silica-NACs through X-ray irradiation (High Dosage ~ 600 Gy)

Effect of X-ray dosage on the structural properties of the empty NACs using the X-ray facilities was performed. To determine if there was any effect on shell structure upon X-ray irradiation, we prepared silica NAC sample for irradiation, and found that structural modification of the shell was possible (Fig. 4.11). Capsules consisted of poly allyamine (PAH), citrate, silica nanoparticles (NPs). They were subjected to X-ray irradiation with various dosages ranging from 0 Gy- 600 Gy. The scanning electron microscope (SEM) images of the capsules show that the capsules are pretty robust to high dosages (~ 240 Gy). On subjecting to ~ 420 Gy and ~600 Gy irradiation, the capsule starts to deform and rupture. At high enough dosages these capsules shell starts breaking which is seen around 600 Gy.

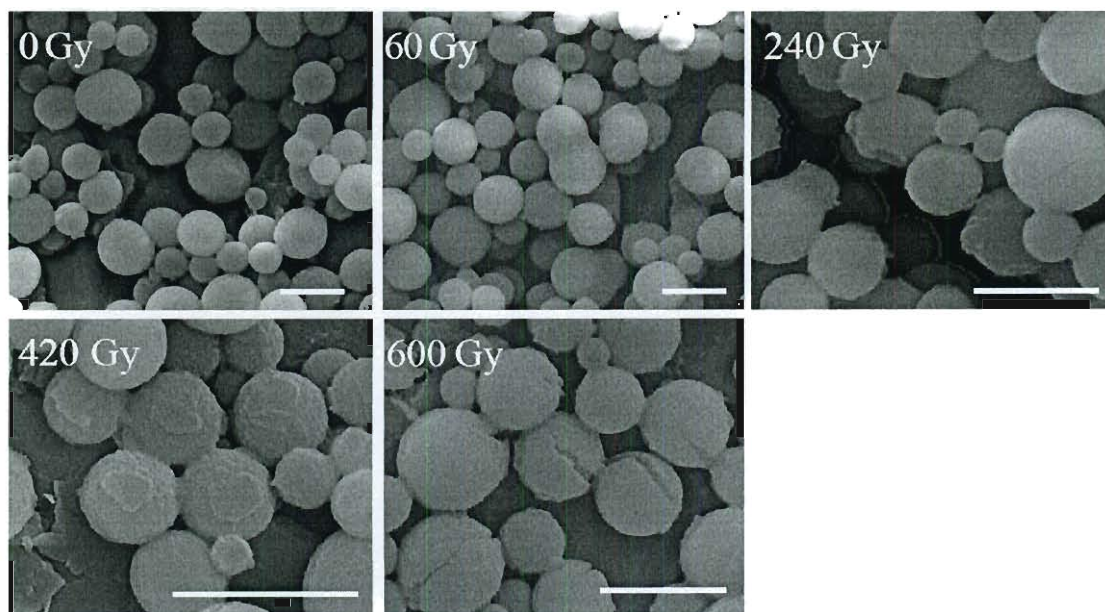


Figure 4.11. a) SEM images of irradiated NACs with various dosages (shown in inset) Scale bar 5 μm .

Demonstration of the surface deformation of Albumin-NACs through X-ray irradiation (Low Dosage ~ 60 Gy)

The concept is to make X-ray sensitive capsule, which show response at low dosage levels. The Silica-NACs are not a good candidate for low-dosage irradiation levels. We plan to decrease the irradiation dosage level and engineer the capsule accordingly. We explored the possibility of using biocompatible species (Albumin) to form the capsule shell wall. Albumin-NACs with poly allylamine(PAH), phosphate and HSA (human serum albumin) composition was made. The Albumin-NACs had shown a prominent effect upon X-ray irradiation as shown in Fig. 4.12. At dosages ~ 60 Gy, the wrinkling of the capsules was observed. This material is promising for making X-ray sensitive capsule.

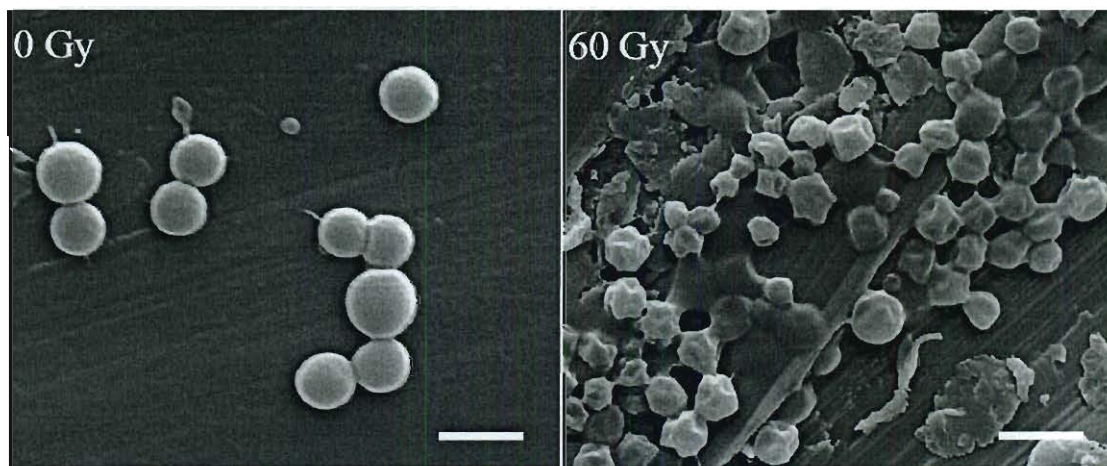


Figure 4.12. a) SEM images of irradiated Albumin NACs with various dosages (shown in inset) Scale bar 2 μ m.

We hypothesize that upon water hydrolysis, OH radicals get generated, which has a prominent effect on the shell material. In the case of Silica-NACs, the shell material consists of PAH and silica NPs. The OH radicals cannot break the entanglement of PAH and silica NPs at low dosages. Whereas in the case of Albumin-NACs, the OH radicals

are able to chemically react with protein molecule (albumin) and break the shell material at even low dosages.

4.3.6. Polyamine - Iron oxide composite microcapsules and responsive studies

Magnetic nanoparticles (MNPs) have been attracting a great amount of attention because of their numerous applications including contrast agents in magnetic resonance imaging (MRI)⁴⁹⁻⁵¹, magnetic targeted drug carriers, and hyperthermia treatments for cancer. However, complications, including aggregation of MNPs, have limited their use in drug delivery applications⁵²⁻⁵⁶. To overcome these limitations, several methods have been developed to coat magnetic particles. One method includes coating them with polymers to produce polymer/MNPs for increasing the MNP dispersion and stability. This method also increases the efficiency of loading and releasing drugs to specific locations for the treatment of various diseases including prostate cancer.

The major objective of this study to was to develop polymer microcapsules loaded with iron oxide magnetic nanoparticles. Transmission electron microscopy indicated the size of our NPs were about 20 nm. NACs would provide a means for magnet targeting capabilities. Synthesis of magnetic capsules and its responsive studies are explained in further section. Fig 4.13a the Fe₃O₄-NACs in DI-water and (b) shows the Fe₃O₄-NACs in suspension and its sensitivity towards a magnet.

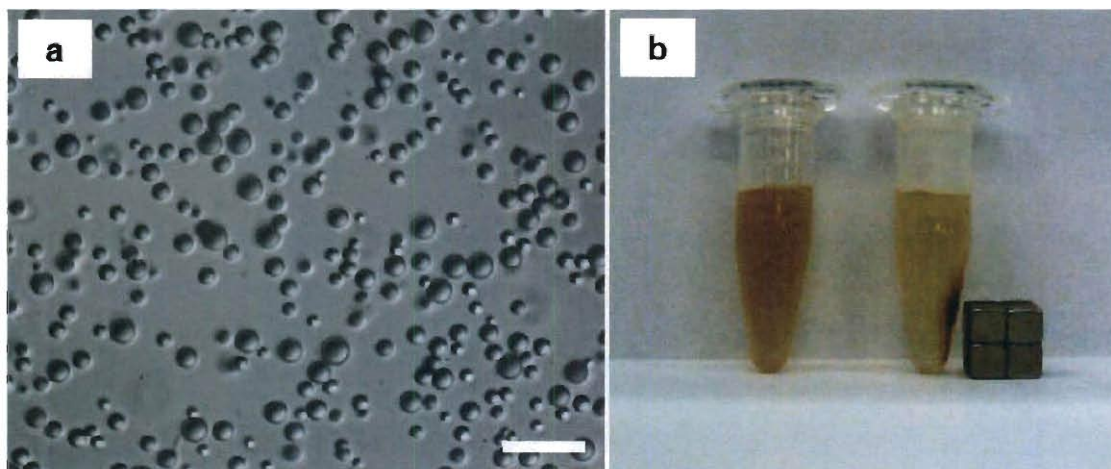


Figure 4.13. (a) Fe₃O₄-NACs in DI-water and (b) shows the Fe₃O₄-NACs in suspension and its sensitivity towards a magnet. Scale bar is 10 μ m

A TGA study of as-synthesized NACs indicated that 85% of the material was non-volatile (*i.e.*, composed of Fe₃O₄), and the balance was the PAH and cit compounds (Fig.4.14). The loss of volatiles occurred in three stages: <100 °C, 185-265 °C, and 265-600 °C. The first stage was likely due to the loss of water. The second and third stages could be due to the decomposition of cit anions and PAH chains, respectively. Since all the organics were volatilized from the NACs by 600 °C, we used a calcination temperature of 600 °C.

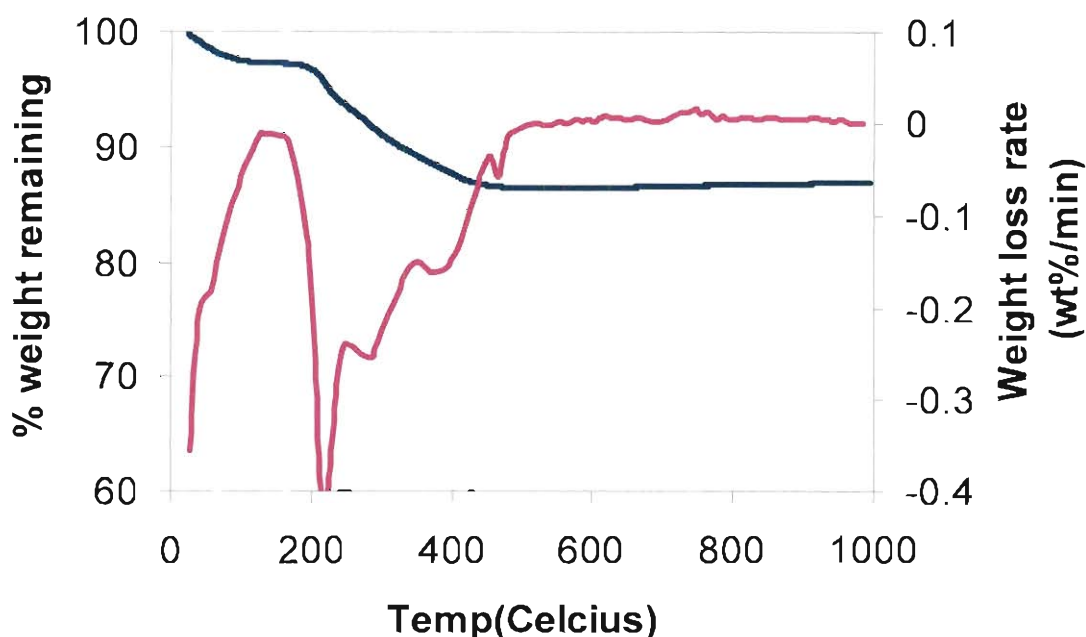


Figure 4.14. TGA weight-loss and weight-loss-rate profiles of Fe_3O_4 -NACs .

Responsive to magnetic field

To test the sensitivity of magnetic field on Fe_3O_4 -NACs, capsules were placed on a glass slide and covered with cover lid and magnetic field strength of 0.01 T is applied in X direction and Y directions. Fig. 4.15a shows Fe_3O_4 -NACs in Brownian motion. Once magnetic field is applied in X direction, Fe_3O_4 -NACs align in a straight line in the direction of applied magnetic field (Fig. 4.15b). The orientation was changed perpendicular to X axis i.e field is in the Y direction. Fe_3O_4 -NACs reorient in Y direction (Fig 4.15c). Fe_3O_4 -NACs return to Brownian motion when the magnetic field is removed (Fig 4.15d).

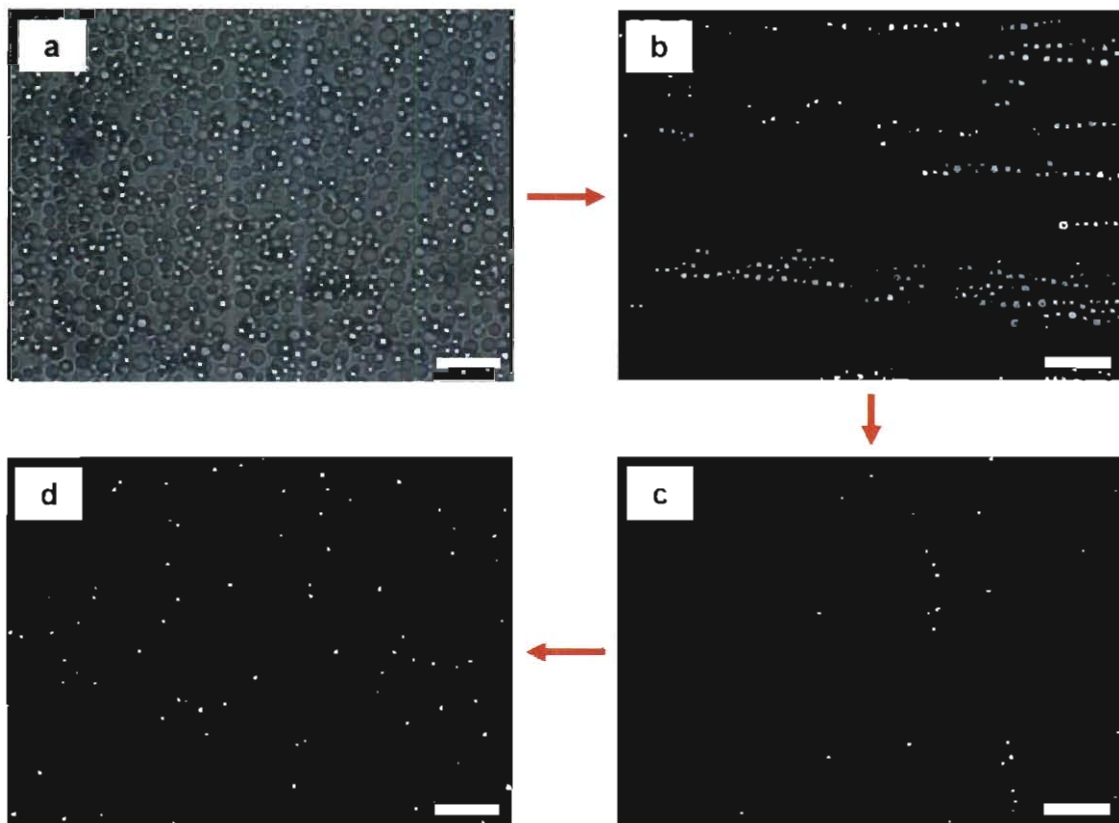


Figure 4.15. (a) Fe_3O_4 -NACs in Brownian motion no magnetic field applied, (b) applied magnetic field in X direction (c). in Y direction, and (d) after removing magnetic field. Magnetic field strength of 0.01 T is applied. Scale bar is 10 μm .

Magnetic heating studies

Magnetic heating on Fe_3O_4 – NACs was carried out on Nova Star 2 kW, Ameritherm. Fig 4.16a shows the instrument used for heating experiments. Fe_3O_4 – NACs were placed at the centre of the coil (Fig. 4.16b) and temperature measurements are taken using a coil temperature detector (Fig 4.16c).

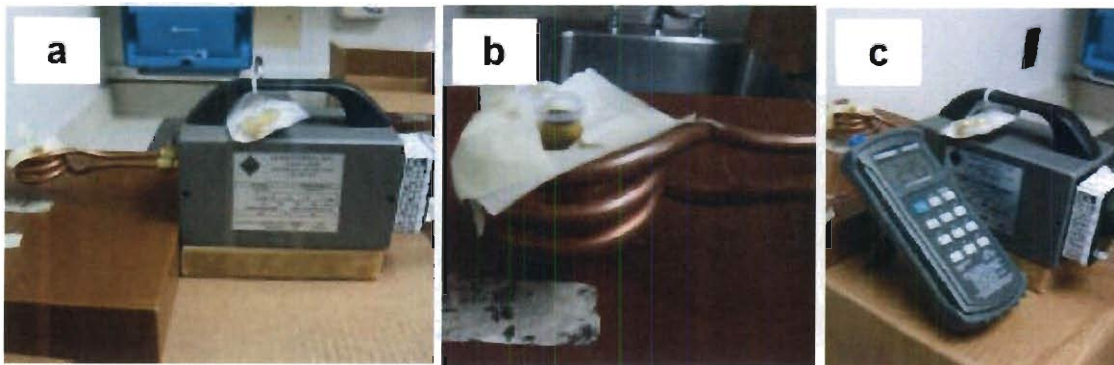


Figure 4.16. (a) Nova Star 2 kW RF Power Supply, Ameritherm, b) Fe_3O_4 – NACs in 1.5 ml centrifuge vial placed at the centre of the coil, c) temperature detector. Magnetic heating experiments were carried at current: 208.3 A, frequency: 267 kHz, Magnetic field strength - $H = 20 \text{ kA/m}$, Magnetic flux density - $B = 0.025 \text{ T}$.

Magnetic heating rates, were carried out with various concentration of Fe_3O_4 – NACs in suspension. Fig. 4.17 shows the heating rates of Fe_3O_4 – NACs with applied magnetic field through induction coil. Fe_3O_4 – NACs with Fe_3O_4 concentration of 2.5 mg/mL heats up the suspension to a temperature of 60°C in 20 min. Only Fe_3O_4 NPs heats upto 63°C in 20 min. The heating rate of Fe_3O_4 – NACs is similar to that of Fe_3O_4 NPs for the same concentration. However, if Fe_3O_4 – NACs concentration goes down to 1.0 mg/mL then the temperature rise goes only upto 40°C and 30°C for 0.3 mg/mL. It has been shown previously by researchers that if the particle diameter of Fe_3O_4 NP is $\sim 15 \text{ nm}$ ^{49, 56}, then it generates maximum heating rate upon applying magnetic field. The heat is generated mostly by Brownian and Neel's relaxation.

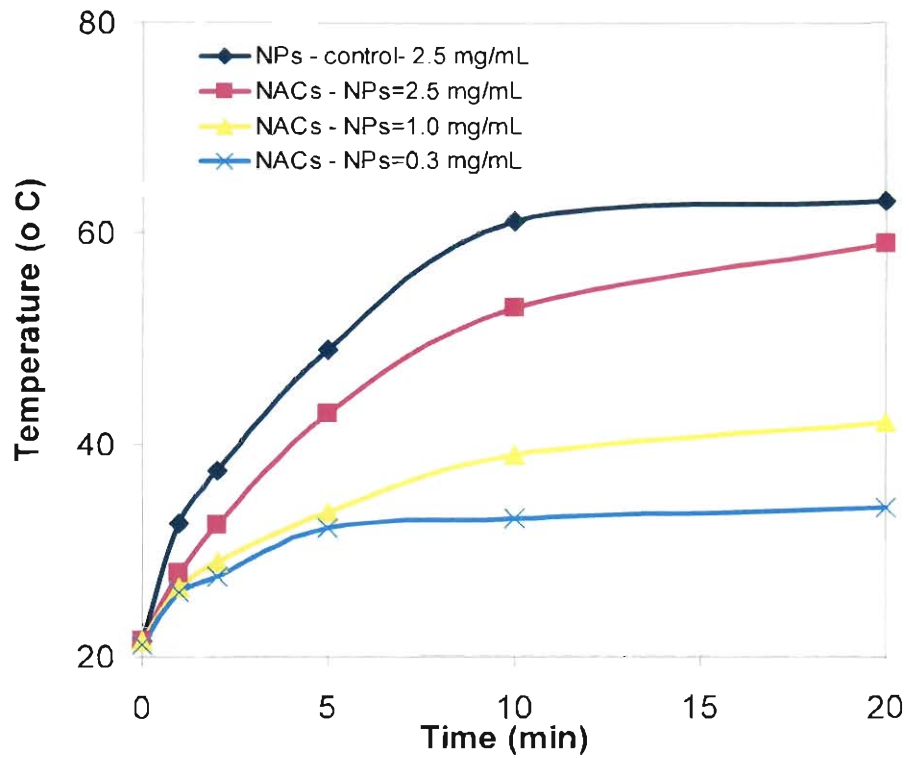


Figure 4.17. Temperature vs time of Fe_3O_4 – NACs in suspension at various concentrations of Fe_3O_4 , magnetic field applied for 20 mins.

Fe_3O_4 – NACs retain spherical nature even after applying magnetic field. Fig 4.18 shows SEM image of Fe_3O_4 – NACs in DIW and Fig shows SEM image of Fe_3O_4 – NACs after applying magnetic field for 20 mins. The surface becomes rougher compared to Fe_3O_4 – NACs in DIW. This could be because of few NPs falling apart from the capsule surface as the result of high local heating rate.

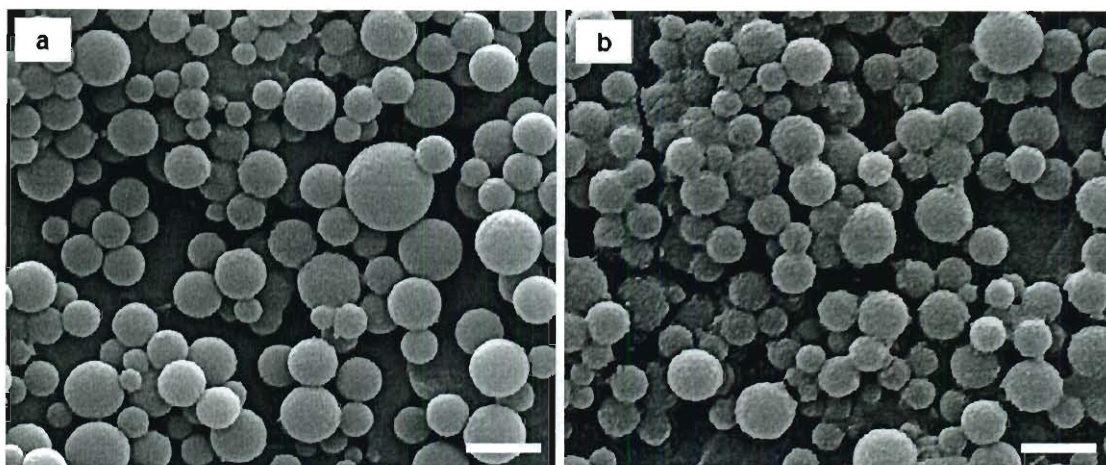


Figure 4.18. (a) SEM image of Fe_3O_4 -NACs in DI-water, (b) SEM image Fe_3O_4 -NACs after subjecting to magnetic field for 20 mins. Scale bar is 2 μm

Encapsulation of ICG in Fe_3O_4 -NACs

ICG was successfully encapsulated in Fe_3O_4 -NACs. Fig 4.19a shows the bright field and confocal microscopy images of ICG- Fe_3O_4 -NACs in DIW. Right half image is confocal image and the other half is the bright field image of the same spot. Confocal images revealed that most of the ICG (green color) is present inside the capsules. Fig 4.19b shows the confocal and bright field images of ICG- Fe_3O_4 -NACs after subjecting them to magnetic field for 20 min. Fig 4.19b clearly indicates that ICG has leaked out of capsules and most of them is present out side NACs. Our results indicated that Fe_3O_4 -NACs could potential be used to encapsulate cargo molecules and can be released upon triggering with applied magnetic field.

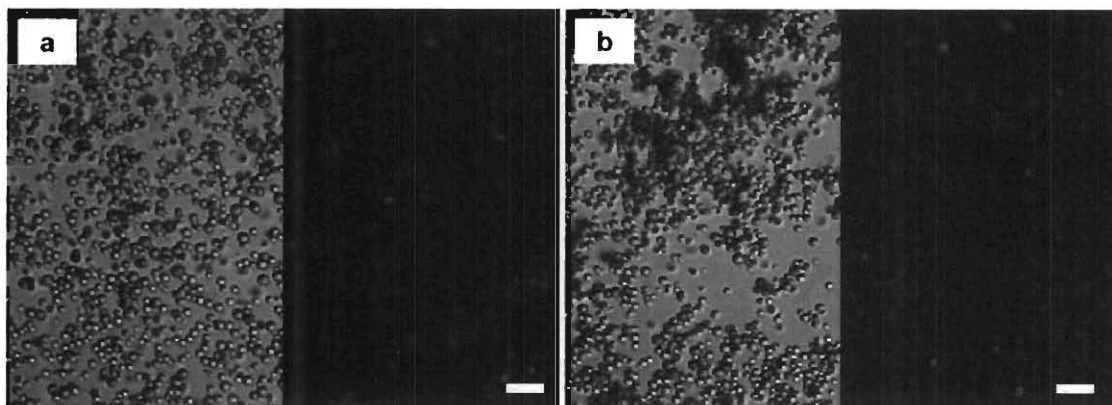


Figure 4.19. Bright field images and confocal images of a) ICG-Fe₃O₄NACs in DI- water, no magnetic field was applied b) ICG-Fe₃O₄NACs, after magnetic field applied for 2 mins. Right half image is confocal image and the other half is the bright field image of the same spot.

4.3.7. Responsive to pH and salt

The structure of NACs is held together by the electrostatic interactions of PAH, citrate and silica NPs. It can therefore be expected that the NACs structure will be sensitive to the solution pH. To test the pH sensitivity, silica NACs were dispersed in solutions of varying pH by keeping the ionic strength as constant. Fig. 4.20 (a, b, c) shows the capsules stability at pH 2, 6 and 12 respectively at 10 mM ionic strength. At very acidic (pH 2) and basic pH (12), the capsules disassemble. Salt concentration is an important physico-chemical parameter which will regulate the strength of electrostatics. The ionic cross-link density and conformations of PAH, Cit and NPs can be varied, therefore should effect the stability of NACs. To study the effect of salt, NACs were suspended in 0 mM (DIW), 150 mM, and 1M ionic strength solutions. Fig 4.20 (d, e, f) shows the capsules stability at various ionic strengths. At high ionic strength (1M), the capsules collapses and fragments into pieces. Detailed explanations on these studies are given in chapter3.

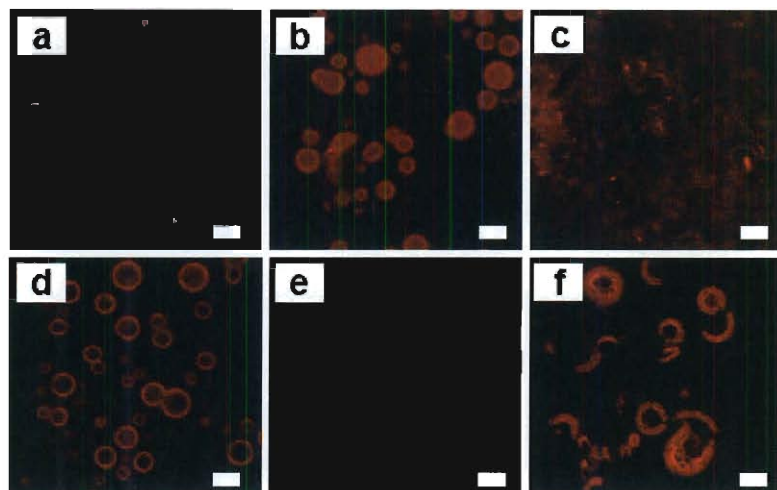


Figure 4.20. Confocal microscopy images of NACs suspended in various final pH conditions (a) pH =2.0, b) pH = 6.0, c) pH = 12.0, and various ionic strength solutions, d) DI-water, e) 150 mM NaCl, and f) 0.5 M NaCl. Scale bar is 5 μm .

4.3.8. Responsive to physical pressure and temperature

NACs were subjected to physical pressure by placing silica- NACs on a glass slide and applying the physical pressure by fingers. Confocal images show that capsules buckle (Fig. 4.21a) upon applying physical pressure. More detailed analysis to determine the mechanical properties of the capsules are discussed in chapter3. To study the effect of

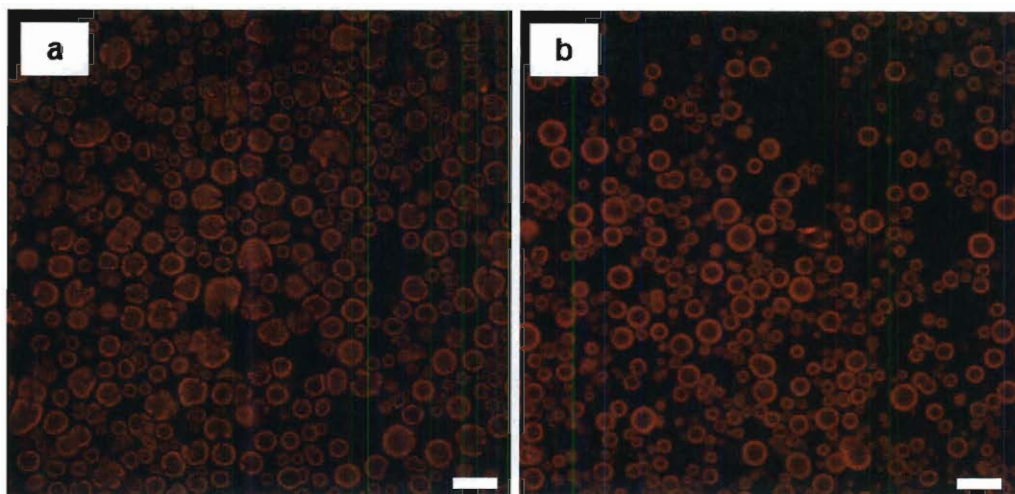


Figure 4.21. Confocal microscopy images of NACs (a) after applying physical pressure=2.0, b) pH = 6.0, c) subjected to a temperature of 80 °C. Scale bar is 10 μm.

temperature, silica-NACs were subjected to 80 °C and the confocal images reveal that it doesn't effect the capsule structure (Fig. 4.21b). Also, capsules retain their structure even after subjected to a calcination temperature of 600 °C.

4.4. Conclusions

In conclusion, we studied the possible encapsulation of molecules such as fluorescein, Gd[DOTP]⁵⁻, anticancer drug - doxorubicin hydrochloride doxorubicin, uracil in our NACs. Our experimental data on fluorescein verified the analytical model developed for dye release from single-shell nanoparticle/polymer capsules by Tavera et al. Based on the analytical model, we estimated diffusion coefficients in the capsule shell and core, which is comparable to experimental values for the similar systems reported in the literature. The result of our studies helps in better understanding about the encapsulation properties of NACs and its potential usage for applications. The shell can be designed in such a way that the cargo can be released at desired time intervals, by triggering the capsules by

varying either one or more of the following parameters such as pH, ionic strength, external pressure, and interaction with X-rays. Our results indicate that NACs, have interesting behavior in response to different pH and ionic strength values. X-ray (via radiation therapy) sensitivity studies are carried out on NACs. Radiation therapy is based on high-energy photons, protons, and electrons; however, the majority of radiotherapy treatments are based on high-energy X-rays. Therefore, X-ray sensitivity is an important design parameter, either for release or protection. NACs could be engineered in such a way that becomes sensitive to X-rays with various levels of irradiation. Magnetic-NACs were tested for their sensitivity with the applied alternating magnetic field. Our results indicate that magnetic-NACs could heat up to ~ 60 °C in 20 mins.

4.5. References

1. Caruso, F., Nanoengineering of particle surfaces. *Advanced Materials* **2001**, 13, (1), 11-+.
2. Caruso, F.; Caruso, R. A.; Mohwald, H., Nanoengineering of inorganic and hybrid hollow spheres by colloidal templating. *Science* **1998**, 282, (5391), 1111-1114.
3. Caruso, F.; Caruso, R. A.; Mohwald, H., Production of Hollow Microspheres from Nanostructured Composite Particles. *Chemistry of Materials* **1999**, 11, (11), 3309-3314.
4. Caruso, F.; Donath, E.; Mohwald, H., Influence of polyelectrolyte multilayer coatings on Forster resonance energy transfer between 6-carboxyfluorescein and rhodamine B-labeled particles in aqueous solution. *Journal of Physical Chemistry B* **1998**, 102, (11), 2011-2016.
5. Caruso, F.; Donath, E.; Mohwald, H.; Georgieva, R., Fluorescence studies of the binding of anionic derivatives of pyrene and fluorescein to cationic polyelectrolytes in aqueous solution. *Macromolecules* **1998**, 31, (21), 7365-7377.
6. Caruso, F.; Lichtenfeld, H.; Donath, E.; Mohwald, H., Investigation of electrostatic interactions in polyelectrolyte multilayer films: Binding of anionic fluorescent probes to layers assembled onto colloids. *Macromolecules* **1999**, 32, (7), 2317-2328.
7. Caruso, F.; Lichtenfeld, H.; Giersig, M.; Mohwald, H., Electrostatic self-assembly of silica nanoparticle - Polyelectrolyte multilayers on polystyrene latex particles. *Journal of the American Chemical Society* **1998**, 120, (33), 8523-8524.
8. Caruso, F.; Mohwald, H., Preparation and characterization of ordered nanoparticle and polymer composite multilayers on colloids. *Langmuir* **1999**, 15, (23), 8276-8281.
9. Caruso, F.; Mohwald, H., Protein multilayer formation on colloids through a stepwise self-assembly technique. *Journal of the American Chemical Society* **1999**, 121, (25), 6039-6046.

10. Caruso, F.; Susha, A. S.; Giersig, M.; Mohwald, H., Magnetic core-shell particles: Preparation of magnetite multilayers on polymer latex microspheres. *Advanced Materials* **1999**, 11, (11), 950-+.
11. Caruso, F.; Trau, D.; Mohwald, H.; Renneberg, R., Enzyme encapsulation in layer-by-layer engineered polymer multilayer capsules. *Langmuir* **2000**, 16, (4), 1485-1488.
12. Ai, H.; Jones, S. A.; de Villiers, M. M.; Lvov, Y. M., Nano-encapsulation of furosemide microcrystals for controlled drug release. *Journal of Controlled Release* **2003**, 86, (1), 59-68.
13. Brown, J. Q.; Srivastava, R.; McShane, M. J., Encapsulation of glucose oxidase and an oxygen-quenched fluorophore in polyelectrolyte-coated calcium alginate microspheres as optical glucose sensor systems. *Biosensors and Bioelectronics* **2005**, 21, (1), 212-216.
14. Chinnayelka, S.; McShane, M. J., Microcapsule Biosensors Using Competitive Binding Resonance Energy Transfer Assays Based on Apoenzymes. *Analytical Chemistry* **2005**, 77, (17), 5501-5511.
15. Petrov, A. I.; Antipov, A. A.; Sukhorukov, G. B., Base - Acid Equilibria in Polyelectrolyte Systems: From Weak Polyelectrolytes to Interpolyelectrolyte Complexes and Multilayered Polyelectrolyte Shells. *Macromolecules* **2003**, 36, (26), 10079-10086.
16. Sukhorukov, G.; Fery, A.; Mohwald, H., Intelligent micro- and nanocapsules. *Progress in Polymer Science* **2005**, 30, (8-9), 885-897.
17. Zhu, H.; McShane, M. J., Loading of Hydrophobic Materials into Polymer Particles: Implications for Fluorescent Nanosensors and Drug Delivery. *Journal of the American Chemical Society* **2005**, 127, (39), 13448-13449.
18. Yu, J.; Yaseen, M. A.; Anvari, B.; Wong, M. S., Synthesis of near-infrared-absorbing nanoparticle-assembled capsules. *Chemistry of Materials* **2007**, 19, (6), 1277-1284.
19. Yu, J.; Murthy, V. S.; Rana, R. K.; Wong, M. S., Synthesis of nanoparticle-assembled tin oxide/polymer microcapsules. *Chemical Communications* **2006**, (10), 1097-1099.
20. Yu, J.; Javier, D.; Yaseen, M. A.; Nitin, N.; Richards-Kortum, R.; Anvari, B.; Wong, M. S., Self-Assembly Synthesis, Tumor Cell Targeting, and Photothermal Capabilities of

Antibody-Coated Indocyanine Green Nanocapsules. *Journal of the American Chemical Society* **2010**, 132, (6), 1929-1938.

21. Yaseen, M. A.; Yu, J.; Wong, M. S.; Anvari, B., In-vivo fluorescence imaging of mammalian organs using charge-assembled mesocapsule constructs containing indocyanine green. *Optics Express* **2008**, 16, (25), 20577-20587.

22. Yaseen, M. A.; Yu, J.; Wong, M. S.; Anvari, B., Stability assessment of indocyanine green within dextran-coated mesocapsules by absorbance spectroscopy. *Journal of Biomedical Optics* **2007**, 12, (6).

23. Yaseen, M. A.; Yu, J.; Wong, M. S.; Anvari, B., Laser-induced heating of dextran-coated mesocapsules containing indocyanine green. *Biotechnology Progress* **2007**, 23, (6), 1431-1440.

24. Yaseen, M. A.; Yu, J.; Jung, B.; Wong, M. S.; Anvari, B., Biodistribution of Encapsulated Indocyanine Green in Healthy Mice. *Molecular Pharmaceutics* **2009**, 6, (5), 1321-1332.

25. Plush, S. E.; Woods, M.; Zhou, Y. F.; Kadali, S. B.; Wong, M. S.; Sherry, A. D., Nanoassembled Capsules as Delivery Vehicles for Large Payloads of High Relaxivity Gd³⁺ Agents. *Journal of the American Chemical Society* **2009**, 131, (43), 15918-15923.

26. Chang, T. M. S., Semipermeable microcapsules. *Science* **1964**, 146, (3643), 524-525.

27. Rambourg, P.; Levy, J.; Levy, M. C., Microencapsulation. III: Preparation of invertase microcapsules. *Journal of Pharmaceutical Sciences* **1982**, 71, (7), 753-758.

28. Hoshino, K.; Muramatsu, N.; Kondo, T., A study on the thermostability of microencapsulated glucose oxidase. *Journal of Microencapsulation* **1989**, 6, (2), 205-211.

29. Rilling, P.; Walter, T.; Pommersheim, R.; Vogt, W., Encapsulation of cytochrome C by multilayer microcapsules. A model for improved enzyme immobilization. *Journal of Membrane Science* **1997**, 129, (2), 283-287.

30. Gole, A.; Dash, C.; Mandale, A. B.; Rao, M.; Sastry, M., Fabrication, characterization, and enzymatic activity of encapsulated fungal protease-fatty lipid biocomposite films. *Analytical Chemistry* **2000**, 72, (18), 4301-4309.

31. Baran, E. T.; Azer, N.; Hasirci, V., Poly(hydroxybutyrate-co-hydroxyvalerate) nanocapsules as enzyme carriers for cancer therapy: An in vitro study. *Journal of Microencapsulation* **2002**, 19, (3), 363-376.
32. Rana, R. K.; Murthy, V. S.; Yu, J.; Wong, M. S., Nanoparticle self-assembly of hierarchically ordered microcapsule structures. *Advanced Materials* **2005**, 17, (9), 1145-+.
33. Tavera, E. M.; Kadali, S. B.; Bagaria, H. G.; Liu, A. W.; Wong, M. S., Experimental and Modeling Analysis of Diffusive Release from Single-Shell Microcapsules. *Aiche Journal* **2009**, 55, (11), 2950-2965.
34. Fujii, T.; Ogiwara, D.; Ohkawa, K.; Yamamoto, H., Alkaline phosphatase encapsulated in gellan-chitosan hybrid capsules. *Macromolecular Bioscience* **2005**, 5, (5), 394-400.
35. Murthy, V. S.; Rana, R. K.; Wong, M. S., Nanoparticle-assembled capsule synthesis: Formation of colloidal polyamine-salt intermediates. *Journal of Physical Chemistry B* **2006**, 110, (51), 25619-25627.
36. Murthy, V. S.; Kadali, S. B.; Wong, M. S., Polyamine-Guided Synthesis of Anisotropic, Multicompartment Microparticles. *Acs Applied Materials & Interfaces* **2009**, 1, (3), 590-596.
37. Kadali, S. B.; Soultanidis, N.; Wong, M. S., Assembling Colloidal Silica into Porous Hollow Microspheres. *Topics in Catalysis* **2008**, 49, (3-4), 251-258.
38. Bagaria, H. G.; Kadali, S. B.; Wong, M. S., Shell Thickness Control of Nanoparticle/Polymer Assembled Microcapsules. *Chemistry of Materials* **2011**, 23, (2), 301-308.
39. Sahoo, Y.; Goodarzi, A.; Swihart, M. T.; Ohulchanskyy, T. Y.; Kaur, N.; Furlani, E. P.; Prasad, P. N., Aqueous Ferrofluid of Magnetite Nanoparticles: Fluorescence Labeling and Magnetophoretic Control. *The Journal of Physical Chemistry B* **2005**, 109, (9), 3879-3885.
40. Hiemenz, P.; Rajagopalan, R., *Principles of colloid and surface chemistry* **1997**, Marcel Dekker, Inc., New York

41. Hunter, R. J., Foundations of Colloid Science. *Oxford University Press, New York* **2001**.
42. Klitzing, R. v.; Mohwald, H., A Realistic Diffusion Model for Ultrathin Polyelectrolyte Films. *Macromolecules* **1996**, *29*, (21), 6901-6906.
43. Kotarek, J. A.; Johnson, K. C.; Moss, M. A., Quartz crystal microbalance analysis of growth kinetics for aggregation intermediates of the amyloid-[beta] protein. *Analytical Biochemistry* **2008**, *378*, (1), 15-24.
44. Aime, S.; Botta, M.; Fasano, M.; Terreno, E., Lanthanide(in) chelates for NMR biomedical applications. *Chemical Society Reviews* **1998**, *27*, (1), 19-29.
45. Aime, S.; Botta, M.; Geninatti Crich, S.; Giovenzana, G. B.; Pagliarin, R.; Piccinini, M.; Sisti, M.; Terreno, E., Towards MRI contrast agents of improved efficacy. NMR relaxometric investigations of the binding interaction to HSA of a novel heptadentate macrocyclic triphosphonate Gd(III)-complex. *Journal of Biological Inorganic Chemistry* **1997**, *2*, (4), 470-479.
46. Bloembergen, N., Proton relaxation times in paramagnetic solutions. *The Journal of Chemical Physics* **1957**, *27*, (2), 572-573.
47. Caravan, P.; Ellison, J. J.; McMurry, T. J.; Lauffer, R. B., Gadolinium(III) chelates as MRI contrast agents: Structure, dynamics, and applications. *Chemical Reviews* **1999**, *99*, (9), 2293-2352.
48. Freed, J. H., Dynamic effects of pair correlation functions on spin relaxation by translational diffusion in liquids. II. Finite jumps and independent T₁ processes. *The Journal of Chemical Physics* **1978**, *68*, (9), 4034-4037.
49. Rosensweig, R. E., Heating magnetic fluid with alternating magnetic field. *Journal of Magnetism and Magnetic Materials* **2002**, *252*, (1-3 SPEC. ISS.), 370-374.
50. Kim, D. H.; Nikles, D. E.; Johnson, D. T.; Brazel, C. S., Heat generation of aqueously dispersed CoFe₂O₄ nanoparticles as heating agents for magnetically activated drug delivery and hyperthermia. *Journal of Magnetism and Magnetic Materials* **2008**, *320*, (19), 2390-2396.

51. Jordan, A.; Wust, P.; Fahling, H.; John, W.; Hinz, A.; Felix, R., Inductive heating of ferrimagnetic particles and magnetic fluids: Physical evaluation of their potential for hyperthermia. *International Journal of Hyperthermia* **1993**, *9*, (1), 51-68.
52. Roca, A. G.; Costo, R.; Rebolledo, A. F.; Veintemillas-Verdaguer, S.; Tartaj, P.; González-Carretero, T.; Morales, M. P.; Serna, C. J., Progress in the preparation of magnetic nanoparticles for applications in biomedicine. *Journal of Physics D: Applied Physics* **2009**, *42*, (22).
53. Kalambur, V. S.; Han, B.; Hammer, B. E.; Shield, T. W.; Bischof, J. C., In vitro characterization of movement, heating and visualization of magnetic nanoparticles for biomedical applications. *Nanotechnology* **2005**, *16*, (8), 1221-1233.
54. Hu, S. H.; Tsai, C. H.; Liao, C. F.; Liu, D. M.; Chen, S. Y., Controlled rupture of magnetic polyelectrolyte microcapsules for drug delivery. *Langmuir* **2008**, *24*, (20), 11811-11818.
55. Hergt, R.; Andrae, W.; d'Ambly, C. G.; Hilger, I.; Kaiser, W. A.; Richter, U.; Schmidt, H.-G., Physical limits of hyperthermia using magnetite fine particles. *IEEE Transactions on Magnetics* **1998**, *34*, (5 pt 2), 3745-3754.
56. Bahadur, D.; Giri, J., Biomaterials and magnetism. *Sadhana-Academy Proceedings in Engineering Sciences* **2003**, *28*, 639-656.

Chapter 5. Formation of elongated nanoparticle/polyamine-assembled microcapsules using microfluidizer

5.1. Introduction

We have developed a materials synthesis technique in which synthetic polyamines such as polyallylamine and/or polylysine are crosslinked with multivalent anions (citrate) to form polymer-salt aggregates, that then serve as templates for the deposition of nanoparticles to form micron-sized hollow spheres or "nanoparticle-assembled capsules (NACs)"¹⁻¹⁰ or also called as "polymer-salt aggregate assembly" (PSA). This electrostatically-driven route is attractive for encapsulation and scale-up because encapsulation and materials formation occur in water, at mild pH values, and at room temperature. NACs showed potential applications in using them as MRI contrast agents - showing larger gains in relaxivity³, phototherapy⁶, protease imaging, and siRNA therapy¹¹. NACs can potentially find wide-ranging applications in pharmaceutical, food, and consumer industries by serving as miniature containers to store, deliver, and release substances. One of the most encouraging aspects of NACs is the flexibility in design of materials to tailor them for specific applications. Although synthesis of NACs is well understood, less attention has been paid to their particle shape. Non-spherical NACs could possibly offer unique properties by comparison to spherical NACs.

Typically most of the colloidal particles are spherical in nature. During synthesis, surface tension forces overcome all other forces resulting in the formation of spherical particles. On the other hand, non-spherical particles gives an immense prospective for a wide variety of applications such as in cosmetics, biotechnology, advanced structural

materials, and pharmaceuticals¹²⁻¹⁵. Spherical particles are the most helpful carriers for drug delivery, researchers are finding that rod-shaped carriers may give a benefit of having longer circulation time in the blood stream^{16, 17} (eg: longer circulation times are needed for phototherapy). Researchers have shown that anisotropic particles could be used as rheology modifiers^{18, 19}. Cylindrical particle suspensions influence the rheology behaviour as reported by Wolf et al.¹⁹, under low shear the cylindrical shape influences in increasing the viscosity of the suspension. In high shear zone, the cylindrical particles orient in the direction of shear direction, hence the relative viscosity is lower in the shear direction compared to spherical particles²⁰. The distinctive feature of non-spherical particles is that they can pack more closely than spherical ones²¹. Also they behave differently from spherical ones under similar conditions such as electric, and magnetic fields²²⁻²⁴. Composite materials with light –weight and exhibiting unique mechanical properties have been formed by non-spherical particles such as fibers and platelets²⁵. Such exciting properties can guide to new applications and generate plethora of opportunities for areas that have conventionally used spherical particles.

Various methods for producing non-spherical particles have been developed based on specific application. Techniques such as lithography, microfluidics and photo polymerization are explored to synthesize anisotropic particles²⁶⁻³⁶. Rolland et al., exploited conventional soft lithographic molding methods to generate PEG, PLA, and poly(pyrrole) particles of various shapes³⁷. Xu et al., and Dendukuri et al., used combination of microfluidics and polymerization techniques to form solid particles of several non-spherical geometries^{26, 28, 38}. Alternatively, non-spherical particles could be produced by taking spherical particle as a template and being manipulated to form

different morphology. Manoharan et al., demonstrated the assembly of poly styrene (PS) particles using emulsion droplet as a template²⁹. Ho et al., created ellipsoidal PS particles by stretching PS particles embedded in a polymer film³⁹. Champion et al., has demonstrated the formation over twenty different structures by modifying the stretching protocol on PS particles^{27, 29}. The various methods discussed above have distinctive advantages and limitations^{18, 39-53}. For example, in microfluidic methods, shapes and are limited by microchannel geometry. Design and fabrication of non-spherical particles is more complex with the self-assembly method⁵⁴. Projection photolithography techniques shape sizes are driven by the mask used. It is very expensive to construct equipment that is capable of writing features at the diffraction limit.

In this paper, we discuss transforming spherical NACs to non-spherical NACs using microfluidizer (M-110S model)⁵⁵. Polymer-salt aggregates are very unstable and elastic in nature. This spherical soft polymer-salt aggregate gets elongated upon applying shear, and retracts back to its spherical structure. The aqueous suspension consisting of polymer-salt aggregates behave as visco-elastic material. Visco-elastic is the property of materials that exhibit both viscous and elastic characteristics when undergoing deformation. Our rheology experiments on polymer-salt aggregates suspension revealed the visco-elastic behavior and act as mild shear thinning fluid. We take advantage of the visco-elastic behavior of polymer-salt aggregates. These aggregates under elongation/shear undergo elongation that is afterwards transformed to non-spherical NACs through further simple, processing steps. Process parameters were also explored to control the size and generate more non-spherical structures.

5.2. Experimental methods

5.2.1. Materials

Poly(allylamine hydrochloride) (“PAH,” 56,000 g/mol, Sigma-Aldrich), Poly styrene sodium sulfonate (“PSS-Na”~ 200,000 g/mol, Sigma-Aldrich), trisodium citrate (“cit”, Fisher Scientific), and colloidal SiO₂ (Snowtex-O type, 20.3 wt% SiO₂, pH 3.4, ionic strength I = 16.9 mM, Nissan Chemicals) were the precursors used. The SiO₂ NP diameter was measured to be 13±3 nm by dynamic light scattering. The NPs had a zeta potential of -16 mV, calculated from electrophoretic mobility measurements using Henry’s equation. Deionized water (18.2 MΩ, Barnstead Nanopure Diamond System) was used for the PAH and cit stock solutions, and a HCl solution (1 N, Fisher Science) was diluted with deionized water to a pH value of 3.5. The SiO₂ NP suspension was diluted with this HCl solution to 1.2 wt%.

5.2.2. Synthesis of elongated NACs

An aqueous PAH solution (14 mL, 5 mg/mL or 2 mg/mL) was mixed with an aqueous cit solution (35 mL) in a 50 mL beaker for few seconds. For the *R* charge ratio of 2 studied in this work, the cit concentration was 14.2 mM for [PAH] = 5 mg/mL or 5.68 mM for [PAH] = 2 mg/mL. *R* is defined as the ratio of total number of negative charges from the salt to the total number of positive charges from the polyamine. A turbid mixture immediately resulted, indicating the formation of polymer-salt aggregates. This suspension was immediately poured in into the microfluidizer chamber. Polymer-salt aggregate is then subject to various number of strokes. In the second step NPs are

injected using a syringe into the mixing chamber and then subjected to various numbers of strokes accordingly. The system is maintained in isothermal conditions. The solution is collected and kept for 2 hours before processing it further. Most of the supernatant (2/3 volume) was removed and replaced with the same volume of deionized water, and the mixture was re-agitated and re-centrifuged. This cleaning procedure was repeated twice to remove any unreacted precursors. The washed material NACs are collected and characterized by optical and SEM microscopy.

5.2.3. Characterization

Optical Microscopy: Optical microscopy was performed on a Leica DM2500 upright microscope equipped with 100× oil immersion objective (numerical aperture = 1.4). Bright field and differential interference contrast (DIC) images were taken at 100× magnification.

Scanning Electron Microscopy (SEM): Scanning electron microscopy was carried out using FEI Quanta 400 field emission scanning electron microscope. Secondary electron images of NACs were taken at 20 kV electron beam with a working distance of 10 mm. The NACs suspension containing dye were washed twice with water, loaded on an aluminum stub and dried. The sample was sputter-coated with gold for 1 min (~25 nm of Au film) prior to imaging.

Transmission Electron Microscopy (TEM): Capsules were dried on a carbon-coated copper grid and imaged with a JEOL 1230 High Contrast TEM operated at 80 kV.

5.3. Results and discussions

5.3.1. Formation of polymer-composite elongated structures

It was known from our previous studies that in the first step of NACs synthesis i.e polymer-salt aggregates, they behave like visco-elastic and unstable structures. Upon addition of NPs to these unstable structures, it locks the polymer-salt aggregates and forms a robust polymer filled or water filled structures. In this work, we focus on subjecting the polymer-salt aggregates to shear and elongation flow and elongate them and then lock the elongated polymer-salt aggregates by addition of NPs.

The microfluidizer chamber and a schematic of Y- junction are shown in Fig. 5.1. Our proposed hypothesis was being tested by subjecting the polymer salt aggregate to shear/extensional flow by passing the pre formed polymer-salt aggregate to the reaction chamber and subjected to high shear created when the stroke pressure is 20K PSI for 20 strokes (step A) ~ 6 passes. The NPs are then added to the microfluidizer and subjected to 20 strokes (step B) ~ 6 passes. The resulting suspension was collected and imaged under SEM. It is clearly evident from the Fig. 5.2(d) that the 90% of the structures formed are non-spherical. In contrast, spherical structures were formed in the beaker synthesis in Fig. 5.2(a) where polymer-salt aggregates don't undergo any elongation. Simply by applying shear/extensional the NACs morphology can easily be transformed from spherical to elongated structures. In the following sections, the processing parameters are discussed in detail.

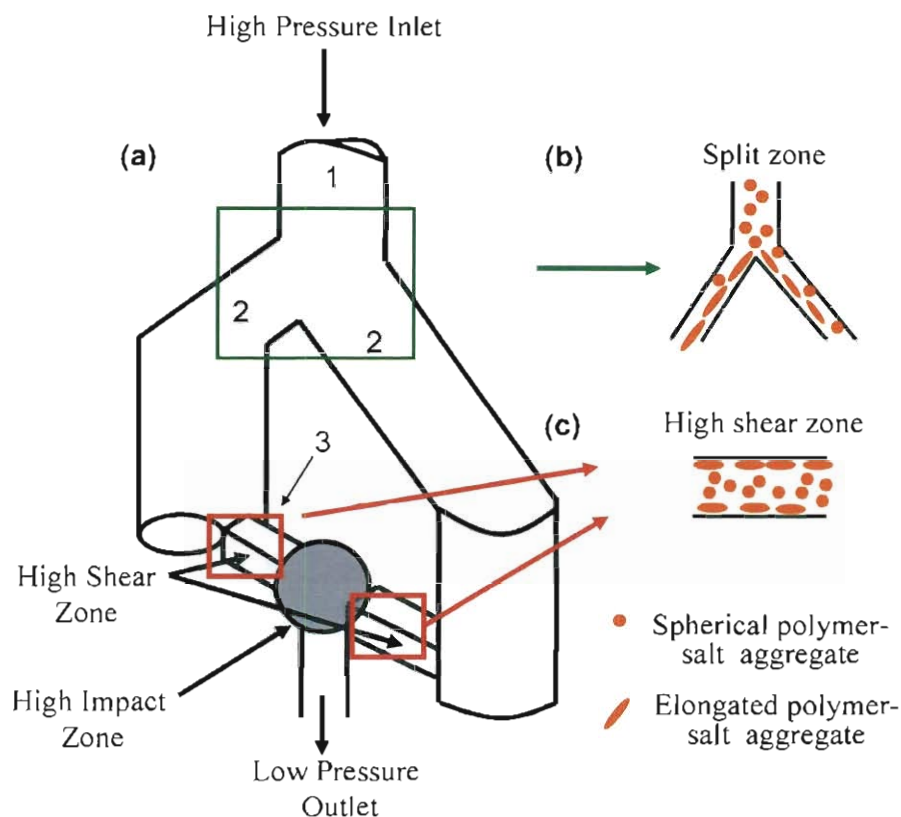


Figure 5.1. (a) Schematic of the microfluidizer chamber (redrawn from microfluidicscorp.com), (b) schematic showing the formation of elongated polymer-salt aggregates in Y –junction. and (c) high shear zone

5.3.2. Effect of pressure.

Pressure could be changed accordingly in the microfluidizer to apply variable stresses (both shear and elongation or extensional) on polymer-salt aggregates. The microfluidizer chamber's width and depth dimensions are typically in the range of 50-300 μm . The minimum dimension used in our experiment is of 75 μm . The input stream is split into two equal channels and then recombines at the end of the chamber as shown in Fig. 5.1a.

In our studies, 0, 5000, 10000, and 20000 PSI pressures were applied by the intensifier pump used to generate a fluid velocity (U_{avg}) of approximately 0, 258.33, 357.82 and 495.62 m/s respectively to produce elongated NACs.

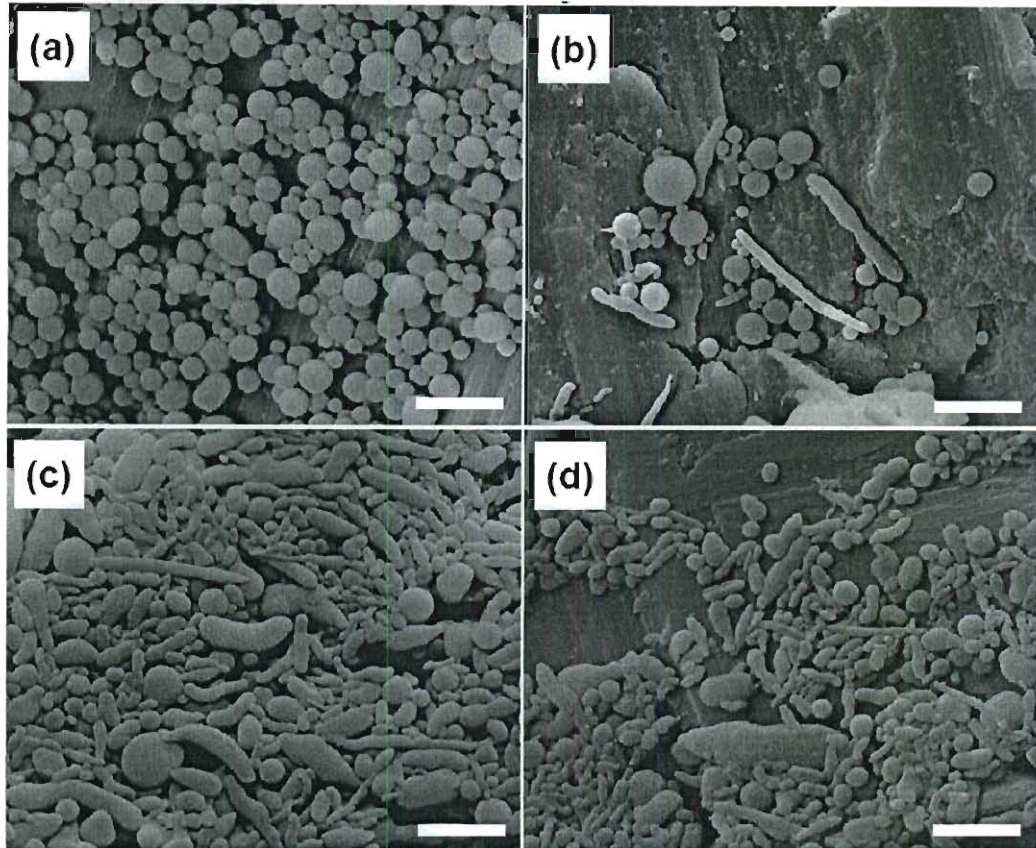


Figure 5.2. SEM images of elongated NACs formed by subjecting polymer-salt aggregates to various to (a) 0K, (b) 5K, (c) 10K, (d) 20K PSI pressure. Approximately 300 particles were counted on the SEM images using ImagePro software to determine the particle size of spherical NACs shown in (a) (mean particle size is 1.5 micron with a relative standard deviation of 28 %) Initial particle size of polymer- salt aggregate is 1.5 micron. Scale micron. Scale bar is 5 micron

As shown in Fig. 5.2 (b to d) the formation of elongated NACs (NACs-E) at 5K, 10K, and 20K PSI pressure respectively. Selectivity of non-spherical NACs increases when polymer-salt aggregates are subjected to increasing shear and elongation stresses. The

selectivity of NACs-E at 5K, 10K and 20K PSI applied pressures is 14 %, 75 %, and 90 % respectively. A thorough analysis was carried out to explain the trends of the length and width elongation of NACs for the various applied pressures. Approximately 300 particles from SEM images were analyzed to calculate average dimension of elongated NACs. The average lengths for 5K, 10K and 20K PSI samples are 3.69, 2.08 and 1.80 micron respectively. The average width for various pressures is 0.75 micron. A log-normal fitting was performed on the experimental data to determine the trends in the distribution. It can be clearly distinguished that in Fig. 5.3 (a, b). The L/W (length to width) ratio for 5K, 10K, and 20K PSI samples are 4.92, 2.78, and 2.40.

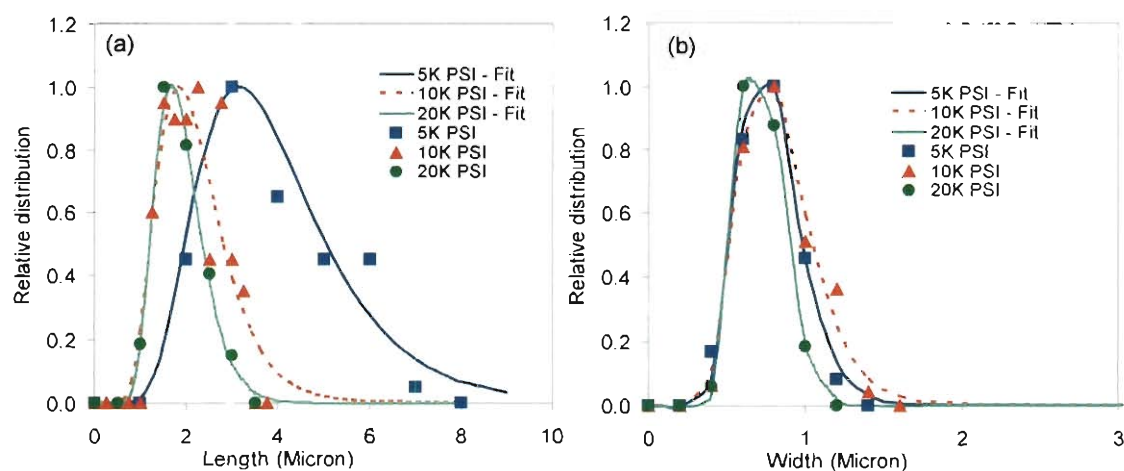


Figure 5.3. (a) Relative distribution plots for length (a) and width (b) for 5K, 10K, 20K PSI pressure along with log-normal fits respectively.

5.3.3. Mathematical model

A mathematical model has been developed to understand the formation of elongated structures. Analysis has been carried to understand if the deformation of polymer-salt aggregates is mainly because of the extensional (elongation) rate or shear rate. All the

treatment was done considering Newtonian fluid behavior. Reynolds number (Re) \sim 21,000 before the split zone (region 1) and after the fluid stream splits (region 2) in half (assuming $\Delta P \sim 5000$ PSI, diameter before split zone diameters as 300 micron, after fluid stream splits in half as 150 micron diameter). Reynolds number indicates that the fluid stream is highly turbulent. Boundary layer thickness (δ) was estimated to be in the range of 2 to 15 micron in the duct of region 1 and 2. The boundary layer \sim 5 % of region 1. The boundary layer is small respect to the dimensions of the duct. The schematic of Y-junction of the microfluidizer is as shown in Fig. 5.4. Assuming an angle of $-\lambda\pi$ between the two ducts, a model has been developed to estimate the velocity profiles at the wedge intersection in X and Y directions are shown in the schematic. U_x and, U_y represent velocities in x and y axis respectively. V_o is upstream velocity.

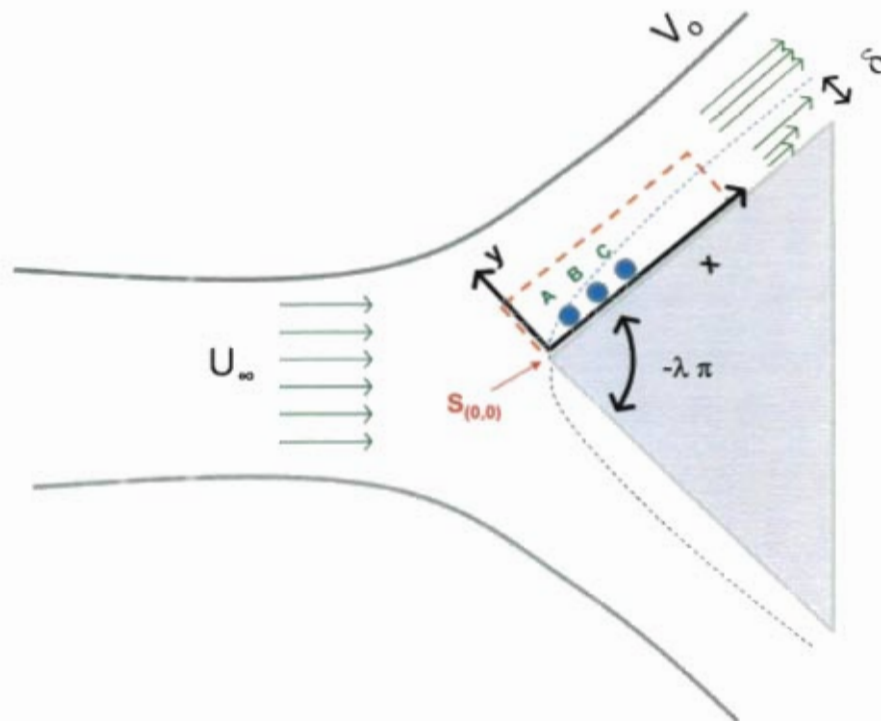


Figure 5.4. Variables used in the transformation technique. The analysis of the boundary layer and the flow is done in section shown as a red dashed line rectangle.

Assuming the boundary layer is small respect to the dimensions of the duct. The equation of motion can be written for x-direction as:

$$U_x \frac{\partial U_x}{\partial x} + U_y \frac{\partial U_x}{\partial y} = \nu \frac{\partial^2 U_x}{\partial y^2} - \frac{1}{\rho} \frac{dP}{dx} \quad (E.1)$$

In equation E.1, the x-direction is the direction parallel to the physical boundary solid-fluid, and y is the axis normal to the solid-fluid interface. Assuming mechanical energy conservation, the x-momentum balance is simplified to the form

$$U_x \frac{\partial U_x}{\partial x} + U_y \frac{\partial U_x}{\partial y} = \nu \frac{\partial^2 U_x}{\partial y^2} + V_o \frac{dV_o}{dx} \quad (E.2)$$

Where ρ is density, μ is viscosity, $\nu = \mu/\rho$ is the kinematic viscosity, V_o is the fluid stream velocity. Equation (E.2) was written in dimensionless form via transformation technique, and using the free parameter method⁵⁶. It is converted in the differential equation form known as Falkner and Skan equation⁵⁷. This equation is used to predict the flow past edge with an angle $\lambda\pi$.

Using transformation technique, we can convert this differential equation into a well known Falkner and Skan equation⁵⁷ and flow past a wedge with an angle $\lambda\pi$.

$$f''' + ff'' - \lambda(1 - (f')^2) = 0 \quad (E.3)$$

The boundary conditions are:

$$f = f' = 0 \text{ for } \eta \rightarrow 0 \text{ indicates velocities at the surface for x and y are zero} \quad (E.4)$$

$$f' = 1 \text{ for } \eta \rightarrow \infty \text{ Indicated constant velocity beyond the boundary layer} \quad (E.5)$$

Where $m = \frac{-\lambda}{\lambda+1}$, $Re_L = \frac{L U_L}{\nu}$, $\eta = \frac{y}{L} \sqrt{\frac{(m+1)}{2}} Re_L^{1/2} \left(\frac{x}{L}\right)^{\frac{(m-1)}{2}}$, L is the characteristic

length. Equation E.3 can be solved numerically and the velocity components and the

extensional strain may be calculated using transformation variables. The final obtained equations are

$$U_x = \frac{\partial \psi}{\partial y} = B x^m f' \quad (\text{E.6})$$

$$-U_y = \frac{\partial \psi}{\partial x} = \sqrt{\frac{(m+1)\nu B}{2}} x^{\frac{(m-1)}{2}} \left(f + \left(\frac{m-1}{m+1} \right) \eta f' \right) \quad (\text{E.7})$$

The extensional strains are calculated with the derivatives of each velocity:

$$\frac{\partial U_x}{\partial x} = B m x^{m-1} f' + B x^m f'' \frac{d\eta}{dx} \quad (\text{E.8})$$

$$-\frac{\partial U_y}{\partial y} = \sqrt{\frac{(m+1)\nu B}{2}} x^{\frac{(m-1)}{2}} \left(f' + \left(\frac{m-1}{m+1} \right) (\eta f'' + f') \right) \frac{d\eta}{dy} \quad (\text{E.9})$$

Writing all the equations in dimensionless form:

$$\frac{U_x}{B L^m} = \left(\frac{x}{L} \right)^m f' \quad (\text{E.10})$$

$$-\frac{U_y}{L^m B} \text{Re}_L^{1/2} = \sqrt{\frac{m+1}{2}} \left(\frac{x}{L} \right)^{\frac{(m-1)}{2}} \left(f + \left(\frac{m-1}{m+1} \right) \eta f' \right) \quad (\text{E.11})$$

$$\frac{L}{L^m B} \frac{\partial U_x}{\partial x} = m \left(\frac{x}{L} \right)^{m-1} f' + \left(\frac{x}{L} \right)^m f'' L \frac{d\eta}{dx} \quad (\text{E.12})$$

$$-\frac{L}{L^m B} \text{Re}_L^{1/2} \frac{\partial U_y}{\partial y} = \left(\frac{x}{L} \right)^{\frac{(m-1)}{2}} \left(f' + \left(\frac{m-1}{m+1} \right) (\eta f'' + f') \right) L \frac{d\eta}{dy} \quad (\text{E.13})$$

Where ψ is stream function, B is proportionality constant; see appendix equation A.27. The extensional rates are calculated with equations (E.8) and (E.9). The shear stress close to the inlet of the ducts can be estimated using Blasius approach (See appendix for calculations). Assuming an angle of 135° between the two ducts (estimated from Fig.

5.4), the dimensionless velocity profile is shown in Fig. 5.5. It can be seen in the diagram the component of the velocity in y direction is negligible for a length of $x=4$. The steeper extensional strain rate is located close to the inlet zone $(0,1)$. This can be verified in the Fig. 5.6.

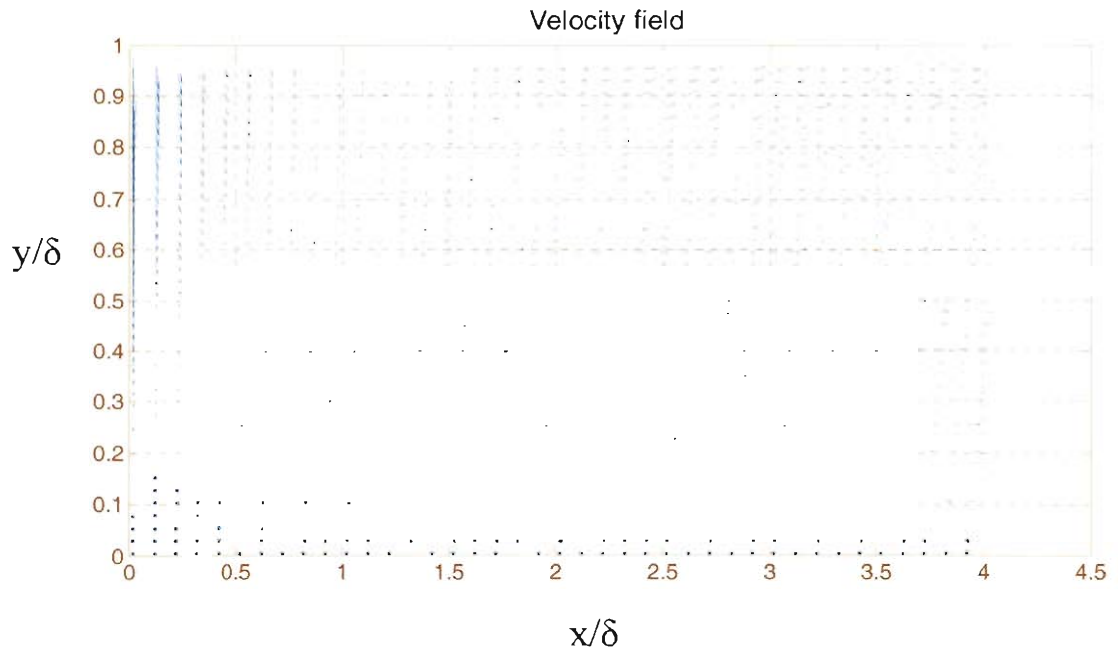


Figure 5.5. Dimensionless velocity profiles, this section corresponds to the zone of dashed red line box in the Fig. 5.4 near point $S_{(0,0)}$. If $y/\delta = 1.0$ indicates the end region of boundary layer. $(x/\delta, y/\delta) = (0,0)$ corresponds to $S_{(0,0)}$.

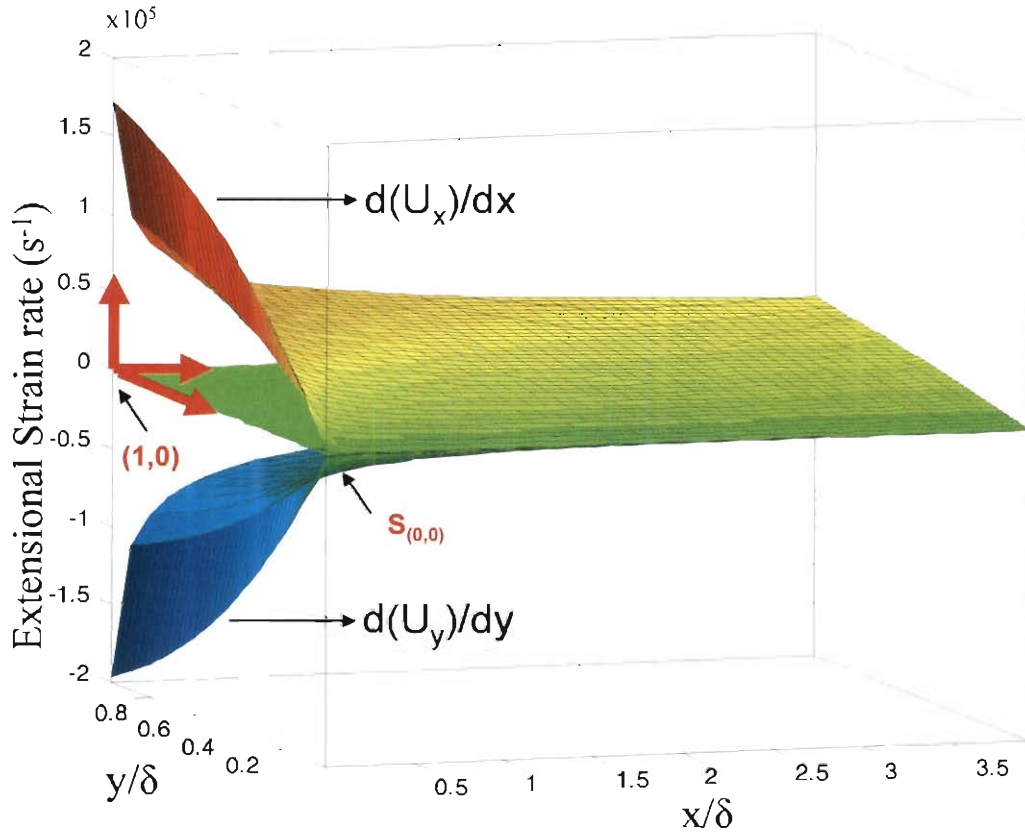


Figure 5.6. The extensional strain in the zone of the dashed red rectangle in Fig. 5.4. Plot indicates the zone for higher deformation of particles is the point where the fluid stream splits in the corner ($S_{(0,0)}$) having the highest value of extensional strain. The calculations are done for 5K PSI and a duct of 300 micron region is considered.

The estimated elongation rates in the microfluidizer are in the range of $(0.02-2) \times 10^7$ S^{-1} and the shear rate (dy/dt) in the impact zone based on the geometry can range from $(0.05-0.8) \times 10^7$ S^{-1} (for 50 micron and 300 micron dimensions, dy/dt are 0.05×10^7 S^{-1} and 0.8×10^7 S^{-1} respectively). All calculations are done for 5k PSI applied pressure ~ velocity of 258 m/s. Our results match very well with the shear rate reported by Panagiotou et al⁵⁸⁻⁶⁰. However, they report only about shear stress contribution but not the extensional rate. We would like to bring out that in Y- chamber of microfluidizer extensional rate has an equal contribution like shear rate. It can be observed from the

estimated stresses that at the Y- junction, elongation stress plays a dominant role compared to shear stress. Also, at the high impact zone, elongation rate and shear rate both play a dominant role in the elongation of the polymer-salt aggregate. From Fig. 5.3, it is observed that as pressure increases from 5K to 20K PSI, L/W goes from 4.92 to 2.40. Width of the elongated particle remains constant but L increases. We hypothesize that the polymer-salt aggregates elongates as they undergo elongation and shear stresses. As pressure increases from 5K to 20K PSI, the polymer-salt aggregates elongates and eventually fragments into 2 or more pieces, thus decreasing the L/W ratio. It has been shown previously that droplets can break upon applying shear and/or elongation rate⁶¹. Effect of pressure on PS aggregates is shown in schematic Fig. 5.7. When ΔP is 0, then polymer-salt aggregates are in spherical shape. As ΔP increase to 5K PSI, the PS aggregates elongate as they undergo elongation and shear stresses.

The deformation of PS aggregates at various co-ordinates such as A (0.5, 0.5), B (1.0, 0.5), and C (1.5, 0.5). $y/\delta = 0.5$ indicates that it is well below the boundary layer thickness region. A (0, 1), B (0.5, 1), and C (1, 1) according to Fig. 5.4 are shown in Fig. 5.7. As pressure increases to 10K PSI, we hypothesize that PS aggregates can fragment into smaller pieces at position A. These smaller PS aggregates behave like independent aggregates and undergo further stresses as they move to B and C positions. Appendix C has the detailed information on mathematical modeling.

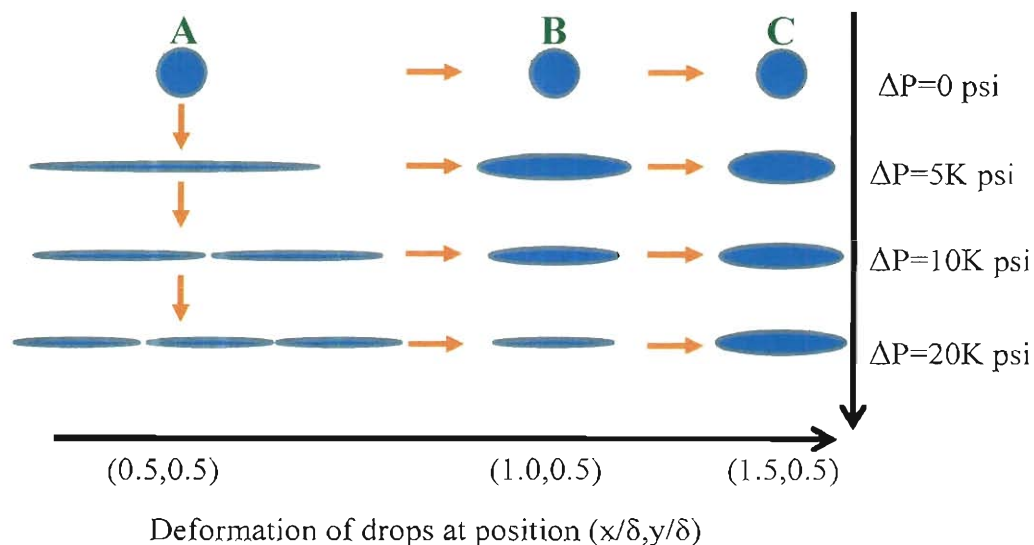


Figure 5.7. Schematic showing the deformation of polymer-salt aggregates at position $(x/\delta, y/\delta)$ with respect to various pressures. Position $(x/\delta, y/\delta)$ are related to A, B and C as shown in Fig. 5.4.

We hypothesize that polymer-salt aggregates undergo deformation only when they lie below the boundary layer region. Fig.5.8 shows the probable behavior of polymer-salt aggregates at various $(x/\delta, y/\delta)$. At $(x/\delta, y/\delta) = (0.5, 0.5)$, the polymer-salt aggregates undergo elongation. At the boundary layer periphery i.e at $(0.5, 1.0)$, the polymer-salt aggregates undergoes slight change in their shape. Outside the boundary layer, polymer-salt aggregates don't undergo any elongation. Further detailed analysis is given in further sections.

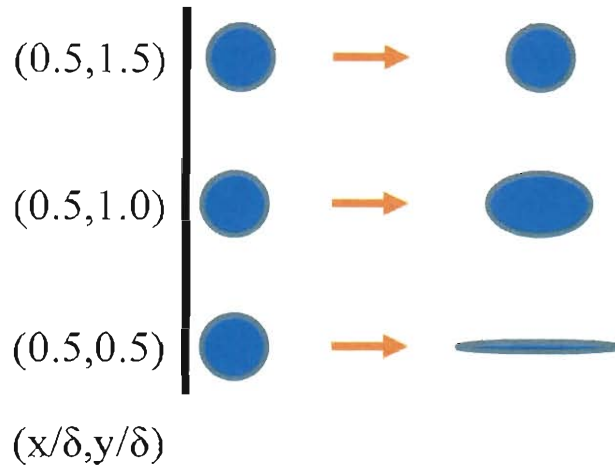


Figure 5.8. Schematic showing the deformation of polymer-salt aggregates at position $(x/\delta, y/\delta)$ keeping x/δ at 0.5.

5.3.4. Impact of high shear zone on polymer-salt aggregates elongation

To determine the effect of high shear zone, Pohlhausen approximate solution⁶² was considered to study the impact of high shear zone. Based on the geometry, a 50 micron dimension in height was assumed. Considering laminar and transitional flow ($Re \sim 10^5 - 3 \times 10^6$)⁶³, we calculated that the transitional flow ranges upto 400 micron in X direction. The boundary layer thickness was ~ 8 micron which is 16 % of the height of the high shear zone. Our calculations using Pohlhausen approximate solution depicts the deformation of polymer-salt aggregate at various regions in high shear zone. Three regions (A, B, and C) have been chosen to show the deformation of polymer salt aggregate. Region A is the below the boundary layer ($y/\delta < 1.0$), region B at the boundary layer ($y/\delta = 1.0$), and region C ($y/\delta > 1.0$). Pohlhausen approximate solution calculations for the high shear zone are explained in the next section.

Pohlhausen approximate solution. Considering a laminar flow with the pressure gradient as a parameter, Pohlhausen assumes a fourth order polynomial for the

dimensionless velocity distribution as a function of $\eta' = y/\delta(x)$ with the pressure gradient (Λ) as a parameter. Where $\Lambda = -\frac{dp}{dx} \frac{\delta}{\mu \frac{V_0}{\delta}}$, dp/dx is the pressure drop. The

velocity profile can be expressed as

$$\frac{u}{V_0} = (2\eta' - 2(\eta')^3 + (\eta')^4) + \frac{\Lambda}{6}(\eta' - 3(\eta')^2 + 3(\eta')^3 - (\eta')^4) \quad (E.14)$$

To track the position of the particle, the velocity (u) obtained from E.10 was integrated over dimensionless time (τ). If the polymer-salt aggregate is in region A (below boundary layer, Fig 5.9), it undergoes deformation and transforms to elongated polymer-salt aggregate. Considering, polymer-salt aggregate in the region B (at the boundary layer), it almost remains spherical with only small distortion. Polymer-salt aggregate in the region C (above boundary layer) has no impact, since the polymer-salt aggregates undergoes stress in all the directions (no velocity gradient), keeping the particle intact. Elongation is observed in region A since the fluid motion is laminar and has gradient in velocity flow. This study clearly indicated the impact of high shear zone significantly. The impact zone as shown in Fig 5.4 is the place where high turbulent mixing of materials takes place.

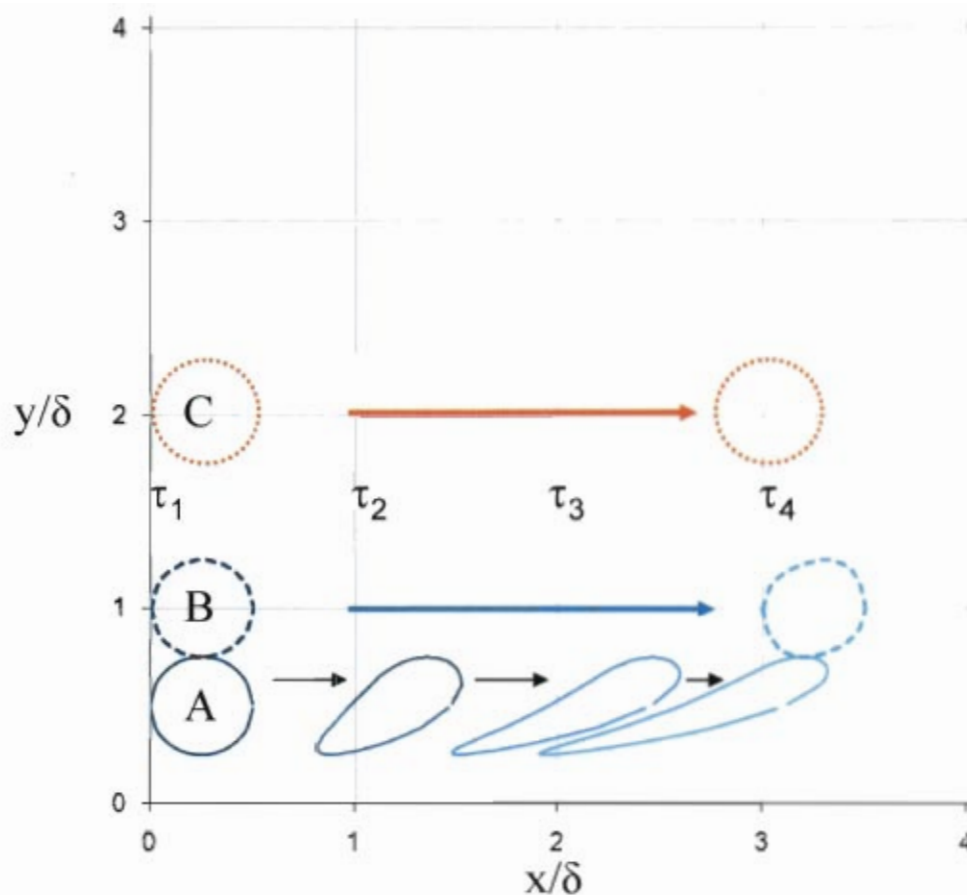


Figure 5.9. Schematic showing the deformation of polymer-salt aggregates at various positions (x/δ , y/δ) in high shear-zone.

5.3.5. Effect of polymer-salt aggregate size.

A similar analysis as performed on 1.5 micron size particles were carried out on 1.0 micron polymer-salt aggregate size particle to see the effect of initial particle size of polymer – salt aggregates. As shown in Fig. 5.10 (c, d) shows the formation of elongated NACs at 10K, and 20K PSI pressure. Selectivity of non-spherical NACs increases when polymer-salt aggregates are subjected to increasing to increasing shear and elongation stresses. Surprisingly, elongated NACs didn't appear when 5K PSI pressure applied.

Elongated NACs are formed when applied pressure was 10K and 20K PSI respectively. The selectivity of NACs-E at 5K, 10K and 20K PSI applied pressures is 0 %, 18 %, and 85 % respectively. A thorough analysis was carried out to explain the trends of the length and width elongation of NACs for the various applied pressures. Approximately 300 particles obtained from SEM images were analyzed to calculate average dimension of elongated NACs.

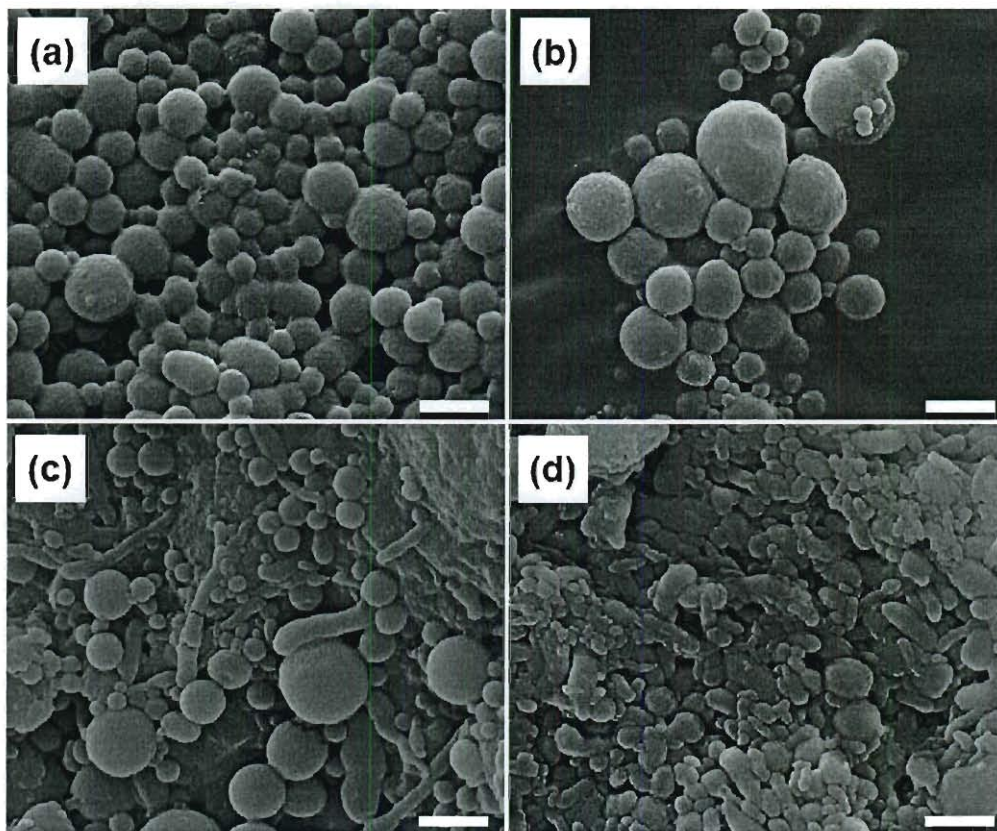


Figure 5.10. SEM images of elongated NACs formed by subjecting polymer-salt aggregates to various to (a) 0K, (b) 5K, (c) 10K, (d) 20K PSI pressure. Approximately 300 particles were counted on the SEM images using ImagePro software to determine the particle size of spherical NACs shown in (a) (mean particle size is 1.0 micron with a relative standard deviation of 33)Initial particle size of polymer- salt aggregate is 1.0 micron. Scale bar is 5 micron

The average lengths for 10K and 20K PSI samples are 1.66, and 1.13 microns respectively. The average width for 10K and 20K PSI samples are is 0.45 micron. A log-normal fitting was performed on the experimental data to determine the trends in the distribution. It can be clearly distinguished that in Fig. 5.11 (a, b). The L/W (length to width) ratio for 10K and 20K PSI samples are 3.68, and 2.51. The decrease in L/W with respect to pressure is similar to the trend observed in the earlier case. We hypothesize polymer-salt aggregate break as we increase the pressure as explained in our previous sections.

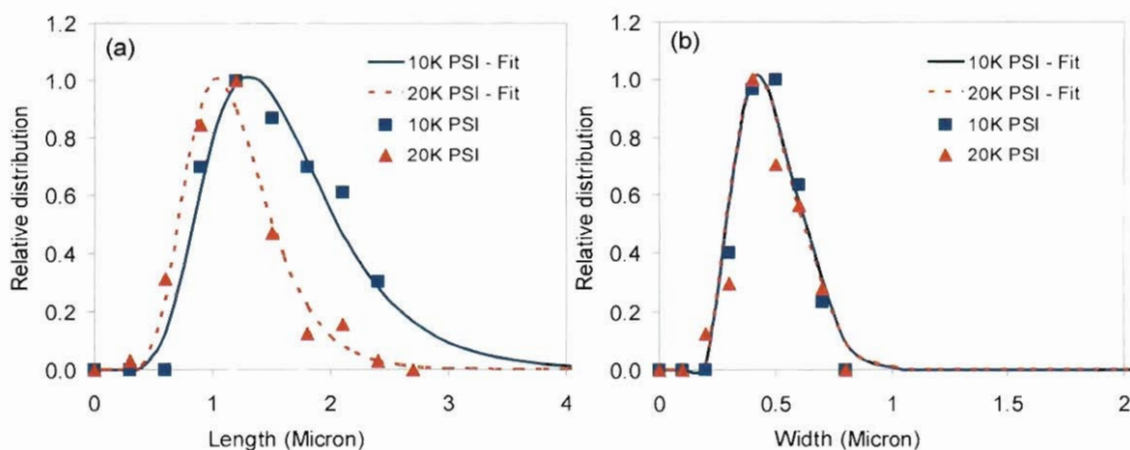


Figure 5.11. (a) Relative distribution plots for length (a) and width (b) for 5K, 10K, 20K PSI pressure along with log-normal fits respectively.

Fig. 5.12 shows the % of elongated NACs at various applied pressures for two different starting materials of PS aggregates. Also, for smaller particle of PS aggregates (1 micron) they undergo elongation at higher elongation/shear rates. A controlled experiment was carried to test the elastic behavior of PS aggregates. PS aggregates were passed through microfluidizer for 20 strokes and collected in a beaker and then 1.2 wt %

of silica NPs are added to them. Surprisingly, optical images revealed that it formed spherical NACs (supporting Fig. C.4). The formation of spherical NACs reveals the elastic behavior of PS aggregates. PS aggregates undergo elongation in microfluidizer, they retract back to its spherical shape after it is collected in the beaker, resulting in the formation of spherical NACs.

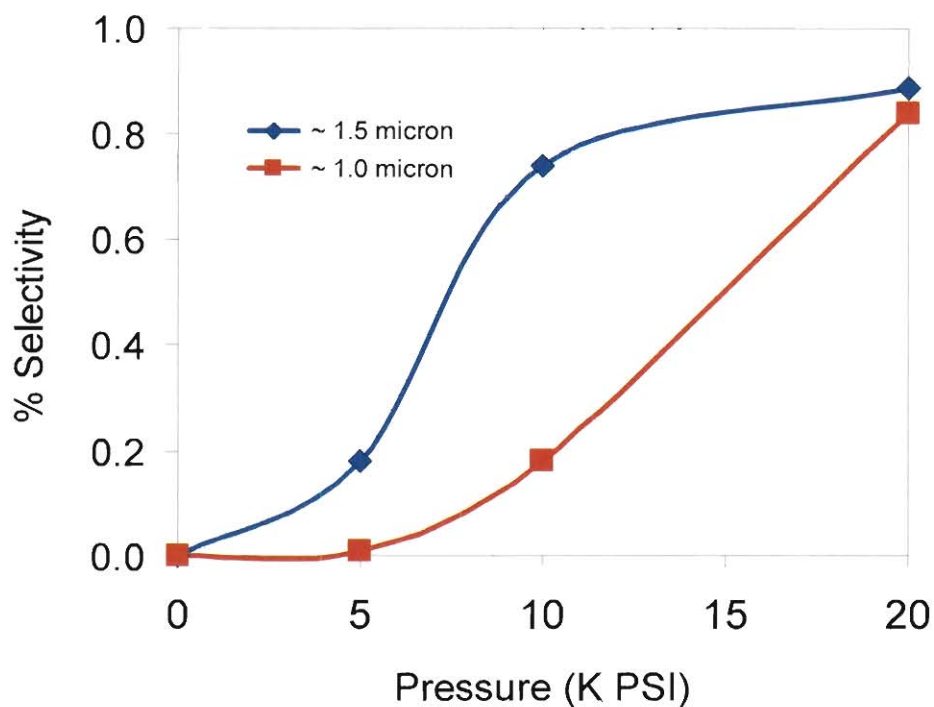


Figure 5.12. Selectivity vs. Pressure for 5K, 10K, 20K PSI pressure along for initial polymer-salt aggregate size of 1.5 and 1 microns.

5.3.5. Formation of polymer composite micro-wires.

Recipe is the exact same as the previous case of Silica - NACs, only Snowtex is replaced with polystyrene sulfonate ($[\text{PSS}]_{\text{initial}} = 1 \text{ mg/mL}$). Spherical PSS-NACs were

formed when NACs were synthesized in a beaker. In Fig. 5.13 a, it is observed that NACs made of PSS buckle as they are dried on a SEM stub. It is hypothesized that NACs made of PSS are not robust like silica-NACs. They are very soft and easy to buckle upon drying. Polymer-salt aggregates were subjected to undergo shear and elongations rate and subsequently PSS was added and are passed in the microfluidizer for 20 strokes.

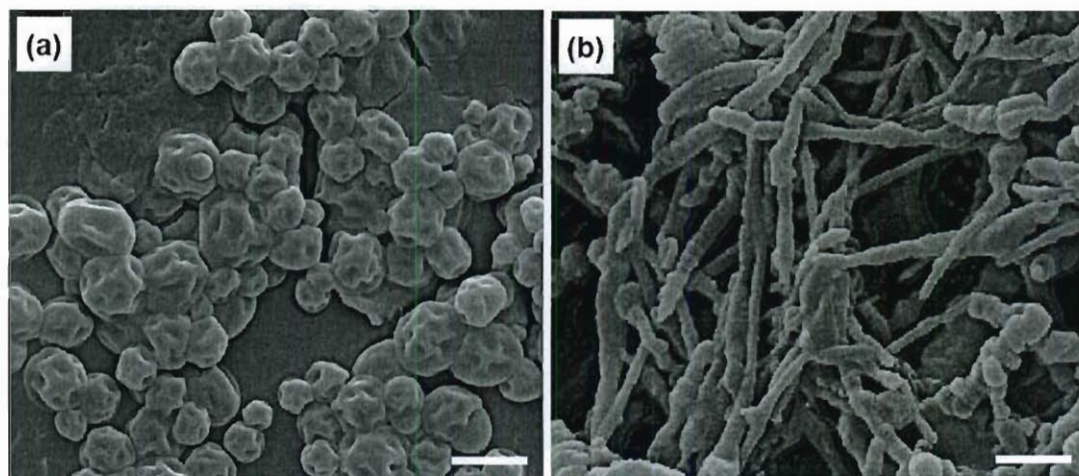


Figure 5.13. (a) SEM images of NACs formed by PSS as shell material, (b) Micro-wires formed by subjecting polymer-salt aggregates to elongation/shear and followed by addition of PSS and subjecting to elongation/shear.

This resulted in the formation for polymer- salt composite micro wires. PSS is a very soft material and can easily undergo elongation even after cross linking with PAH (Fig. 5.13b). Unlike silica NPs which would cross link with PAH and stops the further elongation of NACs.

5.4. Conclusions

In this work, we focus on subjecting the polymer-salt aggregates to shear and elongation flow and elongate them and generate elongated NACs. With these hybrid

structures taking on the shape of the polyamine-salt aggregate precursors, it is hypothesized that shape anisotropy can be induced through manipulation of fluid flow in a "microfluidizer." Our results show that elongated NACs of various lengths (1 μm to 8 μm) can be generated by varying the process parameters such as velocity of fluid flow (250 m/s to 500 m/s). Selectivity of elongated vs spherical can be reached as high as 90%. The elongation of polymer-salt aggregates and resulting in the formation of elongated NACs happens by two phenomena i.e by elongation rate and shear rate generated due the dimensions of microfluidic interaction chamber or Y-junction geometry, and high shear zone .A fluid mechanics model has been developed to quantify the extensional and shear rates at various locations in the microfluidizer chamber. Non-spherical NACs could possibly offer unique properties by comparison to spherical NACs.

Notation

ψ = Stream function

D= Drag force

D_0 =Duct diameter

L= Characteristic length

L_1 = Length of the duct

U_x, U_y = Velocities in x and y axis respectively.

V_0 = Upstream velocity.

B = Proportionality constant, see E.27

x,y = components, parallel and normal to the interface solid-fluid

$W=2 \pi D_0$

δ = Thickness of the boundary layer

$d\gamma/dt$ = shear rate

μ = viscosity

ρ = density

$\nu = \mu/\rho$, Kinematic viscosity

5.5. References

1. Yaseen, M. A.; Yu, J.; Jung, B. S.; Wong, M. S.; Anvari, B., Biodistribution of Encapsulated Indocyanine Green in Healthy Mice. *Molecular Pharmaceutics* **2009**, *6*, (5), 1321-1332.
2. Tavera, E. M.; Kadali, S. B.; Bagaria, H. G.; Liu, A. W.; Wong, M. S., Experimental and Modeling Analysis of Diffusive Release from Single-Shell Microcapsules. *Aiche Journal* **2009**, *55*, (11), 2950-2965.
3. Plush, S. E.; Woods, M.; Zhou, Y. F.; Kadali, S. B.; Wong, M. S.; Sherry, A. D., Nanoassembled Capsules as Delivery Vehicles for Large Payloads of High Relaxivity Gd³⁺ Agents. *Journal of the American Chemical Society* **2009**, *131*, (43), 15918-15923.
4. Murthy, V. S.; Kadali, S. B.; Wong, M. S., Polyamine-Guided Synthesis of Anisotropic, Multicompartment Microparticles. *Acs Applied Materials & Interfaces* **2009**, *1*, (3), 590-596.
5. Kadali, S. B.; Soutanidis, N.; Wong, M. S., Assembling Colloidal Silica into Porous Hollow Microspheres. *Topics in Catalysis* **2008**, *49*, (3-4), 251-258.
6. Yu, J.; Murthy, V. S.; Rana, R. K.; Wong, M. S., Synthesis of nanoparticle-assembled tin oxide/polymer microcapsules. *Chemical Communications* **2006**, (10), 1097-1099.
7. Murthy, V. S.; Rana, R. K.; Wong, M. S., Nanoparticle-assembled capsule synthesis: Formation of colloidal polyamine-salt intermediates. *Journal of Physical Chemistry B* **2006**, *110*, (51), 25619-25627.
8. Rana, R. K.; Murthy, V. S.; Yu, J.; Wong, M. S., Nanoparticle self-assembly of hierarchically ordered microcapsule structures. *Advanced Materials* **2005**, *17*, (9), 1145-+.
9. Murthy, V. S.; Cha, J. N.; Stucky, G. D.; Wong, M. S., Charge-driven flocculation of poly(L-lysine)-gold nanoparticle assemblies leading to hollow microspheres. *Journal of the American Chemical Society* **2004**, *126*, (16), 5292-5299.
10. Kini, G. C.; Lai, J.; Wong, M. S.; Biswal, S. L., Microfluidic Formation of Ionically Cross-Linked Polyamine Gels. *Langmuir* **2004**, *20*, (9), 6650-6656.

11. Zhao, N.; Bagaria, H.; Wong, M.; Zu, Y., A nanocomplex that is both tumor cell-selective and cancer gene-specific for anaplastic large cell lymphoma. *Journal of Nanobiotechnology* **9**, (1), 2.
12. Bonderer, L. J.; Studart, A. R.; Gauckler, L. J., Bioinspired design and assembly of platelet reinforced polymer films. *Science* **2008**, 319, (5866), 1069-1073.
13. Murray, M. J.; Snowden, M. J., The preparation, characterisation and applications of colloidal microgels. *Advances in Colloid and Interface Science* **1995**, 54, 73-91.
14. Shekunov, B. Y.; Chattopadhyay, P.; Tong, H. H. Y.; Chow, A. H. L., Particle size analysis in pharmaceuticals: Principles, methods and applications. *Pharmaceutical Research* **2007**, 24, (2), 203-227.
15. Yamamoto, S.; Matsuoka, T., VISCOSITY OF DILUTE SUSPENSIONS OF RODLIKE PARTICLES - A NUMERICAL-SIMULATION METHOD. *Journal of Chemical Physics* **1994**, 100, (4), 3317-3324.
16. Williams, P. S.; Carpino, F.; Zborowski, M., Magnetic Nanoparticle Drug Carriers and Their Study by Quadrupole Magnetic Field-Flow Fractionation. *Molecular Pharmaceutics* **2009**, 6, (5), 1290-1306.
17. Zhang, L.; Gu, F. X.; Chan, J. M.; Wang, A. Z.; Langer, R. S.; Farokhzad, O. C., Nanoparticles in Medicine: Therapeutic Applications and Developments. *Clin Pharmacol Ther* **2007**, 83, (5), 761-769.
18. Goldsmith, H. L.; Turitto, V. T., Rheological aspects of thrombosis and haemostasis: basic principles and applications. ICTH-Report--Subcommittee on Rheology of the International Committee on Thrombosis and Haemostasis. *Thrombosis and haemostasis* **1986**, 55, (3), 415-435.
19. Wolf, B.; Frith, W. J.; Singleton, S.; Tassieri, M.; Norton, I. T., Shear behaviour of biopolymer suspensions with spheroidal and cylindrical particles. *Rheologica Acta* **2001**, 40, (3), 238-247.
20. Liu, S. J.; Masliyah, J. H., Rheology of suspensions. *Suspensions: Fundamentals and Applications in the Petroleum Industry* **1996**, 251, 107-176.

21. Donev, A.; Cisse, I.; Sachs, D.; Variano, E. A.; Stillinger, F. H.; Connelly, R.; Torquato, S.; Chaikin, P. M., Improving the Density of Jammed Disordered Packings Using Ellipsoids. *Science* **2004**, 303, (5660), 990-993.
22. Gupta, S.; Zhang, Q.; Emrick, T.; Russell, T. P., "Self-Corralling" Nanorods under an Applied Electric Field. *Nano Letters* **2006**, 6, (9), 2066-2069.
23. Hwang, D. K.; Dendukuri, D.; Doyle, P. S., Microfluidic-based synthesis of non-spherical magnetic hydrogel microparticles. *Lab on a Chip* **2008**, 8, (10), 1640-1647.
24. Yoshida, M.; Roh, K.-H.; Lahann, J., Short-term biocompatibility of biphasic nanocolloids with potential use as anisotropic imaging probes. *Biomaterials* **2007**, 28, (15), 2446-2456.
25. Hull, D., An introduction to composite materials. *An Introduction to Composite Materials* **2004**.
26. Dendukuri, D.; Pregibon, D. C.; Collins, J.; Hatton, T. A.; Doyle, P. S., Continuous-flow lithography for high-throughput microparticle synthesis. *Nature Materials* **2006**, 5, (5), 365-369.
27. Champion, J. A.; Mitragotri, S., Role of target geometry in phagocytosis. *Proceedings of the National Academy of Sciences of the United States of America* **2006**, 103, (13), 4930-4934.
28. Dendukuri, D.; Tsoi, K.; Hatton, T. A.; Doyle, P. S., Controlled synthesis of nonspherical microparticles using microfluidics. *Langmuir* **2005**, 21, (6), 2113-2116.
29. Manoharan, V. N.; Elsesser, M. T.; Pine, D. J., Dense packing and symmetry in small clusters of microspheres. *Science* **2003**, 301, (5632), 483-487.
30. Yin, Y.; Xia, Y., Self-assembly of monodispersed spherical colloids into complex aggregates with well-defined sizes, shapes, and structures. *Advanced Materials* **2001**, 13, (4), 267-271.
31. Shinde Patil, V. R.; Campbell, C. J.; Yun, Y. H.; Slack, S. M.; Goetz, D. J., Particle diameter influences adhesion under flow. *Biophysical Journal* **2001**, 80, (4), 1733-1743.

32. Pillai, O.; Panchagnula, R., Polymers in drug delivery. *Current Opinion in Chemical Biology* **2001**, 5, (4), 447-451.
33. Moghimi, S. M.; Hunter, A. C.; Murray, J. C., Long-circulating and target-specific nanoparticles: Theory to practice. *Pharmacological Reviews* **2001**, 53, (2), 283-318.
34. May, R. C.; Machesky, L. M., Phagocytosis and the actin cytoskeleton. *Journal of Cell Science* **2001**, 114, (6), 1061-1077.
35. Lamprecht, A.; SchÄ¶fer, U.; Lehr, C. M., Size-dependent bioadhesion of micro- and nanoparticulate carriers to the inflamed colonic mucosa. *Pharmaceutical Research* **2001**, 18, (6), 788-793.
36. Berkland, C.; Kim, K.; Pack, D. W., Fabrication of PLG microspheres with precisely controlled and monodisperse size distributions. *Journal of Controlled Release* **2001**, 73, (1), 59-74.
37. Rolland, J. P.; Maynor, B. W.; Euliss, L. E.; Exner, A. E.; Denison, G. M.; DeSimone, J. M., Direct Fabrication and Harvesting of Monodisperse, Shape-Specific Nanobiomaterials. *Journal of the American Chemical Society* **2005**, 127, (28), 10096-10100.
38. Xu, S.; Nie, Z.; Seo, M.; Lewis, P.; Kumacheva, E.; Stone, H. A.; Garstecki, P.; Weibel, D. B.; Gitlin, I.; Whitesides, G. M., Generation of monodisperse particles by using microfluidics: Control over size, shape, and composition. *Angewandte Chemie - International Edition* **2005**, 44, (5), 724-728.
39. Ho, C. C.; Keller, A.; Odell, J. A.; Ottewill, R. H., Preparation of monodisperse ellipsoidal polystyrene particles. *Colloid & Polymer Science* **1993**, 271, (5), 469-479.
40. Goode, B. L.; Drubin, D. G.; Barnes, G., Functional cooperation between the microtubule and actin cytoskeletons. *Current Opinion in Cell Biology* **2000**, 12, (1), 63-71.
41. Dunne, M.; Corrigan, O. I.; Ramtoola, Z., Influence of particle size and dissolution conditions on the degradation properties of polylactide-co-glycolide particles. *Biomaterials* **2000**, 21, (16), 1659-1668.

42. Uhrich, K. E.; Cannizzaro, S. M.; Langer, R. S.; Shakesheff, K. M., Polymeric Systems for Controlled Drug Release. *Chemical Reviews* **1999**, 99, (11), 3181-3198.
43. Zambaux, M. F.; Bonneaux, F.; Gref, R.; Maincent, P.; Dellacherie, E.; Alonso, M. J.; Labrude, P.; Vigneron, C., Influence of experimental parameters on the characteristics of poly(lactic acid) nanoparticles prepared by a double emulsion method. *Journal of Controlled Release* **1998**, 50, (1-3), 31-40.
44. Park, T. G.; Lee, H. Y.; Nam, Y. S., A new preparation method for protein loaded poly(D,L-lactic-co-glycolic acid) microspheres and protein release mechanism study. *Journal of Controlled Release* **1998**, 55, (2-3), 181-191.
45. Edwards, D. A.; Hanes, J.; Caponetti, G.; Hrkach, J.; Ben-Jebria, A.; Eskew, M. L.; Mintzes, J.; Deaver, D.; Lotan, N.; Langer, R., Large porous particles for pulmonary drug delivery. *Science* **1997**, 276, (5320), 1868-1871.
46. Storm, G.; Belliot, S. O.; Daemen, T.; Lasic, D. D., Surface modification of nanoparticles to oppose uptake by the mononuclear phagocyte system. *Advanced Drug Delivery Reviews* **1995**, 17, (1), 31-48.
47. Stolnik, S.; Illum, L.; Davis, S. S., Long circulating microparticulate drug carriers. *Advanced Drug Delivery Reviews* **1995**, 16, (2-3), 195-214.
48. Gref, R.; Minamitake, Y.; Peracchia, M. T.; Trubetskoy, V.; Torchilin, V.; Langer, R., Biodegradable long-circulating polymeric nanospheres. *Science* **1994**, 263, (5153), 1600-1603.
49. Tabata, Y.; Ikada, Y., Phagocytosis of polymer microspheres by macrophages. *Advances in Polymer Science* **1990**, 94, 106-141.
50. Langer, R., New methods of drug delivery. *Science* **1990**, 249, (4976), 1527-1533.
51. Poste, G.; Kirsh, R., Site-specific (targeted) drug delivery in cancer therapy. *Bio/Technology* **1983**, 1, (10), 869-878.
52. Hsieh, D. S. T.; Rhine, W. D.; Langer, R., Zero-order controlled-release polymer matrices for micro- and macromolecules. *Journal of Pharmaceutical Sciences* **1983**, 72, (1), 17-22.

53. Illum, L.; Davis, S. S.; Wilson, C. G., Blood clearance and organ deposition of intravenously administered colloidal particles. The effects of particle size, nature and shape. *International Journal of Pharmaceutics* **1982**, 12, (2-3), 135-146.
54. Champion, J. A.; Katare, Y. K.; Mitragotri, S., Particle shape: A new design parameter for micro- and nanoscale drug delivery carriers. *Journal of Controlled Release* **2007**, 121, (1-2), 3-9.
55. <http://www.microfluidicscorp.com/images/stories/pdf/m-110s.pdf>.
56. Hansen, A., G. , Similarity Analyses of Boundary Value Problems in Engineering. *Prentice Hall* **1964**.
57. Brodkey, R. S., The phenomena of fluid Motions. *Lightning Source Inc.(US)* **2005**.
58. Panagiotou, T.; Mesite, S. V.; Fisher, R. J., Production of Norfloxacin Nanosuspensions Using Microfluidics Reaction Technology through Solvent/Antisolvent Crystallization. *Industrial & Engineering Chemistry Research* **2009**, 48, (4), 1761-1771.
59. http://www.microfluidicscorp.com/images/stories/pdf/whitepapers/polymers_08.pdf.
60. Panagiotou, T.; Fisher, R. J., Form Nanoparticles via Controlled Crystallization. *Chemical Engineering Progress* **2008**, 104, (10), 33-39.
61. Zhao, X. Y., Drop breakup in dilute Newtonian emulsions in simple shear flow: New drop breakup mechanisms. *Journal of Rheology* **2007**, 51, (3), 367-392.
62. Schobeiri, M., T., Fluid Mechanics for Engineers. *Springer* **2010**, 368.
63. Cengel A, Y.; Cimbala, M., John., Fluid Mechanics. *Mcgraw Hill* **2006**, 514.

Chapter 6. Summary and recommendations for future work

We recently developed a materials synthesis technique in which synthetic polyamines such as polyallylamine and/or polylysine were crosslinked with multivalent anions like citrate to form polymer-salt aggregates, that then served as templates for deposition of nanoparticles to form micron-sized hollow spheres or "nanoparticle-assembled capsules" (NACs) also referred as polymer-salt assembly (PSA). This electrostatically-driven route is carried out in water, at mild pH and room temperature, making it attractive for encapsulation and scale-up in comparison to other techniques like layer-by-layer assembly and related sacrificial templating routes (which are labor-intensive and expensive to scale up). Another encouraging aspect of NACs is the flexibility in design of materials to tailor them for specific applications. NACs can potentially find wide-ranging applications in pharmaceutical, food, and consumer industries by serving as miniature containers to store, deliver, and release substances. Although synthesis of NACs is well understood, less attention has been paid to their structural properties and stability. Comparatively, little has been done to assess the physical properties of NACs under varying pH and ionic strength conditions. This dissertation involved in studying the effects of pH, ionic strength, and nature of the multivalent anions. The concept of enhanced stability of NACs using multivalent anions has been demonstrated. This concept could be extended to other charge mediated assembly to make microcapsules. Mechanical strength of NACs was studied through osmotic pressure testing. Elongated NACs have been synthesized by applying shear and elongation stresses on polymer-salt aggregates. Encapsulation studies have been carried on NACs. A new approach to determine the diffusion coefficient of molecules in polymer-films has been proposed.

6.1. Recommendations

Results presented in this dissertation are encouraging and lead to the establishment of several recommendations for future work:

6.1.1. Mechanical properties of single NAC using molecular force probe technique

The elasticity and mechanical stability of the NACs are of crucial importance for a variety of practical applications and use. While most applications may require that NACs not disassemble or deform under shear stress, some may require triggered release under specific conditions to release the encapsulated material (e.g., drug delivery). At present, however, the mechanical properties of the capsules are known by studying the bulk properties of NACs by probing with polyelectrolytes. Understanding the mechanical properties would help us to engineer the material according to the applications such as encapsulation of cargo molecules for drug delivery or potential usage as a catalyst support material. Therefore, the goal of this would be to determine the mechanical properties, in particular the Young's modulus of NACs of various formulations. At a more fundamental level, this study will also help us gain a better understanding between the electrostatic assembly of various polymer/NP compositions and the corresponding mechanical properties.

It would be interesting to know whether our NACs undergo a purely elastic response of the shell wall towards deformations i.e the capsules should fully collapse once the pressure is higher than the buckling threshold or plastic deformation in which the plastic deformations of the material limits the growth of the buckled zone. Experimental demonstration is shown in Figure 6.1. Depending on the application, NACs may be used

either in a wet or dry state. From our experience we know that NACs would be soft (squishy) when wet, and brittle (crunchy) when dried. It would therefore be interesting to know the range of Young's modulus between these conditions. Further in the wet conditions, pH and ionic strength (which affect the structure of NACs) would strongly influence the mechanical properties of NACs. The results from these studies, where we plan to systematically vary each of these parameters, will enable us to compare NACs with capsules made by layer-by-layer (LbL) assembly approach, which have a reported Young's modulus between 500 to 750 MPa.

Two methods have recently been reported to characterize the mechanical properties of microcapsules. The first involves the controlled application of osmotic pressure by introducing polyelectrolytes like polystyrenesulfonate to exert forces on the microcapsules. While extremely simple, this method has two major drawbacks: (i) the magnitude of force that can be applied is limited by the solubility of the polyelectrolyte and (ii) the adsorption of the polyelectrolyte on the capsule may introduce artifacts. The other method of obtaining mechanical properties involves measuring the deformation of microcapsules under applied load using an Asylum MFP-3D Atomic Force Microscope system. This technique has several advantages including accuracy, the possibility of studying a wider range of materials, richer experimental information (force-deformation curves), superior control over the applied forces, a greater range of forces (10^{-11} and 10^{-6} N) and the possibility to change forces in situ.

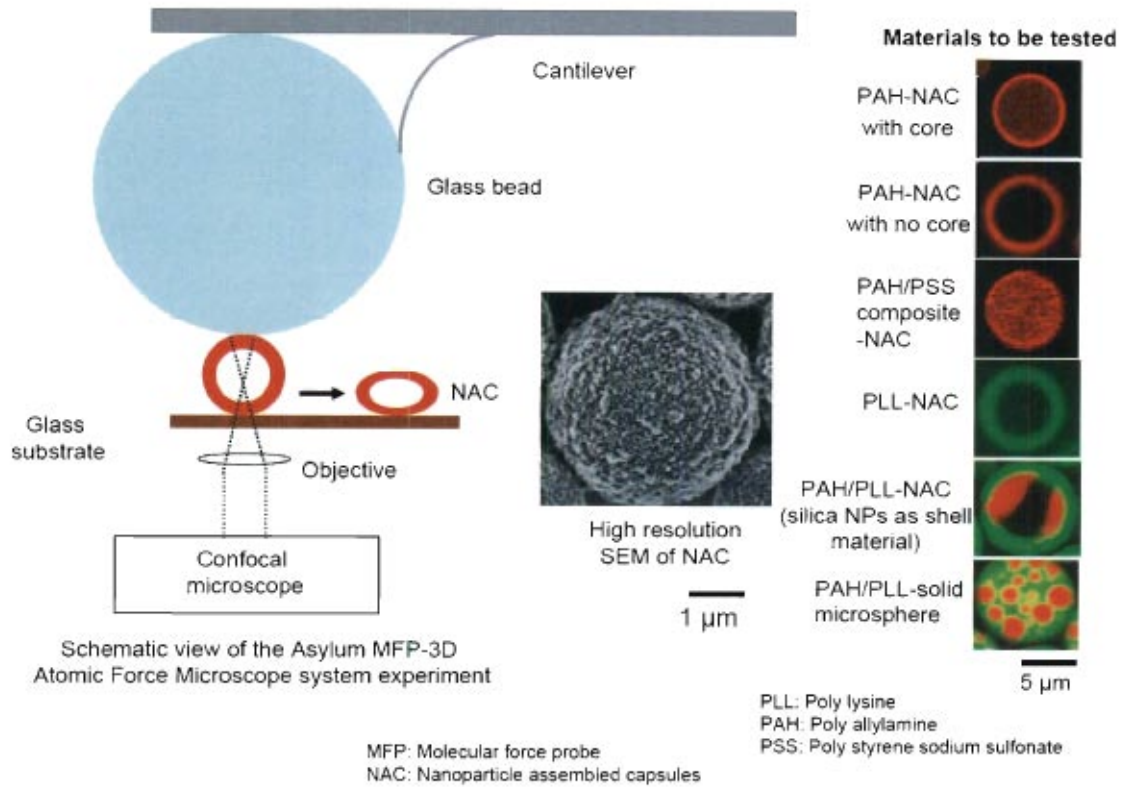


Figure 6. 1. Schematic showing the proposed experiment using Asylum MFP-3D atomic force microscopy.

MF3-D asylum AFM has a nanoindentation accessory, works only in dry conditions. It also has a fluid cell, and cantilever-based measurements are possible in fluid. This might give better Load (force) versus deformation curves, which are then back co-related to mechanical properties. The result of measurements from MF3-D represents the deflection (Δ) versus the position of the piezotranslator at a single approach (loading). The load F was determined from the cantilever deflection, $F = k * \Delta$, where k is the spring constant. The deformation is calculated as the difference between the position of the piezotranslator and cantilever deflection. Fitting the Load-deformation profiles for the NACs to equations reported by Lelevich et al., taking the Young's modulus E as a fitting

parameter, where F is the total reaction force (load) would provide information to determine its mechanical strength. Detailed information on Load-deformation force equation was given by Lulevich et al. A change in the formulation of either the core or the shell material, or even the absence of the core is expected to significantly affect the mechanical properties of NACs. Hence, in this project we are interested in studying how the strength of capsules is affected by exploring these degrees of freedom.

6.1.2. Concept of reverse charge assembly

It has been successfully shown in our earlier work that NACs assembly has been limited to cationic polymer, multivalent anions, and negatively charged or positively charged NPs. We are not aware if our NACs assembly could be made in a reverse assembly methodology, comprising of anionic polymer, multivalent cations, and negative or positively charged NPs. By proving the concept of reverse assembly, we can generalize our NP assembly chemistry. Also, our earlier work has shown that NACs cannot encapsulate positively charged compounds with greater loading. By the approach of reverse assembly, we hypothesize that we can achieve high loadings of positively charged compounds.

Preliminary results

The concept of making NACs using the reverse charge assembly has been demonstrated in our preliminary work as shown in Figure 6.2. The details of the synthesis are explained in experimental methods.

Experimental Methods

Materials: Poly(acrylic acid) solution (“PAA,” 100,000 g/mol, ~1400 acrylic units per molecule, 35 wt. % in water, Sigma-Aldrich), Ethylenediamine (EDA) was procured from J.T. Baker and a SiO₂ NP suspension (Snowtex-O type, 20.3 wt% SiO₂, pH 3.5, ionic strength I = 16.9 mM, Nissan Chemicals) and pH was adjusted using 150 mM HCl to a pH value of 5.5. Deionized water (18.2 MΩ, Barnstead Nanopure Diamond System) was used for the PAA and EDA stock solutions, and a HCl solution (1 N, Fisher Science) was diluted with deionized water to a pH value of 5.5. The SiO₂ NP suspension (NP diameter of 13±3 nm, according to dynamic light scattering; zeta potential of -25 mV, at pH 5.5 and I = 10 mM, calculated from electrophoretic mobility measurements using Henry’s equation).

Synthesis of NACs

An aqueous PAA solution (215 μL, 5 mg/mL) was mixed with an aqueous EDA solution (535 μL) in a 1.5 mL centrifuge vial and vortex mixed for 10 seconds at low speed (‘5’ speed on a 1-10 scale). For the *R* charge ratio of 0.125 studied in this work, the EDA concentration was 0.11 M, respectively. *R* is defined as the ratio of total number of negative charges from PAA to the total number of positive charges from the EDA. A turbid mixture immediately resulted, indicating the formation of PAA-EDA aggregates. This suspension was aged for 10 sec, before an aqueous SiO₂ NP suspension (535 μL; concentration of ~20.3 wt %) was added. The resultant mixture was stirred vigorously (at ‘7’ speed) for 10 sec and aged for 2 hrs. The resulting material is the silica/polymer microcapsules as shown in Figure 6.2.

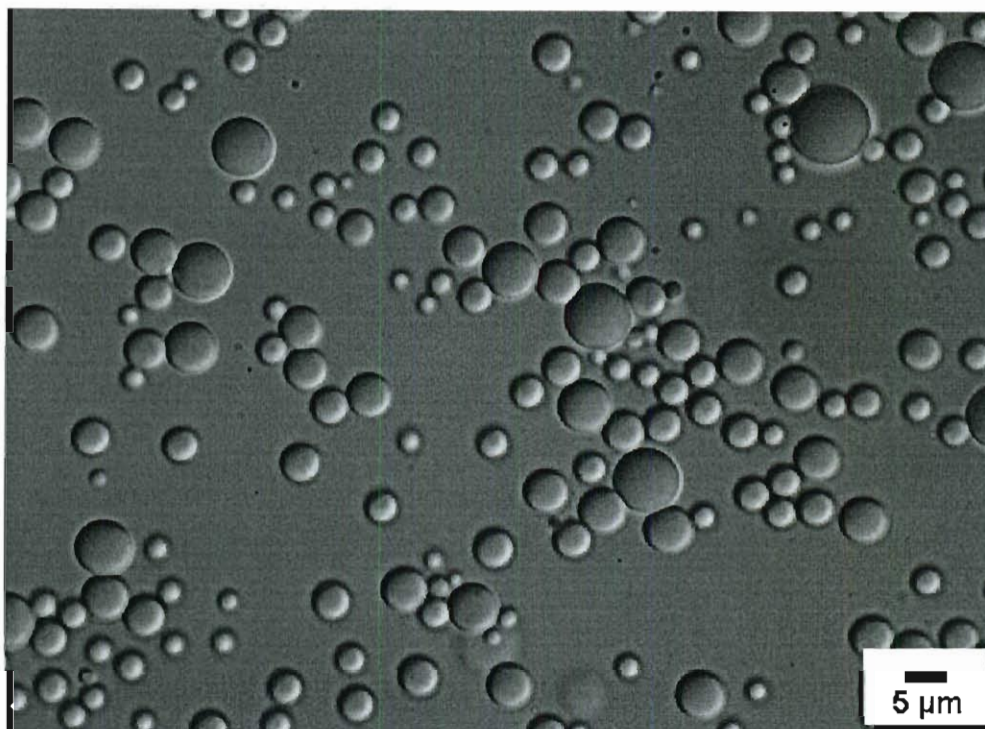


Figure 6. 2. Optical DIC image of PAA-EDA-Silica capsules

However, it is important to build this concept of reverse charge assembly and extend it to other anionic polymers and nanoparticles. Encapsulation studies of cationic compounds and their release property studies would be worth investigating.

6.1.3. Thermo-sensitive NACs

It would be very interesting to make thermo-sensitive NACs. Thermo-sensitive polymers such as poly (N-Isopropylacrylamide) (PNIPAAM) could be utilized to conjugate with cationic polymer PAH. An attempt should be made to synthesize NACs using conjugated PAH-PNIPAAM. It would be interesting to study encapsulation and

release properties with respect to temperature. This work would potentially have a great impact in the field of drug delivery.

6.1.4. NACs to encapsulate MRI contrast agents

In our earlier work in collaboration with Dr. Sherry, we have successfully shown that NACs could be potentially used to encapsulate MRI contrast agents and shown the enhancement in the relaxivity studies by 3-4 fold compared to bare contrast agent. Its worth studying the encapsulation of other MRI contrast agents and tuning the NACs properties (such as size, permeability) to further enhance relaxivity. Also, it would be ideal to make the NACs with non-toxic components.

Appendix A. Ionic strength and pH effects on nanoparticles-polyamine microcapsules

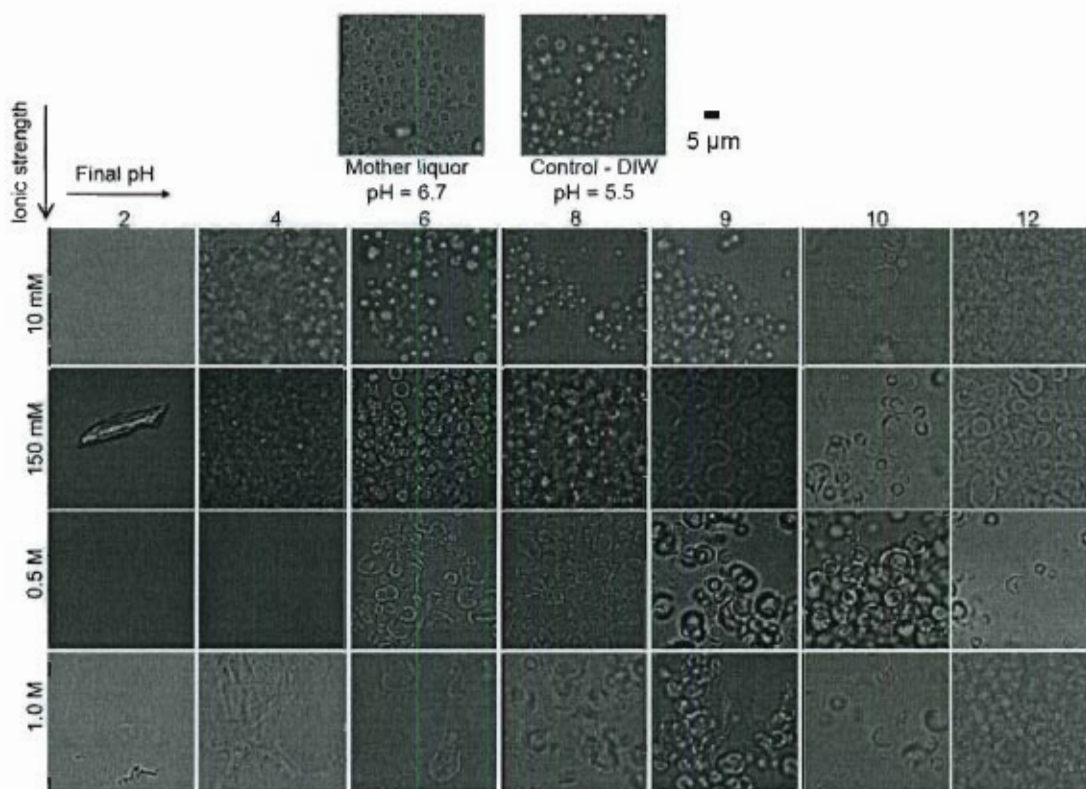


Figure A.1. Bright field microscopy images of NACs as made (mother liquor), in DI-water, suspended in various pH conditions from (L to R, pH range of 2-12) and various ionic strength solutions, 10 mM NaCl, 150 mM NaCl, 0.5 M NaCl, 1.0 M NaCl

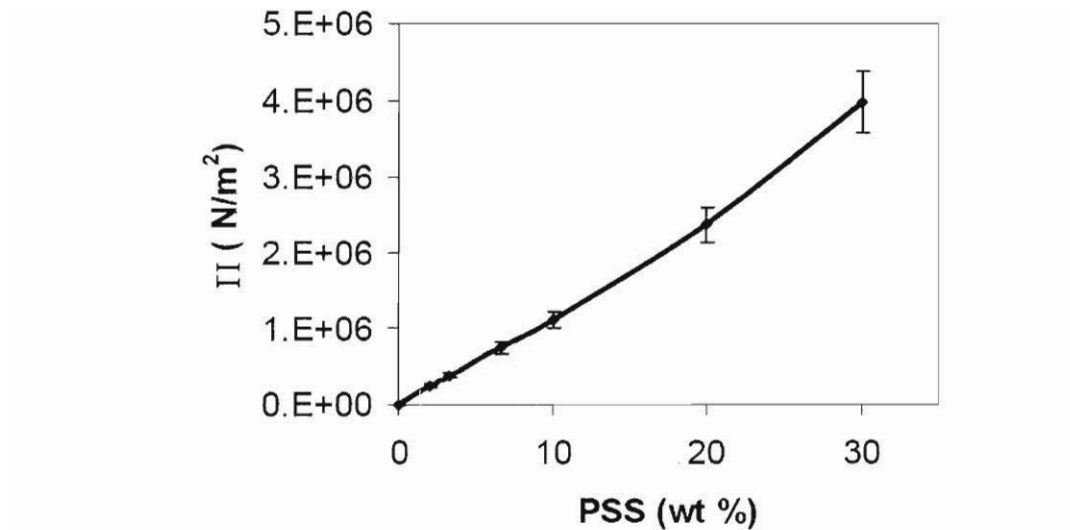


Figure A.2. Osmotic pressure calibration curve

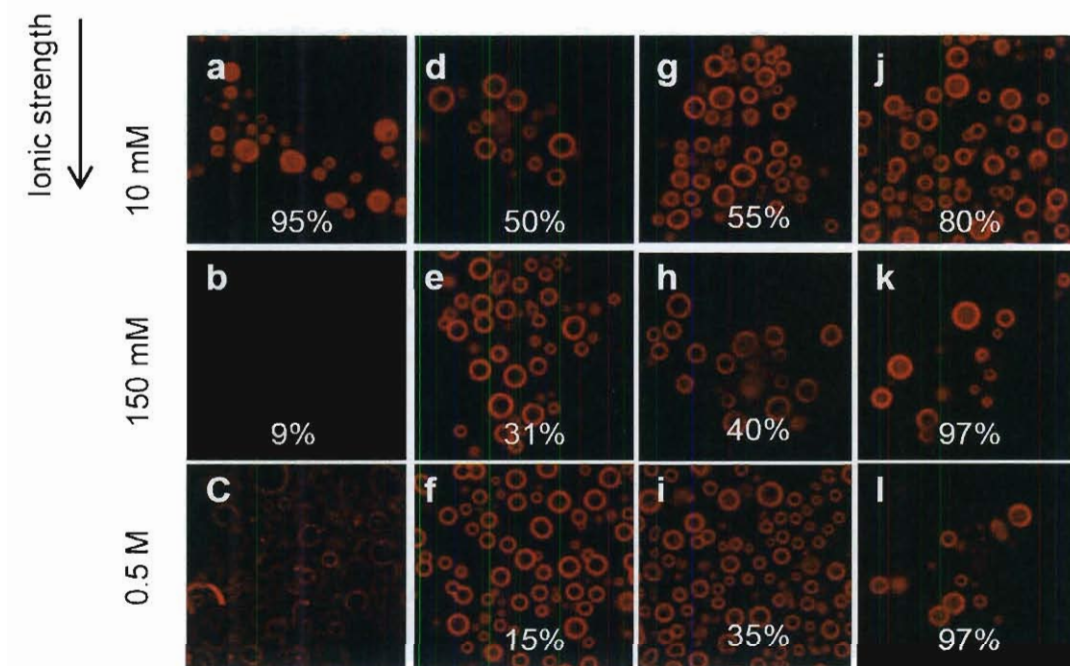


Figure A.3. Confocal microscopy images of NACs suspended in various ionic strength solutions (a-c) NaCl, (d-f) Phos.,(g-i) Sulf, (j-l) Cit.

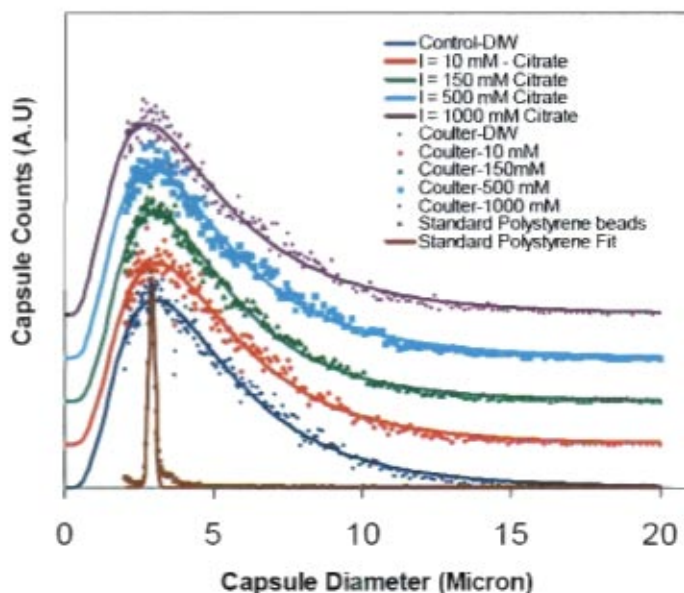


Table 1

Mean diameter (μm), ionic strength	Std.Dev. (μm)
5.32 (DIW)	3.37
5.36 (10 mM)	3.39
5.03 (150 mM)	3.18
5.20 (500 mM)	3.30
5.27 (1000 mM)	3.37
2.92 (Standard Polystyrene- 3 μ)	0.10

Figure A.4. Capsule diameter distributions of NACs obtained from Coulter counter measurements and the solid lines indicate distribution fit to lognormal distributions. Table 1: indicates the mean diameter and standard deviation for NACs suspended in DIW, 10 mM, 150 mM, 500 mM, 1000 mM ionic strength solutions using cit and pH maintained at 8.0.

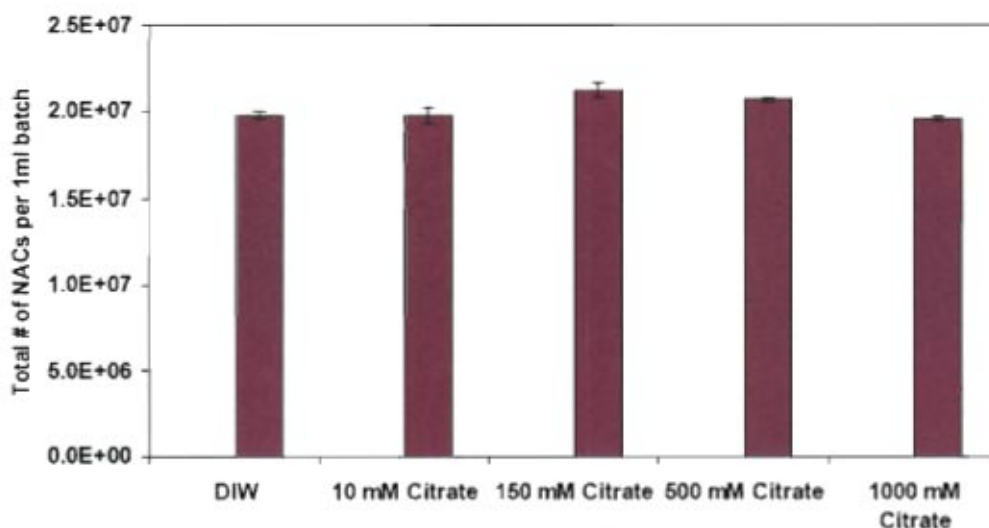


Figure A.5. Total # of NACs count NACs obtained from Coulter counter measurements. NACs suspended in DIW, 10 mM, 150 mM, 500 mM, 1000 mM ionic strength solutions using cit and pH maintained at 8.0.

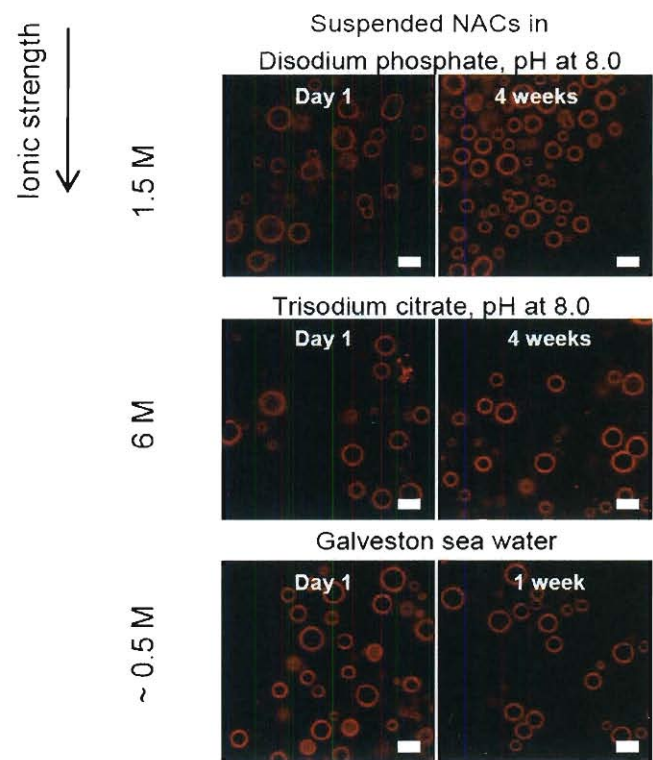


Figure A.6. Confocal microscopy images of NACs suspended in phos (ionic strength 1.5M, molar concentration of phos is 0.5M) and cit (ionic strength 6M, molar concentration of cit is 1M) for 1 day and 4 weeks, pH maintained at 8.0, and in sea water (Gulf of Mexico, Galveston, Tx, USA) for 1 day and 1 week.

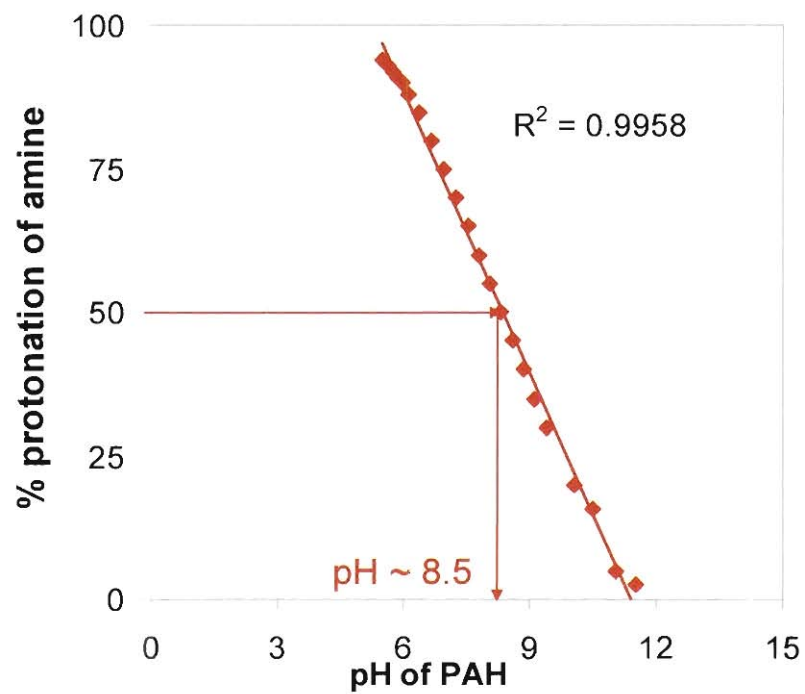


Figure A.7. Percentage protonation of amine group vs pH of PAH solution. pH= pKa when % protonation is 50.

Appendix B. Quartz crystal microbalance-(QCM-D) for determining diffusion coefficient of various molecules in polymer-salt film systems¹

Introduction

Polymer-films have been extensively used for various applications biomedical, tissue engineering, semiconductor manufacturing and fuel cell membranes¹⁻²¹. It is crucial to determine the diffuse of various molecules such as drugs/nanoparticles/ through these films and to know the time scales^{1, 17, 22, 23}. In this work, we propose a new approach in determining the diffusion coefficient in polymer-films through QCM-D²⁴. The purpose of this experiment was to monitor the diffusion of a model molecule, Sodium-fluorescein (Na-Flu), into a polymer-salt matrix through the use of a quartz crystal microbalance with dissipation monitoring (QCM-D). It enables the measurement of mass and viscoelastic property changes over time of a material deposited on a quartz crystal resonator, which is a flat disk made of quartz crystal with electrodes on the surface of the crystal. Polymer-salt films were developed for ~ 25 hours, prior to the flow of Na-Flu. Based on the dissipation values the film could be considered a rigid, non-viscoelastic film and the Sauerbrey model could be used for mass and thickness calculations. The calculated thickness of the deposited PAH/cit film was ~150 nm after 25 hours, as estimated by both the Sauerbrey model²⁴. To perform the quantitative analysis, a molecular transport in one dimension was assumed and using Fick's second law, the mass diffused with respect to time was modeled. The diffusion coefficient was found to be $\sim 10^{-19}$ m²/sec. This is in

¹ This work was done in collaboration with Amy W. Liu, Enrique M. Tavera, and Michael S. Wong

good agreement with what has already been reported for diffusion of rhodamine in polyelectrolyte films²⁵.

Experimental Methods

Materials

Polyallylamine hydrochloride (PAH, 56,000 g/mol, ~600 allylamine units per molecule), fluorescein sodium salt, was purchased from Sigma-Aldrich. Trisodium citrate dihydrate salt (citrate), NaOH pellets and 1 N HCl solution were obtained from Fisher Scientific. H₂AuCl₄ solution (0.25 M; AuCl₃ 99.99%, Sigma-Aldrich). An aqueous colloidal suspension of silica NPs (Snowtex-O, 20.5 wt% silica, pH 3.5, ionic strength I = 16.9 mM) was kindly provided by Nissan Chemicals. These NPs have a diameter of 13±2 nm based on dynamic light scattering and a zeta potential value of -16 mV (Henry's equation) by electrophoretic measurements.

QCM-D experimental setup

Solutions of 0.1 g/L aqueous PAH and 0.285 mM Na₃Cit were vortexed together for 10 seconds in a 2:5 volume ratio at room temperature and aged for 10 minutes. The R-ratio of this suspension was 2. This suspension was then flowed onto the Q-sense E4 chamber with a mounted Au-coated quartz crystal sensor at 50.1 μL/min for about 25 hours. Milli-Q water was then flowed through the chamber to rinse off any excess polymer-salt aggregates from the surface of the sensor for about 30 mins. Followed by passing an aqueous solution of 0.1 g/L Na-Flu through the chamber at 50.1 μL/min for 8 hours. The schematic of QCM-D setup is shown in Fig. B.1 and diffusion of Na-Flu on PAH-Cit film is shown in Fig. B.2.

Synthesize gold nanoparticles

To synthesize gold nanoparticles of 4- and 20-nm diameters, procedures previously developed by Nutt et al.^{26, 27} were used. For 20 nm gold nanoparticles, 200 μL of a HAuCl_4 solution (0.25 M; AuCl_3 99.99%, Sigma-Aldrich) was first diluted in 200 g of Nanopure water ($>18 \text{ M}\Omega\text{-cm}$, Barnstead Nanopure Diamond). The solution was heated and stirred to boiling, after which 12 mL of a trisodium citrate solution (0.0345 M) was added. After about 10 minutes of gentle boiling of the nearly colorless solution, the solution was removed from the heat source. The product liquid was a dark wine red color from the gold nanoparticles. This procedure was modified for 4-nm Au NPs in that the initial gold salt solution was heated only to 60°C , a solution of tannic acid and trisodium citrate replaced the trisodium citrate solution in the 20-nm Au NP procedure, and boiling time was increased to 30 minutes.

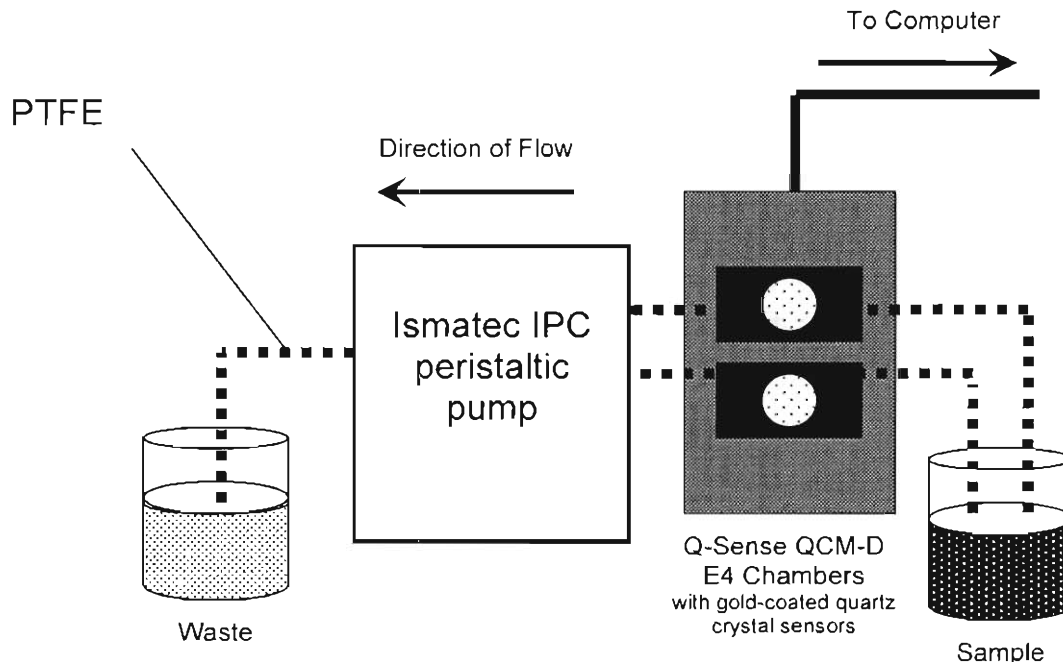


Figure B.1. Schematic of QCM-D experimental set up, PTFE (Poly(tetrafluoroethylene)).

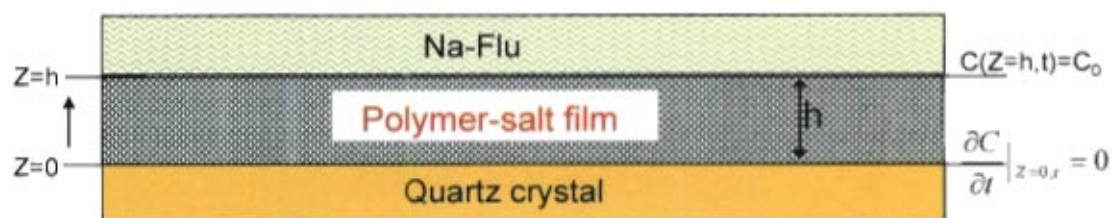


Figure B.2. Schematic of Na- Fluorescein diffusing in PAH-Cit film.

QCM-D working principle

A QCM-D (Q-sense E4) was used in this study. Gold-coated quartz crystal sensors used (purchased from Q-sense). According to company specifications, quartz crystal sensors were coated with a gold layer of 100 nm thickness. The resonance frequency of the crystal sensor was $4.95 \text{ MHz} \pm 50 \text{ kHz}$ and was excited during experimentation at the fundamental frequency, as well as the 3rd, 5th, 7th, 9th, 11th, and 13th overtones (15, 25, 35, 45, 55, and 65 MHz, respectively). To take frequency and dissipation measurements, an AC voltage was applied intermittently to the sensor, inducing oscillation. The change in frequency at each overtone was measured, and immediately after stopping excitation of the crystal sensor, the energy dissipation value, which describes the dampening of the crystal oscillation, was also measured. Measurements were taken every 0.5 seconds and the data was condensed to data points at every 5 seconds. All crystals were cleaned in a 5:1:1 solution of milli-Q water, 35% H_2O_2 and 25% NH_3 at $75 \text{ }^\circ\text{C}$ for 10 min before the experiment, then washed in milli-Q water and dried. QCM-D could analyze the kinetic adsorption behavior of Na-Flu on the polymer-salt film. The energy dissipation value, D , is defined as $D = E_{\text{dissipated}}/(2\pi E_{\text{stored}})$, where $E_{\text{dissipated}}$ is the energy dissipated from the

total system oscillation energy, E_{stored} , due to the viscoelastic and frictional properties of the film adsorbed on the sensor²⁸.

Because the dissipation values never exceeded 1×10^{-6} per 10 Hz of frequency change, the film could be considered a rigid, non-viscoelastic film and the Sauerbrey model could be used for mass and thickness calculations²⁴. For the Sauerbrey model, frequency data from the 7th overtone was used for calculation of the deposited film mass and thickness. The density of the film was estimated to be 1100 kg/m^3 . The Sauerbrey equation relates change in frequency of the oscillating sensor to the change in adsorbed mass on the sensor by the $\Delta m = -C \cdot \Delta f / \nu$, where Δm is the change in mass, or mass of the deposited film; $C (= 17.7 \text{ ng cm}^2 \text{ Hz}^{-1} \text{ at } f_{n=1} = 5 \text{ MHz})$ is a constant, Δf is the change in frequency of the oscillating system, and ν is the overtone number²⁹. To approximate the film thickness, a density must be specified for the film. Previous literature reported polyelectrolyte films as having densities at around 1.1 g/cm^3 , so this value was used to estimate the PAH/citrate film thicknesses³⁰⁻³². The actual density of the film could differ from this theoretical value, however, due to swelling or other possible effects. Frequency and Energy dissipation vs Time are plotted (Fig. B.3).

Data analysis

Both the Voigt viscoelastic model and Sauerbrey models were used to estimate mass and thickness changes of the film. Both one- and two-layer Voigt viscoelastic models were used. The results of all models were compared.

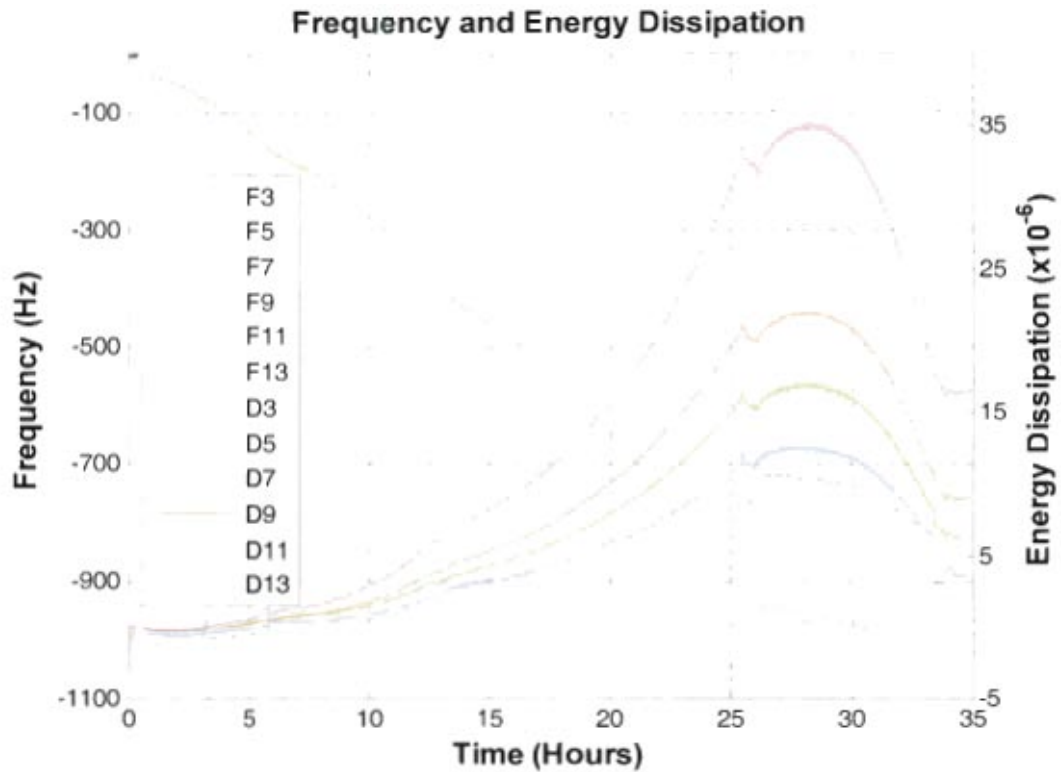


Figure B.3. Experimental data obtained from QCM-D. Frequency and Energy dissipation vs Time are plotted.

Parameters Used

For the Voigt model, data from 7th, 9th, and 11th overtones were used. The density of layer 1 was entered as 1100 kg/m³. The density of layer 2 for the two-layer model was 1200 kg/m³. The Voigt model requires entering in minimum and maximum values between which the actual value of a certain parameter is expected to fall. The following ranges were used (L_1 indicates the layer of material covering the sensor): L_1 Viscosity: 0.001-0.1 kg/m•s, L_1 Shear: $10^4 - 10^8$ Pa, L_1 Thickness: $10^{-10} - 10^{-5}$ m. The Voigt model also allows certain parameters to fix to an inputted value. The following parameters were fixed: L_1 Density: 1100 kg/m³. Fluid Density, or density of fluid passing over sensor:

1000 kg/m³ (the same as that of water). Fluid Viscosity, or viscosity of fluid passing over sensor: 0.001 kg/m-s (the same as that of water). For the Sauerbrey model, data from the 7th overtone was used.

Results and Discussion

The final thickness of the fluorescein and PAH/cit film on the sensor was estimated to be 150 nm (Fig.B.4), or an increase of 6 nm after the addition of fluorescein. Fig. B.5 shows the adsorbed mass of fluorescein on PAH/cit film vs. time, in which a sodium fluorescein solution was passed over the quartz crystal sensor and fluorescein was adsorbed onto the PAH/cit film until saturation.

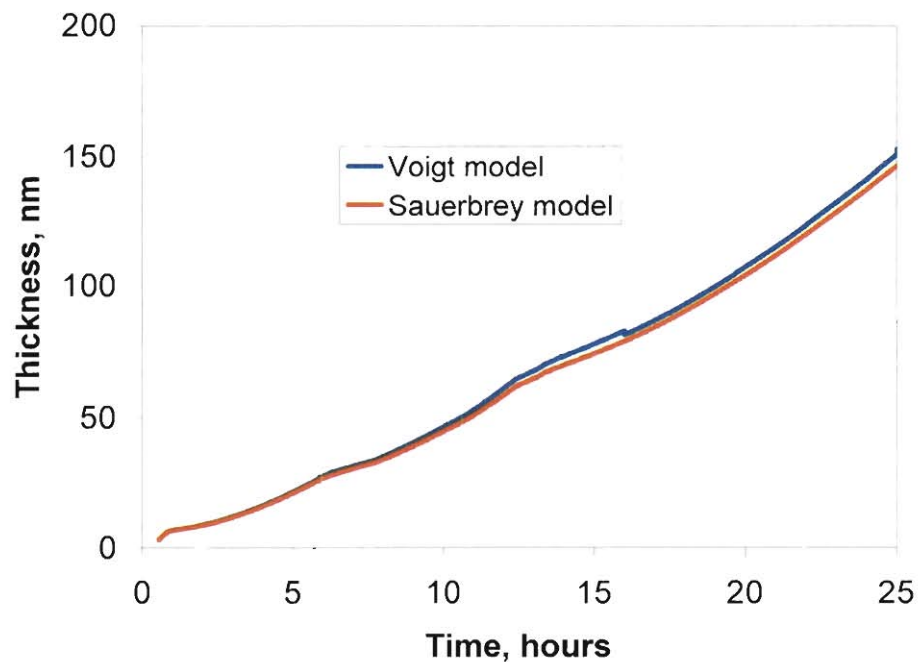


Figure B.4. Thickness vs. time of PAH/cit film on gold-coated sensor. Thickness of the film was estimated using both the models

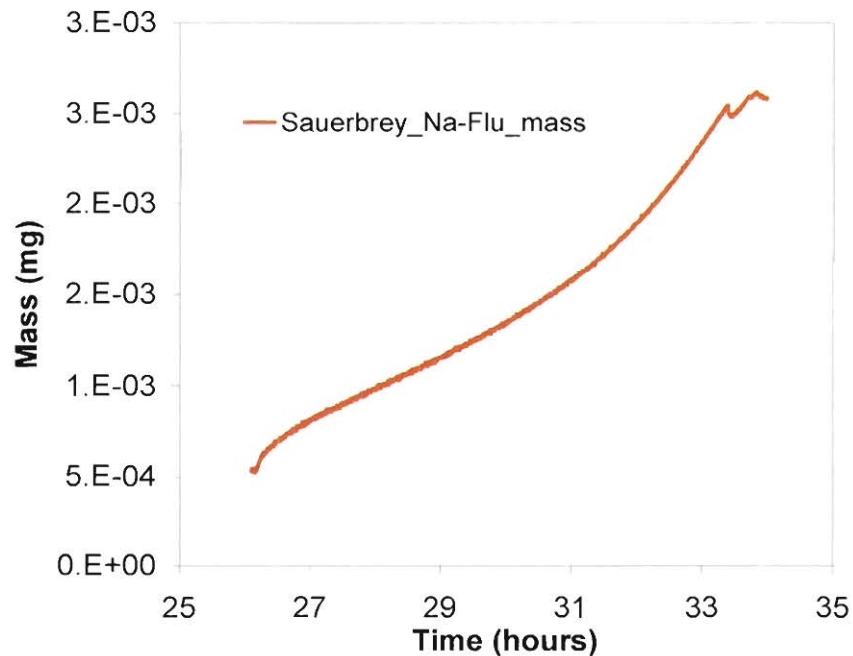


Figure B.5. Adsorbed mass of Na-Flu on PAH/cit film vs. time

The Sauerbrey model slightly underestimated the thickness onto the sensor in comparison to the Voigt model, but both resulted in a final deposited mass of approximately 3.5×10^{-3} mg. The Sauerbrey estimated an amount of adsorbed fluorescein mass of approximately 1.0×10^{-3} mg.

Diffusion model

Fick's Second Law of Diffusion predicts how diffusion of a solute into a material affects the concentration field of the film and surrounding bulk solution with respect to time. Because the QCM-D measure mass changes of the film with respect to time, an equation was needed that would directly obtain the diffusion coefficient from the mass change over time. See below equations for the derivation. Schematic (Fig. B.2) shows the boundary conditions.

$$\frac{\partial C}{\partial t} = D \frac{\partial^2 C}{\partial t^2} \quad (1)$$

Boundary conditions

(i) $C(Z, 0) = 0$

(ii) $C(Z = h, t) = C_0$

(iii) $\frac{\partial C}{\partial Z}(Z = 0, t) = 0$

$$\frac{C(Z, t)}{C_0} = 1 - \frac{4}{\pi} \sum_{n=0}^{\infty} \frac{(-1)^n}{2n+1} e^{-\frac{(2n+1)^2 \pi^2}{4 h^2} D t} \times \cos\left(\frac{(2n+1) \pi Z}{h}\right) \quad (2)$$

$$J_z = -D \frac{\partial C}{\partial Z} \Big|_{z=h} = \frac{\dot{M}(t)}{\pi R^2} \quad (3)$$

$$\dot{M}(t) = \frac{\pi R^2}{h} \times 2 D C_0 \sum_{n=0}^{\infty} e^{-\frac{(2n+1)^2 \pi^2}{4 h^2} D t} \quad (4)$$

$$M(t) = \int_0^t \dot{M}(t') dt' \quad (5)$$

$$M(t) = \frac{8h}{\pi} \times C_0 \sum_{n=0}^{\infty} \frac{1 - e^{-\frac{(2n+1)^2 \pi^2}{4 h^2} D t}}{(2n+1)^2} \quad (6)$$

$$M(t) \approx \frac{8h}{\pi} \times C_0 \left[1 - e^{-\frac{\pi^2}{4h^2} D t} \right] \quad (7)$$

Where, C is concentration of Na-Flu in the polymer-salt film, Z is height, t is time,

D is Diffusion of Na-Flu in polymer-salt film, h is the thickness of film. J_z : Mass-flux of

Na-Flu at the interface between the Na-Flu and polymer-salt film. $\dot{M}(t)$: Rate of Na-Flu

diffusing in the polymer-salt film. $M(t)$: Mass diffused in the film. Eq(7) explicitly

shows the relationship between mass change over time and the diffusion coefficient for the film

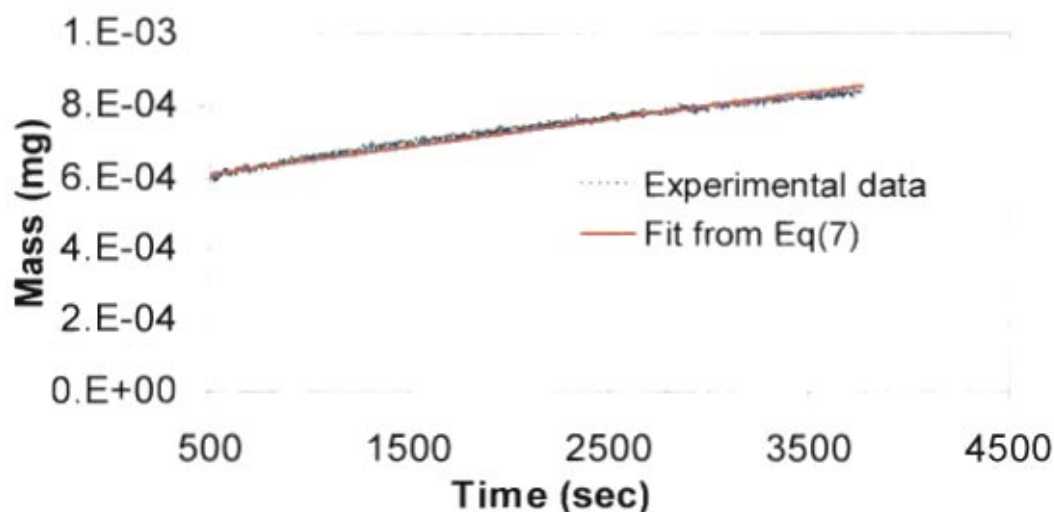


Figure B.6. Mass of fluorescein adsorbed on PAH/cit film vs. time. Eq(7) and experimental data are plotted vs time.

Three types of nanoparticles were used in QCM-D experiments, gold nanoparticles (4 nm diameter), gold nanoparticles (20 nm), and silica nanoparticles (13 nm). See Table B.1 for a summary of results.

Table B. 1. Summary of QCM-D Results.

Material	Nanoparticle or Molecular Diameter, nm	Zeta Potential, mV	Solution or Suspension pH	Diffusion Coefficient, $D(m^2/s)$
Gold NP	4	-20.61	6	2.55×10^{-18}
Gold NP	20	-17.87	6	4.45×10^{-20}
Silica NP	13±2	-19.5	3.52	4.47×10^{-17}
Fluorescein	0.69±0.02	-	3.52	6.64×10^{-20}

Our results show that the diffusion deposition model may be able to explain the results obtained by QCM-D experimentation in this project. Changing the size of a nanoparticle was found to have an effect on the diffusion deposition model. Gold nanoparticles of 4 nm diameter were found to have a diffusion coefficient one order of magnitude higher than gold nanoparticles of 20 nm. This could be explained by the smaller size of the 4-nm gold nanoparticles allowing them to penetrate more deeply into the polymer-salt film, therefore increasing the diffusion rate and therefore the diffusion coefficient D . Our preliminary results also suggest that increasing the surface charge of a nanoparticle was found to lead to a higher diffusion coefficient. Silica nanoparticles are significantly more negatively charged than gold nanoparticles in their native pH conditions, as indicated by experimental zeta potential results. Though the 13-nm silica nanoparticles are smaller than the 20-nm gold nanoparticles and therefore cannot be directly compared solely on the basis of surface charge, the finding that the silica nanoparticles' diffusion coefficient was larger by one order of magnitude than that of the 20-nm gold nanoparticles should indicate that something about the silica nanoparticles other than their diameter was clearly playing a part in their diffusion rate – i.e., the nanoparticle surface charge density. Though the silica and gold nanoparticle diffusion coefficient differences are suspected to be a result of the nanoparticles' surface charge, these results do not rule out other possible explanations for the different diffusion coefficients. For example, the synthesis of gold nanoparticles leads to various extraneous ions and other components in the product suspension, including citrate and tannic acid. This could lead to different properties of the silica and gold nanoparticle suspensions, including ionic strength and pH. The silica nanoparticles could have had a higher

diffusion coefficient as a result of ion competition in the gold nanoparticle suspension. It is possible that ions in the gold nanoparticle suspension could be competing with the gold nanoparticles in binding to positive sites on the PAH/citrate film and slowing the gold nanoparticles from adsorbing onto and diffusing into the films. It was expected that fluorescein would have a relatively high diffusion coefficient due to the small size of the molecule in comparison to the nanoparticles used. However, sodium fluorescein was found to have the smallest diffusion coefficient of all tested materials, indicating that molecular surface charge or pKa value may have played a part in the characteristics of sodium fluorescein diffusion into the film.

Conclusions

We measured the diffusion coefficient of sodium fluorescein, Au and Silica NPs in the polymer-salt matrix alone, using QCM-D technique. This involves a planar, rather than a spherical geometry. Polymer-salt films were developed for ~ 25 hours, prior to the flow of Na-Flu. Based on the dissipation values the film could be considered a rigid, non-viscoelastic film and the Sauerbrey model could be used for mass and thickness calculations. The calculated thickness was estimated by Sauerbrey model. To perform the quantitative analysis, a molecular transport in one dimension was assumed and using Fick's second law, the mass diffused with respect to time was modeled. The diffusion coefficient was found to be $\sim 10^{-19}$ m²/sec. This is in good agreement with what has already been reported for diffusion of rhodamine in polyelectrolyte films

References:

1. Agrawal, A.; Park, J.; Ryu, D. Y.; Hammond, P. T.; Russell, T. P.; McKinley, G. H., Controlling the location and spatial extent of nanobubbles using hydrophobically nanopatterned surfaces. *Nano Letters* **2005**, 5, (9), 1751-1756.
2. Bennett, R. D.; Hart, A. J.; Miller, A. C.; Hammond, P. T.; Irvine, D. J.; Cohen, R. E., Creating patterned carbon nanotube catalysts through the microcontact printing of block copolymer micellar thin films. *Langmuir* **2006**, 22, (20), 8273-8276.
3. Berg, M. C.; Yang, S. Y.; Hammond, P. T.; Rubner, M. F., Controlling mammalian cell interactions on patterned polyelectrolyte multilayer surfaces. *Langmuir* **2004**, 20, (4), 1362-1368.
4. Chuang, H. F.; Smith, R. C.; Hammond, P. T., Polyelectrolyte multilayers for tunable release of antibiotics. *Biomacromolecules* **2008**, 9, (6), 1660-1668.
5. DeLongchamp, D. M.; Hammond, P. T., Highly ion conductive poly(ethylene oxide)-based solid polymer electrolytes from hydrogen bonding layer-by-layer assembly. *Langmuir* **2004**, 20, (13), 5403-5411.
6. Kim, B. S.; Park, S. W.; Hammond, P. T., Hydrogen-bonding layer-by-layer assembled biodegradable polymeric micelles as drug delivery vehicles from surfaces. *Acc Nano* **2008**, 2, (2), 386-392.
7. Krogman, K. C.; Lowery, J. L.; Zacharia, N. S.; Rutledge, G. C.; Hammond, P. T., Spraying asymmetry into functional membranes layer-by-layer. *Nature Materials* **2009**, 8, (6), 512-518.
8. Krogman, K. C.; Zacharia, N. S.; Schroeder, S.; Hammond, P. T., Automated process for improved uniformity and versatility of layer-by-layer deposition. *Langmuir* **2007**, 23, (6), 3137-3141.
9. Lee, H. I.; Lee, J. A.; Poon, Z. Y.; Hammond, P. T., Temperature-triggered reversible micellar self-assembly of linear-dendritic block copolymers. *Chemical Communications* **2008**, (32), 3726-3728.
10. Lee, S. W.; Kim, B. S.; Chen, S.; Shao-Horn, Y.; Hammond, P. T., Layer-by-Layer Assembly of All Carbon Nanotube Ultrathin Films for Electrochemical Applications. *Journal of the American Chemical Society* **2009**, 131, (2), 671-679.

11. Lowman, G. M.; Tokuhisa, H.; Lutkenhaus, J. L.; Hammond, P. T., Novel solid-state polymer electrolyte consisting of a porous layer-by-layer polyelectrolyte thin film and oligoethylene glycol. *Langmuir* **2004**, 20, (22), 9791-9795.
12. Lutkenhaus, J. L.; Olivetti, E. A.; Verploegen, E. A.; Cord, B. M.; Sadoway, D. R.; Hammond, P. T., Anisotropic structure and transport in self-assembled layered polymer-clay nanocomposites. *Langmuir* **2007**, 23, (16), 8515-8521.
13. Macdonald, M.; Rodriguez, N. M.; Smith, R.; Hammond, P. T., Release of a model protein from biodegradable self assembled films for surface delivery applications. *Journal of Controlled Release* **2008**, 131, (3), 228-234.
14. Nguyen, P. M.; Hammond, P. T., Amphiphilic linear-dendritic triblock copolymers composed of poly(amidoamine) and poly(propylene oxide) and their micellar-phase and encapsulation properties. *Langmuir* **2006**, 22, (18), 7825-7832.
15. Tokuhisa, H.; Hammond, P. T., Nonlithographic micro- and nanopatterning of TiO₂ using polymer stamped molecular templates. *Langmuir* **2004**, 20, (4), 1436-1441.
16. Vazquez, E.; Dewitt, D. M.; Hammond, P. T.; Lynn, D. M., Construction of hydrolytically-degradable thin films via layer-by-layer deposition of degradable polyelectrolytes. *Journal of the American Chemical Society* **2002**, 124, (47), 13992-13993.
17. Wood, K. C.; Boedicker, J. Q.; Lynn, D. M.; Hammond, P. T., Tunable drug release from hydrolytically degradable layer-by-layer thin films. *Langmuir* **2005**, 21, (4), 1603-1609.
18. Wood, K. C.; Chuang, H. F.; Batten, R. D.; Lynn, D. M.; Hammond, P. T., Controlling interlayer diffusion to achieve sustained, multiagent delivery from layer-by-layer thin films. *Proceedings of the National Academy of Sciences of the United States of America* **2006**, 103, (27), 10207-10212.
19. Wood, K. C.; Little, S. R.; Langer, R.; Hammond, P. T., A family of hierarchically self-assembling linear-dendritic hybrid polymers for highly efficient targeted gene delivery. *Angewandte Chemie-International Edition* **2005**, 44, (41), 6704-6708.
20. Wood, K. C.; Zacharia, N. S.; Schmidt, D. J.; Wrightman, S. N.; Andaya, B. J.; Hammond, P. T., Electroactive controlled release thin films. *Proceedings of the National Academy of Sciences of the United States of America* **2008**, 105, (7), 2280-2285.

21. Yoo, P. J.; Nam, K. T.; Qi, J. F.; Lee, S. K.; Park, J.; Belcher, A. M.; Hammond, P. T., Spontaneous assembly of viruses on multilayered polymer surfaces. *Nature Materials* **2006**, *5*, (3), 234-240.
22. Bagaria, H. G.; Kadali, S. B.; Wong, M. S., Shell Thickness Control of Nanoparticle/Polymer Assembled Microcapsules. *Chemistry of Materials* **2011** *23*, (2), 301-308.
23. Tavera, E. M.; Kadali, S. B.; Bagaria, H. G.; Liu, A. W.; Wong, M. S., Experimental and Modeling Analysis of Diffusive Release from Single-Shell Microcapsules. *Aiche Journal* **2009**, *55*, (11), 2950-2965.
24. Kotarek, J. A.; Johnson, K. C.; Moss, M. A., Quartz crystal microbalance analysis of growth kinetics for aggregation intermediates of the amyloid-[beta] protein. *Analytical Biochemistry* **2008**, *378*, (1), 15-24.
25. Klitzing, R. v.; Mohwald, H., A Realistic Diffusion Model for Ultrathin Polyelectrolyte Films. *Macromolecules* **1996**, *29*, (21), 6901-6906.
26. Nutt, M. O.; Heck, K. N.; Alvarez, P.; Wong, M. S., Improved Pd-on-Au bimetallic nanoparticle catalysts for aqueous-phase trichloroethene hydrodechlorination. *Applied Catalysis B: Environmental* **2006**, *69*, (1-2), 115-125.
27. Nutt, M. O.; Hughes, J. B.; Wong, M. S., Designing Pd-on-Au bimetallic nanoparticle catalysts for trichloroethene hydrodechlorination. *Environmental Science & Technology* **2005**, *39*, (5), 1346-1353.
28. Turon, X.; Rojas, O. J.; Deinhammer, R. S., Enzymatic Kinetics of Cellulose Hydrolysis: A QCM-D Study. *Langmuir* **2008**, *24*, (8), 3880-3887.
29. Picart, C.; Lavallo, P.; Hubert, P.; Cuisinier, F. J. G.; Decher, G.; Schaaf, P.; Voegel, J. C., Buildup Mechanism for Poly(l-lysine)/Hyaluronic Acid Films onto a Solid Surface. *Langmuir* **2001**, *17*, (23), 7414-7424.
30. Ariga, K.; Lvov, Y.; Onda, M.; Ichinose, I.; Kunitake, T., Alternately assembled ultrathin film of silica nanoparticles and linear polycations. *Chemistry Letters* **1997**, (2), 125-126.

31. Silva, C. P.; Carapuca, H. M., Glassy carbon electrodes coated with poly(allylamine hydrochloride), PAH: Characterization studies and application to ion-exchange voltammetry of trace lead(II) at combined PAH/mercury film electrodes. *Electrochimica Acta* **2006**, 52, (3), 1182-1190.

32. Silva, C. P.; Carapuca, H. M.; Rocha, L. S.; Pinheiro, J. P., Evaluation of poly(sodium 4-styrenesulfonate) film coating in thin mercury film electrodes for lead determination. *Journal of Electroanalytical Chemistry* **2009**, 626, (1-2), 192-196.

Appendix C. Mathematical modeling for understanding the formation of elongated NACs

Assuming the boundary layer is small respect to the dimensions of the duct. The equation of motion can be written for x-direction as:

$$U_x \frac{\partial U_x}{\partial x} + U_y \frac{\partial U_x}{\partial y} = \nu \frac{\partial^2 U_x}{\partial y^2} - \frac{1}{\rho} \frac{dP}{dx} \quad (C.1)$$

In this equation the x-direction is the direction parallel to the physical boundary solid-fluid, and y is the axis normal to the solid-fluid interface.

Assuming mechanical energy conservation:

The x-momentum balance is simplified to the form:

$$U_x \frac{\partial U_x}{\partial x} + U_y \frac{\partial U_x}{\partial y} = \nu \frac{\partial^2 U_x}{\partial y^2} + V_o \frac{dV_o}{dx} \quad (C.2)$$

The continuity equation is:

$$\frac{\partial U_x}{\partial x} + \frac{\partial U_y}{\partial y} = 0 \quad (C.3)$$

Using stream function, the velocity field can be obtained with:

$$U_x = \frac{\partial \psi}{\partial y} \quad U_y = -\frac{\partial \psi}{\partial x} \quad (C.4.a \text{ and } C.4.b)$$

$$\frac{\partial \psi}{\partial y} \frac{\partial^2 \psi}{\partial x \partial y} - \frac{\partial \psi}{\partial x} \frac{\partial^2 \psi}{\partial y^2} = \nu \frac{\partial^3 \psi}{\partial y^3} + V_o \frac{dV_o}{dx} \quad (C.5)$$

Using transformation technique, we can convert this differential equation into a well known Falkner and Skan equation : (flow past a wedge with an angle: $\lambda\pi$)

$$f''' + ff'' - \lambda(1 - (f')^2) = 0 \quad (C.5.b)$$

The boundary conditions are:

$$f = f' = 0 \text{ for } \eta \rightarrow 0 \quad (C.7) \quad \text{Velocities at the surface for x and y are zero}$$

$$f' = 1 \text{ for } \eta \rightarrow \infty \quad (C.8) \quad \text{Constant velocity beyond the boundary layer}$$

Which can be solved numerically and the velocity components and the extensional strain may be calculated as:

Transformation variables:

$$V_o = B x^m \quad (\text{C.9}) \quad \text{Free stream velocity}$$

$$\xi = \frac{x^{m+1}}{m+1} \quad (\text{C.10})$$

$$\eta = y \sqrt{\frac{(m+1)B}{2\nu}} x^{\frac{(m-1)}{2}} \quad (\text{C.11}) \quad \text{Dimensionless independent variable}$$

$$\psi = \sqrt{\frac{2\nu B}{m+1}} x^{\frac{(m+1)}{2}} f(\eta) \quad (\text{C.12}) \quad \text{Stream function}$$

$$m = \frac{-\lambda}{\lambda+1} \quad (\text{C.13})$$

Velocity components using the Falkner-Skan equation:

$$U_x = \frac{\partial \psi}{\partial y} = B x^m f' \quad (\text{C.14})$$

$$-U_y = \frac{\partial \psi}{\partial x} = \sqrt{\frac{(m+1)\nu B}{2}} x^{\frac{(m-1)}{2}} \left(f + \left(\frac{m-1}{m+1} \right) \eta f' \right) \quad (\text{C.15})$$

The extensional strains are calculated with the derivatives of each velocity:

$$\frac{\partial U_x}{\partial x} = B m x^{m-1} f' + B x^m f'' \frac{d\eta}{dx} \quad (\text{C.16})$$

$$-\frac{\partial U_y}{\partial y} = \sqrt{\frac{(m+1)\nu B}{2}} x^{\frac{(m-1)}{2}} \left(f' + \left(\frac{m-1}{m+1} \right) (\eta f'' + f') \right) \frac{d\eta}{dy} \quad (\text{C.17})$$

Where:

$$\frac{d\eta}{dx} = y \left(\frac{m-1}{2} \right) \sqrt{\frac{(m+1)B}{2\nu}} x^{\frac{(m-3)}{2}} \quad (\text{C.18})$$

$$\frac{d\eta}{dy} = \sqrt{\frac{(m+1)B}{2\nu}} x^{\frac{(m-1)}{2}} \quad (\text{C.19})$$

Writing all the equations in dimensionless form:

$$\frac{U_x}{B L^m} = \left(\frac{x}{L} \right)^m f' \quad (\text{C.20})$$

$$-\frac{U_y}{L^m B} \text{Re}_L^{1/2} = \sqrt{\frac{m+1}{2}} \left(\frac{x}{L}\right)^{\frac{(m-1)}{2}} \left(f + \left(\frac{m-1}{m+1}\right) \eta f'\right) \quad (\text{C.21})$$

$$\frac{L}{L^m B} \frac{\partial U_x}{\partial x} = m \left(\frac{x}{L}\right)^{m-1} f' + \left(\frac{x}{L}\right)^m f'' L \frac{d\eta}{dx} \quad (\text{C.22})$$

$$-\frac{L}{L^m B} \text{Re}_L^{1/2} \frac{\partial U_y}{\partial y} = \left(\frac{x}{L}\right)^{\frac{(m-1)}{2}} \left(f' + \left(\frac{m-1}{m+1}\right) (\eta f'' + f')\right) L \frac{d\eta}{dy} \quad (\text{C.23})$$

Where:

$$L \frac{d\eta}{dx} = \left(\frac{m-1}{2}\right) \left(\sqrt{\frac{m+1}{2}}\right) \text{Re}_L^{1/2} \left(\frac{y}{L}\right) \left(\frac{x}{L}\right)^{\frac{(m-3)}{2}} \quad (\text{C.24})$$

$$L \frac{d\eta}{dy} = \sqrt{\frac{m+1}{2}} \text{Re}_L^{1/2} \left(\frac{x}{L}\right)^{\frac{(m-1)}{2}} \quad (\text{C.25})$$

$$\eta = \frac{y}{L} \sqrt{\frac{(m+1)}{2}} \text{Re}_L^{1/2} \left(\frac{x}{L}\right)^{\frac{(m-1)}{2}} \quad (\text{C.26})$$

$$V_o = B x^m \quad (\text{C.27})$$

$$U_L = B L^m \quad (\text{C.28})$$

$$\text{Re}_L = \frac{L U_L}{\nu} \quad (\text{C.29})$$

And the solution of the Falkner-Skan in dimensionless form:

$$\frac{\psi}{B L^m L} \text{Re}_L^{1/2} = \sqrt{\frac{2}{(m+1)}} \left(\frac{x}{L}\right)^{\frac{(m+1)}{2}} f(\eta) \quad (\text{C.30})$$

The extensional rates are calculated with equations (C.16) and (C.17)

The shear stress close to the inlet of the ducts can be estimated using Blasius approach.

$$\text{For the boundary layer thickness: } \delta(x) = 4.64 \sqrt{\frac{\nu x}{U_o}}$$

And for the drag coefficient:

$$D = (1.328/2) \sqrt{\rho \mu L_1 W^2 U_o^3}$$

Then the shear rate can be estimated with:

$$\dot{\gamma} = \frac{D}{\mu W L_1}$$

f = Falkner-Skan f function, see equation (C.5.b) and the boundary conditions (C.7) and (C.8) where,

ψ = Stream function

D = Drag force

D_0 =Duct diameter

L = Characteristic length

L_1 = Length of the duct

U_x, U_y = Velocities in x and y axis respectively.

V_0 = Upstream velocity.

B = Proportionality constant, see C.27

x, y = components, parallel and normal to the interface solid-fluid

$W = 2 \pi D_0$

δ = Thickness of the boundary layer

$d\gamma/dt$ = shear rate

μ = viscosity

ρ = density

$\nu = \mu/\rho$ kinematic viscosity

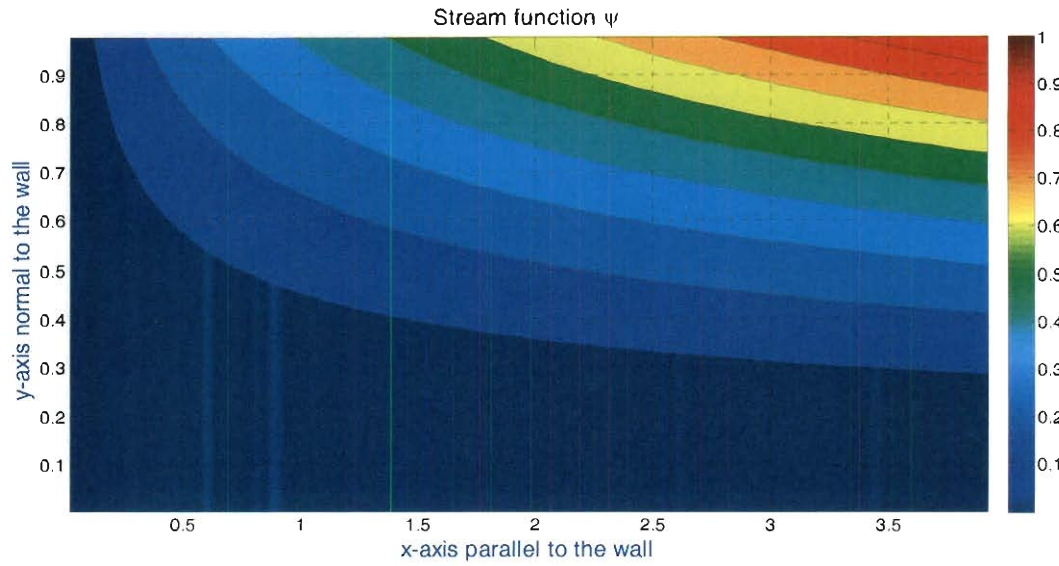


Figure C. 1. Magnitude of the stream function for a flow past a wedge (135π). Position (x,y) are shown in Fig. 5.4.

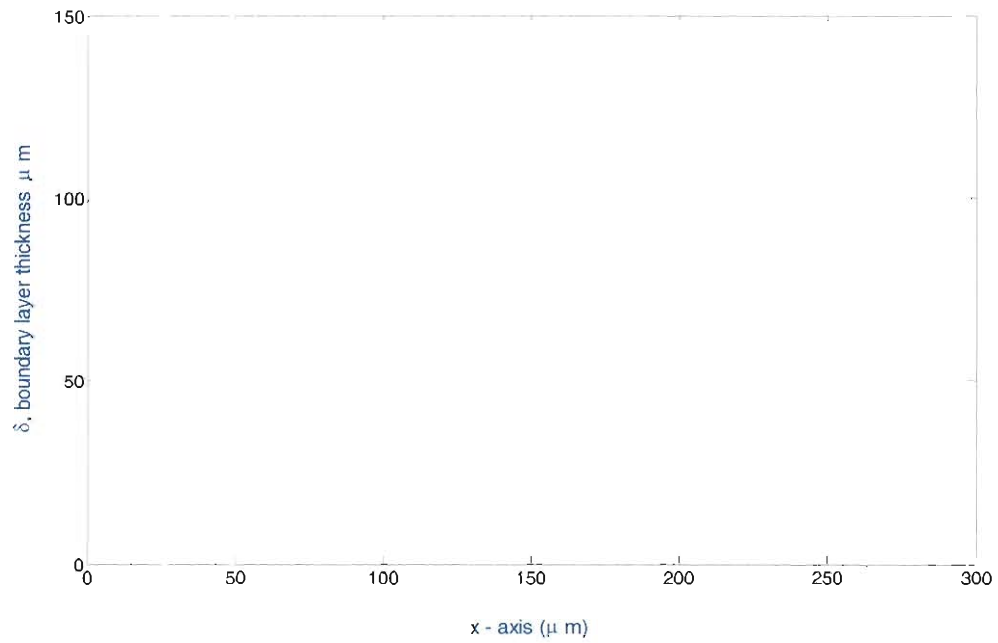


Figure C. 2. Boundary layer assuming average velocity of 9.72 m/s. See appendix notes for justification of the use of this velocity as a reference. Position (x,y) are shown in Fig. 5.4.

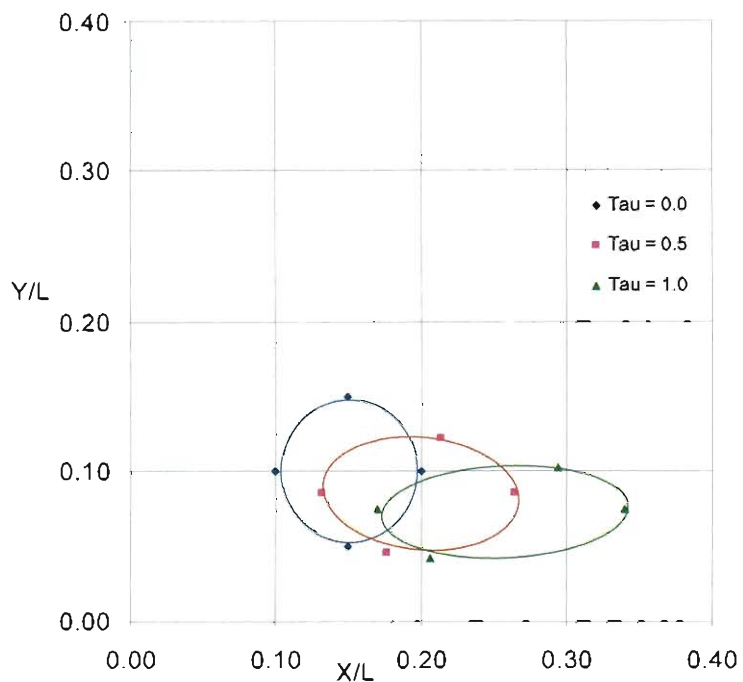


Figure C.3. Particle tracking of PS aggregate. Position (x,y) are shown in figure 5.4. Tau presents the dimensionless time scale. The transformation from spherical (blue circle) to elongated circle (green) could clearly be observed. Particle tracking code is given at the end appendix.

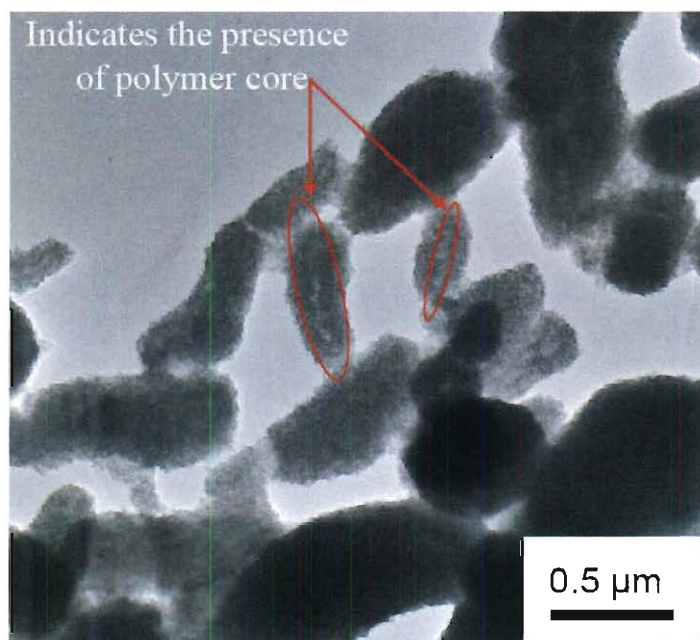


Figure C.4. TEM image of elongated NACs. Elongated NACs made at 20K PSI, initial particle size of polymer- salt aggregate is 1.5 micron.

Notes

The apparatus has specifications by the manufacturers about the velocity of the system vs pressure applied. Looking carefully what they did is just calculated using $V = \sqrt{\frac{2\Delta P}{\rho}}$.

Method to calculate shear rate and boundary layer thickness for various dimensions such as 50, 75, 300 μm in the Y- chamber is calculated by using the following equations using Engineering equation solver (EES) solver.

$$V2 = 250 \text{ [m/s]}$$

$$D2 = 0.00005 \text{ [m]}$$

$$D3 = 0.000075 \text{ [m]}$$

$$V3 \cdot D3^2 = V2 \cdot D2^2$$

$$D = 0.0003 \text{ [m]}$$

$$V \cdot D^2 = 2 \cdot V2 \cdot D2^2$$

$$\rho = 1000 \text{ [kg/m}^3\text{]}$$

$$\mu = 0.001 \text{ [kg/m-s]}$$

$$L = 0.1 \text{ [m]}$$

$$\text{Re} = \rho \cdot V \cdot \frac{D}{\mu}$$

$$\text{RR} = 0$$

$$f = \text{MoodyChart} [\text{Re}, \text{RR}]$$

$$\frac{\Delta P}{\rho} = f \cdot \frac{L}{D} \cdot \frac{V^2}{2}$$

$$\Delta P_y = [\Delta P + \Delta P_e] \cdot \left| 0.000145038 \cdot \frac{\text{psi}}{\text{Pa}} \right|$$

$$\frac{\Delta P_e}{\rho} = 0.45 \cdot \left[1 - \frac{D2^2}{D^2} \right] \cdot \frac{V2^2}{2} + 0.95 \cdot \frac{V2^2}{2}$$

$$x = 20 \cdot 0.00003 \text{ [m]}$$

$$\text{Rex} = \rho \cdot V \cdot \frac{x}{\mu}$$

$$\delta = 4.64 \cdot \sqrt{\mu \cdot \frac{x}{\rho \cdot V}}$$

$$\delta_{um} = \frac{\delta}{0.000001}$$

$$\dot{\gamma} = \frac{V}{\delta}$$

$$x_1 = 5 \cdot D$$

$$x_2 = 5 \cdot D^2$$

$$x_3 = 5 \cdot D^3$$

$$\text{Re}x_1 = \rho \cdot V \cdot \frac{x_1}{\mu}$$

$$\text{Re}x_2 = \rho \cdot V^2 \cdot \frac{x_2}{\mu}$$

$$\text{Re}x_3 = \rho \cdot V^3 \cdot \frac{x_3}{\mu}$$

$$\frac{\delta_{x,1}}{x_1} = \frac{0.671}{\sqrt{\text{Re}x_1}}$$

$$\frac{\delta_{x,2}}{x_2} = \frac{0.671}{\sqrt{\text{Re}x_2}}$$

$$\frac{\delta_{x,3}}{x_3} = \frac{0.671}{\sqrt{\text{Re}x_3}}$$

$$\dot{\gamma}_1 = \frac{V}{\delta}$$

$$\dot{\gamma}_2 = \frac{V^2}{\delta}$$

$$\dot{\gamma}_3 = \frac{V^3}{\delta}$$

Code1. Matlab code to Falkner-Skan solution to the boundary layer, shear and extensional stress rates, and boundary layer thickness

```

% Falkner-Skan solution to the boundary layer, computed numerically
% f'''+f*f''+beta*(1-f'^2)=0 or f'''=-f*f''-beta*(1-f'^2)
% f is function of similarity variable, eta
% f(0)=0, f'(0)=0, f'(infinity)=1
% f''(0)= to be estimated to satisfy condition at infinity
% Y=[f f' f''], dY/deta=[f' f'' f''']=[Y(2) Y(3) -f*f''-beta*(1-
f'^2)]
clear all
clf reset
global range
figure(2)
clf reset
beta=[1.0];
range=linspace(0,8,160);
soln=[]; betad=[];
for ibeta=1:length(beta)

```

```

niter=10;
A=linspace(0,2,niter); % initial estimate for f''
flag=0;
figure(1)
clf reset
for iter=1:niter % compute ODE to verify solution is
possible
    clear eta Y
    Vinit=[0 0 A(iter)];
    options=odeset('Events',@events,'RelTol',1.e-6,'AbsTol',1.e-7);

    [eta,Y]=ode45(@falknerf,range,Vinit,options,beta(ibeta));
    plot(eta,Y(:,2),'-')
    pause
    hold on
    if flag==0&Y(end,2)>1 % find where f' crosses +1
        iflag=iter;
        flag=1;
    end
end
clear eta Y
figure(2)
warning off MATLAB:fzero:UndeterminedSyntax
opt=optimset('Display','iter');
if iflag==1
    iflag=2;
end
A1=fzero('fpeq1',[A(iflag-1) A(iflag)],[],beta(ibeta));
Vinit=[0 0 A1];
[eta,Y]=ode45(@falknerf,range,Vinit,options,beta(ibeta));
plot(eta,Y(:,2),'-k')
pause
% hold on
axis([0 1 0 1])
xlabel('\eta')
ylabel('Dimensionless velocity')
title(['Falkner-Skan , \beta = ',num2str(beta)])
pause
plot(eta,Y(:,1),'bo-',eta,Y(:,2),'r+:')
axis([0 1 0 1])
xlabel ('\eta')
ylabel ('f (blue) & df/d\eta (red)')
text (0.75,0.4,'f','FontSize',[18],'Color','b')
text (0.5,0.75,'df/d\eta','FontSize',[18],'Color','r')
pause
soln=[ eta Y(:,1) Y(:,2)];
% soln=[soln eta Y(:,1) Y(:,2)];
betad=[betad beta(ibeta)];
end
save solnd.dat soln -ascii
save betad.dat beta -ascii
x=2*[0.01:0.05:2];
y=x/4;
% [n1,n2]=size(eta)
% for i=1:n1
%     for j=1:n1
%         x(i)=eta(i);

```

```

%         y(j)=eta(i);
%         XX(i,j)=x(i);
%         YY(i,j)=y(j);
%     end
% end
% etal=eta;
% fun=Y(:,1);
% ffun=Y(:,2);
% y1=etal;
% psil=y1*fun';
% [fx,fy]=gradient(psil);
% quiver(XX,YY,fx,fy)
etal=eta;
fun=Y(:,1);
ffun=Y(:,2);
fffun=Y(:,3);
[n1,n2]=size(y);
mm=beta;

% Properties
nu=1.0e-6;           % m2/s
D=300e-6;           % m
Uo=10;              % m/s
Uinf=4*Uo/D; % This is valid only for mm=1, verify for other
scenarios
L=D;
UL=Uinf*L^mm;
ReL=(UL*L/nu);
C0=sqrt((mm+1)*nu*Uinf/2)*L^((mm-1)/2)/(Uinf*L^mm);
C5=sqrt((mm+1)*Uinf/(2*nu))*L^((mm+1)/2);
% End of the properties
for i=1:n2
    for j=1:n2
        etm(i,j)=y(j)*x(i)^((mm-1)/2);
    end
end
for i=1:n2
    for j=1:n2
        fi(i,j)=interp1(eta,fun,etm(i,j));
        fpi(i,j)=interp1(eta,ffun,etm(i,j));
        fbpi(i,j)=interp1(eta,fffun,etm(i,j));
        dedy(i,j)=x(i)^((mm-1)/2)*sqrt((mm+1)/2)*ReL^(1/2);
        dedx(i,j)=y(j)*((mm-1)/2)*x(i)^((mm-
3)/2)*sqrt((mm+1)/2)*ReL^(1/2);
    end
end
for i=1:n2
    for j=1:n2
        XX(i,j)=x(i);
        YY(i,j)=y(j);
        ZZ(i,j)=fi(i,j)*x(i)^((mm+1)/2);
        ux(i,j)=x(i)^(mm)*fpi(i,j);
        uy(i,j)=-x(i)^((mm-1)/2)*(fi(i,j)+((mm-
1)/(mm+1))*etm(i,j)*fpi(i,j));
        uy(i,j)=uy(i,j)*sqrt((mm+1)/2);
        uxx(i,j)=mm*x(i)^(mm-
1)*fpi(i,j)+x(i)^(mm)*fbpi(i,j)*dedx(i,j);

```

```

        uyy(i,j)=(etm(i,j)*fbpi(i,j)+fpi(i,j))*(mm-
1)/(mm+1)+fpi(i,j);
        uyy(i,j)=-x(i)^((mm-1)/2)*dedy(i,j)*uyy(i,j);
    end
end
rux=ux*UL;
ruy=uy*UL/sqrt(ReL);
ruxx=uxx*UL/L;
ruyy=uyy*UL/(L*sqrt(ReL));
[FX,FY] = gradient(ZZ);
%quiver(XX,YY,FY,-FX,5)
%axis([0 1 0 1])
%pause
quiver(XX,YY,ux,uy,2)
xlabel('x-axis','FontSize',[16],'Color','k')
ylabel('y-axis','FontSize',[16],'Color','k')
title('Velocity field','FontSize',[18],'Color','k')
% axis([0 2 0 1])
pause
contourf(XX,YY,ZZ)
% quiver(XX,YY,ux,uy,5)
title('Stream function \psi','FontSize',[18],'Color','k')
xlabel('x-axis parallel to the wall','FontSize',[18],'Color','b')
ylabel('y-axis normal to the wall ','FontSize',[18],'Color','b')
colorbar
pause

surface(XX,YY,ruxx)
surface(XX,YY,ruyy)
title('The extensional strain rates','FontSize',[18],'Color','k')
xlabel('x-axis')
ylabel('y-axis')
zlabel('d(U_y)/dy & d(U_x)/dx')
nu=1e-3/1000; % 1e-3 kg/m-s / 1000 kg/m3
Uinf= 9.72; % m/s
amp=300e-6/4; % m
for i=1:n2
    delta(i)=4.64*sqrt(nu*amp*x(i)/Uinf);
end
pause
plot(amp*x/1e-6,delta/1e-6)
xlabel('x - axis (\mu m)','FontSize',[18],'Color','b')
ylabel('\delta, boundary layer thickness \mu
m','FontSize',[18],'Color','b')

```


Code2. Matlab code to perform particle tracking

```
Tspan=[0.0 2];
% y(1), Dimensionless abcsissa
Y0(1)=0.1;
Y0(2)=0.1;
[time,Y]=ode45('Kin17',Tspan,Y0);
plot(time,Y(:,1),time,Y(:,2))

% plot(time,Y(:,1),time,Y(:,2),time,Y(:,3))
% plot(Y(:,1),Y(:,2))
pause

F=[time Y]
save reac17.dat F -ascii

function yprime=Kin17(t,y)
yprime=[0 0]';
B=0.45;
tol=0.00001;
m=1.0;
ReL=40;
a0=-5.18512e-3;
a1=3.09153e-2;
a2=5.89439e-1;
a3=-1.8361e-1;
a4=3.08239e-2;
a5=-2.648727e-3;
a6=9.1289e-5;
b0=-7.833143e-3;
b1=1.314886;
b2=-6.95605e-1;
b3=1.90579e-1;
b4=-2.852835e-2;
b5=2.214996e-3;
b6=-6.981759e-5;
% x =y(1)
% y=y(2)
eta=y(2)*y(1)^((m-1)/2)*sqrt((m+1)/2)*sqrt(ReL);
f=a0+a1*eta+a2*eta^2+a3*eta^3+a4*eta^4+a5*eta^5+a6*eta^6;
fp=b0+b1*eta+b2*eta^2+b3*eta^3+b4*eta^4+b5*eta^5+b6*eta^6;
yprime(1)=y(1)^m*fp;
yprime(2)=(f+((m-1)/(m+1))*eta*fp);
yprime(2)=yprime(2)*(y(1)^((m-1)/2)*sqrt((m+1)/2));
yprime(2)=-yprime(2)/sqrt(ReL);
```